

**Molybdenum Trioxide and Molybdenum Carbide as Promising
Hydrodeoxygenation Catalysts for Biomass Conversion**

by

Karthick Murugappan
M.S. Chemical Engineering Practice
Massachusetts Institute of Technology (2014)
B.S. Chemical Engineering
University of California, Berkeley (2011)

Submitted to the Department of Chemical Engineering
In Partial Fulfillment of the Requirements for the Degree of
Doctor of Philosophy
at the
MASSACHUSETTS INSTITUTE OF TECHNOLOGY
June 2017

© 2017 Massachusetts Institute of Technology. All rights reserved.

Signature of Author..... **Signature redacted**

Department of Chemical Engineering

May 18th, 2017

Certified by..... **Signature redacted**

Yuriy Román-Leshkov

Associate Professor of Chemical Engineering

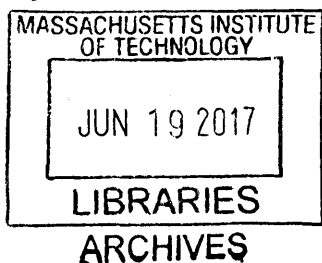
Thesis Supervisor

Accepted by..... **Signature redacted**

Daniel Blankschtein

Herman P. Meissner '29 Professor of Chemical Engineering

Chairman, Committee for Graduate Students



Molybdenum Trioxide and Molybdenum Carbide as Promising Hydrodeoxygenation Catalysts for Biomass Conversion

by

Karthick Murugappan

Submitted to the Department of Chemical Engineering
On May 18th, 2017 in Partial Fulfillment of the Requirements for the
Degree of Doctor of Philosophy in Chemical Engineering

Abstract

Growing concerns due to rising CO₂ emissions have made biomass an indispensable source of renewable fuels and chemicals. However, biomass inherently has high oxygen content, which translates to low energy density, thereby necessitating a deoxygenation step before being utilized as fuels. Recently, MoO₃ and Mo₂C have emerged as promising earth-abundant cheap catalysts that perform hydrodeoxygenation (HDO) at relatively low temperatures (≤ 673 K) and ambient H₂ pressures wherein oxygen is selectively removed as water. However, there exists a significant knowledge gap in understanding the stability and the active phases responsible for HDO of these catalysts. Furthermore, their applicability for real biomass conversions has not been largely demonstrated.

In this thesis, first, HDO of m-cresol, a biomass-derived model compound, is investigated over bulk and supported MoO₃ catalysts. Detailed reactivity and characterization studies reveal that Mo⁵⁺ species plays a critical role during HDO. Specifically, TiO₂ and ZrO₂ are identified as ideal supports as they feature superior HDO reactivity and stability over bulk MoO₃ by stabilizing intermediate Mo oxidation states (i.e. Mo⁵⁺) while bulk MoO₃ over-reduces to inactive metallic Mo. Translating from model compound studies, supported MoO₃ catalysts are demonstrated to be effective in converting biomass (pine) pyrolysis vapors to hydrocarbons (*ca.* 30 % yield).

In comparison with MoO₃, Mo₂C is significantly more stable and selective for HDO of 4-methylanisole to toluene under identical reaction conditions. Mo₂C predominantly breaks the stronger phenolic C-O bond while MoO₃ also breaks the weaker aliphatic C-O bond, likely due to the presence of Brønsted acid sites. To gain insights into the surface active sites, operando near-ambient XPS is employed during HDO and this technique revealed that HDO seems to operate via distinct active sites over both these materials. Finally, Mo₂C is shown to be effective in upgrading real lignin streams to a single product – propylbenzene, a precursor for renewable polymer. Overall, this thesis demonstrates the applicability of MoO₃ and Mo₂C in real biomass conversions and provides insights on the working nature of these catalysts, which will enable the design of more effective HDO catalysts.

Thesis Supervisor: Yuriy Román-Leshkov

Title: Associate Professor of Chemical Engineering

Acknowledgements

This thesis would not have been possible without the help, guidance and encouragement of many people.

First and foremost, I would like to sincerely thank my thesis advisor, Prof. Yuriy Román-Leshkov, for taking me into this group and guiding me throughout my thesis work. I always walk out of meetings with him, more motivated than before the meeting. His guidance and motivation have been highly instrumental in allowing me to push myself to achieve more throughout my PhD.

I would also like to thank my thesis committee – Prof. William H. Jr. Green and Prof. Karen K. Gleason for their insightful questions and thoughtful comments during all my committee meetings.

I would like to thank many people from the Román Group, without whom this thesis would not have been possible. First, I would like to acknowledge Dr. Teerawit Prasomsri, who laid the foundation for my thesis project in the group before I joined. He showed me how to use the vapor phase reactor, and taught me troubleshooting skills in lab. I would also like to thank Manish Shetty, with whom, I very closely worked during the initial stages of my thesis work, specifically on molybdenum oxides. I enjoyed our frequent insightful discussions both on research and non-research aspects and benefited a lot from all our interactions. Eric M. Anderson was a great bouncing board, always a fun person to discuss any ideas and we had a blast working together in Berlin while we performed *in situ* XPS measurements. We worked very closely on the lignin oil project. Dr. Sean T. Hunt set up the framework for lot of the molybdenum carbide synthesis work performed during my thesis. I thoroughly enjoyed all my discussions with him, and he was always willing to share his immense knowledge with us. Jen was a phenomenal lab safety representative, ensuring that the lab was safe and well-maintained. I would also like to thank Dr. Stijn Van de Vyer and Dr. Maria Milina, former postdocs in our lab, who were great friends and I learnt so much from both of them during their stint in MIT. Dr. Yuran Wang helped me a lot with things in lab on the weekends since she used to be in lab so often. Angry Karthik, my namesake, was a good friend to have in lab, and I enjoyed our late night conversations in lab, when probably both our experiments failed. Stan has now taken over the role from Yuran, with respect to helping me with things in lab when I am physically not there. I would also like to thank Dr. David Simakov for allowing me to inherit his LabVIEW system and also teaching me some of the reactor automation. I would also like to thank all the past and current members of the Román group, who made coming to lab a more enjoyable experience throughout my five years of PhD.

I would like to extend special thanks to BP, my industrial sponsor, for funding my thesis work and who made this PhD possible. Our frequent discussions with BP scientists, specifically Dr. Casey Hetrick and Dr. John Shabaker, provided me with an industrial perspective to my thesis project. I would also like to thank my collaborators at NREL, particularly, Dr. Mark. Nimlos, Dr. Calvin Mukarakate and Dr. Sridhar Budhi for both allowing and teaching me to use their set up for performing the catalytic fast pyrolysis experiments with real biomass. Similarly, I would like to thank Dr. Detre Teschner and Dr. Katarzyna Skorupska, scientists at BESSY II, Berlin, for going out of their way in helping us during our *in situ* XPS measurements. I would also like to thank my practice school station director, Dr. Robert Hanlon, whose teachings still resonate with me till today.

PhD is an extremely tough journey, and I am deeply indebted to my friends outside my lab who kept me sane and cheerful throughout this arduous journey. First, I would like to thank Ankur Gupta, who has been a phenomenal friend, and always being there for me regardless of the ups and downs during my PhD. Our daily frequent texts and coffee talks always cheered me up, and you were and always will be a constant source of inspiration. AG – the real STUD. I would also like to thank my friends from Southeast Asia – Sue and Siah, for all the fun times we had together in MIT. I would also like to thank my roommate, Mikhil Ranka, for all the discussions we had at home, regardless of the topic. We bonded well over these discussions and has been a great friend throughout my PhD. Rushabh Shah, the ultra-social guy, always ensured I come out of my lab and have fun, despite my deadlines. Rohit, never failed to amuse me with his one-liners and was a great lunch/coffee buddy, and thoroughly enjoyed all our conversations. Raju, aka Karthik, always kept encouraging me to automate whenever I said I have to go turn off a button in lab. He gave me practical suggestions and was always up for planning many travel adventures with me. I would also like to thank all my other friends – Krishna, Yamini, Ramya, Mila, Varuni, Mel, Himani with whom I have travelled and explored other areas in New England. A special shout-out to my undergraduate friends, especially Lucky aka Karthik and Uppu aka Upasna, who were always just a whatsapp away from me, and always there for me when I needed them.

Obviously, this would not have been possible without the love and support from my family. Though my family lives thousands of miles away from me, I have always been among their prayers and well-wishes, and their encouragement has always wanted me to strive for better. My mom has been a huge support since day 1, and she never failed to motivate me, and always told me that “Karthick, I will be praying for you”. Your prayers and well-wishes have always ensured that I do my work to my best abilities. Dad, you always gave me such practical advice that sometimes I end up just admiring you for your practicality. Your meticulousness and organization will always make me feel less accomplished than you, but I strive to reach your standards. My

brother, Arun, has been a great source of comfort as we enjoyed our frequent phone conversations. I would also like to acknowledge my in-laws for their affection, well-wishes and support throughout the final year of my PhD.

Last but not least, I would like to thank my wife, Lakshmi, who has been a tremendous source of support, especially in the final year of my PhD. She literally moved to USA for me, after our marriage and she quit her job to do that. It is extremely selfless of her to do this, and I am not sure if I would have been able to do what she did for me. I love you, and no words are enough to thank you for all that you have done for me (and will do for me). You are a more practical person than me, and you always motivated me to work to get my thesis done. You have been highly understanding of my situation and my late lab nights. Thank you for everything!

Table of Contents

Abstract	3
Acknowledgements	5
Chapter 1. Introduction	11
Chapter 2. Investigating bulk and supported MoO ₃ for HDO of lignin-derived model compounds	23
Chapter 3. Supported MoO ₃ as effective catalysts for the catalytic fast pyrolysis of lignocellulosic biomass	35
Chapter 4. Investigating Mo ₂ C for HDO of lignin-derived model compounds	75
Chapter 5. Probing the nature of surface active sites on MoO ₃ and Mo ₂ C during HDO of anisole using operando near-ambient XPS	101
Chapter 6. Mo ₂ C as a highly selective HDO catalyst for lignin upgrading	147
Chapter 7. Conclusions and Outlook	163
References	171

Chapter 1

Introduction

1. Lignocellulosic biomass as a renewable source of fuels and chemicals

With the world economy expected to double over the next 20 years,¹ the global energy demand is predicted to increase by around 30%¹ to sustain such growths. Though fossil fuels are predicted to constitute a major share (77%) of the energy usage in 2035, renewables, besides hydro and nuclear, are expected to grow rapidly to supply about 10% of global energy (**Figure 1.1**).¹

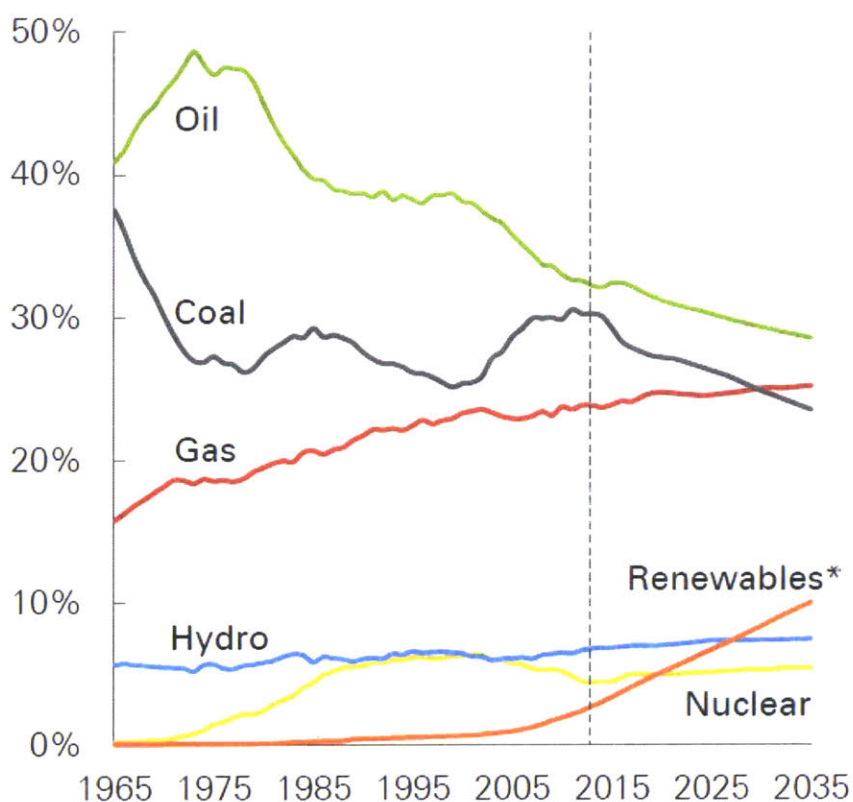


Figure 1.1 Shares of global primary energy. * Renewables includes wind, solar, geothermal, biomass and biofuels. Reproduced from BP Outlook 2035.

Among the renewables, there is a strong case for biomass-based liquid fuels due to its superior energy density, and compatibility with conventional hydrocarbon fuels as they can directly replace fossil fuel based gasoline, diesel and jet fuel.² Furthermore, growing concerns due to rising greenhouse gas emissions associated with fossil fuel usage have made biomass an indispensable renewable source of fuels and chemicals due to its net zero carbon emission.³ In the United States, Renewable Fuel Standard (RFS2), a federal initiative, mandates the annual production of 36 billion gallons of renewable fuels by 2022, or approximately 7% of yearly conventional fuel consumption.⁴ Among the renewable fuels, there is a significant increase in the requirement for second generation biofuels compared to first generation biofuels. First-generation biofuels refer to: 1) ethanol produced from food crops such as corn, sugarcane and wheat, and 2) bio-diesel from biomass. However, the production of these first-generation biofuels is controversial due to the “food vs. fuel” debate.⁵ Increasing concerns over reduction in greenhouse gas emissions have also raised questions over the long-term viability of these first-generation biofuels.⁶ In order to overcome these limitations, second-generation biofuels i.e. fuels from non-edible lignocellulosic biomass have gained a lot of attention in the last decade to produce biofuels in a more sustainable fashion. In addition to fuels, lignocellulosic biomass, is also considered to be the most promising renewable source for production of chemicals.^{7,8}

2. Fast pyrolysis as a viable technology to convert lignocellulosic biomass to fuels

Lignocellulosic biomass includes agricultural wastes like corn stover and sugarcane bagasse, perennial grasses like switchgrass and miscanthus, woody biomass and municipal solid waste.⁹ Biomass consists of three main structural components – 1) cellulose: 40-50 weight%; glucose polymer, 2) hemicellulose: 20-40 weight%; short chain, branched polysaccharide of five and six carbon sugars, and 3) lignin: 10-25 weight%; complex aromatic polymer.¹⁰ The exact compositions vary depending on the source of biomass. Lignocellulosic biomass can be converted to liquid fuels via three main routes.¹⁰ First, biomass can undergo fast pyrolysis to produce bio-oil which can

then be catalytically upgraded to fuel-grade quality oil. Second, biomass can be gasified to form syngas, namely CO-H₂ mixture, which can then be used as building blocks to produce larger liquid fuel molecules via Fischer-Tropsch syntheses. Third, biomass can be hydrolyzed to form sugar monomers, which can then be subsequently converted to fuel molecules. The first two strategies utilize all fractions of biomass while the third strategy only utilizes the hemicellulose and cellulose portions of biomass.¹¹ The advantage of fast pyrolysis lies in the direct production of a liquid fuel, which can be easily transported and stored.¹² Specifically, fast pyrolysis has been demonstrated to be able to convert solid biomass to higher energy density liquid bio-oils with typical yields of ca. 65 wt%.¹³⁻¹⁵ Fast pyrolysis essentially entails two key steps - first, a very high heating rate of the biomass particles in an inert gas (i.e. in the absence of air) at temperature ranges of 500-550° C, followed by immediate quenching to obtain the bio-oil product. Bio-oil is the dominant product (~ 65 wt% yield), with rest of the biomass converted to char and light gases. Given the advantages associated with fast pyrolysis, for my thesis, I will be predominantly focusing on upgrading of biomass via fast pyrolysis.

3. Deoxygenation critical for biomass upgrading

Bio-oil is a complex mixture of over 300 organic compounds.¹⁶ The organic compounds present in bio-oil can be categorized based on their functional groups. These categories are acids, esters, alcohols, ketones, aldehydes, miscellaneous oxygenate, sugars, furans, phenols, guaiacols and syringols. The chemical composition of bio-oil can vary drastically depending on the source of biomass. As such, general strategies to upgrade these groups of molecules would be beneficial in trying to upgrade the entire bio-oil as not all bio-oil is chemically equivalent. The various compounds are obtained from depolymerization and fragmentation reactions of the three main constituents of bio-oil: cellulose, hemicellulose and lignin.¹⁰ Phenols, guaiacols and syringols are obtained from the lignin fractions while miscellaneous oxygenates, sugars and furans are derived from cellulose and hemicellulose fractions.¹⁰ Remaining acids, esters, alcohols, ketones and aldehydes are obtained from the decomposition of miscellaneous oxygenates, sugars and furans.¹⁰

Figure 1.2 highlights differences in elemental composition between fast pyrolysis oil obtained from wood and conventional fuel oil. A major striking difference is the amount of oxygen content. Since pyrolysis oil or bio-oil is obtained from biomass, the elemental composition of bio-oil resembles more of biomass than that of petroleum oils.¹⁶ Clearly, bio-oil has significantly higher oxygen content than conventional fuel oil. This high oxygen content lowers the heating value of bio-oil (16-20 MJ/kg) compared to conventional fuels (40 MJ/kg)¹¹ and the polarity of oxygen rich molecules makes bio-oil immiscible with non-polar hydrocarbon molecules found in conventional oil. Bio-oil also has much higher water content (15-30%) than conventional fuel oils (0.1%), which also lowers the heating value as well as the flame temperature.¹⁶ Excess water also leads to ignition delays and lowers the combustion rate compared to diesel fuels.¹⁶ The presence of a wide range of compounds in bio-oil translates to a wide range in boiling points, thereby causing polymerization of some reactive

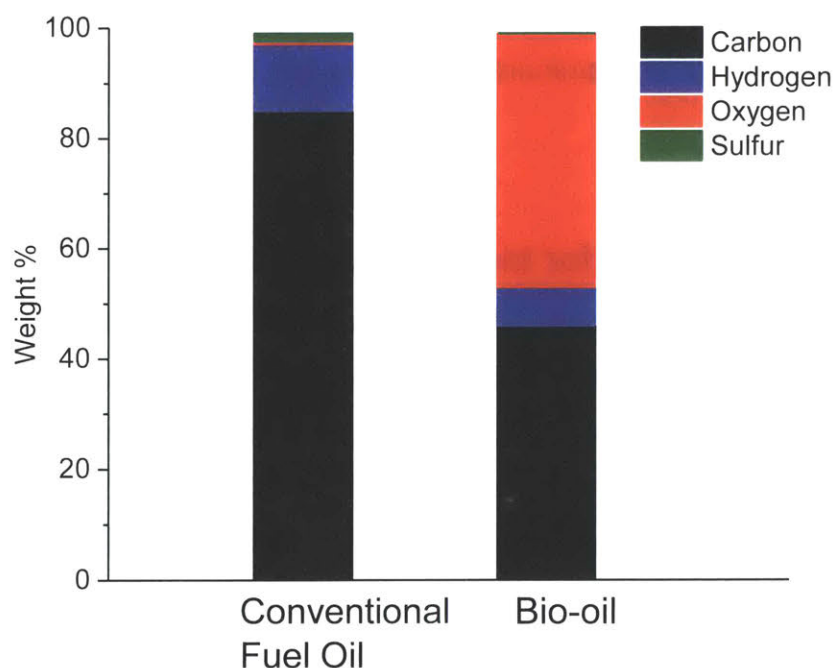


Figure 1.2 Elemental composition of conventional fuel oil and bio-oil obtained from fast pyrolysis of wood. Adapted from *ACS Catal.*, 2013, 3, 1047–1070¹¹

compounds upon slow heating during distillation, which leaves 35-50% of initial material as residues.¹⁶ Bio-oil is also very acidic with a pH of about 2.5, mostly due to the presence of formic acid and acetic acid.¹⁶ This high acidity corrodes most materials like

carbon steel and aluminum. Bio-oil also exhibits a range of viscosities, with the viscosities increasing in time when handled at high temperatures, thereby making bio-oil highly unstable.¹⁶ In summary, bio-oil has many undesirable fuel properties due to its extremely high oxygen content. This is exactly why fast pyrolysis bio-oil needs to be effectively deoxygenated before it can be used as a fuel, in order to resemble more like conventional fuel oil (**Figure 1.2**).

Though fast pyrolysis is an attractive avenue to convert whole biomass to fungible fuels, in the last decade, increasing research efforts have focused specifically on lignin extraction and transformation to valuable fuels and chemicals.¹⁷⁻²¹ Various technologies already exist to utilize cellulose and hemicellulose fractions of biomass, but lignin valorization poses significant technical challenges. At present, lignin is mostly burnt for process heat and power.²² Several cellulosic ethanol plants have been commissioned in USA,²³ which will generate huge quantities of lignin by-product. Due to the technical barriers associated with lignin utilization, lignin produced in these plants is currently designated for combustion to supply process heat and power. However, reports have indicated that ca. 60% more lignin will be produced than that will be required for energy needs.^{24,25} Furthermore, lignin valorization has shown to be critical for economics and sustainability of these cellulosic biorefineries,^{24,26} with a projected 30-40 % improvement in process economics.²⁷ Notably, lignin is also the largest renewable source of aromatics^{24,28}. However, similar to bio-oils obtained from fast pyrolysis, monomers obtained after lignin extraction also have significant quantities of oxygen. Once again, deoxygenation is a relevant critical step in valorizing lignin to chemicals and fuels.

4. State of current deoxygenation catalysts

Typically, deoxygenation of biomass based compounds occurs via two main routes: 1) Hydrodeoxygenation (HDO), wherein molecular hydrogen is used to selectively remove oxygen in the form of water,^{16,29} and 2) zeolite upgrading, wherein oxygen is rejected as CO₂ and H₂O in the absence of reducing gases such as H₂.²⁹ Several classes of HDO catalysts have been used and excellent review articles on HDO have been published.^{11,29,30} Typically, traditional industrial hydrotreating catalysts such as sulfided

Cobalt Molybdenum (CoMo) and Nickel Molybdenum (NiMo), supported on $\gamma\text{-Al}_2\text{O}_3$ have shown to be effective catalysts for HDO of bio-oil³¹ but these reactions are usually performed at high hydrogen pressures of up to 200 bars, thereby consuming large amounts of hydrogen.³² These high pressures also translate to a high operating cost. Moreover, these catalysts need to be continuously contacted with a sulfur source such as H_2S to prevent deactivation.^{11,33} However, sulfur is environmentally unfriendly, and adding extra sulfur to low-sulfur biomass is impractical. In addition, $\gamma\text{-Al}_2\text{O}_3$ supports are unstable in high water content typically present in bio-oil.³² Noble metals like Pt, Ru, Rh and Pd have also been explored for HDO but they usually favor a hydrogenation-deoxygenation mechanism as compared to a direct deoxygenation pathway for hydrotreating catalysts, thereby again consuming large quantities of hydrogen and resulting in more saturated hydrocarbons as the products.^{11,34,35} Furthermore, these noble metals are scarce, expensive, and extremely sensitive towards impurities such as iron and sulfur, thereby making them unsustainable in the long-term.²⁹

In comparison to HDO catalysts, zeolite upgrading seems to be a promising upgrading pathway, since zeolites such as HZSM-5 can deoxygenate bio-oils at atmospheric pressures without requiring external H_2 .¹¹ However, these zeolites suffer from poor hydrocarbon yields due to loss of carbon as CO and CO_2 and also deactivate rapidly due to coke formation.¹⁰ As such, there arises a need for an earth-abundant, cheap catalyst which can perform deep deoxygenation while consuming minimum hydrogen and not requiring sulfur. The optimal catalyst should also preserve the carbon number by selectively cleaving the C-O bond while leaving C-C bond intact and should also have high stability in water-rich bio-oil environment. The catalyst should also display high stability, recyclability and regenerability.

5. Molybdenum trioxide (MoO₃) and Molybdenum Carbide (Mo₂C) as an alternative HDO catalyst platform

Reducible metal oxides like Molybdenum Trioxide (MoO₃) have been widely used in catalysis for their unique redox properties, especially in oxidation of hydrocarbons, hydrocracking, and hydroisomerization.³⁶⁻³⁸ Density functional theory calculations have shown that hydrodeoxygenation of acetaldehyde (CH₃CHO) to ethylene (C₂H₄) and acrolein to propene are both favorable over MoO₃.^{39,40} These catalysts are believed to operate via an oxygen vacancy driven reverse Mars-van Krevelen mechanism. Hydrogen creates a vacancy on the MoO₃ surface by removing oxygen as water. Oxygenated reactant can then adsorb onto this vacancy, before the C-O bond is cleaved in the reactant, with the adsorbed oxygen then becoming part of the catalyst surface, thus regenerating the initial oxidized MoO₃ surface.^{39,40} Based on these computational studies, MoO₃ seems to be an attractive HDO catalyst. Recent work in our group screened many reducible metal oxides (MoO₃, V₂O₅, Fe₂O₃, CuO, WO₃) for HDO of acetone and revealed that MoO₃ featured the highest reactivity and selectivity (98%) to deoxygenated hydrocarbon products.⁴¹ A series of subsequent HDO experiments performed over MoO₃ with various biomass-derived oxygenates such as acetone, 2-hexanone, cyclohexanone, 2-methylfuran, 2,5-dimethylfuran and anisole revealed that MoO₃ is indeed capable of deoxygenating all these molecules at low H₂ pressures (≤1 bar) with high selectivity (>97%) towards unsaturated hydrocarbons. In addition, MoO₃ is also very cheap at just \$0.02 per gram, thereby making it an even more attractive deoxygenation catalyst.⁴² The catalyst was also regenerated easily by a simple calcination in air at 600°C for 1 hour. However, these were just preliminary experiments performed at one set of reaction conditions for short time on streams. Stability of catalyst needs to be investigated and the identity of the catalytically active phase still remains largely unknown. Moreover, the applicability of these catalysts for real biomass upgrading has not been demonstrated.

Similarly, Mo₂C has also shown to be active for HDO of biomass-derived oxygenates such as propanal, furfural and anisole.⁴³⁻⁴⁶ The properties of carbides are drastically different from their parent metals due to the insertion of carbon in the metal lattice. This carbon insertion in the metallic lattice contributes electron density, thereby

mimicking that of noble metals.²⁹ For example, Levy *et al.* showed that tungsten carbide can successfully isomerize 2,2-dimethylpropane, typically only catalyzed by noble metals like Platinum (Pt).⁴⁷ Metallic tungsten was not active for this reaction. This clearly showed that insertion of carbon into the metallic tungsten lattice altered the electronic properties, thereby making tungsten carbide behave more like Pt.⁴⁷ On the other hand, recent studies have shown that transition metal carbides do not have “Pt-like” properties in the presence of oxygen-containing molecules.⁴⁸ These unique properties of transition metal carbides have made Mo₂C an attractive catalyst for performing HDO. Though Mo₂C has shown deactivation during HDO of biomass-based model compounds, the reasons for deactivation are not clearly understood. Catalyst deactivation is likely attributed to coking and/or oxidation.^{44,46} However, no studies have been performed to distinguish between these two deactivation mechanisms. This understanding of deactivation mechanism will be crucial in tailoring the design of more effective HDO catalysts. Based on detailed kinetic studies, Bhan and co-workers have suggested that HDO on Mo₂C requires two distinct sites - one for H₂ dissociative adsorption and one for oxygenate activation.^{44,49,50} The site required for oxygenate adsorption was hypothesized to be metal-like in nature based on the invariant product generation rates normalized by *ex situ* CO chemisorption.^{44,49} Though CO is typically used to titrate metal sites, CO can also bind to oxygen vacancies on the surface of MoO_xC_yH_z, similar to that observed during HDO over MoO₃.⁵¹ Hence, the potential active site for oxygenate adsorption could be either metallic in nature or surface oxygen vacancies similar to that observed over MoO₃.

In summary, both MoO₃ and Mo₂C have recently emerged as promising HDO catalysts but there still remains a significant knowledge gap in terms of understanding the stability of the catalysts and elucidating the active phases responsible for HDO over both these materials. Detailed HDO reactivity studies coupled with bulk and surface characterization techniques will be crucial in allowing us to gain insights into the catalytically active phases and the deactivation mechanisms over both these materials. This knowledge will allow us to design more effective HDO catalysts as well as tune the operating conditions for better HDO performance.

6. Outline of the Thesis

Going forward, this thesis is organized into six chapters (**Chapter 2** to **Chapter 7**). In **Chapter 2**, MoO_3 is investigated for HDO of m-cresol, a lignin-derived model compound, wherein MoO_3 is demonstrated to be an effective HDO catalyst, capable of generating toluene at high selectivities (~99%). Detailed reactivity studies in combination with characterization techniques revealed that MoO_3 suffers from rapid deactivation at high temperatures (673 K) due to over-reduction to MoO_2 while the catalyst undergoes partial carburization during reaction to form an oxycarbide ($\text{MoO}_x\text{H}_y\text{C}_z$) at temperatures < 623 K. The presence of this oxycarbide is likely attributed to the higher stability observed at these lower temperatures. Based on the insights obtained from bulk MoO_3 , reducibility of the Mo species was determined to be a critical aspect in HDO reactivity. A detailed follow-up study was conducted on the influence of supports on the reducibility of dispersed molybdena species on reactivity and stability during HDO of m-cresol. TiO_2 and ZrO_2 are shown to be the best supports in enhancing HDO reactivity and stability as these supports stabilize intermediate Mo oxidation states while preventing the over-reduction to lower oxidation states which feature poor HDO reactivity. The reactivity data coupled with catalyst characterization point to the role of coordinately unsaturated (CU) sites in HDO across bulk and supported MoO_3 , consistent with an oxygen vacancy driven mechanism. These best performing catalysts for HDO of m-cresol i.e. $\text{MoO}_3/\text{TiO}_2$ and $\text{MoO}_3/\text{ZrO}_2$ are then selected for catalytic fast pyrolysis of real lignocellulosic biomass (pine). **Chapter 3** demonstrates the applicability of supported MoO_3 catalysts as a potential HDO catalyst platform for upgrading real biomass pyrolysis streams. Both these supported MoO_3 catalysts are shown to be promising alternative HDO catalysts as they produce ca.30 C% hydrocarbon products from pine, comparable to conventional zeolites.

In **Chapter 4**, Mo_2C nanoparticles supported on SiO_2 are synthesized and investigated for HDO of 4-methylanisole (another lignin-derived model compound). Reactivity studies show that though the catalyst features high selectivity to aromatic hydrocarbon toluene (97% on C_6^+ basis), but it suffers from rapid deactivation at atmospheric H_2 pressures. *Ex situ* Extended X-ray and Fine Structure (EXAFS) and XPS performed on spent $\text{Mo}_2\text{C}/\text{SiO}_2$ reveal that the bulk and surface structure of Mo_2C

respectively remain relatively unchanged throughout the reaction, indicating that neither bulk nor surface oxidation can account for the drastic deactivation. Deactivation is likely attributed to the build-up of carbonaceous species on the catalyst surface. To mitigate the effects of coking, the effect of elevated H₂ pressures is investigated in this study. Clearly, higher H₂ pressures promote catalyst stability, with Mo₂C/SiO₂ at 5 bar, 350 °C featuring the lowest first-order deactivation rate constant of 0.017 h⁻¹. Specifically, Mo₂C/SiO₂ exhibits 40 % conversion even after 140 h time-on-stream, indicating a highly stable catalyst. Again, the catalyst preferentially cleaves the stronger phenolic C-O bond to yield toluene as the major product. In contrast, MoO₃/SiO₂ operated at identical reaction conditions showed much lower conversions (~ 15%) and lower toluene selectivities (60% at steady state). The presence of oxygenates such as p-cresol throughout the reaction indicates that MoO₃/SiO₂ also cleaves the weaker aliphatic C-O bond, likely catalyzed by the presence of Brønsted sites in MoO₃.

To reconcile the differences in reactivity between the two materials, both bulk and surface characterization were performed on spent catalysts as detailed in chapter 2- 4, but these were all performed on an *ex situ* basis. These *ex situ* techniques do not capture the dynamics of the catalyst surface during the reaction. **Chapter 5** details operando near-ambient XPS studies performed over MoO₃ and Mo₂C during HDO of anisole to gain fundamental insights into the active sites responsible for HDO as well as attempt to understand the causes of deactivation. Briefly, near-ambient XPS studies reveal that MoO₃ goes through an initial oxidation followed by a subsequent reduction during HDO, consistent with an oxygen vacancy driven mechanism. In contrast, Mo₂C maintains its dominant Mo²⁺ speciation throughout the reaction. This invariance in Mo²⁺ contribution clearly indicates that *in situ* oxidation cannot account for the observed deactivation over Mo₂C, and that coking is indeed the likely cause of deactivation. Overall, this study suggests that the HDO seems to operate via distinct active sites on both these Mo-based catalysts.

Since now we have a better understanding of the two catalysts, Mo₂C is then chosen for its high selectivity in breaking the strong phenolic C-O bonds for application of HDO in the context of upgrading real lignin streams from biomass. **Chapter 6** demonstrates that Mo₂C is a remarkable HDO catalyst capable of deoxygenating all

lignin monomers present in lignin oils from both poplar wood and corn stover to produce propylbenzene and ethylbenzene as the main products. Both these alkylbenzenes can be dehydrogenated to produce styrene and methylstyrene in high purity. Preliminary ASPEN simulations also suggest that separation of methylstyrene from propylbenzene should be easier than that between styrene and ethylbenzene. Overall, using lignocellulosic biomass to produce potential styrene replacements has been demonstrated.

Chapter 7 summarizes the main findings of the research conducted during this thesis, discusses the limitation of the current work and presents the future outlook.

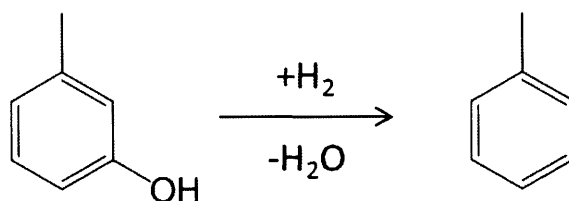
Most chapters of this thesis were written based on one or more separate publications⁵²⁻⁵⁴ and can be read independently.

Chapter 2

Investigating bulk and supported MoO₃ for HDO of lignin-derived model compounds

1. Investigating bulk MoO₃ for HDO of m-cresol^{*52}

Since lignin constitutes up to 30 wt% of lignocellulosic biomass, this chapter will specifically be focused on HDO of lignin-based model compounds. Lignin is a complex polymer of aromatic subunits that feature many oxygen functionalities such as C-O-C ether linkages, hydroxyl (-OH) and methoxy (-OMe) side groups. Specifically, since functionalized phenols are major constituents of bio-oil produced from lignin portion of biomass,¹¹ m-cresol is chosen as a model compound to investigate the stability of MoO₃ catalyst under different temperature regimes from 573 K to 673 K. MoO₃ (99 wt%) was purchased from Sigma-Aldrich and used as received.



^{*52} Adapted from Energy Environ. Sci., 2014, 7 (8), 2660-2669 with permission from the Royal Society of Chemistry.

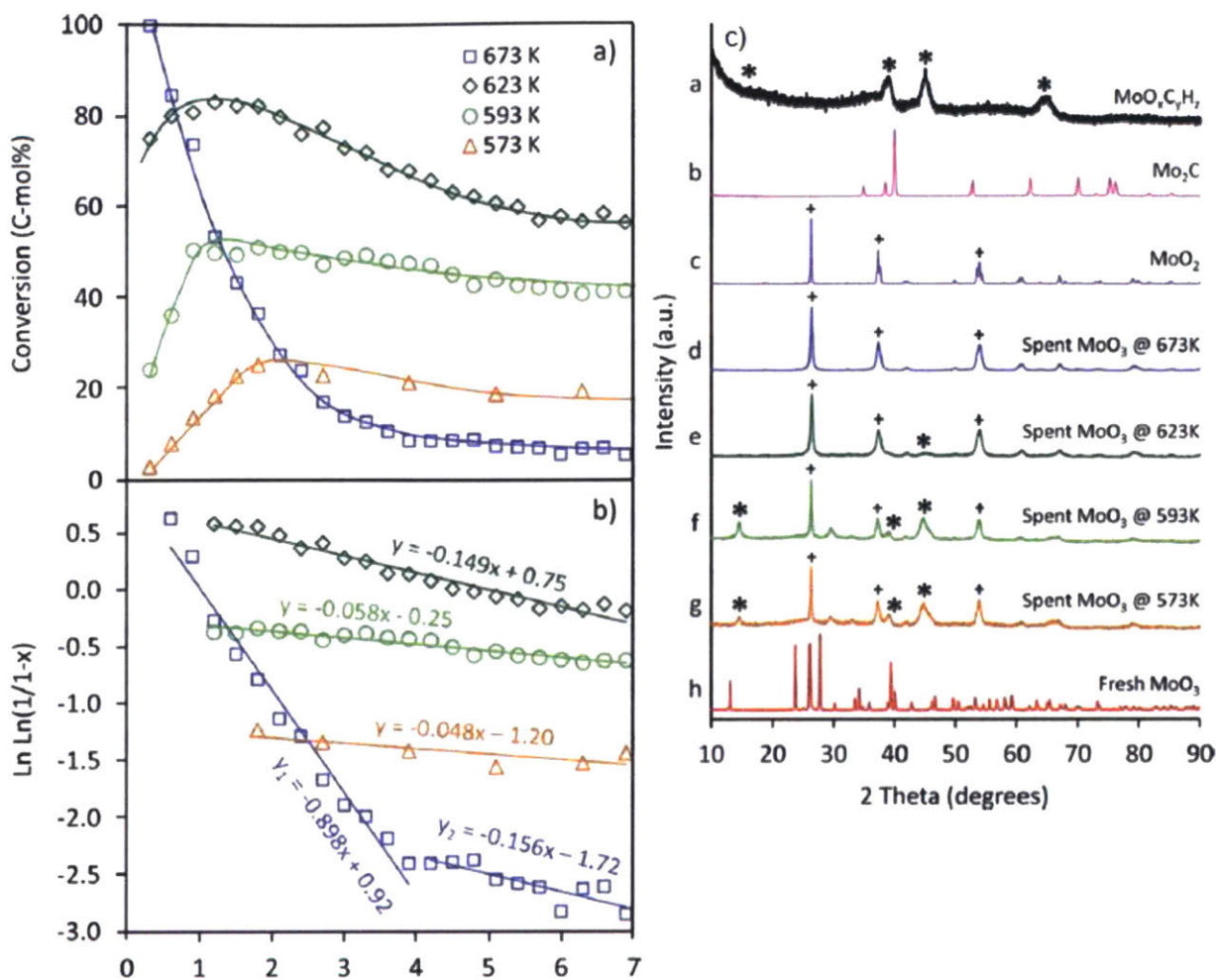


Figure 2.1 (a) Conversion of m-cresol as a function of time-on-stream (TOS) at various reaction temperatures, and (b) the corresponding catalyst deactivation profiles. (c) Normalized PXRD patterns of the spent MoO_3 catalysts in comparison with fresh MoO_3 , MoO_2 , Mo_2C and $\text{MoO}_x\text{C}_y\text{H}_z$ samples. Reaction conditions: $P_{\text{Total}} = 1.013$ bar (0.015 bar $P_{\text{m-cresol}}$, balance H_2), $W/F = 0.035$ $\text{g}_{\text{Cat}} (\text{mmol}_{\text{m-cresol}} \text{h}^{-1})^{-1}$, and no H_2 pre-reduction. Reproduced from *Energy Environ. Sci.*, 2014, 7 (8), 2660-2669

MoO_3 shows very high selectivity towards toluene ($\sim 99\%$) at all temperatures investigated. Toluene is a very valuable compound in terms of fuel quality due to its high octane number, and thus it is typically used as a gasoline additive. Though the catalyst is effective for HDO at all temperatures, the deactivation profiles are drastically different. At 673 K, MoO_3 shows the highest initial activity (100% conversion) but it deactivates very rapidly to 10% conversion in about 4 h (**Figure 2.1 (a)**). In contrast, at temperatures below ≤ 623 K, the catalyst exhibits much slower deactivation kinetics (**Figure 2.1 (b)**). Notably, an induction period < 2 h is observed before the catalyst

features full reactivity. The catalyst activity is recovered easily after regeneration by calcination with air at 673 K for 3 h.

Spent catalysts were characterized using Powder X-ray Diffraction (PXRD) (**Figure 2.1(c)**). PXRD pattern of spent catalyst at 673 K shows complete reduction of MoO_3 to MoO_2 as only peaks corresponding to MoO_2 are seen. Independent experiments revealed that MoO_2 is unreactive for HDO of m-cresol, consistent with the observed drastic deactivation at 673 K. This observation clearly shows that over-reduction of catalyst from MoO_3 to MoO_2 is the main cause of deactivation at 673 K. Interestingly, spent catalysts at temperatures below 623 K featured three new peaks in addition to MoO_2 peaks, associated with a molybdenum oxycarbohydride ($\text{MoO}_x\text{H}_y\text{C}_z$) phase.^{55,56} In order to probe the catalyst surface after reaction, X-ray Photoelectron Spectroscopy (XPS) was performed on spent catalysts (**Figure 2.2**).

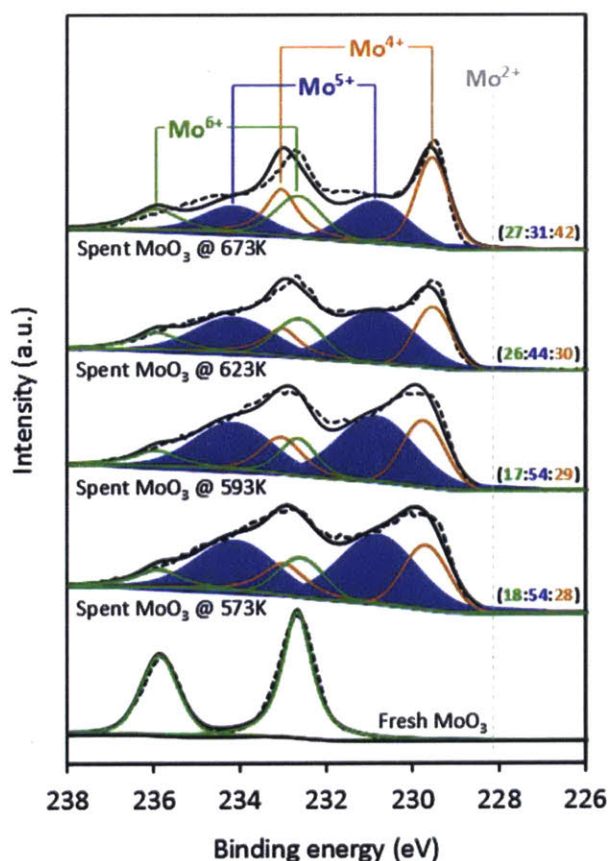


Figure 2.2 XPS of the Mo 3d energy region of the fresh and spent MoO_3 samples. The numbers in parentheses are the corresponding oxidation state percentages of Mo^{6+} , Mo^{5+} and Mo^{4+} , respectively. Reproduced from *Energy Environ. Sci.*, 2014, 7 (8), 2660-2669

The largest amount of Mo^{4+} present on spent catalyst at 673 K is consistent with the higher degree of reduction observed in PXRD as seen by the presence of MoO_2 phase. Similarly, the greater prevalence of Mo^{5+} at temperatures below 623 K seems to be consistent with the formation of oxycarbohydride. Overall, XPS data is consistent with the PXRD patterns showing the presence of MoO_2 at higher temperature and $\text{MoO}_x\text{C}_y\text{H}_z$ at lower temperatures. Comparing post-reaction characterization with reactivity data, it can be inferred that Mo^{5+} species are important to maintain stability and reactivity. These partially reduced species are stabilized by a partial carburization of the surface to form $\text{MoO}_x\text{C}_y\text{H}_z$, which might slow down the over-reduction to inactive MoO_2 (Mo^{4+}) species.

2. Reactivity and stability investigation of supported MoO_3 for HDO of m-cresol^{*53}

Based on the insights obtained from HDO over bulk MoO_3 in the previous section 2.1, the reducibility of Mo species is a critical aspect in controlling the HDO reactivity. MoO_3 was dispersed on various supports such as SiO_2 , $\gamma\text{Al}_2\text{O}_3$, TiO_2 , ZrO_2 , and CeO_2 to investigate the effect of supports on HDO reactivity and stability. 10 wt% MoO_3 loading on supports were prepared in order to obtain near-monolayer coverage of oligomeric molybdena species on the surface of the support. These supported catalysts were synthesized by wet impregnation method. Ammonium paramolybdate tetra (para) hydrate was used as the molybdenum precursor, which was added dropwise to the support under vigorous mixing. The sample was then left to dry at 373 K for 12 h before being calcined at 823 K under air flow for 3 h.

PXRD patterns of synthesized catalysts revealed a good dispersion of MoO_3 on the support surface.⁵³ All supported MoO_3 catalysts except $\text{MoO}_3/\text{TiO}_2$ showed only peaks corresponding to the respective supports. $\text{MoO}_3/\text{TiO}_2$ showed peaks associated with crystalline MoO_3 at these loadings. Raman spectroscopy was employed to probe the nature of dispersion of molybdenum species on the supports. Consistent with

***⁵³ Adapted from J.Catal, 2015, 331, 86–97, Copyright 2015, with permission from Elsevier.**

PXRD, only MoO₃/TiO₂ showed bands associated with crystalline MoO₃. However, these bands are lower in intensities than that associated with oligomeric Mo species, thereby indicating that molybdenum is predominantly present in the form of oligomeric species on these catalysts. Overall, PXRD and Raman spectroscopy indicate that molybdena species are dispersed as oligomeric moieties on the support surface across all supports investigated in this study. Oxygen chemisorption was performed to quantify the number of redox-active Mo sites while H₂-temperature programmed reduction (TPR) was used to investigate the reducibility.

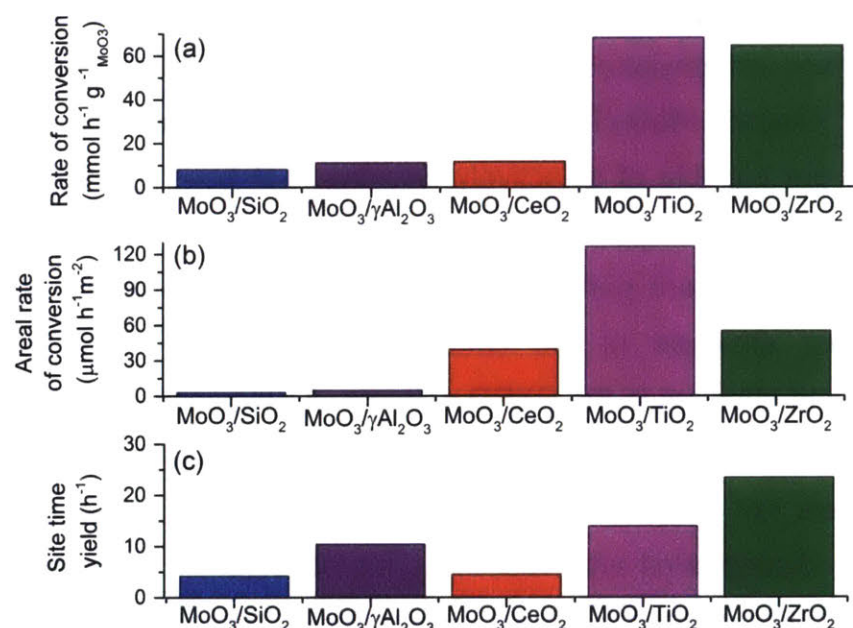


Figure 2.3 Initial rates of toluene production for supported MoO₃ catalysts (10 wt%). (a) Rate of conversion normalized by unit mass of MoO₃ (b) areal rate of conversion normalized by catalyst surface area and (c) toluene site time yield. Reaction conditions: T = 593 K, P_{Total} = 1.013 bar (0.0102 P_{m-cresol}, balance H₂), WHSV = 8.27 h⁻¹. Reproduced from *J.Catal.*, 2015, 331, 86–97

Figure 2.3 shows the initial reactivity data obtained across all supported MoO₃ catalysts which were normalized in three different ways: (a) by unit mass of MoO₃ (b) by total surface areas and (c) by number of oxygen-uptake sites. Clearly, MoO₃/TiO₂ and

MoO₃/ZrO₂ are the most reactive catalysts regardless of the way of normalization. Notably, both these catalysts also showed superior HDO reactivity than bulk MoO₃ on molybdenum mass basis. This shows that these supports clearly promote HDO reactivity. MoO₃ supported on TiO₂, ZrO₂ and CeO₂ featured > 97% selectivity to toluene while MoO₃ on SiO₂ and γ -Al₂O₃ showed lower selectivities of 90% and 76% respectively. This high selectivity to toluene shows that MoO₃ selectively cleaves the strong aromatic C-O bond via direct deoxygenation pathway instead of hydrogenation/dehydration pathway typically observed with noble metals.⁵⁷ Furthermore, the absence of sequential hydrogenation product of toluene such as methyl cyclohexane implies that MoO₃ does not catalyze undesired hydrogenation under these reaction conditions. However, MoO₃/ γ -Al₂O₃ featured additional products such as phenol and dimethylphenol, likely due to the presence of acid sites present on this support.⁵⁸ Overall, MoO₃/TiO₂ and MoO₃/ZrO₂ were the best performing HDO catalysts which are capable of selectively cleaving C-O bond to form toluene at very high selectivity (99 %).

PXRD and XPS were performed on spent catalysts to obtain insights into the bulk and surface structure of the catalysts post-reaction. Only bulk MoO₃ and MoO₃/TiO₂ showed changes in the PXRD patterns. As expected, bulk MoO₃ reduced to a mixture of MoO_xC_yH_z and MoO₂, consistent with observations in section 2.1. However, these peaks were not observed for MoO₃/TiO₂ though the peaks corresponding to crystalline MoO₃ disappeared after reaction. This observation suggests that the phase transformation of unsupported MoO₃ or surface MoO_x domains to MoO_xC_yH_z probably cannot be detected with PXRD. Peaks associated with MoO₂ overlap with TiO₂ peaks, and therefore cannot be resolved.

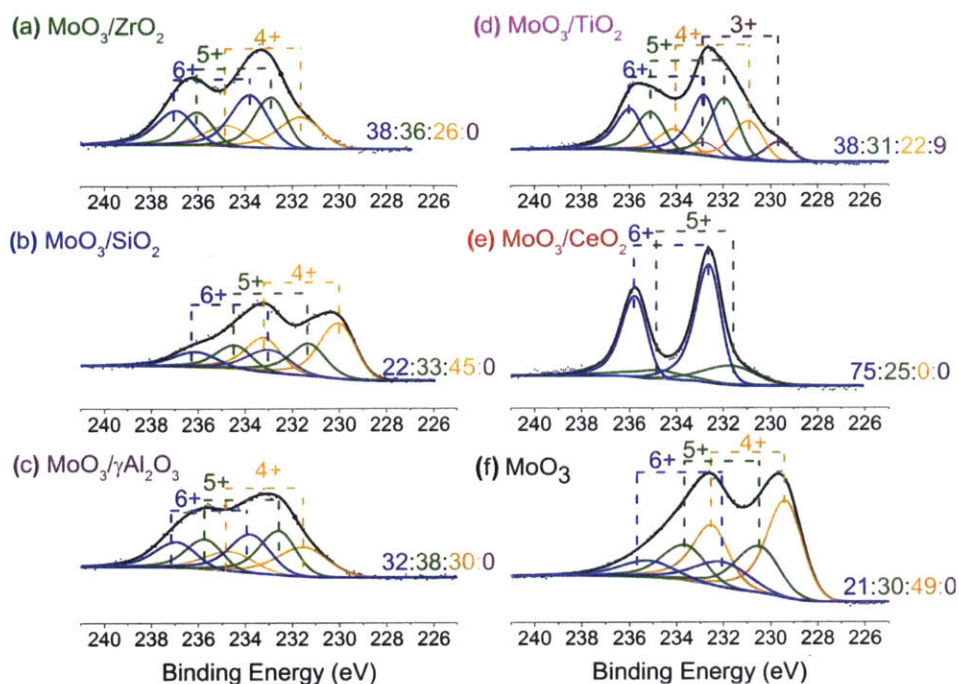


Figure 2.4 XPS analysis showing the Mo 3d energy region of the spent catalysts at time on stream (TOS) = 7.5 h. The ratios displayed correspond to the proportion of Mo oxidation states of Mo⁶⁺, Mo⁵⁺, Mo⁴⁺, and Mo³⁺, respectively. Reaction conditions: T = 593 K, P_{Total} = 1.013 bar (0.0102 P_{Feed}, balance H₂), WHSV = 8.27 h⁻¹. Reproduced from *J.Catal.*, 2015, 331, 86–97

XPS analysis performed on spent catalysts after 7.5 h of reaction reveal that all samples contain reduced Mo oxidation states (Mo⁵⁺ and Mo⁴⁺) as seen in **Figure 2.4**. Notably, MoO₃/CeO₂ featured the highest proportion of Mo⁶⁺ state (75%) with remaining 25% attributed to Mo⁵⁺ species. All other catalysts show the presence of Mo⁵⁺ in the range of 30% to 40%. Furthermore, MoO₃/TiO₂ showed a unique Mo³⁺ species, consistent with observations by Thompson and co-workers.⁵⁹ Importantly, MoO₃ supported on TiO₂, ZrO₂ and γAl₂O₃ exhibit the lowest extent of reduction as seen by the presence of ca. 25% of Mo⁴⁺ species while bulk MoO₃ and MoO₃/SiO₂ feature ca. 50% of Mo species in the form of Mo⁴⁺.

The best performing HDO catalysts, MoO₃/TiO₂ and MoO₃/ZrO₂ were then investigated for long-term stability in comparison with bulk MoO₃. Since bulk MoO₃ is less active than MoO₃ supported on TiO₂ and ZrO₂, 4 times more mass of MoO₃

compared to equivalent molybdenum mass on supported catalysts was loaded in order to compare the stability of these catalysts at similar conversions.

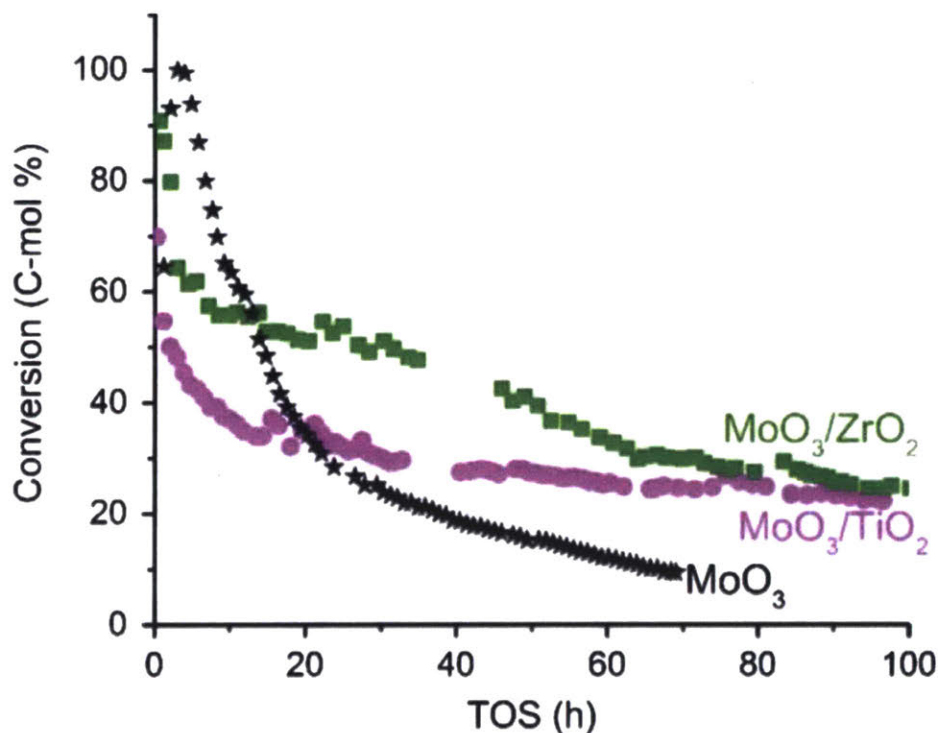


Figure 2.5 Reactivity data of m-cresol HDO to toluene for time on stream (TOS) = 100 h, on MoO₃/ZrO₂, MoO₃/TiO₂, and bulk MoO₃ catalysts. Reaction conditions: T = 593 K, P_{Total} = 1.013 bar (0.0102 P_{m-cresol}, balance H₂), WHSV = 8.27 h⁻¹ for supported catalyst, 2.06 h⁻¹ for bulk MoO₃. Reproduced from *J.Catal.*, 2015, 331, 86–97

As seen in **Figure 2.5**, supported MoO₃ catalysts display higher stability than bulk MoO₃. Though bulk MoO₃ initially features a 2 h induction period before reaching full conversion, the catalytic reactivity drops to about 10% over 70 h. The deactivation can be split into three zones with first-order deactivation rate constants of 0.317, 0.085, and 0.026 h⁻¹ for TOS ranges from 4-8.5, 8.5-24, and 24-70 h. However, both MoO₃/TiO₂ and MoO₃/ZrO₂, showed no induction period and featured initial conversions of 70% and 90% respectively. Specifically, MoO₃/TiO₂ featured three zones of deactivation with first-order deactivation rate constants of 0.305, 0.039 and 0.006 h⁻¹ during TOS ranges from 0-2, 2-14.5 and 14.5-100 h. Similarly, MoO₃/ZrO₂ featured two deactivation zones with first-order deactivation rate constants of 0.197 and 0.013 h⁻¹ for TOS values from 0-5.5

h and 5.5-100 h. Overall, both the supported catalysts showed drastically lower deactivation than bulk MoO₃ as seen by the lower deactivation rate constants and they both display ca. 30% conversion even after 100 h of reaction. This observation clearly shows that supporting MoO₃ on TiO₂ and ZrO₂ imparts superior stability for HDO of m-cresol as compared to bulk MoO₃.

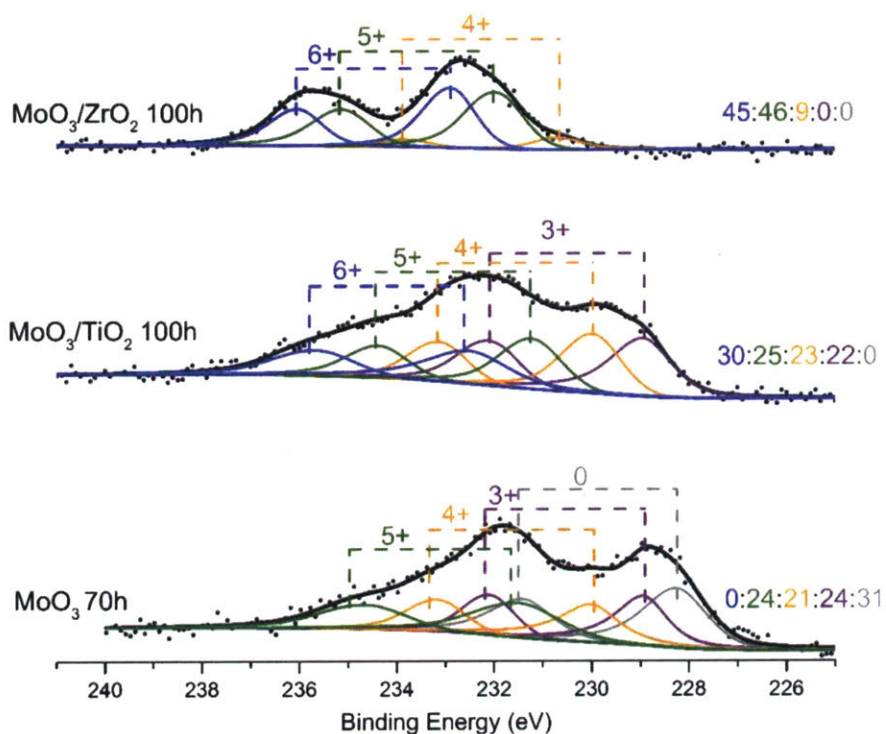


Figure 2.6 XPS analysis showing the Mo 3d energy region of the spent catalysts at time on stream (TOS) = 100 h for supported MoO₃ catalysts and 70 h for bulk MoO₃. The ratios displayed correspond to the proportion of Mo oxidation states of Mo⁶⁺, Mo⁵⁺, Mo⁴⁺, Mo³⁺ and Mo⁰ respectively. Reaction conditions: T = 593 K, P_{Total} = 1.013 bar (0.0102 P_{m-cresol}, balance H₂), WHSV = 8.27 h⁻¹ for supported catalysts, 2.06 h⁻¹ for bulk MoO₃. Reproduced from *J.Catal.*, 2015, 331, 86–97

XPS of spent catalysts after long-term stability runs (**Figure 2.6**) showed that bulk MoO₃ predominantly reduced to Mo⁴⁺ and Mo⁰, with no Mo⁶⁺ peaks seen after 70 h. C 1s spectra does not feature any strong signals associated with carbidic carbon (**Figure 2.7**).

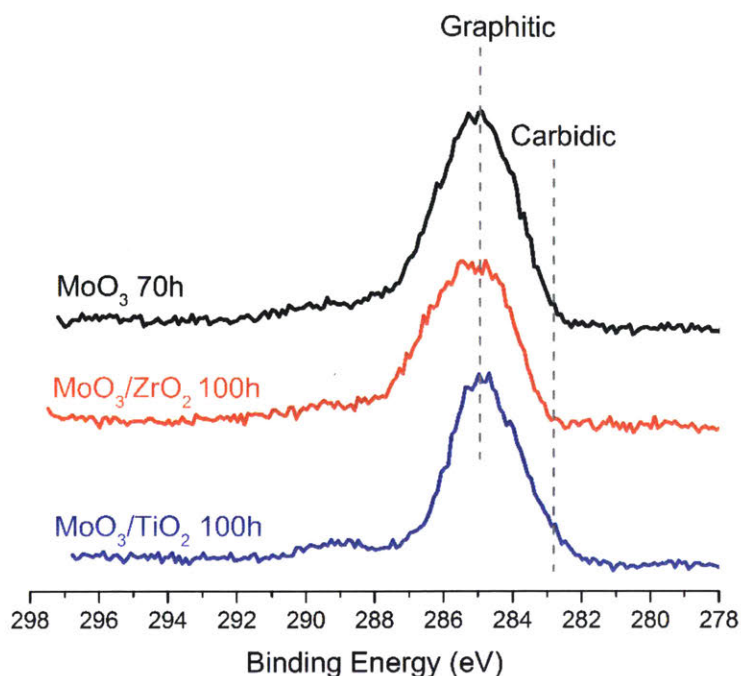


Figure 2.7 XPS analysis showing the C 1s 3d energy region of the spent catalysts at time on stream (TOS) = 100 h for supported MoO₃ catalysts and 70 h for bulk MoO₃. Reaction conditions: T = 593 K, P_{Total} = 1.013 bar (0.0102 P_{m Cresol}, balance H₂), WHSV = 8.27 h⁻¹ for supported catalysts, 2.06 h⁻¹ for bulk MoO₃. Reproduced from *J.Catal.*, 2015, 331, 86–97

However, the large amount of graphitic carbon might subsume the carbidity carbon, thus we cannot exclude the formation of Mo₂C during reaction. Clearly, the drastic deactivation observed for bulk MoO₃ can be attributed to the over-reduction of Mo⁶⁺ species to Mo⁴⁺ (MoO₂) and Mo⁰ (metallic Mo), consistent with the over-reduction and deactivation observed at 673 K in section 2.1. In stark contrast, both MoO₃/TiO₂ and MoO₃/ZrO₂ featured predominantly intermediate Mo oxidation states (Mo⁵⁺ and Mo⁴⁺). Similar to the Mo 3d XPS spectra acquired after 7.5 h (**Figure 2.4**), MoO₃/TiO₂ again showed the presence of Mo³⁺ species. However, both supported MoO₃ catalysts did not show any signals associated with metallic Mo, while peaks associated with Mo⁶⁺ were still seen in both spectra. This observation strongly indicates that the presence of supports prevents the over-reduction of Mo to lower oxidation states while keeping the molybdenum in intermediate oxidation states, which could account for the superior stability observed with these catalysts. Independent experiments also revealed that the

initial reactivity of both these supported MoO₃ catalysts can be completely recovered after a simple calcination under O₂ flow at 673 K for 6 h. This reactivation implies that the deactivation is reversible in nature, and likely due to both over-reduction of Mo species to oxidation states with lower reactivity and accumulation of carbonaceous species.

Prior reports in literature have shown that reduction of supported molybdenum catalysts creates coordinatively unsaturated (CU) sites that are active for other reactions such as hydrogenation and hydrodesulfurization.⁶⁰ The metal-support interaction should influence the reducibility of Mo species, thereby having an effect on the number of oxygen vacancies created on the surface, thus directly affecting the HDO reactivity. This is in line with our hypothesis that HDO on bulk MoO₃ occurs via an oxygen vacancy driven mechanism, as explained in previous section 2.1. The prevalence of Mo⁵⁺ on supported MoO₃ catalysts indicates the presence of CU sites, which are likely responsible for the activation of oxygenate species (m-cresol). This observation is consistent with that seen on bulk MoO₃ in section 2.1 wherein presence of larger amounts of Mo⁵⁺ species is attributed to higher stability at temperature ≤ 623 K. On bulk MoO₃, Mo⁵⁺ can be generated either by carbon incorporation of MoO₃ to form MoO_xC_yH_z or just reduction of MoO₃ to MoO_{3-x} under H₂ flow.⁵² Though PXRD patterns of spent supported MoO₃ catalysts did not show any peaks associated with molybdenum oxycarbohydride (MoO_xC_yH_z), the presence of Mo⁵⁺ moieties seems to correlate with HDO reactivity. Post-reaction XPS on catalysts after 100 h on stream indicates the stabilization of intermediate Mo oxidation states (Mo⁵⁺ for MoO₃/ZrO₂, and Mo⁵⁺ and Mo³⁺ for MoO₃/TiO₂) in contrast to the complete reduction to metallic Mo on bulk MoO₃ catalysts. Thus, the enhanced stability of these supported catalysts can be explained by the stabilization of these intermediate Mo oxidation states upon dispersion of MoO₃ on these supports. Overall, the supports allow easier formation of CU sites at lower temperatures as well as slow down the over-reduction to lower oxidation states with poorer HDO reactivity. Furthermore, the differences in toluene site time yield (STY) i.e. toluene production rates normalized by moles of redox active Mo species, across different supports indicate differences in intrinsic HDO reactivity. This difference can be rationalized with electronegativity of the support cation. Largely, toluene STY increases

with decreasing electronegativity of the support cation. Supports with lower cation electronegativity lead to higher electron density in the Mo-O-support bridging oxygen, thereby increasing reactivity for redox reactions.⁶¹ These Mo-O-support bridging oxygen atoms are hypothesized to play a key role in H abstraction which is the first step in the HDO pathway. Overall, the results obtained in this study are consistent with an oxygen vacancy mechanism.

In summary, all supported MoO₃ catalysts feature high toluene selectivity during HDO of m-cresol at relatively low temperature of 593 K and atmospheric H₂ pressures. Molybdenum species predominantly exist as oligomeric domains across all supports. The intrinsic HDO activity was compared by normalizing toluene production rates by number of redox active Mo species, which was quantified based on O₂ chemisorption. The intrinsic differences in HDO reactivity observed based on toluene STY values can be attributed to the ease of reducibility of Mo species on the surface as well as the electronegativity of the support cation. Our study shows that among the supports investigated, TiO₂ and ZrO₂ are the best supports in enhancing HDO reactivity and stability. Post reaction XPS on spent catalysts reveal that these two supports promote the stabilization of intermediate Mo oxidation states while preventing the over-reduction to lower oxidation states which feature poor HDO reactivity. Catalyst deactivation is reversible and likely caused by reduction to lower oxidation species as well as build-up of carbon deposits. Both MoO₃/ZrO₂ and MoO₃/TiO₂ can be easily regenerated by simple calcination at 673 K under O₂ flow. The reactivity data coupled with catalyst characterization point to the role of CU sites in HDO, consistent with an oxygen vacancy driven mechanism.

Acknowledgements

Dr. Teerawit Prasomsri and Manish Shetty are gratefully acknowledged for their major contributions to this chapter.

Chapter 3

Supported molybdenum oxides as effective catalysts for the catalytic fast pyrolysis of lignocellulosic biomass*

1. Introduction

The demand for the production of renewable transportation fuels and chemicals from lignocellulosic biomass has increased over the last decade in our efforts to lower the carbon footprint of the transportation and chemicals sectors. Among the many conversion technologies currently available, fast pyrolysis has emerged as a promising avenue to convert low energy density biomass to higher energy density liquid bio-oils with typical yields of *ca.* 65 wt%.¹³⁻¹⁵ However, these bio-oils cannot be directly used as or blended with transportation fuels due to their high oxygen, water, and acid content.^{11,16} As a result, a catalytic upgrading step to stabilise and deoxygenate bio-oil is required before it can be processed with regular transportation fuels. Recently, increasing research efforts have focused on catalytic fast pyrolysis (CFP)—a single step bio-oil upgrading process wherein the hot pyrolysis vapours are contacted with a catalytic bed prior to condensation.^{58,62-64} CFP is a promising alternative to the conventional two-step bio-oil upgrading process as it is simpler and avoids cumbersome condensation and re-evaporation steps.⁶³⁻⁶⁵ *Ex situ* CFP takes place when the pyrolysis and upgrading processes are decoupled by placing a catalytic bed downstream of the pyrolysis reactor.⁵⁸ In contrast, during *in situ* CFP the feedstock is mixed with the upgrading catalyst prior to heating.⁵⁸ Both strategies have been shown to produce higher quality bio-oils than the non-catalytic pyrolysis process.⁶² Although *in situ* CFP features more intimate contact between biomass and the catalyst, the catalyst is exposed to char and ash, which can be detrimental to the catalyst performance.^{66,67} Recent techno-economic and uncertainty analyses have also indicated that the *ex situ*

*Reproduced from *Green Chem.*, 2016, 18 (20), 5548-5557⁵⁴ with permission from the Royal Society of Chemistry.

operating mode could offset more commercialisation risks than the *in situ* mode.⁶⁷

Proton-exchanged zeolites, such as HZSM-5, are the state-of-the-art catalysts used for the production of hydrocarbons from biomass via CFP.^{63,68-72} Although gasoline-range aromatics are obtained with these materials, typically low carbon yields, high light gas production, and rapid catalyst deactivation due to coking are observed.^{32,68,73} These shortcomings are a consequence of the inherently hydrogen deficient nature of lignocellulosic biomass (it features an effective hydrogen to carbon ratio ranging from 0 to 0.3)⁷⁴ coupled with the lack of external H₂ gas addition to the process, which forces high degrees of deoxygenation to occur by decarbonylation, decarboxylation, dehydration and coking. As such, large catalyst quantities are needed to achieve high conversions.^{68,75-78} Indeed, the development of alternative CFP catalysts that can overcome these technical barriers remains an important challenge.

Hydrodeoxygenation (HDO) is a common upgrading strategy that uses hydrogen to selectively remove oxygen as water without breaking molecular carbon backbones. Recently, Román-Leshkov *et al.* showed that molybdenum trioxide (MoO₃) is an effective HDO catalyst that produces olefinic and aromatic hydrocarbons at high selectivities (> 97%) from various biomass-derived oxygenates under mild conditions (T = 320°C and P_{H₂} ≤ 1 bar).^{41,52} These studies revealed that Mo⁵⁺ species were important for maintaining the activity of the catalyst over extended time periods and were stabilised by a partial carburisation of the surface that prevented over-reduction to less reactive Mo⁴⁺ species.⁵² Coupled reactivity and characterisation studies showed that dispersing MoO₃ on high surface area oxides, such as ZrO₂ and TiO₂, significantly improved both the reactivity and stability of the catalyst during the HDO of *m*-cresol.⁵³ An oxygen vacancy driven mechanism was hypothesized to be responsible for the HDO of oxygenates over both bulk and supported MoO₃ catalysts.^{41,53} Similarly, Bhan and co-workers have shown that a combination of metallic and Brønsted acid sites in partially oxidized molybdenum carbide can effectively hydrodeoxygenate biomass-derived molecules using atmospheric H₂ pressures and low temperatures (420-520 K).^{46,79-81}

MoO₃ has been tested in CFP of lignocellulosic biomass with some success. Budhi *et al.* investigated molybdenum supported on KIT-5 mesoporous silica for the CFP of pine in the absence of H₂ gas.⁸² The catalysts preferentially produced furans

and phenols with small amounts of aromatic hydrocarbons.⁸² Nolte *et al.* performed CFP of cellulose, lignin, and corn stover in a tandem microreactor using bulk MoO₃ at low H₂ pressures and biomass:catalyst ratios of ca. 0.006, producing mainly linear alkanes and aromatics.⁸³ Although the HDO of model compounds has been demonstrated with supported MoO₃ catalysts, the performance and stability of these catalysts have not been investigated for the CFP of lignocellulosic biomass using atmospheric hydrogen pressures.

In this contribution, 10 wt% MoO₃ supported on TiO₂ and ZrO₂ catalysts are investigated for the CFP of pine at 500°C and H₂ pressures ≤ 0.75 bar. A 10 wt% MoO₃ loading was used to obtain a near-monolayer coverage of oligomeric molybdena species on the surface of the support, as reported by Shetty *et al.* during the HDO of m-cresol.⁵³ This study also showed that oligomeric molybdena species supported on TiO₂ and ZrO₂ were the optimal supports for HDO of all oxide supports investigated.⁵³ For this reason, 10 wt% MoO₃/TiO₂ and MoO₃/ZrO₂ catalysts were selected for this work. Catalyst HDO performance is monitored in real time by coupling an *ex situ* catalytic fast pyrolysis unit with a molecular beam mass spectrometer (MBMS). An *ex situ* processing mode was selected to independently study the effect of catalyst on the hydrodeoxygenation of pyrolysis vapours.⁶⁶ We use a multivariate analysis of the MBMS data to group products with varying degrees of deoxygenation into “bins”, which are then tracked as a function of the cumulative amount of pyrolysis vapours exposed to the catalytic bed for biomass:MoO₃ mass ratios ranging from 0 to 20. These data are complemented by detailed product identification and quantification using a tandem microreactor-Gas Chromatography Mass Spectrometry (GCMS) system. The catalysts are compared to a state-of-the-art acid zeolite with the MFI topology (HZSM-5) tested in the microreactor-GCMS system at similar reaction conditions. The spent catalysts are then characterised using powder X-ray diffraction (PXRD) and X-ray photoelectron spectroscopy (XPS) to provide insights on the changes in bulk structure and stabilisation of specific Mo oxidation states, respectively.

2. Experimental

2.1 Materials and synthesis

Southern yellow pine (42% cellulose, 21% hemicellulose, and 30% lignin) supplied by Idaho National Laboratory was used as lignocellulosic biomass feedstock for all the experiments.⁶⁸ The C, H and N contents were measured using a LECO TruSpec CHN module, as discussed previously,⁸⁴ and the oxygen content was measured by difference from known stoichiometries. The elemental analysis on a dried biomass sample showed that it contains 50% carbon, 43% oxygen, 6% hydrogen, and less than 1% nitrogen. The moisture content was 2%. Bulk molybdenum (VI) oxide (MoO_3 , $\geq 99.5\%$), molybdenum (IV) oxide (MoO_2 , $\geq 99\%$), and molybdenum carbide (Mo_2C , $\geq 99.5\%$) were purchased from Sigma-Aldrich. HZSM-5, with a silica-to-alumina ratio (SAR) of 30 and a 20 wt% silica binder, was purchased from Nexceris. Titanium (IV) oxide (TiO_2 , anatase phase, 21 nm, $\geq 99.5\%$, Sigma Aldrich) was used directly as a support while zirconium(IV) oxide (ZrO_2) nanoparticles were synthesised using previously reported methods.⁸⁵ Supported 10 wt% $\text{MoO}_3/\text{TiO}_2$ and $\text{MoO}_3/\text{ZrO}_2$ were prepared by wet impregnation of aqueous solutions of ammonium paramolybdate tetra(para) hydrate ($(\text{NH}_4)_6\text{Mo}_7\text{O}_{24}\cdot 4\text{H}_2\text{O}$, 99%, Alfa Aesar) as described previously.⁵³ Catalysts were sieved to 500-1000 μm pellets before use in the CFP experiments.

2.2 Catalytic fast pyrolysis

2.2.1 Horizontal reactor-MBMS

CFP of pine was performed in a horizontal quartz annular reactor coupled to a MBMS (**Figure S3.9**).^{68,82} The reactor was mounted in a five-zone furnace where small boats loaded with pine were pyrolyzed in a batch-wise fashion; the pyrolysis vapours were then carried over a catalytic bed in a $400\text{ cm}^3\text{ min}^{-1}$ of 50 vol% H_2 -He mixture. Both the pyrolysis and upgrading zones were typically maintained at 500°C . More specifically, a total of 40 quartz boats containing 50 mg of pine per boat were introduced one by one about every 2 min into the pyrolysis chamber. The catalytic bed consisted of 1.0 g of catalyst mixed with 0.5 g of an inert (sand) packed between two layers of quartz wool. Prior to sampling by the MBMS, the H_2 -He gas mixture was diluted with more He at the

end of the reactor ($4000 \text{ cm}^3 \text{ min}^{-1}$) to meet the required flow demands of the MBMS sampling orifice. Upon entering the MBMS, this mixed gas stream undergoes adiabatic expansion through a $250 \text{ }\mu\text{m}$ orifice leading into a vacuum chamber held at 0.1 Torr, which cools the gas and quenches any secondary reactions. The gas is then skimmed into a molecular beam for ionisation with an electron impact ionisation source (22.5 eV), producing positive ions that are detected by a quadrupole mass spectrometer. Mass spectra for all compounds with an m/z range between 10 and 450 are collected simultaneously every second. A dilute flow of Ar ($40 \text{ cm}^3 \text{ min}^{-1}$) mixed into the He diluent stream serves as an internal standard to correct for any shifts in signal due to flow fluctuations. The reactor was operated at a nominal weight hourly space velocity (defined as the ratio between the mass flow rates of pyrolysis vapours and the mass of the catalyst) of 3.6 h^{-1} , assuming a 60% mass yield of pyrolysis vapours from pine pyrolysis is obtained for each boat, and that pyrolysis event lasts for 0.5 min.⁶⁸

2.2.2 Multivariate analysis of MBMS spectra

Multivariate analysis was performed to identify correlated groups of mass spectral peaks in the upgraded vapours and to track their dynamics as a function of biomass to catalyst ratio in the horizontal reactor-MBMS CFP experiments. The analysis was performed using the multivariate curve resolution optimised by alternate least squares (MCR-ALS) method found in the software package “The Unscrambler” (Camo Software AS, version 9.7). Multivariate curve resolution (MCR) resolves the principal component analysis results into mathematically constructed components, which have mathematically derived sub-spectra that are used to partition the original variance of the data set into the estimates of constituent concentrations.^{68,82} As a result, the concentration profiles of each component in an unresolved mixture of two or more constituents can be determined as long as the data has enough degrees of freedom to identify the separate sources of variance.^{68,82} This capability is extremely useful to analyze highly complex mixtures where the components are unavailable as pure components (PCs). The Unscrambler MCR algorithm performs the selection of pure-variables from a principal component analysis (PCA) of independent standard loadings to find the initial estimates of spectral profiles, and then uses alternating least squares to optimise resolved spectral concentration profiles.^{68,82} Constraints are placed to

ensure non-negative concentration profiles and mass spectra, but no constraints were imposed for unimodality and equality in concentration profiles to ensure accurate representation of the relative variation of PC concentration with respect to the biomass:catalyst ratio. Further details on the application of multivariate analysis can be found in previous reports.^{4,86}

2.2.3 Tandem micropyrolyzer-GCMS

Since the MBMS cannot differentiate ions with the same nominal mass, a tandem micropyrolyzer-GCMS system was used complementarily to identify and quantify the products of CFP (**Figure S3.10**). The tandem micropyrolyzer (Rx-3050TR, Frontier Laboratories) is equipped with an autosampler (AS-1020E) and a microjet cryo-trap (MJT-1030Ex). The micropyrolyzer has two vertical heating zones in series: one for pyrolysis and one for upgrading of the pyrolysis vapours. Helium ($57 \text{ cm}^3 \text{ min}^{-1}$) was used as the carrier gas in the pyrolysis zone, with H_2 ($140 \text{ cm}^3 \text{ min}^{-1}$) added prior to the upgrading zone. The temperatures of pyrolysis and upgrading zones were typically maintained at 500°C . Stainless steel boats containing ca. 0.5 mg of pine were dropped in the pyrolysis zone using the autosampler. The pyrolysis vapours were then carried over a fixed bed of 40 mg of catalyst, supported on a plug of quartz wool. In a typical experiment, 3-4 boats of 0.5 mg of pine were sequentially pyrolyzed over the same catalytic bed. The upgraded vapours passed through the microjet cryo-trap that was housed inside the GC oven and maintained at -196°C . Most of the product vapours were adsorbed, before being rapidly desorbed into the capillary column of the GC (7890B, Agilent Technologies) interfaced with the MS (5977A, Agilent Technologies). These trapped vapours were separated along a capillary column (Ultra Alloy-5, Frontier Laboratories) with a 5% diphenyl and 95% dimethylpolysiloxane stationary phase. The GC oven was set to hold at 40°C for 4.5 min and then ramped to 300°C at $20^\circ\text{C min}^{-1}$. The trapped vapours were identified and quantified using the MS and the flame ionisation detector (FID) respectively. The GC analysis took ca. 31 min before the next pine boat was introduced to the reactor. During this time, H_2 and He continued to flow over the catalyst bed. Though most of the products were quantified using FID, it is unable to detect light gases such as CO_2 . To do so, the experiments were repeated with

the cryo-trap temperature set at -80°C to prevent condensation of CO_2 and analyzed using a thermal conductivity detector (TCD).

The furnace heat transfer rates in both the reactor configurations are comparable to that typically seen for fast pyrolysis. Although no direct measurement of the pine heating rate was performed in the current study, both the horizontal reactor and the micropyrolyzer were connected to the MBMS in two separate experiments. In both cases, the pyrolysis products appeared within 1-2 seconds after introducing the pine boat into the reactors set to 500°C . The total mass spectral ion counts, which can be used to profile the duration of pyrolysis of each boat, took on average 33 seconds. Based on the rise time to peak pyrolysis vapour evolution observed by the total mass spectral ion count curves, the heating rates were estimated to be greater than 30°C/s , which are typical for fast pyrolysis. Similar conclusions for fast pyrolysis have been reported for such reactor configurations in a previous study.⁸⁶

2.3 Spent catalyst characterisation

PXRD patterns were collected using a Bruker D8 diffractometer with Nickel-filtered $\text{Cu-K}\alpha$ radiation ($\lambda = 1.5418 \text{ \AA}$). Diffraction data were recorded on a 2D image plate rotated at a speed of 15 rpm, between 2θ values of $20\text{-}90^{\circ}$ with a step size of $0.2^{\circ} \text{ s}^{-1}$.

XPS spectra were collected on a PHI Versaprobe II instrument equipped with a multi-channel hemispherical analyser and an aluminum anode X-ray source operating at 100 W, featuring a $100 \mu\text{m}$ beam scanned over a 1.4 mm line across the sample surface. A dual-beam charge neutralisation system was used with an electron neutraliser bias of 1.2 eV and an Ar ion beam energy of 10 eV. The spent catalysts were mixed with niobium oxide (Nb_2O_5 , 99.99 %, Sigma Aldrich) as an internal standard for charge correction. The binding energies were corrected to 207.4 eV ($\text{Nb } 3d_{5/2}$). A 7-point Shirley background correction was then applied to the Mo 3d XPS spectra after charge correction. The Mo 3d spectra were deconvoluted to estimate the composition of Mo oxidation states. The following constraints were used for deconvolution: (1) splitting energy of 3.15 eV for Mo $3d_{5/2}$ - Mo $3d_{3/2}$, (2) area intensity ratio of 3:2 for Mo $3d_{5/2}$ - Mo $3d_{3/2}$, and (3) equal full width at half maximum (FWHM) of Mo $3d_{5/2}$ and Mo $3d_{3/2}$.

The amount of carbonaceous species on the spent supported MoO₃ catalysts was quantified using a CHNS analyser (Elementar, Vario EL cube). Sulfanilamide was used to calibrate the equipment prior to carbon content measurements. Similarly, coke deposited on spent HZSM-5 catalyst was quantified by thermogravimetric analysis in a TGA Instruments Q500 analyser using a previously reported protocol.⁷³

3. Results and discussion

3.1 Horizontal reactor-MBMS

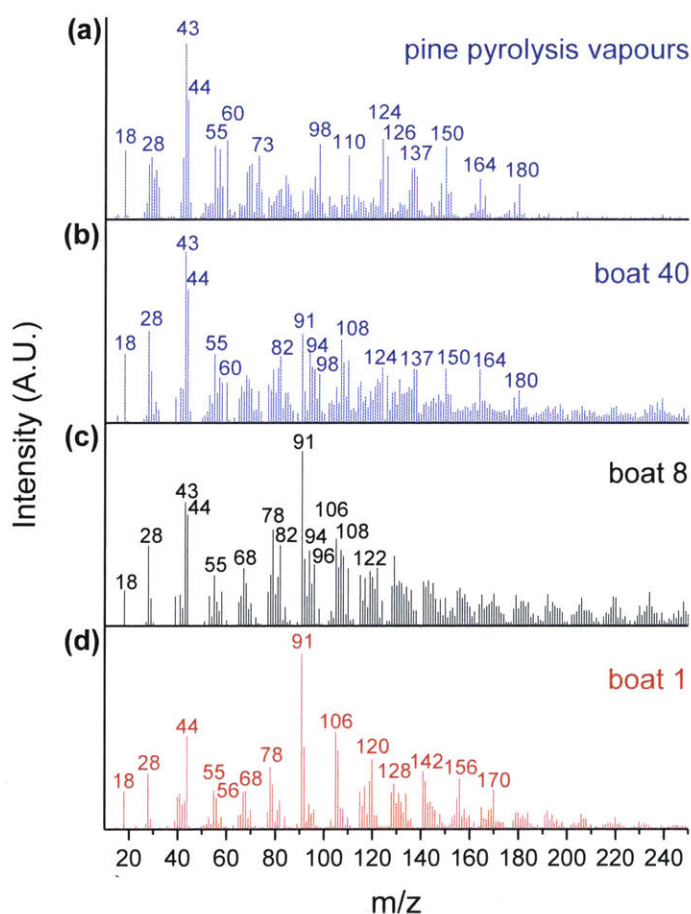


Figure 3.1 Averaged mass spectra obtained in the absence of catalyst (a) and from CFP of pine over MoO₃/TiO₂ at different stages of the experiment in the horizontal reactor-MBMS setup (b-d). Reaction conditions: catalyst = 1.0 g MoO₃/TiO₂, biomass = 40 boats of 50 mg pine, T = 500°C, P_{total} = 1.013 bar (50% H₂, He)

CFP of pine was investigated in a horizontal reactor-MBMS set up using 10 wt% MoO₃/TiO₂, 10 wt% MoO₃/ZrO₂, and bulk MoO₃ catalysts. A total of 40 quartz boats containing 50 mg of pine per boat were sequentially pyrolyzed over 1.0 g of catalyst. **Figure 3.1** shows the mass spectra of a control sample obtained by pyrolyzing 50 mg of pine in the absence of a catalyst. As expected, oxygenated hydrocarbons, such as aldehydes, ketones, carboxylic acids, alcohols and phenolics, were detected in addition to water, carbon monoxide and carbon dioxide (*m/z* 18, 28 and 44). Guaiacol, methyl guaiacol, vinyl guaiacol, isoeugenol and coniferyl alcohol (*m/z* 124, 137, 150, 164 and 180) are pyrolysis products from the lignin portion of pine, while acetic acid/glycoaldehyde, furfuryl alcohol and levoglucosenone/5-hydroxymethyl furfural (*m/z* 60, 98 and 126) are pyrolysis products from the cellulose and hemicellulose portions of pine.⁶⁸ The peaks at *m/z* 43, 55 and 73 are known carbohydrate fragments.^{4,68,86}

Figures 3.1(b), (c) and (d) show the products obtained during the CFP of pine using the MoO₃/TiO₂ catalyst after the 40th, 8th and 1st boat, respectively. The 1st boat was predominantly converted into fully deoxygenated products, including alkenes (butene, *m/z* 56) and aromatic hydrocarbons such as benzene, toluene, xylenes, trimethylbenzenes, naphthalene, methylnaphthalenes, dimethylnaphthalenes and trimethylnaphthalenes (*m/z* 78, 91, 106, 120, 128, 142, 156 and 170).⁶⁸ A carbohydrate-based fragment (*m/z* 55) and furan (*m/z* 68) were also detected. After the 8th boat, additional peaks corresponding to methyl furan, dimethyl furan, phenol, cresol and xylenol (*m/z* 82, 96, 94, 108 and 122) were detected.^{68,82} These furanic and phenolic components are likely partially hydrodeoxygenated intermediates formed during the CFP of pine with a catalyst bed that has begun deactivating.⁶⁸ The spectrum obtained after the 40th boat shows mostly peaks analogous to those observed during the control experiment with no catalyst, including peaks associated with primary pyrolysis vapours from both lignin (*m/z* 124, 137, 150, 164, 180) and carbohydrates (*m/z* 43, 55, 60, 98, 126). The presence of primary pyrolysis components in combination with furans, toluene, and phenol indicates drastic, but not total, catalyst deactivation. Taken together, these data show that the catalyst effectively hydrodeoxygenates pyrolysis vapours into olefinic and aromatic products, but undergoes progressive deactivation that

results in products with increasing amounts of oxygen with increasing cumulative amounts of pyrolysis products contacted with the catalyst bed.

A multivariate analysis was performed to identify, group, and track the relative yield of the hundreds of species produced during the CFP experiments. This analysis allows us to follow the complex change in product distributions as the catalyst undergoes deactivation. Specifically, the MCR-ALS approach reported by Mukarakate *et al.* and Budhi *et al.* for tracking the distribution of CFP products over HZSM-5⁶⁸ and BEA zeolites,⁷³ as well as molybdenum supported on mesoporous silica⁸² was used in the present study to extract pure components from the data set with overlapping mass spectra.⁸² We used the top 100 masses with the largest variances for each of the 40 boats to produce a 4000-point data set. The objective of MCR is to mathematically decompose our data set of overlapping mass spectra into pure contribution of each component involved during CFP of the 40 boats.⁶⁸ We optimised the MCR-ALS analysis for 3 pure components (PCs): Hydrocarbons, Furans/Phenols, and Primary Vapours. We note that attempts to further increase the number of PCs did not lead to significant changes in the residual error.

Effectively, the MCR-ALS analysis allows us to reconstruct the complex CFP mass spectrum into 3 separate spectra where molecules for each PC are binned (**Figure 3.2**). The Hydrocarbons PC is comprised of fully deoxygenated products, including olefins and aromatic hydrocarbons, similar to the products identified after the CFP of the 1st boat (*vide supra*). The Furans/Phenols PC represents partially deoxygenated products, including the products observed during the CFP of the 8th boat (methyl furan, dimethyl furan, phenol, cresol, xylenol) as well as trimethylfuran (m/z 110) and trimethylphenol (m/z 136).⁸² Note that peaks associated with primary pyrolysis vapours from lignin (m/z 150 and 164) and sugars (m/z 43) are also seen in this PC. The Primary Vapours PC includes carbohydrate oxygenated fragments, acetic acid, furfuryl alcohol, guaiacol, levoglucosenone or 5-hydroxymethylfurfural, methyl guaiacol, vinyl guaiacol, isoeugenol and coniferyl alcohol.

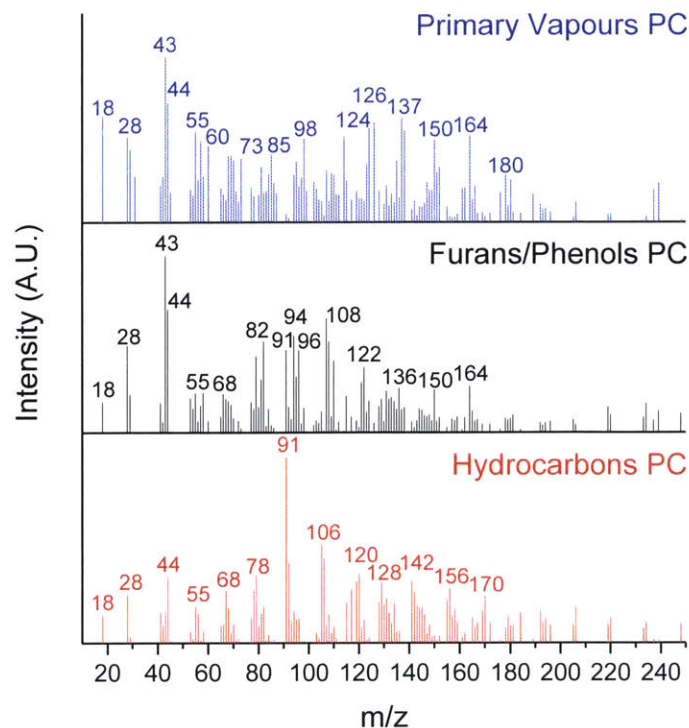


Figure 3.2 Reconstructed spectra for each pure component (hydrocarbons, furans/phenols, and primary vapours) from MCR-ALS analysis in the horizontal reactor-MBMS set up. Reaction conditions: catalyst = 1.0 g MoO₃/TiO₂, biomass = 40 boats of 50 mg pine, T = 500°C, P_{total} = 1.013 bar (50 vol% H₂-He)

Figure 3.3 shows a scores plot for the 3 PCs as a function of increasing biomass-to-catalyst mass ratio for both MoO₃/TiO₂ and MoO₃/ZrO₂ catalysts. Initially, only products associated with the Hydrocarbons PC are observed for both catalysts, demonstrating their capability of fully deoxygenating the primary pyrolysis vapours of pine. This behaviour is similar to that of HZSM-5 during the CFP of pine performed in the horizontal reactor-MBMS set up as reported previously.⁶⁸ Note that for HZSM-5, aromatic hydrocarbons such as benzene, toluene, xylene and naphthalene are produced as major products.⁶⁸ The intensity of the Hydrocarbons PC increases until biomass:MoO₃ ratios of 1 and 2 are reached for MoO₃/TiO₂ and MoO₃/ZrO₂, respectively, and then decreases gradually. Products associated with Furans/Phenols start forming at biomass:MoO₃ ratios of ca. 1 and 2 for MoO₃/TiO₂ and MoO₃/ZrO₂, respectively. The proportion of the Furans/Phenols PC increases steadily until

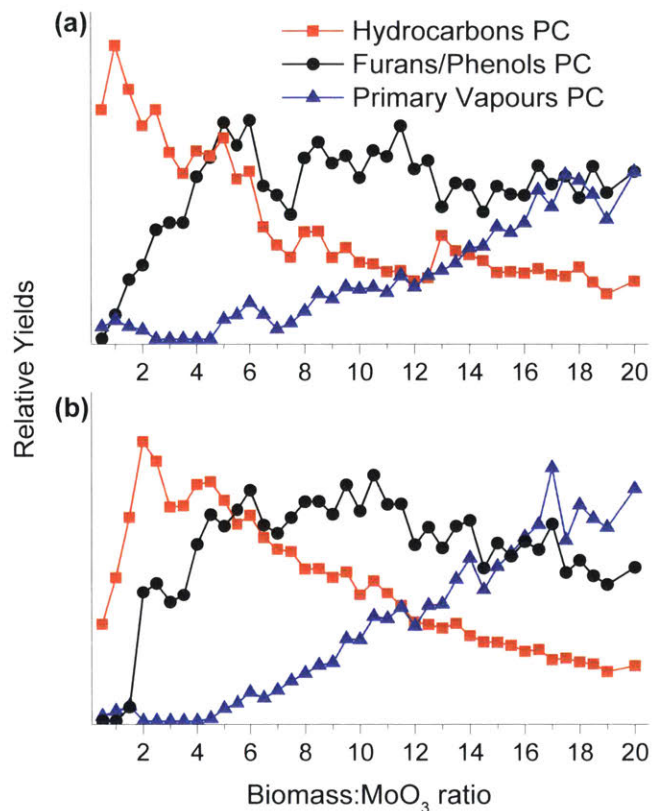


Figure 3.3 Scores plot for each pure component from MCR-ALS analysis in the horizontal reactor-MBMS set up over (a) $\text{MoO}_3/\text{TiO}_2$ and (b) $\text{MoO}_3/\text{ZrO}_2$. Reaction conditions: catalysts = 1.0 g, biomass = 40 boats of 50 mg pine, $T = 500^\circ\text{C}$, $P_{\text{total}} = 1.013 \text{ bar}$ (50 vol% $\text{H}_2\text{-He}$)

biomass: MoO_3 ratios of 5 and 6 are reached for $\text{MoO}_3/\text{TiO}_2$ and $\text{MoO}_3/\text{ZrO}_2$, respectively, decreasing slightly before reaching steady state. These data suggest that although the catalysts produce less fully deoxygenated products at biomass:catalyst ratios above 5, they are still active for HDO. For biomass: MoO_3 ratios ≥ 5 , the amount of Furans/Phenols starts to decline and the Primary Vapours start breaking through the catalyst bed. We hypothesise that at this point both $\text{MoO}_3/\text{TiO}_2$ and $\text{MoO}_3/\text{ZrO}_2$ undergo severe deactivation likely due to coke deposition on the surface and over-reduction of Mo^{6+} species to lower oxidation states that feature lower reactivity. Note that for HZSM-5 operated in the horizontal reactor-MBMS setup, the Primary Vapours PC started breaking through the bed at biomass:catalyst ratios ≤ 1 .^{68,73} Control experiments with

bare supports showed no appreciable HDO activity, thus ascribing the observed activity to Mo species.

Bulk MoO₃ was tested under identical reaction conditions. Primary vapours and no HDO products were detected after pyrolysis of the 1st boat. Note that bulk MoO₃ was not activated under a H₂ flow before the reaction, and previous reports have shown that bulk MoO₃ undergoes an induction period during the HDO of *m*-cresol without a prior activation step.^{52,53}

3.2 Tandem micropyrolyzer-GCMS

To gain further information regarding product distribution and overall mass balances attained with supported molybdenum oxide catalysts, the CFP of pine was investigated in a tandem micropyrolyzer-GCMS set up. The gas chromatograms after sequential pyrolysis of 3 boats loaded with ca. 0.5 mg of pine each over 40 mg of the MoO₃/TiO₂ catalyst show that the catalyst predominantly produces aromatic hydrocarbons, alkenes and alkanes (see **Figure 3.4**). Specifically, benzene, toluene, ethylbenzene, xylenes, propylbenzene, 1-ethyl-3-methylbenzene, trimethylbenzenes, indane, indene, naphthalene, methylnaphthalenes, dimethylnaphthalenes, propene, 2-methyl-2-propene, butene, 2-methyl-2-butene and ethane were identified. Other than a very small amount of acetaldehyde, acetone, butanone and furan, no other oxygenates were detected (see **Table S3.1** for the full list of products). This product distribution remains relatively constant across the 3 boats, which corresponds to a total biomass:MoO₃ mass ratio of 0.375. These GCMS data are in close agreement with the MBMS data (**Figure 3.1(d)**), indicating that when the catalyst is still fresh, it is able to fully deoxygenate the primary pyrolysis vapours to form mostly aromatic hydrocarbons and alkenes under the reported reaction conditions. In contrast to the MBMS analysis, the GCMS-based analysis helps in distinguishing structural isomers. For example, the peak at *m/z* 120 in MBMS can be separated in the GCMS into methylethylbenzene, trimethylbenzene and propylbenzene. We note that, akin to the MoO₃/TiO₂, the MoO₃/ZrO₂ catalyst (**Figure S3.11**) displayed a similar hydrocarbon product distribution across the 3 pine boats (see **Table S3.2** for the full list of products). Similar to the MBMS experiments, control experiments with bare supports showed no appreciable HDO activity (see **Figure S3.12** and **S3.13**).

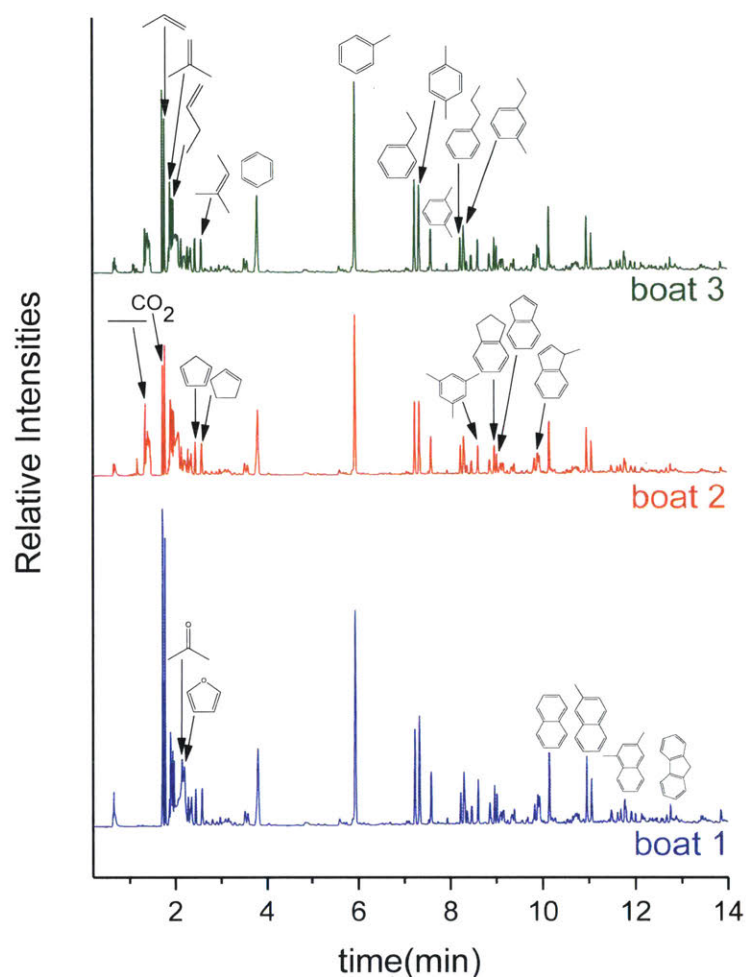


Figure 3.4 GCMS chromatograms of CFP of pine over 40 mg of 10 wt% MoO₃/TiO₂ in the tandem micropyrolyzer-GCMS set up. Reaction conditions: catalyst = 40 mg, biomass = 3 boats of 0.5 mg pine, T = 500 °C, P_{total} = 1.013 bar (71 vol% H₂-He)

Bulk MoO₃ was investigated for CFP of pine in the same set up. Although no products were observed after the first pine boat (see **Figure S3.14**) the same aromatic hydrocarbon products as those obtained with the supported MoO₃ catalysts were observed after the pyrolysis of the 2nd pine boat. These peaks increased in intensity as more pine boats were introduced up to a total of 4 boats. Taken together, these data suggest bulk MoO₃ undergoes an induction period similar to that previously reported during the CFP of cellulose⁸³ and HDO of bio-oil model compounds.⁵² Therefore, the difference in reactivity data from the MBMS and GCMS instruments for bulk and

supported MoO₃ catalysts could be rationalised by the favourable metal-support interaction for the latter. Indeed, Shetty *et al.* demonstrated that TiO₂ and ZrO₂ accelerate the generation and stabilisation of intermediate Mo oxidation states, which appear to promote reactivity during the HDO of *m*-cresol.⁵³

We note that the reactivity and catalytic performance data cannot be compared quantitatively between the MBMS and the microreactor-GCMS reactor configurations, given that the reaction conditions are drastically different in both set ups. For example, the hydrogen flow rate to catalyst mass is 18 times higher in the microreactor-GCMS system than in the horizontal reactor MBMS system. Also, although the feed is introduced in a pulse-like fashion in both systems, the frequency of these events is much lower in the microreactor-GCMS (every 30 min) compared to that used for the MBMS (every 2 min). Thus, the catalysts are exposed to greater amounts of hydrogen over a longer duration before a subsequent pulse of biomass is introduced in the microreactor-GCMS system than in the horizontal reactor-MBMS configuration. Indeed, while hydrogen is crucial for retaining HDO activity in bulk MoO₃, it can also change the speciation of active species on the catalyst surface by over-reduction.⁴¹ Despite these differences, both instruments generate data showing that MoO₃/TiO₂ and MoO₃/ZrO₂ are clearly better catalysts for CFP of pine than bulk MoO₃, since they are active in both reactor conditions using only a tenth of the equivalent mass of bulk MoO₃. The reactivity data also suggest that the supported MoO₃ catalysts are active over a wider operating window than bulk MoO₃ at the reaction conditions investigated here.

3.3 Quantification of products

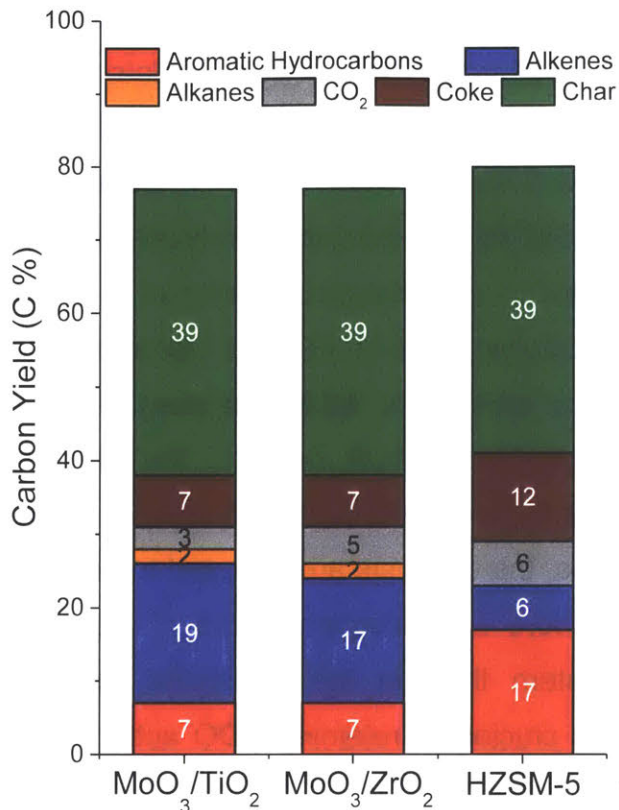


Figure 3.5 Average product distribution from CFP of pine over MoO₃/TiO₂, MoO₃/ZrO₂ and HZSM-5 in the tandem micropyrolyzer-GCMS system. Reaction conditions: catalysts = 40 mg of MoO₃/TiO₂ and MoO₃/ZrO₂, 30 mg of HZSM-5, biomass = 3 boats of 0.5 mg pine, T = 500°C, P_{total} = 1.013 bar (71 vol% H₂-He)

Most of the products were identified with MS and quantified using FID while CO₂ was quantified using TCD. Average product yields were obtained by pyrolyzing 3 pine boats over each supported catalyst (**Figure 3.5**). Overall, both catalysts showed similar product distributions of *ca.* 7 C% aromatic hydrocarbons, 17-19 C% alkenes, 2 C% alkanes, 3-5 C% CO₂, 7 C% coke and 39 C% char. Comparing the two supported catalysts, we note that both are equally effective for CFP of pine as they produce equal amounts of most products, except for the slight difference (*ca.* 2%) observed in the amounts of alkenes and CO₂ produced. Among the aromatic hydrocarbons, benzene and toluene are produced in similar yields and account for a total of 56-60% of the total aromatic hydrocarbons yield over both catalysts. The remaining aromatics include xylenes (10-11%), multisubstituted benzenes (14-17%), naphthalenes (9-10%) and

indanes/indenes (4-7%). Butane and ethane comprise the majority of the alkanes (67-80%), while propene is the predominant alkene (62-69%). The remaining alkenes are butene (14%), methylbutene (4-5%), methylpropene (5%), cyclopentadiene (2-4%), cyclopentene (3-4%), ethylene (2%) and pentene (2-3%). CO and CH₄ are the other light gases. A detailed list of identified products is shown in **Table S3.3**. Coke yield was determined by CHNS analysis of several spent catalyst samples. The char content was measured by averaging the weight of pine remaining after pyrolysis across 10 boats. An independent elemental analysis of char revealed that it contained approximately 85% carbon. A very small fraction of oxygenates (< 0.5 C%) was observed only for MoO₃/TiO₂, including acetone, acetaldehyde, butanone and furan. Overall, the carbon balance is in the range of 80 %. The unaccounted carbon could have been either lost during condensation of the light gases in the liquid nitrogen trap or some of the coke could have been scavenged by hydrogen flow between successive pulses of biomass. Assuming a 60% mass yield of pyrolysis vapours from pine pyrolysis⁶⁸ (i.e., excluding char and light gases) and similar carbon composition as pine, the catalysts can be assessed for their effectiveness to perform HDO. Both supported MoO₃ catalysts yield about 12 C% aromatic hydrocarbons, 31 C% alkenes, 4 C% alkanes, 6 C% CO₂ and 12 C% coke based on the carbon content of the pyrolysis vapours. These values translate to >40 C% of upgraded products for supported Mo catalysts when char is excluded. Overall, both MoO₃/TiO₂ and MoO₃/ZrO₂ showed similar product distributions during CFP of pine. They produced ca. 30 C% hydrocarbon products, with the remaining carbon in the form of CO₂, char and coke on the catalysts. Although the upgrading temperature used in this study is 100°C higher than that used by Nolte *et al.* during the CFP of corn stover over bulk MoO₃, the product distributions are similar.⁸³ Importantly, in contrast to bulk MoO₃, supported MoO₃ catalysts are capable to work at high biomass:catalyst ratios without requiring a hydrogen pre-activation step.

In order to assess the performance of the supported MoO₃ catalysts with respect to state-of-the-art HZSM-5 catalysts, the zeolite was tested under identical CFP reaction conditions (**Figure 3.5**). HZSM-5 yielded 17 C% aromatic hydrocarbons, 6 C% alkenes, 6 C% CO₂, 12 C% coke and 39 C% char. Overall, HZSM-5 produced ca. 23 C% hydrocarbon products, comparable to the hydrocarbon yield from supported

MoO₃ catalysts (ca. 27 C%). A full list of products identified is shown in **Table S3.3**. These results are comparable to those obtained by Thangalazhy-Gopakumar *et al.*⁸⁷ and Wang *et al.*⁴⁴ for the *ex situ* CFP of pinewood chips and hybrid poplar, respectively, over HZSM-5 in a microreactor set up at reaction conditions (**Table S3.4**) similar to those used in this study. Although supported MoO₃ catalysts produced less aromatic hydrocarbons than HZSM-5, the combined selectivities to BTX (70%) were higher than those obtained with HZSM-5 (51 %) in this study. Furthermore, the supported MoO₃ catalysts produced about 3 times more olefins than HZSM-5. These olefins are valuable as they can be further treated with aromatics to form more useful alkylated aromatic products. As expected, HZSM-5 also showed a higher propensity to coking (12 C%) than supported MoO₃ catalysts (7 C%). Although the reaction conditions were kept identical across the supported MoO₃ and HZSM-5 catalysts, the effective catalyst mass used was different (4 mg MoO₃ in supported MoO₃ catalysts vs. 24 mg HZSM-5 in HZSM-5/SiO₂) to obtain comparable conversions. Taken together, these results indicate that supported MoO₃ catalysts are indeed promising alternative CFP catalysts to zeolites as they can operate at high biomass:catalyst ratios and produce hydrocarbons under mild conditions with yields comparable to those obtained with state-of-the-art catalysts.

3.4 Post-reaction characterisation

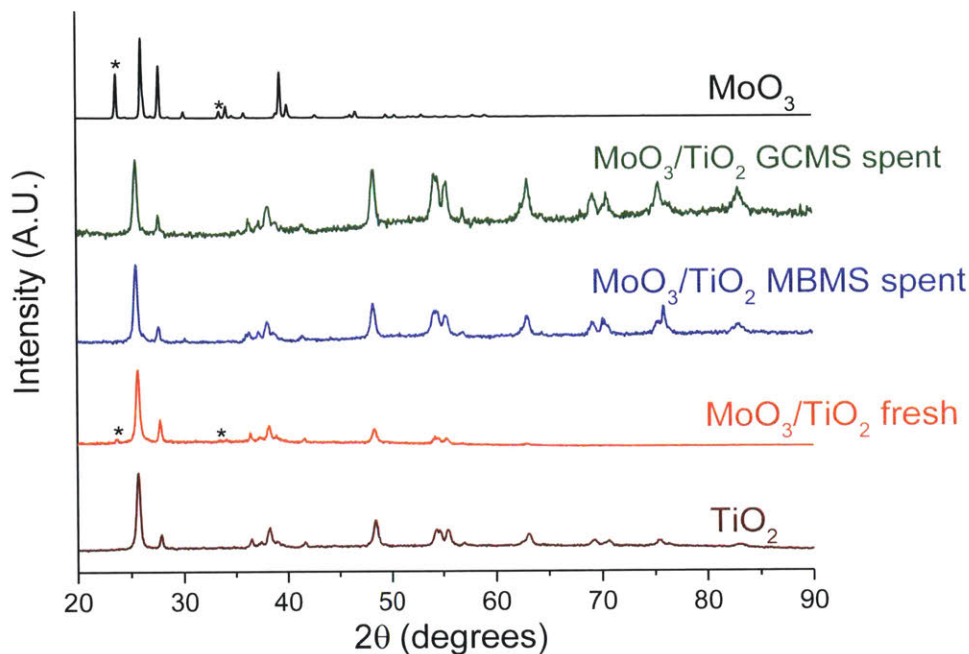


Figure 3.6 Normalised PXRD patterns of the fresh and spent MoO₃/TiO₂ catalysts in comparison with fresh TiO₂ and MoO₃ samples. The spent MoO₃/TiO₂ samples from both reactor systems were derived after experiments shown in **Figure 3.3(a)** and **3.4**.

The catalysts were characterised post-reaction to reconcile the differences in reactivity observed in both reactor setups. PXRD patterns of fresh and spent MoO₃/TiO₂, MoO₃/ZrO₂ and bulk MoO₃ are shown in **Figure 3.6**, **Figure S3.15**, and **Figure 3.7**, respectively. Only MoO₃/TiO₂ and bulk MoO₃ show appreciable changes in PXRD patterns after reaction. Fresh MoO₃/TiO₂ features mostly peaks corresponding to the support TiO₂ but two additional peaks are observed at $2\theta = 23.7^\circ$ and 34.2° associated with crystalline MoO₃ clusters. These diffractions disappear after reaction in both reactors, similar to the PXRD diffractions observed after HDO of *m*-cresol.⁵³ Although no diffractions associated with molybdenum oxycarbohydride (MoO_xC_yH_z) are detected, their presence cannot be ruled out given that these species might be below the detection limit of the diffractometer.

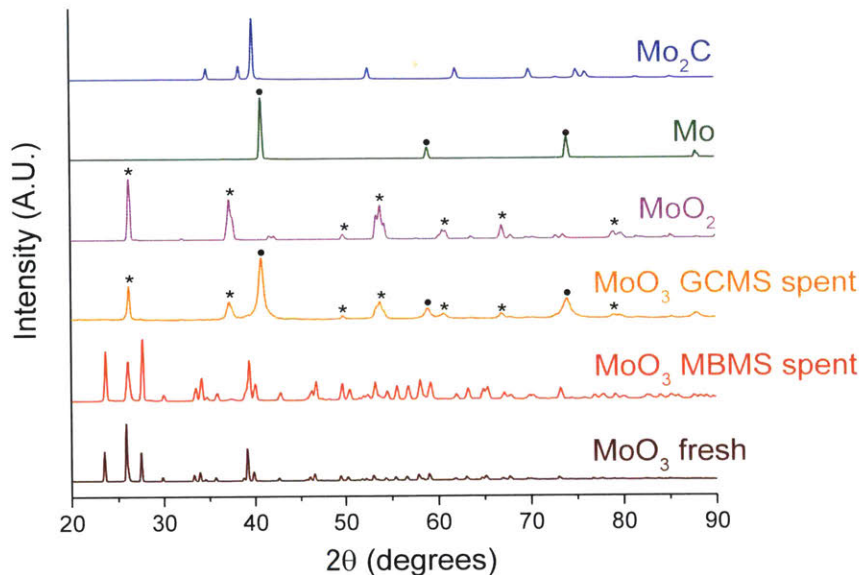


Figure 3.7 Normalised PXRD patterns of the spent bulk MoO_3 catalysts in comparison with fresh MoO_3 , MoO_2 , Mo and Mo_2C samples. The symbol (*) and (•) indicates the peak assignment corresponding to MoO_2 and Mo respectively. The spent bulk MoO_3 sample from micropyrolyzer-GCMS setup was retrieved after experiment shown in **Figure S3.6**.

The PXRD patterns for spent bulk MoO_3 from the MBMS experiment feature peaks associated with fully oxidised MoO_3 . We note that MoO_3 was not activated under H_2 thus explaining the lack of catalytic activity (**Figure 3.7**). In contrast, after reaction in the micropyrolyzer-GCMS set up, only diffractions corresponding to MoO_2 and metallic Mo are present. These results are consistent with the previously observed phase transformation of bulk MoO_3 to a mixture of MoO_2 and molybdenum oxycarbohydride ($\text{MoO}_x\text{C}_y\text{H}_z$) during the HDO of *m*-cresol.⁵² However, since the temperature in this study is 180°C higher than that used for the HDO of *m*-cresol, the full reduction of MoO_3 to metallic Mo without the presence of oxycarbohydride or carbide peaks is expected.

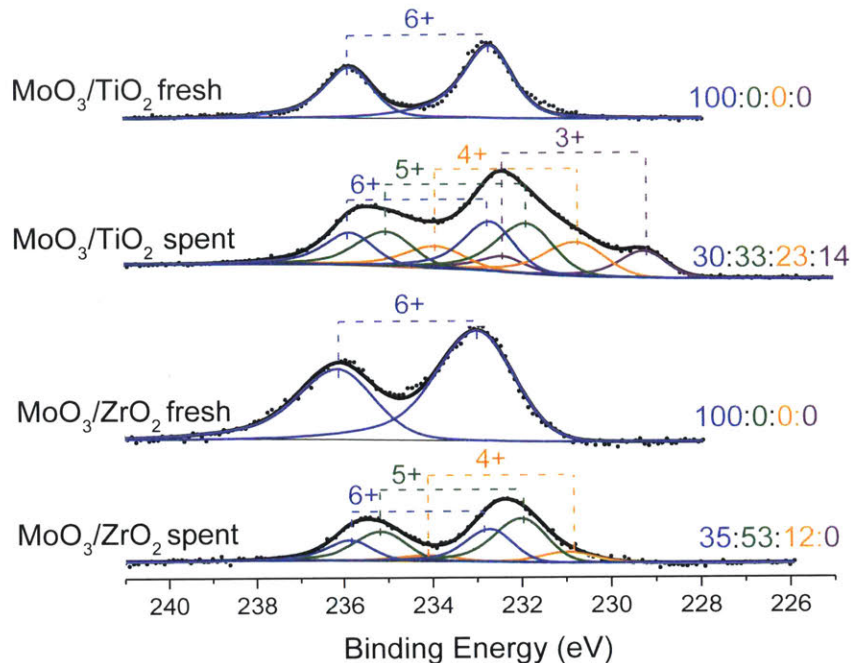


Figure 3.8 XPS spectra showing the Mo (3d) binding energy region of fresh and spent MoO₃/TiO₂ and MoO₃/ZrO₂ from the horizontal reactor-MBMS system. The spent catalysts were retrieved after experiments shown in **Figure S3.11**. The ratios displayed correspond to the proportion of oxidation states Mo⁶⁺, Mo⁵⁺, Mo⁴⁺, and Mo³⁺ respectively.

XPS spectra were acquired to determine the oxidation states of the supported molybdenum oxide catalysts (**Figure 3.8**). Pre-reaction spectra show only peaks associated with Mo⁶⁺ valence states, while after reaction, both catalysts show the presence of Mo⁵⁺ states, and, for MoO₃/TiO₂, a Mo³⁺ state as assigned by Choi *et al.*⁵⁹ Both catalysts show that *ca.* 50% of Mo species on the surface exist in their intermediate oxidation states (Mo⁵⁺ and Mo³⁺). Such distribution of oxidation states on the supported catalysts is very similar to that observed for the same catalysts after the HDO of *m*-cresol.⁵³ Taken together, these data suggest that the prevalence of Mo⁵⁺ and Mo³⁺ could lead to higher HDO activity and on-stream stability even after the catalyst observes biomass:MoO₃ ratios of 20. Since the reactivity data from horizontal reactor-MBMS set up is not quantitative, a semi-quantitative approach was used to gain insight on the deactivation kinetics. The relative yields for the Hydrocarbons, Furans/Phenols and Primary Vapours PCs (**Figure 3.3**) were normalized by their total sum to determine the fractional conversion of primary vapours to hydrocarbons/furans/phenols,

respectively. The deactivation rates for both catalysts follow a first order deactivation model (see **Figure S3.16**). This deactivation behaviour is consistent with our observations from prior studies on the HDO of model compounds.^{41,52,53} A first order deactivation profile is strong evidence that coking is responsible for the observed loss in activity.⁸⁸ However, we note that this analysis is semi-quantitative in nature and further studies are needed to obtain quantitative deactivation rates and to determine the exact nature of coke deposits on the catalyst surface.

3.5 Potential industrial scale application

The current study was performed to show that supported MoO₃ catalysts can serve as alternative upgrading catalysts to zeolites (e.g., HZSM-5) and that they can be indeed used for CFP of lignocellulosic biomass. Although our direct comparison results (**Figure S3.5** and **Table S3.3**) show that more favourable catalyst-to-biomass ratios can be achieved with these Mo-based catalysts when compared to zeolites, this ratio needs to be optimized further. The catalyst lifetime can be prolonged when it is operated in a FCC-like fluidized bed system where the vapour residence time is minimized to prevent secondary reactions, which can lead to excessive coking on the catalyst surface. Supported MoO₃ catalysts can be regenerated by simple calcination in air.⁵³ The FCC-like reactor system typically has a regenerator, which burns off the coke and regenerates the catalyst, which can then be recycled back into the ex situ CFP reactor.^{89,90} This mode of operation lowers the cost associated with purchasing fresh catalyst. Moreover, supported MoO₃ is also an economical catalyst that can be manufactured at scale. The current price for bulk MoO₃ is ca. \$0.02/gram.⁴² We note that sulfided Cobalt Molybdenum (CoMo) and Nickel Molybdenum (NiMo) catalysts supported on Al₂O₃ are already being synthesized and used industrially in hydrodesulfurization of petroleum fractions.⁸⁹ These catalysts are initially synthesized in the oxide forms, and presulfided to obtain sulfides prior to reaction.⁸⁹ In contrast to zeolite catalysts, however, these catalysts have not been formulated into attrition-resistant pellets compatible with FCC-like fluidized bed reactors.⁹⁰ Further studies in this direction will be critical in optimizing the catalyst performance before being used industrially. Process parameters⁹¹ such as temperature, biomass-catalyst ratio, biomass

residence time, pyrolysis vapour residence time and catalyst regeneration conditions also need to be optimized prior to scale-up.⁹⁰

4. Conclusions

Supported molybdenum oxide catalysts, MoO₃/TiO₂ and MoO₃/ZrO₂, are effective HDO catalysts capable of producing olefins and aromatic hydrocarbons from the CFP of pine. As the cumulative biomass to MoO₃ mass ratio exposed to the catalytic bed increases, the catalysts become less effective for HDO, forming partially deoxygenated intermediates such as furans and phenols. Though the primary pyrolysis vapours break through at biomass:catalyst ratios ≥ 5 , the catalysts remain active for HDO, as furans, toluene and phenols were observed even at biomass:MoO₃ ratio of 20. Both supported catalysts yielded about 30 C% hydrocarbon products, which are comparable yields to those obtained with HZSM-5. Supported MoO₃ catalysts are more effective CFP catalysts than bulk MoO₃. Post-reaction XPS analyses of the supported catalysts reveal that about half of the Mo surface species exist in their intermediate oxidation states (Mo³⁺ and Mo⁵⁺), which could explain the higher reactivity and stability as compared to bulk MoO₃. Catalyst deactivation is likely associated to coking. Optimising the CFP reaction conditions as well as tuning the synthesis of the supported MoO₃ catalysts are important parameters for improving HDO performance.

Acknowledgements

S. Budhi, C. Mukarakate and M. Nimlos are greatly acknowledged for their contributions to this chapter. This research was funded by BP through the MIT Energy Initiative Advanced Conversion Research Program and the National Science Foundation (award number 1454299). Support for Budhi, Mukarakate and Nimlos was provided by U.S. Department of Energy's Bioenergy Technologies Office (DOE-BETO) under contract no. DE-AC36-08GO28308 with the National Renewable Energy Laboratory. Calvin Mukarakate, Sridhar Budhi, and Mark Nimlos would like to thank Josiah McMillen and Kristina lisa for their help with some of the CFP experiments.

5. Supporting Information

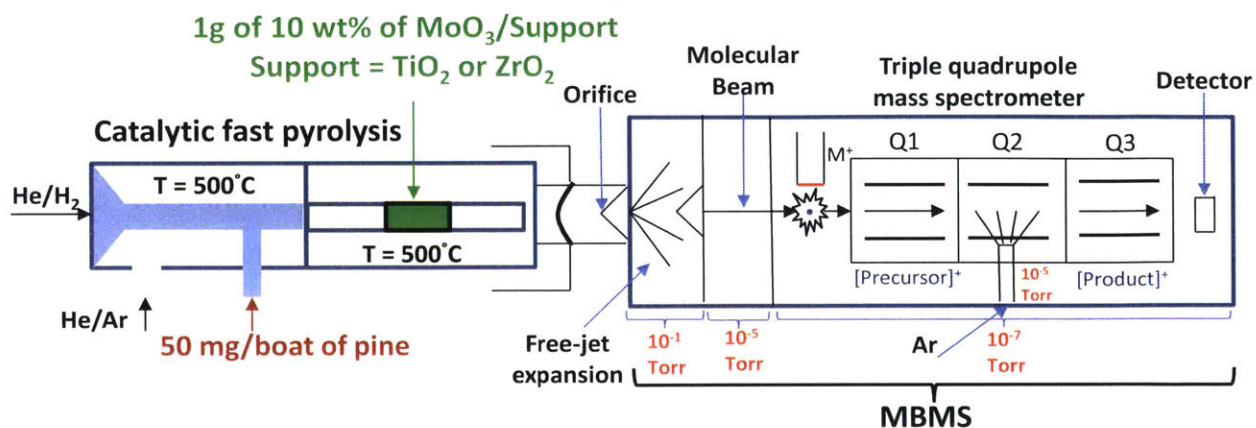


Figure S3.9 Schematic of horizontal reactor-MBMS set up.

Typically, pine boats of 50 mg each were pyrolyzed sequentially and flown over 1.0 g of catalyst in a $400\text{ cm}^3\text{ min}^{-1}$ of 50 vol\% H_2 - He mixture. Prior to sampling by the MBMS, the H_2 - He gas mixture was further diluted with more He ($4000\text{ cm}^3\text{ min}^{-1}$). A dilute stream of Argon ($40\text{ cm}^3\text{ min}^{-1}$) was mixed into the He diluent stream to serve as an internal standard.

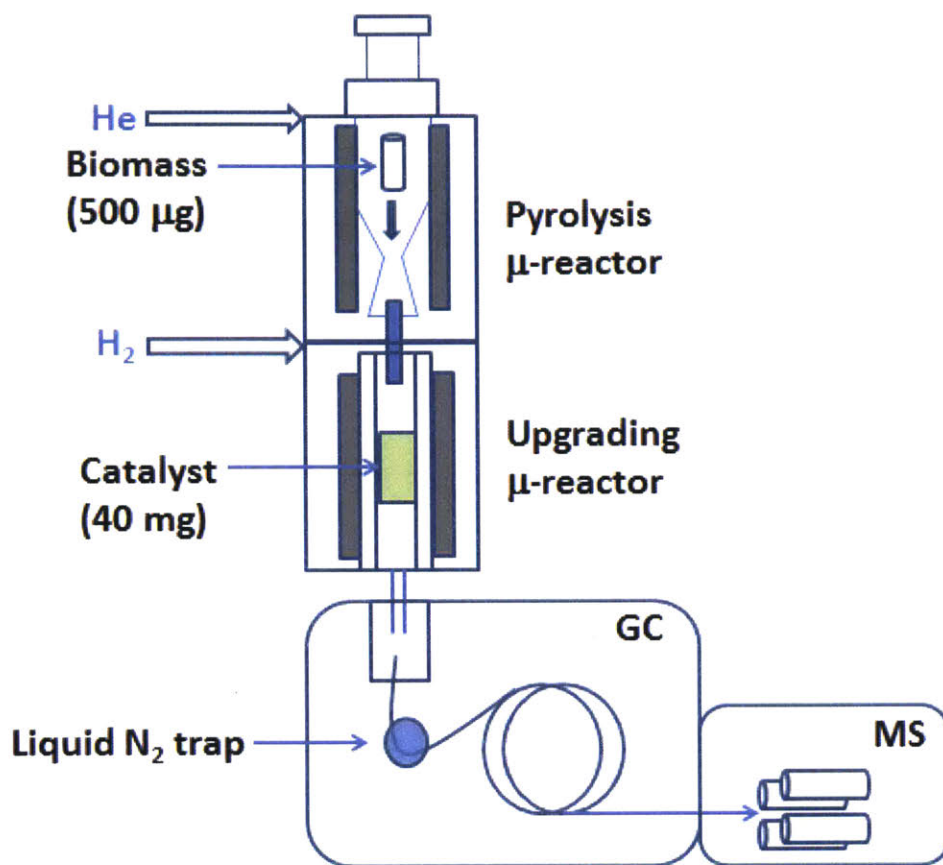
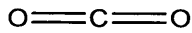
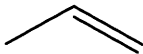
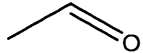
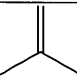
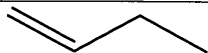
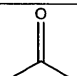
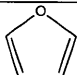
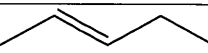
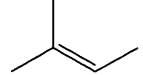


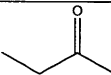
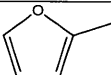
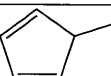
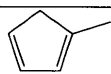
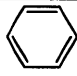
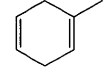
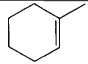
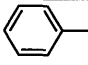
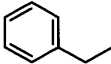
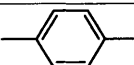
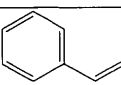
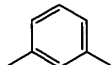
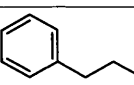
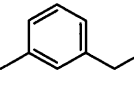
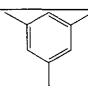
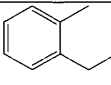
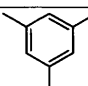
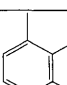
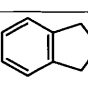
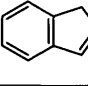
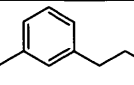
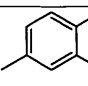
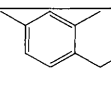
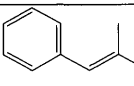


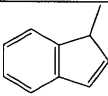
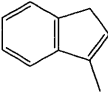
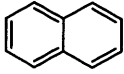
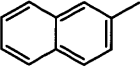
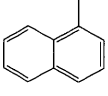
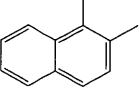
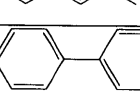
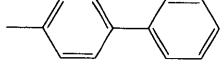
Figure S3.10 Schematic of tandem micropyrolyzer-GCMS set up

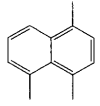
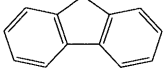
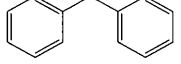
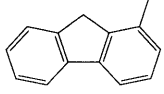
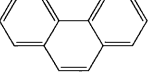
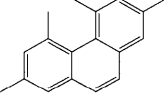
Typically, pine boats of *ca.* 500 μg each were pyrolyzed sequentially and the gases were contacted over 40 mg of catalyst in a $197 \text{ cm}^3 \text{ min}^{-1}$ flow of 71 vol% H_2 -He mixture.

Table S3.1 Products identified by GCMS after the CFP of first pine boat over 10 wt% MoO₃/TiO₂ in the tandem microreactor.

Retention time/min	m/z	Compound	Structure
1.73	44	carbon dioxide	
1.78	42	propene	
1.87	44	acetaldehyde	
1.90	56	2-methyl-1-propene	
1.94, 1.97	56	1-butene	
2.15	58	Acetone	
2.20	68	Furan	
2.28	70	2-pentene	
2.35	70	2-methyl-2-butene	
2.45	66	1,3-cyclopentadiene	
2.58	68	cyclopentene	
2.81	72	2-Butanone	
2.97	82	2-methylfuran	
3.52	80	5-methyl-1,3-cyclopentadiene	
3.58	80	1-methyl-1,3-cyclopentadiene	
3.81	78	benzene	
5.60	94	1-methyl-1,4-Cyclohexadiene	

5.88	96	1-methylcyclohexene	
5.94	92	toluene	
7.23	106	ethylbenzene	
7.33	106	p-xylene	
7.53	104	styrene	
7.58	106	m-xylene	
8.22	120	propylbenzene	
8.30	120	1-ethyl-3-methylbenzene	
8.37	120	1,3,5-trimethylbenzene	
8.47	120	1-ethyl-2-methylbenzene	
8.60	120	1,3,5-trimethylbenzene	
8.85	120	1,2,3-trimethylbenzene	
8.96	118	indane	
9.02	116	indene	
9.10	134	1-methyl-3-propylbenzene	
9.15	134	2-ethyl-1,4-dimethylbenzene	
9.34	134	1-ethyl-2,4-dimethylbenzene	
9.39	132	(2-methyl-1-propenyl)benzene	

9.82	132	2,3-dihydro-4-methyl-1H-indene	
9.89	130	1-methyl-1H-indene	
9.93	130	3-methyl-1H-indene	
10.14	128	naphthalene	
10.64	146	2,3-dihydro-1,2-dimethyl-1H-indene	
10.71, 10.75, 10.78	144	1,3-dimethyl-1H-indene	
10.95	142	2-methylnaphthalene	
11.06	142	1-methylnaphthalene	
11.48	154	2-ethenylnaphthalene	
11.62	156	1,2-dimethyl-naphthalene	
11.69	156	2,3-dimethylnaphthalene	
11.78	156	1,3-dimethylnaphthalene	
11.80	156	1,6-dimethylnaphthalene	
11.91	156	2,7-dimethylnaphthalene	
12.00	156	2,3-dimethylnaphthalene	
12.15	168	4-methyl-1,1'-Biphenyl	

12.68	170	1,4,5-trimethylnaphthalene	
12.77	166	fluorene	
12.89	168	diphenylmethane	
13.42, 13.46	180	1-methyl-9H-Fluorene	
13.86	178	phenanthrene	
15.95	234	2,4,5,7-tetramethylphenanthrene	

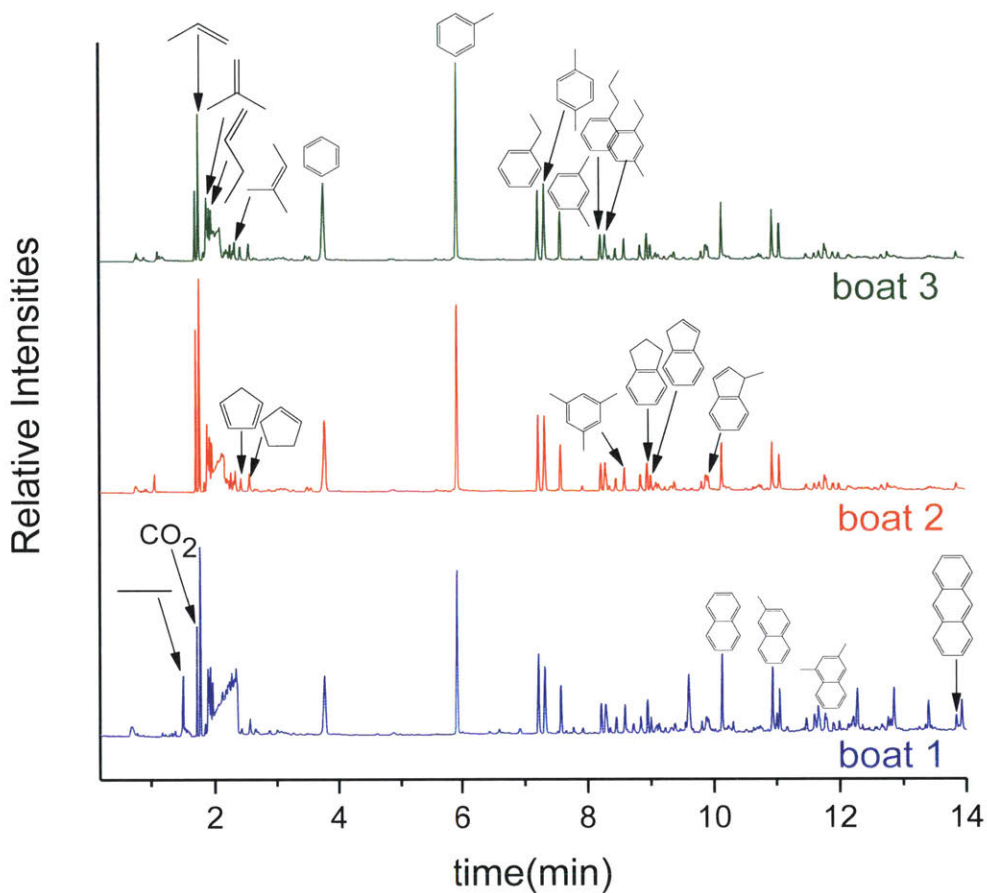
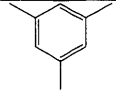
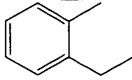
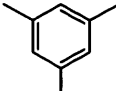
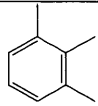
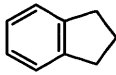
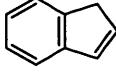
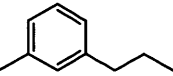
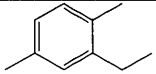
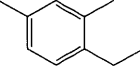
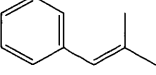
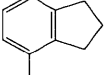
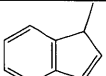
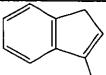
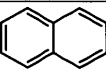
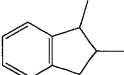
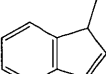
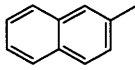
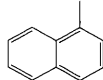
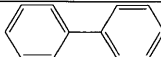
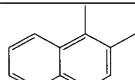
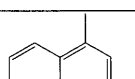
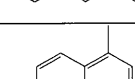
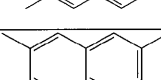
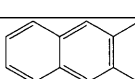
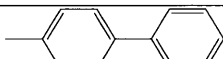
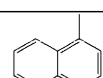
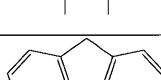
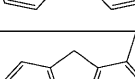
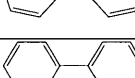
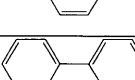
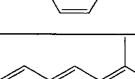


Figure S3.11 Product distribution of CFP of pine over 40 mg of 10 wt% MoO₃/ZrO₂ in the micropyrolyzer-GCMS set up. Reaction conditions: catalyst = 40 mg, biomass = 3 boats of 0.5 mg pine, T = 500°C, P_{total} = 1.013 bar (71 vol% H₂-He)

Table S3.2 Products identified by GCMS after CFP of first pine boat over 10 wt% MoO₃/ZrO₂ in the tandem micropyrolyzer.

Retention time/min	m/z	Compound	Structure
1.51	30	ethane	
1.72	44	carbon dioxide	
1.78	42	Propene	
1.85	58	isobutane	
1.90	56	2-methyl-1-propene	
1.91	58	Butane	
1.94, 1.97	56	1-butene	
2.27	70	2-pentene	
2.33	70	2-methyl-2-butene	
2.42	66	1,3-cyclopentadiene	
2.56	68	cyclopentene	
3.77	78	Benzene	
5.92	92	Toluene	
7.21	106	ethylbenzene	
7.32	106	p-xylene	
7.57	106	m-xylene	
8.21	120	propylbenzene	
8.29	120	1-ethyl-3-methylbenzene	

8.36	120	1,3,5-trimethylbenzene	
8.45	120	1-ethyl-2-methylbenzene	
8.59	120	1,3,5-trimethylbenzene	
8.84	120	1,2,3-trimethylbenzene	
8.95	118	indane	
9.00	116	indene	
9.09	134	1-methyl-3-propylbenzene	
9.13	134	2-ethyl-1,4-dimethylbenzene	
9.32	134	1-ethyl-2,4-dimethylbenzene	
9.39	132	(2-methyl-1-propenyl)benzene	
9.81	132	2,3-dihydro-4-methyl-1H-indene	
9.89	130	1-methyl-1H-indene	
9.91	130	3-methyl-1H-indene	
10.13	128	naphthalene	
10.64	146	2,3-dihydro-1,2-dimethyl-1H-indene	
10.70, 10.74	144	1,3-dimethyl-1H-indene	

10.94	142	2-methylnaphthalene	
11.05	142	1-methylnaphthalene	
11.47	154	biphenyl	
11.60	156	1,2-dimethyl-naphthalene	
11.77	156	1,3-dimethylnaphthalene	
11.79	156	1,6-dimethylnaphthalene	
11.90	156	2,7-dimethylnaphthalene	
11.99	156	2,3-dimethylnaphthalene	
12.14	168	4-methyl-1,1'-Biphenyl	
12.67	170	1,4,5-trimethylnaphthalene	
12.76	166	fluorene	
13.41	180	1-methyl-9H-Fluorene	
13.85	178	phenanthrene	
14.43	192	1-methylphenanthrene	
14.59	192	1-methylantracene	

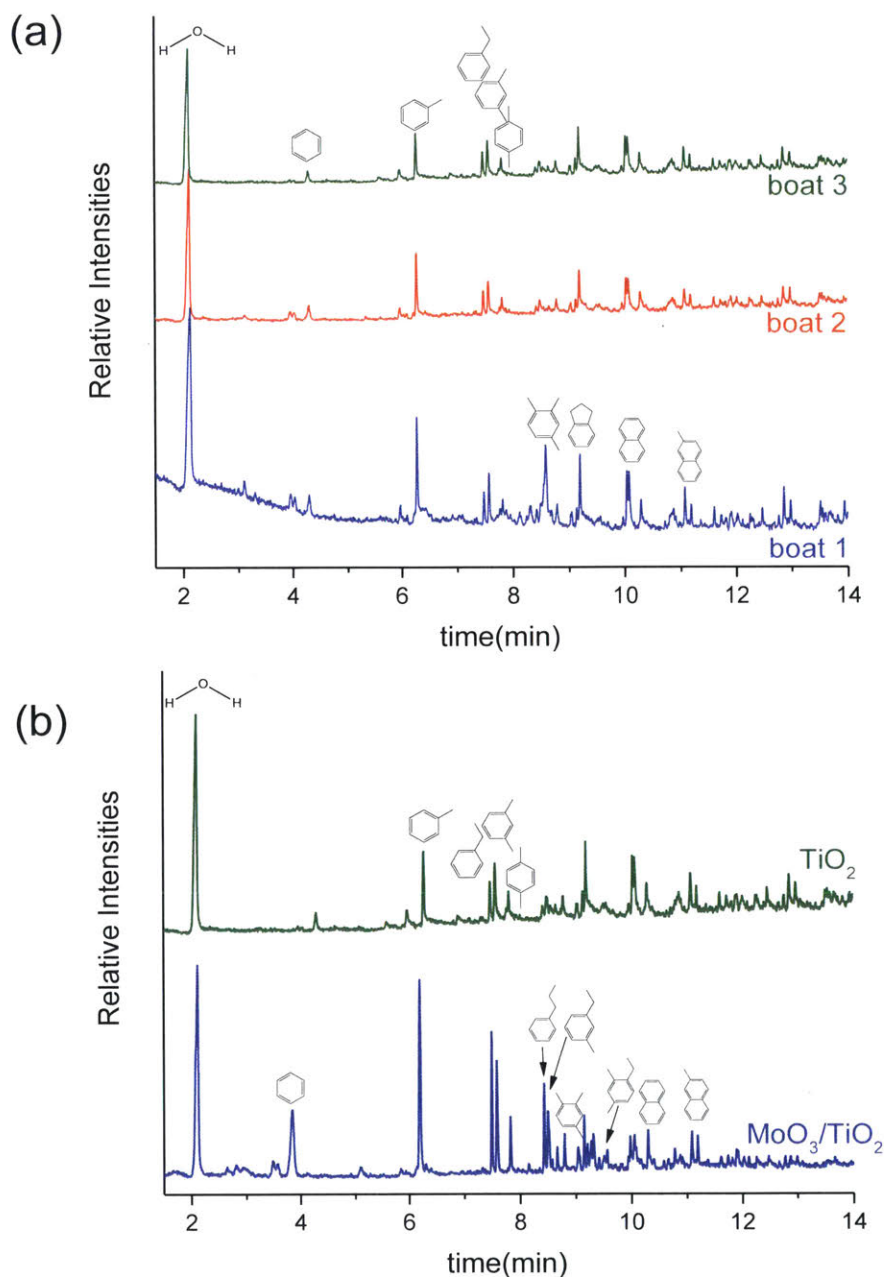


Figure S3.12 (a) GCMS chromatograms of the CFP of 3 pine boats over 40 mg of bare TiO_2 support in the micropyrolyzer-GCMS set up. The TiO_2 support shows minimal catalytic activity, and the deoxygenated products decrease in intensity when more pine boats are fed. **Figure S3.12 (b)** Overlay of GCMS spectra of CFP of the 3rd pine boat over $\text{MoO}_3/\text{TiO}_2$ and support TiO_2 in the micropyrolyzer-GCMS set up. The support TiO_2 shows less intense product peaks than $\text{MoO}_3/\text{TiO}_2$. Reaction conditions: catalysts= 40 mg, biomass = 3 boats of 0.5 mg pine, $T = 500^\circ\text{C}$, $P_{\text{total}} = 1.013$ bar (71 vol% H_2 -He). The cryo-trap temperature was set to -80°C in both experiments, thereby explaining the absence of alkenes and alkanes.

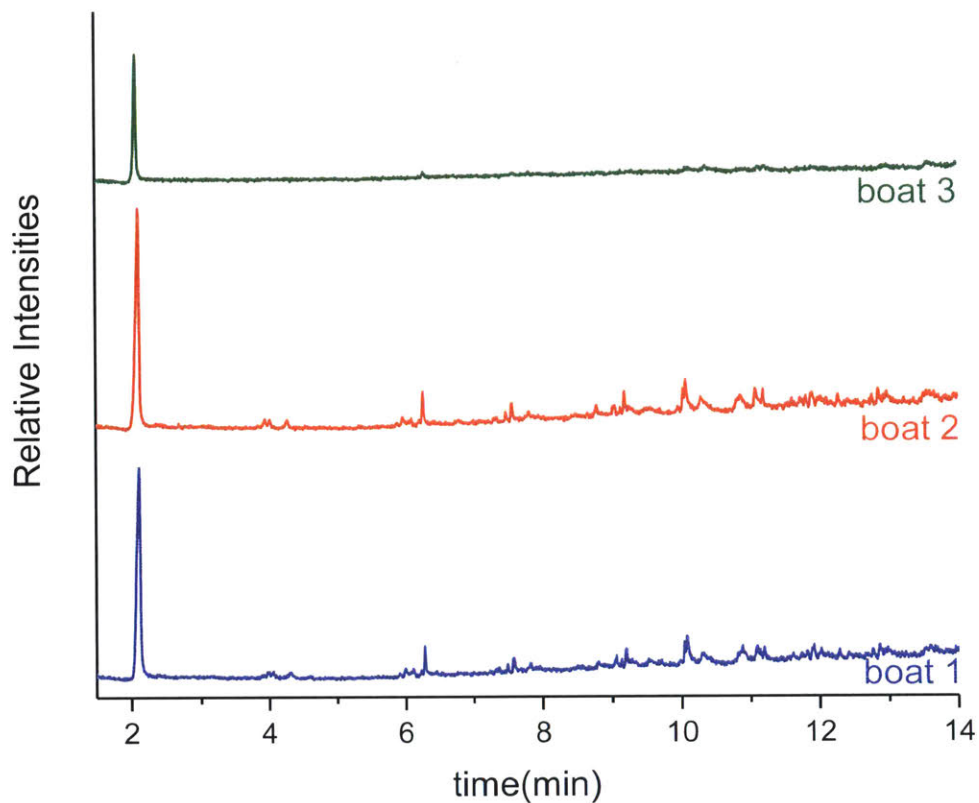


Figure S3.13 GCMS chromatograms of the CFP of 3 pine boats over 40 mg of bare ZrO_2 support in the micropyrolyzer-GCMS set up. The ZrO_2 support shows negligible catalytic activity under the reaction conditions investigated. Reaction conditions: catalyst = 40 mg of ZrO_2 , biomass = 3 boats of 0.5 mg pine, $T = 500^\circ C$, $P_{total} = 1.013$ bar (71 vol% H_2 -He)

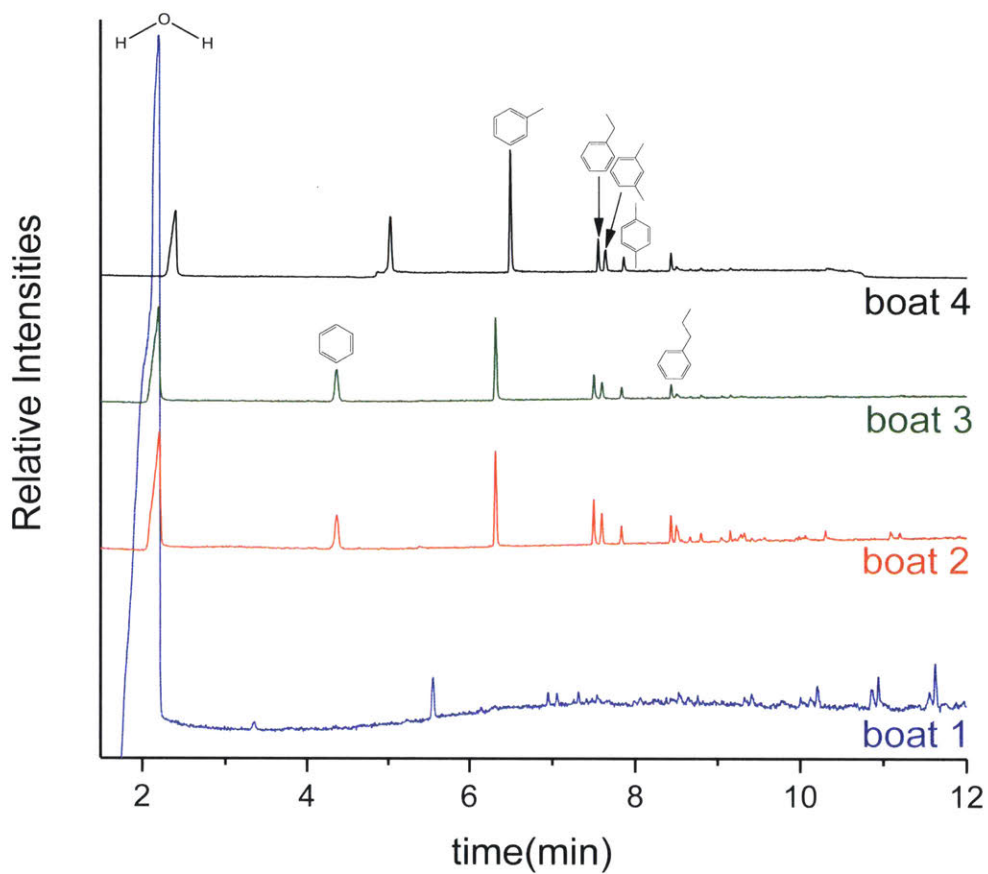


Figure S3.14 Product distribution of CFP of pine over 40 mg of MoO_3 in the micropyrolyzer-GCMS set up. Reaction conditions: catalyst = 40 mg, biomass = 4 boats of 0.5 mg pine, $T = 500^\circ\text{C}$, $P_{\text{total}} = 1.013$ bar (71 vol% H_2 -He). The cryo-trap temperature was set to -80°C in this experiment, thereby explaining the absence of alkenes and alkanes.

Table S3.3 Average product yields and selectivity values for the CFP of 3 pine boats over MoO₃/TiO₂, MoO₃/ZrO₂ and HZSM-5 in the micropyrolyzer-GCMS system.

Catalyst	MoO ₃ /TiO ₂	MoO ₃ /ZrO ₂	HZSM-5
Overall Carbon Yield (%)			
Aromatic hydrocarbons	7.4	7.4	17.3
Olefins	19.4	17.2	6.0
Paraffins	2.4	1.8	0.0
Oxygenates	0.4	0.0	0.0
CO ₂	2.8	5.0	5.5
Coke	6.8	7.3	11.9
Char	39.4	39.4	39.4
Total	78.6	78.2	80.2
Aromatic hydrocarbons selectivity (%)			
Benzene	28.8	28.0	11.9
Toluene	27.6	31.6	24.2
Xylene	10.1	10.5	14.9
Multi-substituted benzenes	16.5	14.4	3.7
Naphthalenes	8.6	9.6	19.8
Indanes/Indenes	6.6	4.0	12.1
Others	1.8	1.8	13.5
Olefins selectivity (%)			
Ethylene	2.0	2.3	36.0
Propene	62.0	68.6	26.4
Butene	13.5	13.8	0.0
Methylpropene	4.9	4.7	37.6
Pentene	2.8	2.2	0.0
Methylbutene	4.6	4.0	0.0
Cyclopentadiene	4.4	1.6	0.0
Cyclopentene	4.4	2.7	0.0
Cyclohexadiene	1.1	0.0	0.0

Others	0.3	0.2	0.0
Paraffins selectivity (%)			
Ethane	75.7	23.0	0.0
Butane	4.8	44.3	0.0
Dimethylcyclopropane	12.6	20.4	0.0
Cyclopentane	3.5	3.8	0.0
Isobutane	3.5	8.5	0.0

Table S3.4 Reaction conditions and product distribution from the CFP of biomass over HZSM-5.^{87,92}

Catalyst	HZSM-5	HZSM-5
Biomass	pinewood	Hybrid poplar
Reactor type	micropyrolyzer	micropyrolyzer
Pyrolysis temperature	550°C	500°C
Upgrading temperature	550°C	500°C
Biomass: Catalyst ratio	0.2	0.05
Overall Carbon Yield (%)		
Aromatic hydrocarbons	9.8	15.3
Olefins	N.A. ^c	7.7
Char	N.A. ^c	18.3
Coke	N.A. ^c	26.5
Light gases	N.A. ^c	21.6
Total		89.4
Aromatic hydrocarbons selectivity (%)		
Benzene	9	11.7
Toluene	15	33.7
Xylene	43	19.2
C ₉ aromatics ^a	16	9.9

C ₁₀₊ aromatics ^b	17	25.8
Olefins selectivity (%)		
Ethylene	N.A. ^c	50.5
Propene	N.A. ^c	43.7
Butene	N.A. ^c	5.9
Light gases selectivity (%)		
CO	N.A. ^c	69.4
CO ₂	N.A. ^c	30.6

^a C₉ aromatics: indane, indene, alkylbenzenes

^b C₁₀₊ aromatics: naphthalenes and higher polyaromatics

^c N.A. – not quantified in the study

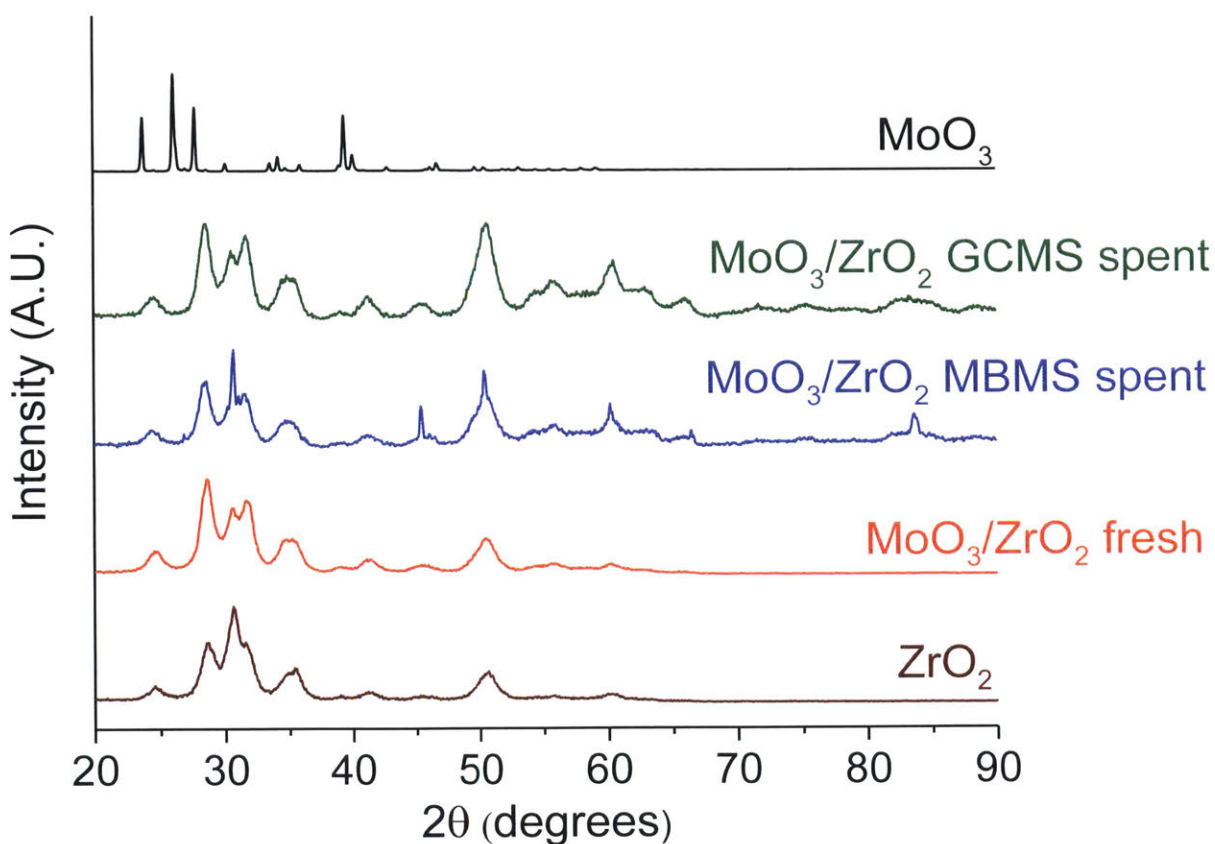


Figure S3.15 Normalised PXRD patterns of the fresh and spent MoO₃/ZrO₂ catalysts in comparison with fresh ZrO₂ and MoO₃ samples. The spent MoO₃/ZrO₂ samples from both reactor systems were derived after experiments shown in **Figure S3.3 (b)** and **S3.11**.

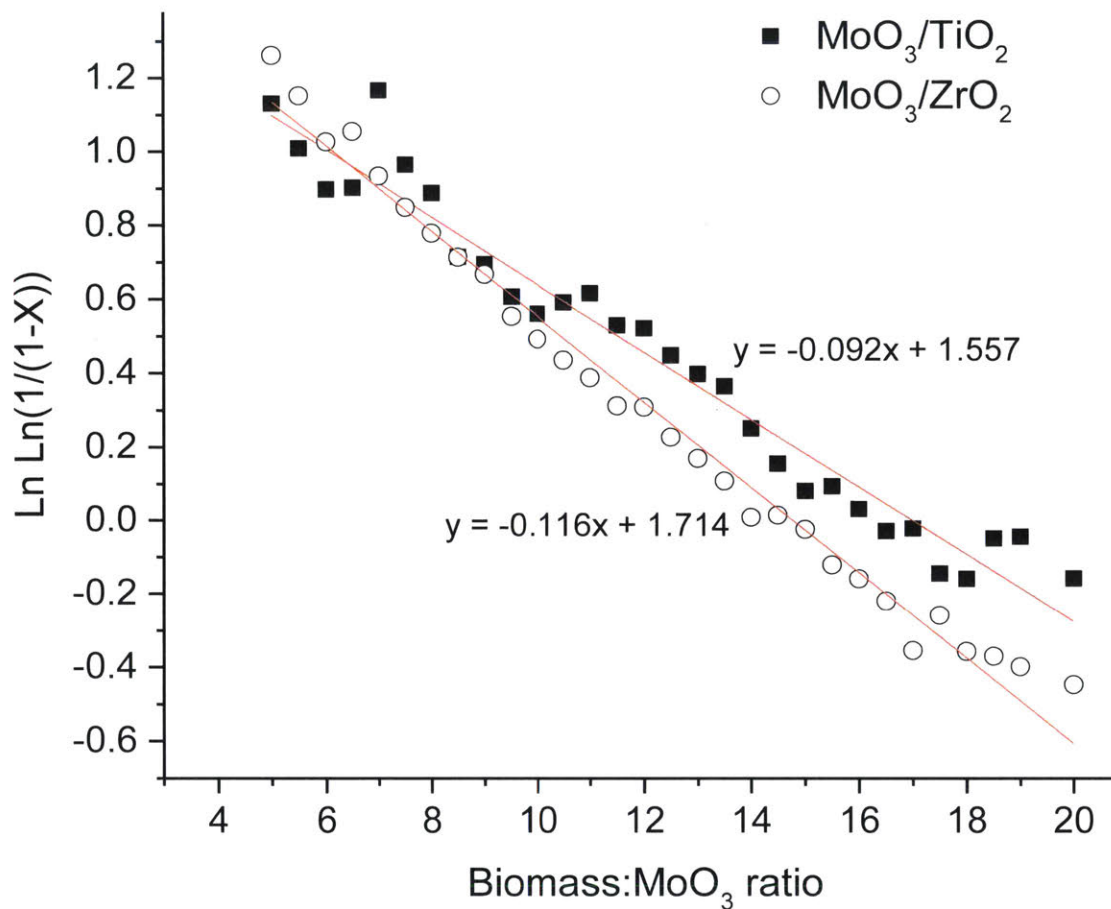


Figure S3.16 Deactivation profiles for $\text{MoO}_3/\text{TiO}_2$ and $\text{MoO}_3/\text{ZrO}_2$ for CFP of pine in the horizontal reactor-MBMS set up fitted to a first-order deactivation model.

Chapter 4

Investigating Mo₂C for HDO of lignin-derived model compounds

1. Introduction

Mo₂C has emerged as an attractive earth-abundant HDO catalyst with high selectivity towards cleaving C-O bond in biomass-derived oxygenates such as furfural, anisole and m-cresol at atmospheric H₂ pressures and relatively low temperatures (420-553 K).^{44-46,50,93} Specifically, Mo₂C featured high selectivity (>90% C₆⁺ basis) to benzene from HDO of anisole at 423 K, showing preferential cleavage of strong phenolic C-O bond. Detailed kinetic studies revealed that HDO on Mo₂C requires two distinct sites - one for H₂ dissociative adsorption and one for oxygenate activation.^{44,46,50} The site required for oxygenate adsorption was hypothesized to be metal-like in nature based on the invariant product generation rates normalized by *ex situ* CO chemisorption.^{44,46} In a subsequent study, oxygen mass balance performed during transient HDO of anisole revealed the incorporation of ~0.29 monolayer of oxygen on the carbide catalyst, suggesting the *in situ* oxidation of molybdenum carbide.⁸⁰ However, no new peaks corresponding to MoO_xC_yH_z, MoO₂ or MoO₃ were observed in PXRD patterns of spent catalysts, indicating no bulk oxidation of Mo₂C.^{46,50,93} *In situ* oxygen modification was therefore hypothesized to be a surface and/or a subsurface effect,⁹³ possibly indicating the existence of surface oxycarbide sites during HDO.⁸⁰ Though CO is typically used to titrate metal sites, CO can also bind to oxygen vacancies on the surface of MoO_xC_yH_z, similar to that observed during HDO over MoO₃.⁸⁰ Hence, the potential active site for oxygenate adsorption could be either metallic in nature or surface oxygen vacancies similar to that observed over MoO₃. Though Bhan and co-workers have shown good HDO reactivity over Mo₂C, the nature of active site over Mo₂C still remains ambiguous. Both coking and surface oxidation have hypothesized to be the cause for deactivation over Mo₂C. To our knowledge, no study has been carried out to distinguish between these two modes of deactivation.^{46,80}

Furthermore, since coking was the likely reason for deactivation observed during CFP over supported MoO_3 catalysts in the previous chapter, hydrogen pressure is a handle that can be tweaked to mitigate coking. Moreover, coking has also been suggested to be responsible for deactivation during HDO of furfural over Mo_2C .⁴⁴ Though hydrogen is expensive and excessive hydrogen pressures can saturate the aromatic hydrocarbons, slightly elevated hydrogen pressures (< 10 bar) can be used to minimize coking without ring saturation. However, MoO_3 catalysts are susceptible to reduction to Mo^{4+} and Mo^0 under high hydrogen pressures. Furthermore, both Mo^{4+} and Mo^0 species are less active for HDO. Hence, using elevated H_2 pressures for HDO over Mo_2C seems like a viable strategy since Mo_2C can withstand relatively high H_2 pressures. Moreover, Bhan and co-workers have only studied vapor phase HDO of oxygenates over atmospheric pressures. The effect of higher H_2 pressures on vapor phase HDO over Mo_2C has not been studied.

In this study, we investigate HDO of lignin-derived model compound 4-methylanisole on molybdenum carbide nanoparticles dispersed on silica. The catalyst was investigated for HDO of 4-methylanisole at atmospheric H_2 pressures and at 320, 350 and 400°C to observe differences in reactivity, selectivity and catalyst stability. Subsequently, Mo_2C was also subjected to higher H_2 pressures, 3-6 bar, to study the effect of H_2 pressures on catalyst stability. $\text{MoO}_3/\text{SiO}_2$ was also run under identical reaction conditions at 5 bar H_2 to compare its HDO behavior to that of $\text{Mo}_2\text{C}/\text{SiO}_2$. Extended X-ray and Fine Structure (EXAFS) and XPS were performed on spent $\text{Mo}_2\text{C}/\text{SiO}_2$ catalysts to investigate changes in the bulk and surface structure of the catalysts to gain insights into the deactivation mechanism.

2. Experimental

2.1 Materials and catalyst synthesis

The feeds, 4-methylanisole (99%, Sigma-Aldrich) and anisole (99%, Sigma-Aldrich) were used as received. H_2 (99.999%), CH_4 (99.999%), Air (dry grade) were purchased from Airgas. Molybdenum carbide (Mo_2C , ≥ 99 wt%), molybdenum (VI) oxide ($\text{MoO}_3 \geq 99.5\%$) and molybdenum (IV) oxide (MoO_2 , (≥ 99 wt%)) were purchased from Sigma-Aldrich. CAB-O-SIL M5 (SiO_2 , untreated fumed silica) was obtained from Cabot.

Silicon carbide powder (SiC, coarse, 46 grit) was used as an inert diluent during catalytic testing.

Our lab has a viable platform for synthesizing transition metal carbide nanoparticles using a reverse microemulsion method.⁹⁴ Though this synthesis technique was primarily used for the synthesis of tungsten carbide, this synthesis protocol has been altered to make Mo₂C nanoparticles, dispersed on silica (SiO₂). Since synthesis of tungsten carbide requires a carburization temperature of around 900°C, the protective encapsulating silica layer loses all its porosity at these high temperatures. This loss in porosity necessitates the dissolution of silica encapsulation layer before the catalyst can be used for reactivity so as to provide access to the sites for reactant molecules. Typically, in the RME method used for synthesis of WC nanoparticles, silica layer is dissolved using HF, while being supported on carbon black for electrochemical testing. However, in the case of Mo₂C, it can be synthesized at much lower temperatures around 600°C. At these temperatures, the molybdenum oxide nanoparticles might not sinter significantly, thereby not requiring silica encapsulation. As such, this synthesis is much simpler and easily scalable since the silica encapsulation and dissolution step are no longer needed.

Typically, Mo₂C/SiO₂ nanoparticles with 25 wt% molybdenum metal loading were synthesized. A reverse microemulsion (RME) is first prepared by mixing 240 ml of n-heptane with 54 ml of surfactant (Brij-L4 ®), followed by addition of 7.8 ml of ultrapure deionized water to obtain a clear solution.⁹⁴ The emulsion was then sonicated for ca. 15 min to allow the formation of water droplets in this RME. 4.35 ml of 10 w/v % Molybdenum(V) isopropoxide (MoIPO) solution in isopropanol was added to 120 ml of n-heptane to form an alkoxide precursor solution. This precursor solution was then transferred to RME under constant stirring at room temperature. MoIPO was allowed to hydrolyze for about 4 h before the addition of known quantities (~ 250 mg) of CAB-O-SIL ® silica. Upon addition of CAB-O-SIL® silica to RME, the high surface area silica particles aggregate with each other. RME-silica mixture is then sonicated for about 20 min or longer till a well dispersed RME-silica solution is obtained. At this point, the solution appears cloudy. Stirring was typically performed for approximately 16.5 hours to allow good dispersion of molybdenum oxide nanoparticles on silica. Molybdenum

oxide nanoparticles dispersed on silica were then recovered by adding 120 ml of isopropanol, stirring for about 20 min, and then letting the nanoparticles settle over 1 h. After this settling period, most of the liquid layer was decanted. The solid nanoparticles were then recovered from the remaining liquid via centrifugation at 6000 rpm for 10 min. These nanoparticles were then rinsed by dispersing them in 25 ml of isopropanol before centrifuging again at 6000 rpm for 10 min. Nanoparticles were then left to dry overnight, before being pulverized to obtain a fine brown powder. At this point, molybdenum oxide exists in an amorphous form dispersed on silica before being calcined at 400°C under air flow (100 ml/min) to form the crystalline domains. $\text{MoO}_3/\text{SiO}_2$ then undergoes a carburization treatment in a tube furnace to form $\text{Mo}_2\text{C}/\text{SiO}_2$. Typically, the carburization procedure involves heating $\text{MoO}_3/\text{SiO}_2$ in a 21% $\text{CH}_4\text{-H}_2$ mixture (total 153 ml/min) from room temperature to 650°C at 3°C/min, and holding at 650°C for 1 h. The resulting sample ($\text{Mo}_2\text{C}/\text{SiO}_2$) was then held under pure H_2 flow (120 ml/min) at 650°C for another hour to scavenge any residual surface carbon. The sample was cooled down in H_2 flow to room temperature, before being passivated under 1% $\text{O}_2\text{-N}_2$ flow (100 ml/min) for 2 h and then being exposed to ambient atmosphere.

2.2 Catalytic reactivity: Vapor phase HDO

Catalytic activity experiments were performed in a down-flow reactor during vapor phase HDO of 4-methylanisole. The reactor is a stainless steel tube (0.95 cm OD) with wall thickness (0.089 cm), which is mounted in a single-zone furnace (Applied Test Systems, Series 3210). Temperature is controlled by a temperature controller (Digi-Sense, model 68900-10), connected to a K-type thermocouple (Omega, model TJ36-CAXL-116u). The thermocouple is mounted downstream in the reactor, in direct contact with the catalyst bed. The catalyst is typically mixed with inert SiC (total 1.0 g), before being dispersed between two inert layers (2.0 g SiC in the bottom layer and 1.0 g SiC in top layer). Bhan and co-workers have shown that BET surface area and CO chemisorption values on passivated Mo_2C catalysts decrease with aging time after exposure to air, and that not all the CO adsorption sites were recovered after H_2 treatment at 450°C. Hence, for all catalytic activity measurements, $\text{Mo}_2\text{C}/\text{SiO}_2$ was prepared *in situ* from $\text{MoO}_3/\text{SiO}_2$ prior to reactivity studies. Similar to the carburization

performed *ex situ*, calcined MoO₃/SiO₂ was heated under 21% CH₄-H₂ mixture to 650°C at 3°C/min and held at 650°C for 1 h, before being subjected to only H₂ flow at 650°C for an extra hour to scavenge any surface carbon. Once the Mo₂C/SiO₂ nanoparticles were synthesized at 650°C, the catalyst was then cooled under H₂ flow to reaction conditions (typically 1 bar, 320°C). For experiments with H₂ pressures > 1 bar, a back pressure control regulator (GO Regulator, BP3 Series, BP3-1A11Q511PG) was used to maintain the higher pressures required. Feed such as 4-methylanisole is delivered to the reactor using a syringe pump (Harvard Apparatus, model 703005) and mixed with H₂ gas at the reactor inlet. Typically, the reactor was operated at a weight hourly space velocity (WHSV) of 3.6 h⁻¹. The standard reaction conditions include 150 mg of 25 wt% (Mo based) MoO₃/SiO₂ under 70 ml/min of H₂ flow with a feed flow rate of 4-methylanisole at 150 μl/h (H₂/4-methylanisole mole ratio ~ 140). This translates to about 40 mg of Mo₂C after carburization.

$$WHSV (h^{-1}) = \frac{\text{mass flow rate of reactant}}{\text{mass of equivalent Mo}_2\text{C}}$$

The reactor outlet lines were heated to 523 K to prevent any condensation. The vapor phase composition was analyzed using an online Gas Chromatograph (GC, Agilent Technologies, model 7890 A), equipped with a mass selective detector (MSD, Agilent Technologies, model 5975 C) and a flame ionization detector (FID). Mass spectrometer was used for identification of species while FID was used for quantification. A DB-5 column (Agilent, 30 m length x 0.25 mm ID x 0.25 μm film) was used with the following GC method: injector temperature of 548 K, detector temperature of 573 K, and split ratio of 1:20. The temperature program started from 343 K, followed by ramping to 523 K at 8 K/min.

The following equations were used to quantify the reactivity data:

$$\text{Conversion (\%)} = \frac{\text{Carbon moles of reactant consumed}}{\text{Carbon moles of reactant fed}} \times 100$$

$$\text{Selectivity (\%)} = \frac{\text{Carbon moles of product}}{\text{Carbon moles of reactant consumed}} \times 100$$

A first-order deactivation model was used to obtain deactivation rate constants.^{41,52}

2.3 Catalyst characterization

PXRD was performed on a Bruker D8 diffractometer using Nickel-filtered Cu-K α radiation ($\lambda = 1.5418 \text{ \AA}$). PXRD patterns were acquired on a 2D image plate, rotated at 15 rpm for 2θ values ranging from 20° to 90° with a step size of 0.04° and a scan speed of 0.2 s per step. BET surface area measurements were performed on Quantachrome Autosorb iQ automated gas sorption system. The surface area was determined using nitrogen adsorption–desorption experiments at liquid nitrogen temperature (77 K). Prior to the measurement, the catalyst was degassed at 623 K for at least 2 h. Transmission electron microscopy was performed on a JEOL 2010F equipped with a field emission gun (FEG) operating at 200 kV. Catalyst was sonicated in isopropanol and a drop was placed on to Cu grid prior to TEM analysis.

EXAFS and XPS catalysts samples were prepared in a stainless steel U-tube reactor (0.64 cm OD) , equipped with valves for isolation of the catalyst after reaction, thus preventing any exposure to air. 100 mg of MoO₃/SiO₂ was dispersed on a quartz wool plug in the reactor, directly in contact with a K-type thermocouple (Omega, model TJ36-CAXL-116u). The reactor was then placed in a furnace (Carbolite, model GTF 11/50/750B), connected to a temperature controller (Digi-Sense, model 68900-10). Anisole was the reactant in these studies, which was introduced to the reactor using a saturator at room temperature (H₂/anisole mole ratios ~ 215). The reaction was carried out at 320°C in flowing H₂ (70 ml/min) after *in situ* carburization in a 21% CH₄-H₂ mixture at 650°C for 1 h. Upon completion of the reaction, the valves on the U-tube reactor were shut and transferred to a N₂-filled glove box for retrieval of catalyst samples.

EXAFS was performed at the Brazilian Synchrotron Light Laboratory (LNLS) at CNPEM, Campinas, Brazil, using the XDS beamline. EXAFS samples were sealed in glovebox, before being shipped to LNLS. The EXAFS measurements were performed in transmission mode at room temperature at Mo K edge (19.9995 keV). Samples were mounted on slides and secured using Kapton tape. Each scan took *ca.* 30 min, and three scans were measured for each sample.

Similar to EXAFS, XPS samples were also prepared in the glovebox, and moved to the XPS instrument using a portable transfer vessel, thus ensuring no exposure to

air. XPS was performed on a PHI Versaprobe II instrument, equipped with a multi-channel hemispherical analyzer and an aluminum anode X-ray source (100 W), featuring a 100 μm beam, which scans over a 1.4 mm line across the surface of the sample. A dual-beam charge neutralization system was used with an electron neutralizer bias of 1.2 eV and an Ar ion beam energy of 10 eV. The binding energies were corrected to the adventitious C 1s signal at 284.8 eV.

Mo loading on SiO_2 was quantified using an Agilent 7900 inductively coupled plasma mass spectrometer (ICP-MS). Known quantities of catalyst samples were dissolved in a 50-50 % mixture of 48% Hydrogen Fluoride (HF) and concentrated nitric acid (HNO_3 , 67-70 w/v %, BDH Aristar). This solution was then diluted in a 2% HNO_3 before ICP analysis. A 5-point calibration curve built using dilutions of a 1000 ppm Mo standard was used to quantitatively determine the Mo loading.

3. Results and Discussion

3.1 Pre-reaction catalyst characterization

ICP-MS on $\text{MoO}_3/\text{SiO}_2$ (23.5 Mo wt%) and $\text{Mo}_2\text{C}/\text{SiO}_2$ (24.0 Mo wt%) revealed that Mo content on the catalyst samples were in close agreement with the nominal Mo loading (25 wt%). PXRD patterns for $\text{Mo}_2\text{C}/\text{SiO}_2$ nanoparticles show only peaks associated with $\beta\text{-Mo}_2\text{C}$ and SiO_2 , indicating a phase pure molybdenum carbide, with no other impurities (**Figure 4.1**). The absence of peaks corresponding to MoO_2 indicates that complete carburization was achieved. Given the high Mo loadings used in this study (25 wt%), the formation of crystalline MoO_3 structures is expected.

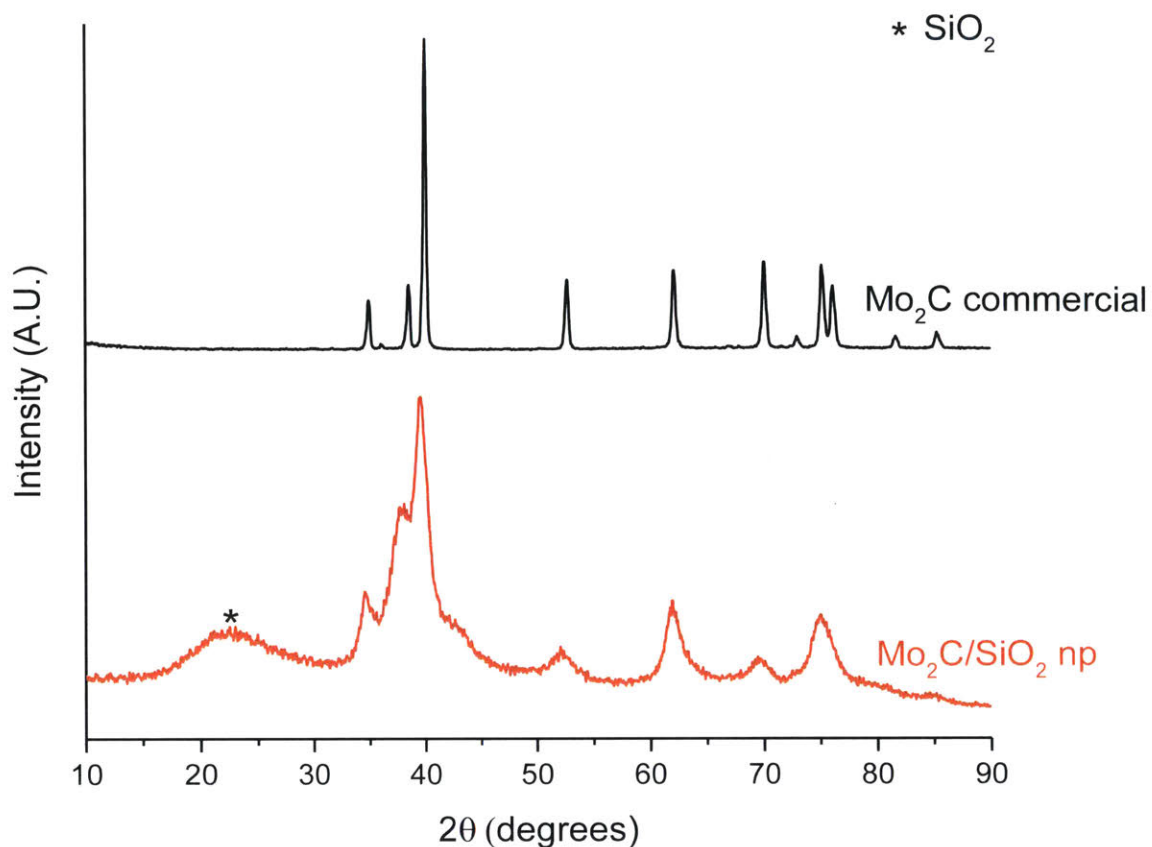


Figure 4.1 Normalised PXRD patterns of synthesized $\text{Mo}_2\text{C}/\text{SiO}_2$ nanoparticles in comparison with commercial Mo_2C .

SiO_2 , $\text{MoO}_3/\text{SiO}_2$ and $\text{Mo}_2\text{C}/\text{SiO}_2$ have BET surface areas of 324, 214 and 128 m^2/g . The decrease in surface area after incorporation of molybdenum oxide on silica support is expected due to the loss of external mesoporous surface area upon dispersion of molybdena species. Similarly, the catalyst loses more surface area after carburization due to the densification of the amorphous silica at the higher temperatures of 650°C.

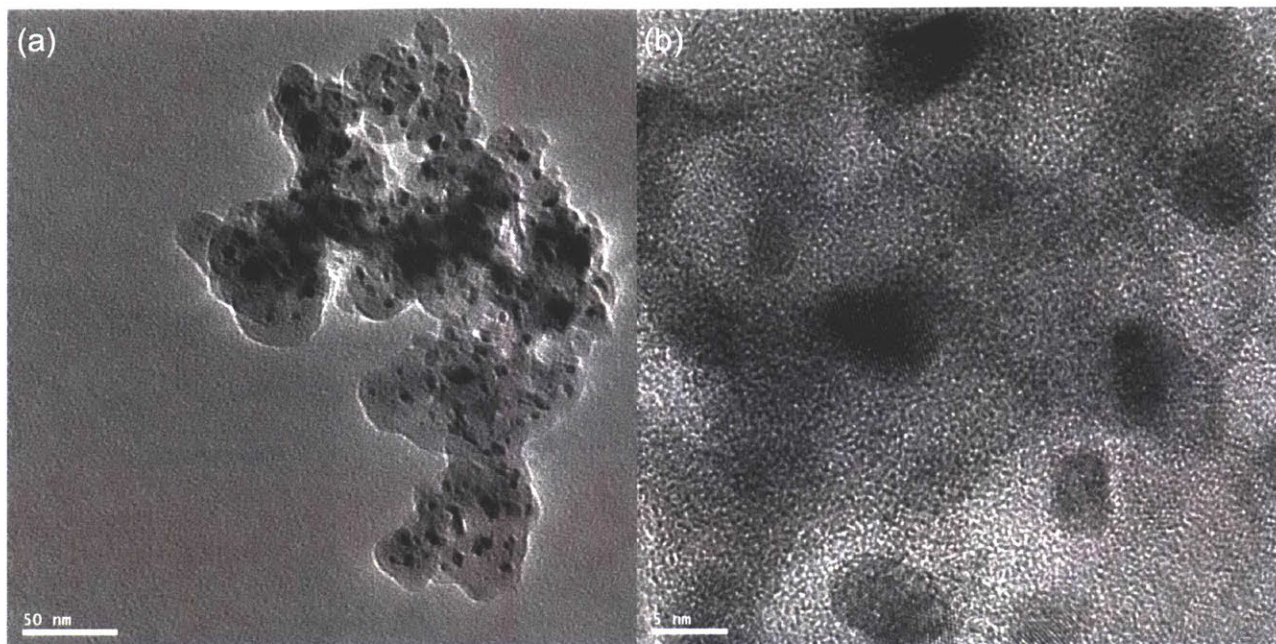


Figure 4.2 TEM images of Mo₂C/SiO₂ nanoparticles. (a) magnification of 50000x (b) magnification of 400000x

TEM images (**Figure 4.2**) confirm the presence of Mo₂C/SiO₂ nanoparticles. Mo₂C nanoparticles appear to be relatively well dispersed, with some amount of visible agglomeration. This relatively good dispersion is encouraging given the simplicity of the synthesis with respect to the direct addition of silica, thus suggesting that the sintering of nanoparticles during carburization at 650°C was minimal. This slight degree of agglomeration is not completely unexpected due to the direct deposition of silica in the RME, instead of encapsulation.⁹⁴ Overall, this direct deposition method of silica seems to strike a good balance between control over particle size and simplicity of synthesis.

3.2 HDO of 4-methylanisole at 1 bar

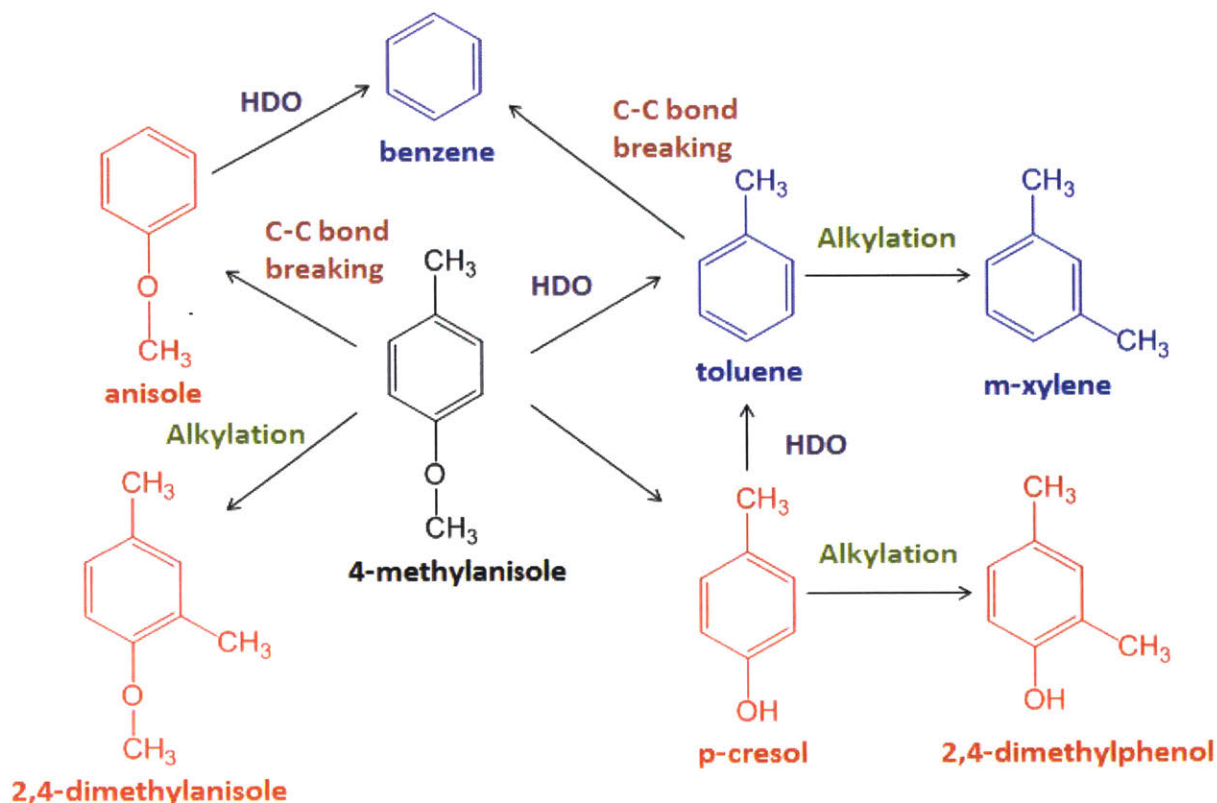


Figure 4.3 Reaction network of HDO of 4-methylanisole over $\text{Mo}_2\text{C}/\text{SiO}_2$. Products in blue are aromatic hydrocarbons while products in red are oxygenated aromatics.

Figure 4.3 shows the possible reaction products from 4-methylanisole. The ideal HDO product from 4-methylanisole is toluene, formed as a result of the cleavage of strong phenolic C-O bond. Methanol is also formed as a by-product of this reaction, which can then undergo HDO to form methane. Alternatively, the weaker aliphatic C-O bond in the methoxy group of 4-methylanisole can be cleaved to yield p-cresol as the product. Furthermore, toluene, p-cresol and 4-methylanisole can undergo alkylation, typically catalyzed by Brønsted acid sites, to form xylene, dimethylphenol, and dimethylanisole respectively. Unfavorable C-C bond breaking can also occur, leading to the formation of anisole, and benzene from 4-methylanisole, and toluene respectively.

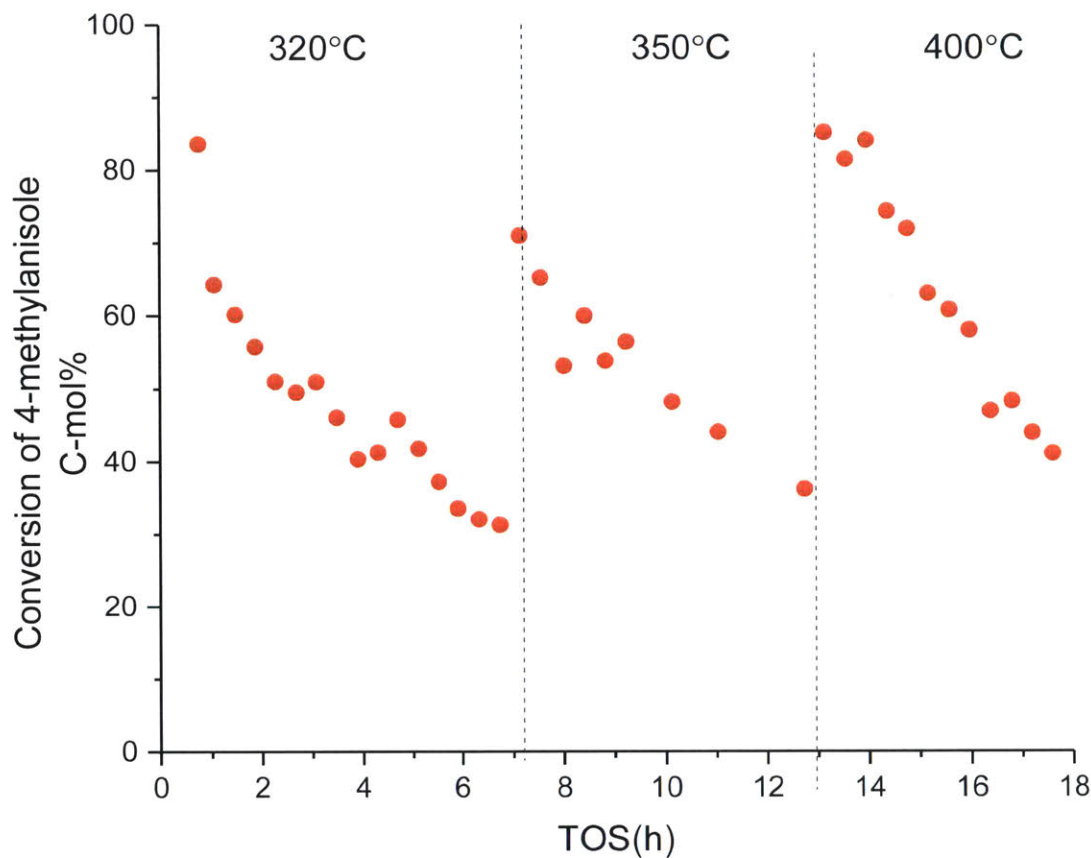


Figure 4.4 Conversion of 4-methylanisole as a function of time-on-stream (TOS) at various reaction temperatures over Mo₂C/SiO₂. Reaction conditions: P_{Total} = 1.013 bar (0.007 bar P_{4-methylanisole}, balance H₂), WHSV= 3.6 h⁻¹.

As seen from **Figure 4.4**, Mo₂C features relatively high conversions of 4-methylanisole at all three reaction temperatures. We note that the same catalytic bed was used for temperature cycling during entire reaction without any recarburation or reduction before switching to a new temperature. Notably, the catalyst tends to deactivate rapidly at all temperatures. Specifically, the conversion of methylanisole drops from ca. 84% to 30% in 7 h at 320°C. As expected, the conversion spikes from 30% to 70% once the reaction temperature is switched to 350°C due to the faster kinetics at higher reaction temperature. Again, at 350°C, conversion falls from 70% to 35% in 6 h, while reactivity plummets from 85% to ca. 40% in just 4.5 h at 400°C. Deactivation profiles can be fit to a first-order deactivation model, thus allowing the quantification of deactivation rate constants. The first-order deactivation rate constants obtained at 320°C, 350°C and

400°C are 0.164, 0.147, and 0.309 h⁻¹ respectively. The larger deactivation rate constant at 400°C indicates that the catalyst deactivates faster at this highest temperature while the near similar deactivation rate constants at 320°C and 350°C suggest that the deactivation kinetics is similar across these lower temperatures.

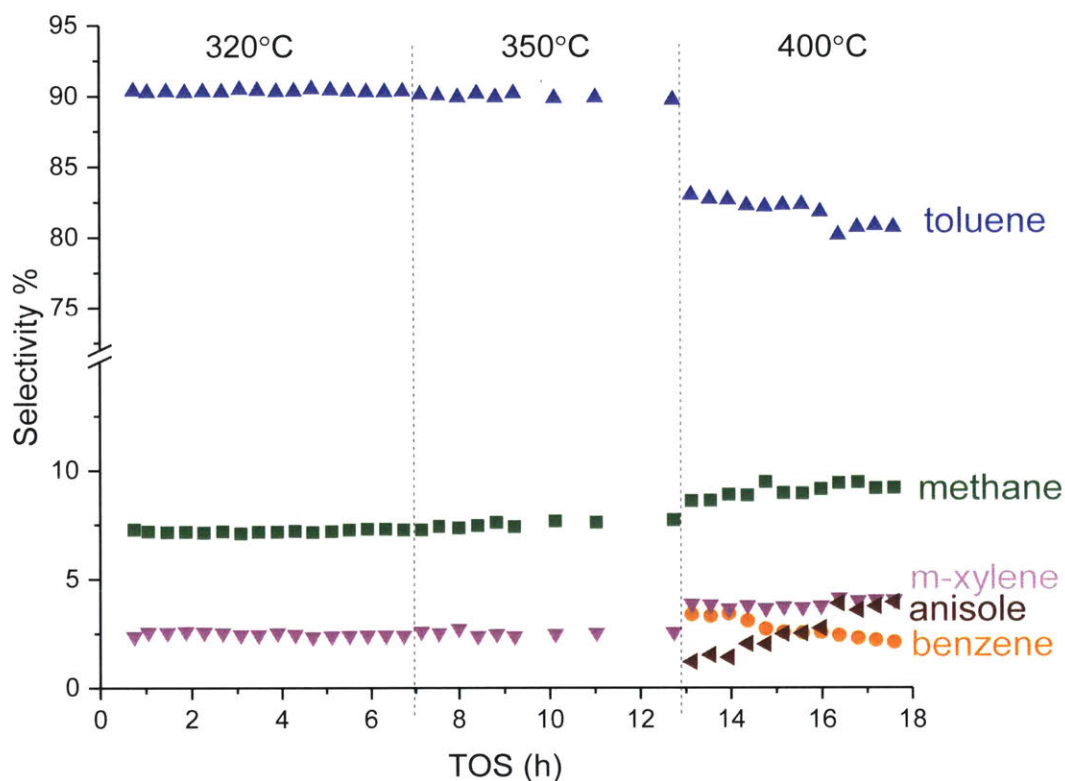


Figure 4.5 Selectivity during HDO of 4-methylanisole as a function of time-on-stream (TOS) at various reaction temperatures over Mo₂C/SiO₂. Reaction conditions: P_{Total} = 1.013 bar (0.007 bar P_{4-methylanisole}, balance H₂), WHSV = 3.6 h⁻¹.

At 320 and 350°C, the catalyst exhibits very similar selectivity profiles (**Figure 4.5**) during the reaction. Mo₂C/SiO₂ features a high selectivity to toluene (90%), with 7% selectivity to methane and 3% selectivity to m-xylene. At 400°C, toluene selectivity dips slightly to ca. 82%, with the formation of new products - anisole and benzene. Selectivity to methane slightly increases up to 9%. Toluene is the dominant product at all temperatures, indicating the selective cleavage of strong phenolic C-O bond. The absence of p-cresol in the product mixture further confirms that HDO on Mo₂C at these

reaction conditions occurs via demethoxylation, and not demethylation. HDO of 4-methylanisole to toluene yields methanol as a by-product, which subsequently gets deoxygenated to produce methane and water, thereby explaining the formation of methane. Minor alkylation product, m-xylene, is also observed, consistent with toluene observed during HDO of anisole over Mo_2C by Bhan and co-workers.⁴⁶ Notably, no sequential hydrogenation product of toluene i.e. methylcyclohexane was observed, indicating that toluene hydrogenation might not be thermodynamically favorable at these higher temperatures. This is in stark contrast to the production of cyclohexane (~10% selectivity on C_6^+ basis) during HDO of anisole at 150°C. However, benzene hydrogenation to cyclohexane is energetically more favorable at these lower temperatures, thus explaining the observation of hydrogenation product at 150°C, but not at 320°C in this study. Interestingly, Mo_2C catalyzes C-C bond cleavage at 400°C, thereby leading to formation of additional products such as benzene from toluene, and anisole from 4-methylanisole, respectively, thus explaining the lower toluene selectivity. We note that the product selectivities remained constant with time-on-stream during reaction at each temperature, indicating that observed drastic deactivation at all temperatures is due to a change in the number and not the nature of the active sites.⁴⁶ Overall, the reactivity data at atmospheric H_2 pressure suggests that $\text{Mo}_2\text{C}/\text{SiO}_2$ is effective in deoxygenating methylanisole to produce toluene at high selectivity (97% on C_6^+ basis) at 320 and 350°C, with minimal side products. However, the catalyst shows rapid deactivation, possibly due to oxidation and/or coking.⁴⁶

3.3 Comparison of rates in this study vs. that observed in literature

Methyl-anisole used in this study is very similar to anisole HDO performed by Bhan and co-workers.⁴⁶ Prior calculations have shown that the number or the type of additional substituents on the benzene ring do not significantly affect the bond-dissociation energies of C-O bond.⁵² Hence, kinetics measured with anisole can be largely translated to methyl-anisole. HDO of anisole over Mo_2C was shown to be zero order and near half-order (~0.6) with respect to anisole and H_2 pressure respectively.⁴⁶ The measured apparent activation energy E_A was ~ 70 kJ/mol.⁴⁶ Thus, the rate equation can be written as:

$$r = kP_{H_2}^{0.6}$$

where r = rate of oxygenate deoxygenation, k = rate constant, which is defined as:

$$k = Ae^{\frac{-E_A}{RT}}$$

where A = pre-exponential factor, E_A = apparent activation energy in J/mol, T = temperature in Kelvin and R = molar gas constant $J\ mol^{-1}\ K^{-1}$

Since HDO of anisole was predominantly performed at 423 K (150°C), the apparent activation energy measured can be extrapolated to 593 K (i.e. 320°C) in this study by rearranging the above equation:

$$\frac{k_2}{k_1} = e^{\frac{-E_A}{R}\left(\frac{1}{T_2} - \frac{1}{T_1}\right)}$$

Where k_2 is rate constant at T_2 and k_1 is rate constant at T_1 .

Deoxygenation rate to benzene from anisole was reported as $\sim 3 \times 10^{-4}$ mole s^{-1} mole $_{COsites}^{-1}$ at 423 K over bulk Mo_2C .⁴⁶ Since the rates are directly proportional to the rate constants, the ratios of rate are essentially the same as ratios of rate constants. By substituting $k_1 = 3 \times 10^{-4}$ mole s^{-1} mole $_{COsites}^{-1}$, $E_A = 70000$ J/mol, $T_1 = 423$ K, $T_2 = 593$ K and $R = 8.314$ J mol^{-1} K^{-1} in the above equation, k_2 can be calculated as:

$$k_{2,calc} = 9.0 \times 10^{-2} \text{ mole } s^{-1} \text{ mole}_{COsites}^{-1}$$

Similarly, k_2 or r_2 can be determined from the measured experimental conversions of 4-methylanisole in this study and compared with the calculated k_2 . Based on 4-methylanisole flow rate (150 μ l/h), mass of Mo_2C in the catalyst, and the initial conversion of 4-methylanisole (~ 90 C-mol % extrapolated to time $t = 0$ h at 593 K, see **Figure 4.4**), a rate of conversion of 4-methylanisole can be obtained. Specifically, this translates to 3.31×10^{-7} mole s^{-1} of 4-methylanisole converted over 39.9 mg of Mo_2C (25 wt % Mo in 150 mg MoO_3/SiO_2). Since each 4-methylanisole molecule has 8 carbon atoms, the rate can be converted to C-mols by simply multiplying by 8. Accounting for the selectivities to toluene at 90.3 C-mol % and that toluene has 7 C atoms/molecule, toluene production rates can be calculated as 3.07×10^{-7} mole s^{-1} . These rates can be subsequently normalized by CO chemisorption values to obtain turn over frequencies or rates in mole s^{-1} mole $_{COsites}^{-1}$. CO chemisorption measured by Bhan can be used as a reference to calculate turn over frequencies. CO chemisorption values ranged from as

low as $\sim 50 \mu\text{mol/g}$ to $220 \mu\text{mol/g}$ over bulk Mo_2C . Hence, experimentally measured k_2 or turn over frequencies were evaluated to be:

At CO Chemisorption of $50 \mu\text{mol/g}$,

$$k_{2,exp-max} = 1.5 \times 10^{-1} \text{ mole s}^{-1} \text{ mole}_{\text{COsites}}^{-1}$$

Similarly, at CO Chemisorption of $220 \mu\text{mol/g}$,

$$k_{2,exp-min} = 3.5 \times 10^{-2} \text{ mole s}^{-1} \text{ mole}_{\text{COsites}}^{-1}$$

The calculated $k_{2,calc}$ i.e. $9.0 \times 10^{-2} \text{ mole s}^{-1} \text{ mole}_{\text{COsites}}^{-1}$ lies right in the middle of experimentally determined k_2 values above. In fact, the average $k_{2,exp}$ corresponds to $9.4 \times 10^{-2} \text{ mole s}^{-1} \text{ mole}_{\text{COsites}}^{-1}$, very close to $k_{2,calc}$. Overall, these kinetic calculations show that 4-methylanisole deoxygenation rates to toluene observed in this study are similar to the anisole deoxygenation rates to benzene observed by Bhan.⁴⁶

3.4 Effect of H_2 pressure on HDO of 4-methylanisole over $\text{Mo}_2\text{C}/\text{SiO}_2$ and $\text{MoO}_3/\text{SiO}_2$

Since high H_2 pressures can mitigate coke formation and potentially prevent oxidation, the effect of different H_2 pressures on the catalyst stability was investigated. A higher H_2 flow rate 140 ml/min was used during the pressure cycling experiment, while keeping all other reaction conditions constant. Initially, the catalyst was subjected to HDO at 1 bar , 320°C before the same catalytic bed was subjected to pressure cycling at 3 bar (320°C), 6 bar (320°C) and 5 bar (350°C). As expected, the first-order deactivation rates decreased significantly at higher pressures, implying higher stability with higher hydrogen pressures (see **Figure 4.6**). Notably, catalyst at 5 bar 350°C featured the lowest deactivation rate constant (0.017 h^{-1}). Specifically, first-order deactivation rate constant at 5 bar , 350°C was 10 times lower than at 1 bar , 320°C . Again, regardless of the pressures, the selectivities to products were predominantly constant throughout – 89% toluene, 9% methane and 2% xylene. This constant selectivity again implies that higher H_2 pressure does not change the identity but only the number of the active sites. We hypothesize that the higher H_2 pressures employed here both reduce the formation of coke, and also aid in the faster removal of coke already formed on the catalyst surface, thus ensuring a larger number of sites to be active for HDO, leading to

enhanced catalyst stability since H_2 is typically known to mitigate coke in various industrial hydrocarbon conversion processes.⁹⁵

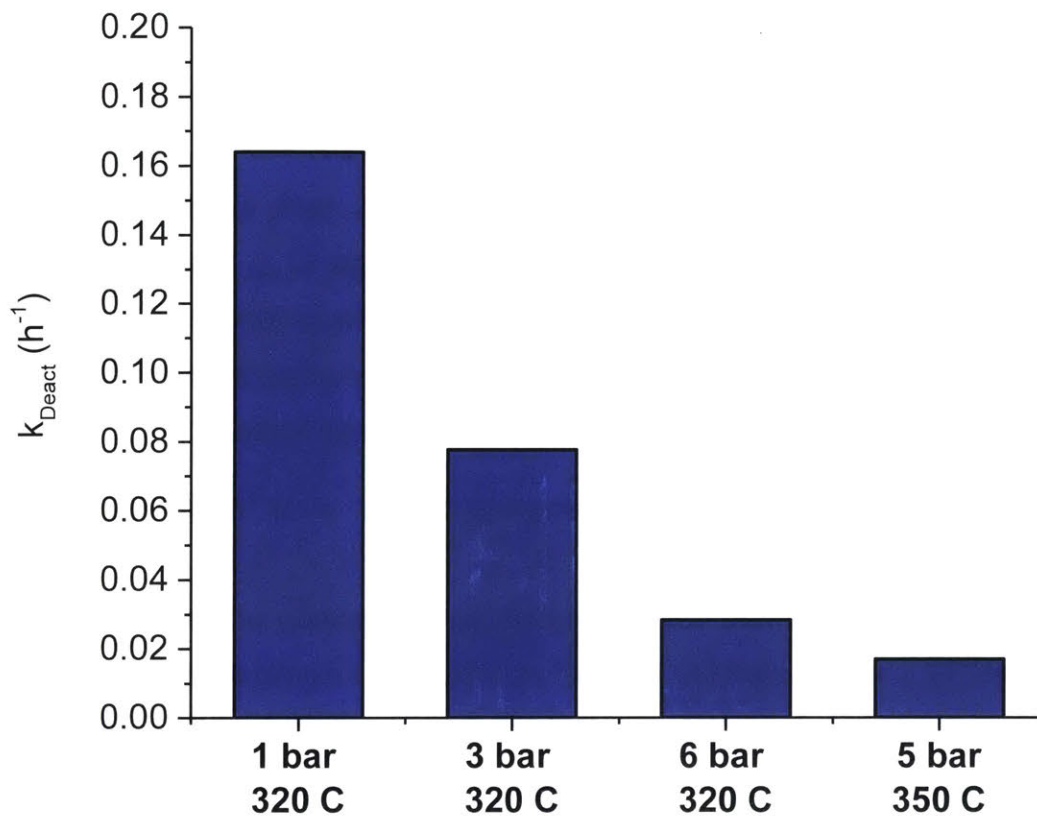


Figure 4.6 First-order deactivation rate constants obtained during HDO of 4-methylanisole over Mo_2C/SiO_2 at various H_2 pressures, $WHSV = 3.6 h^{-1}$.

Since the same catalyst bed was subjected to different H_2 pressures, some of the deactivation observed later at higher H_2 pressures could possibly be a secondary effect of the earlier deactivation. Hence, a fresh Mo_2C/SiO_2 sample was investigated for HDO at the optimal conditions of 5 bar, 350°C. The catalyst showed excellent stability again as it still had 40% of its initial activity even after 140 h time on stream (**Figure 4.7**). The catalyst exhibited constant high selectivities (~90%) to toluene. The deactivation profiles obtained were identical with deactivation rate constants of $0.017 h^{-1}$ across both experiments. This result further confirmed that Mo_2C/SiO_2 is indeed a highly selective and stable catalyst at high hydrogen pressures. In total, ca. 134 mmol of 4-methylanisole were converted over the entire reaction. As a lower estimate, assuming

every mole of Mo is active for HDO, this long-term reactivity translates to 344 mmol methylanisole converted per mmol of Mo. Based on chemisorption values (220 $\mu\text{mol/g}$) obtained over bulk Mo_2C^{46} as a reference, the total turnover number is in the range of 15000 mmol methylanisole converted per mmol CO adsorption site.

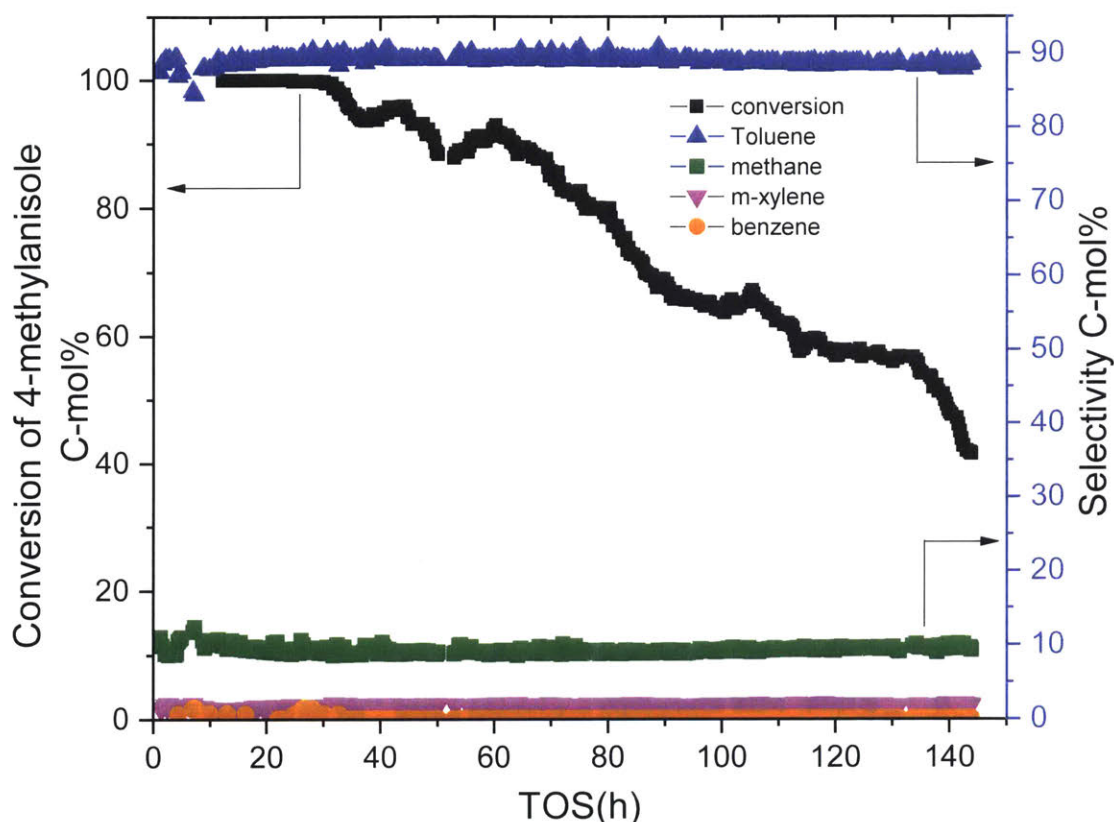


Figure 4.7 Conversion and selectivity during HDO of 4-methylanisole as a function of time-on-stream (TOS) over $\text{Mo}_2\text{C}/\text{SiO}_2$ at 5 bar, 350°C. Reaction conditions: H_2 : 140 ml/min, 4-methylanisole feed rate: 150 $\mu\text{l/h}$, WHSV = 3.6 h^{-1} .

Subsequently, fresh $\text{MoO}_3/\text{SiO}_2$ was also investigated under identical reaction conditions of 5 bar, 350°C. As expected, $\text{MoO}_3/\text{SiO}_2$ showed less reactivity than Mo_2C (**Figure 4.8**). The conversions appear to lie around ca. 15%. However, the selectivities to products were changing with time and were also vastly different from that of the carbide. $\text{MoO}_3/\text{SiO}_2$ featured an initial 80% selectivity to toluene which reduced to ca. 60% after 14 h, and thereafter remained at this steady state value. About 30% combined selectivity to oxygenates, comprising mostly p-cresol, dimethylanisole and

dimethylphenol are observed at steady state. It is worth noting that no such oxygenate products were observed for Mo₂C. The observation of p-cresol in addition to toluene indicates that MoO₃ also cleaves the weaker aliphatic C-O bond. The presence of dimethylanisole and dimethylphenol indicate likely Brønsted acid based alkylation on MoO₃ surfaces. Comparing MoO₃ with Mo₂C, it is apparent that Mo₂C is more selective for HDO than MoO₃ under identical reaction conditions investigated in this study.

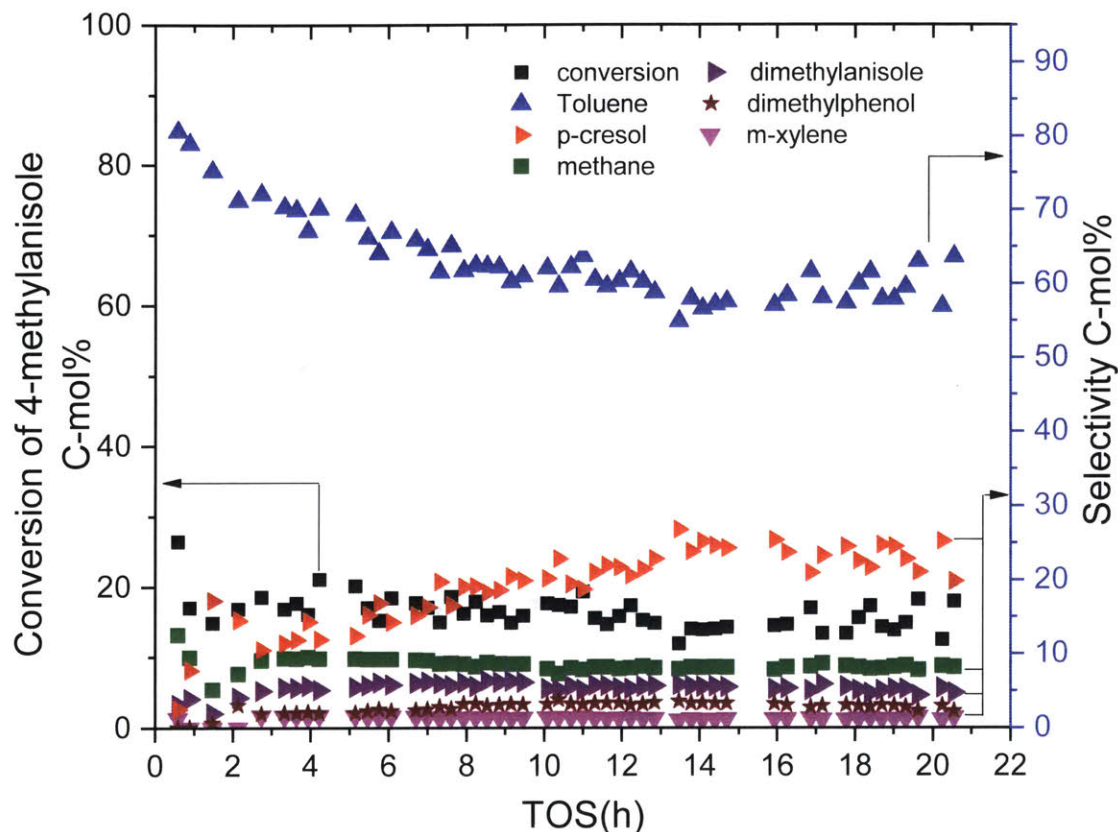


Figure 4.8 Conversion and selectivity during HDO of 4-methylanisole as a function of time-on-stream (TOS) over 150 mg of MoO₃/SiO₂ at 5 bar, 350°C. Reaction conditions: H₂: 140 ml/min, 4-methylanisole feed rate: 150 μl/h, WHSV = 3.6 h⁻¹.

3.5 EXAFS of spent Mo₂C/SiO₂ and MoO₃ catalysts

In order to understand the cause of deactivation observed at 1 bar, spent Mo₂C/SiO₂ catalysts after HDO of anisole (another lignin-derived model compound) at various TOS – after 1h, 9h and 24 h of reaction were retrieved and analyzed with X-ray absorption spectroscopy (XAS) at LNL beamline. To run these experiments with comparable

H₂-feed mole ratios using a saturated vapor stream of feed, Anisole (3.54 mm Hg) was used instead of 4-methylanisole (1.1 mm Hg) due to its higher vapor pressure.

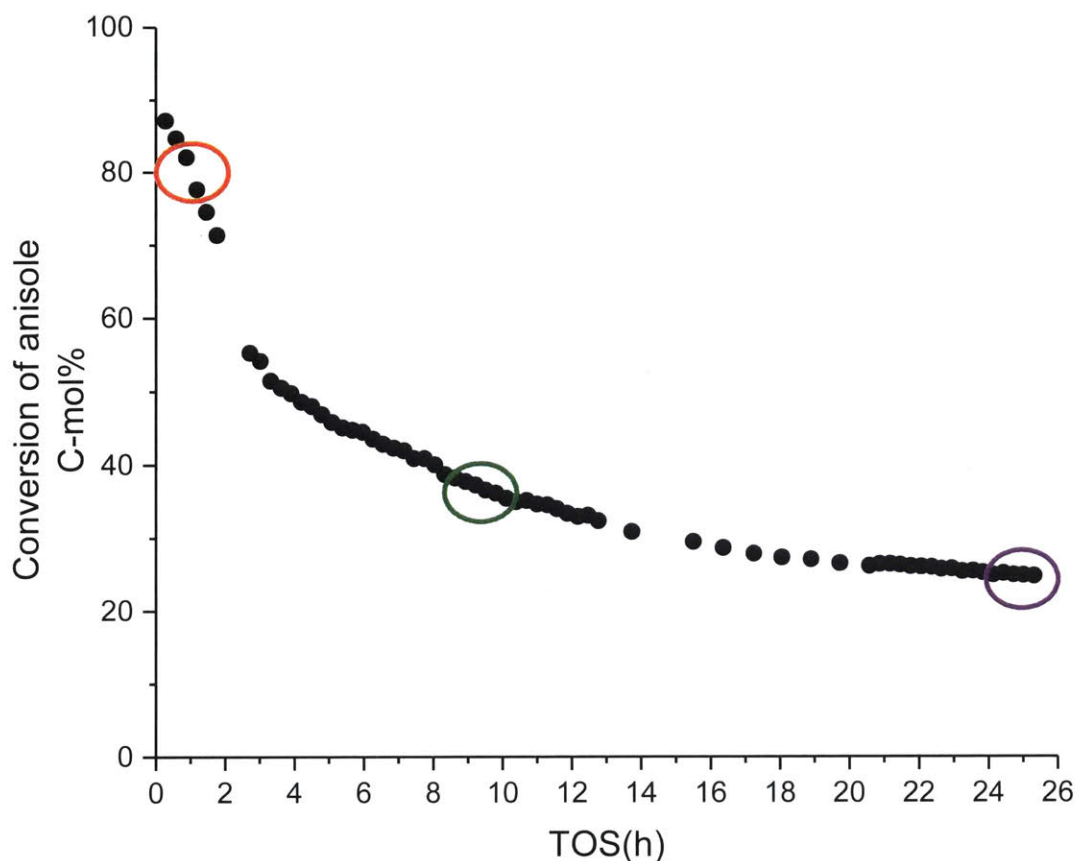


Figure 4.9 Conversion during HDO of anisole as a function of time-on-stream (TOS) over Mo₂C/SiO₂ in a U-tube reactor. Reaction conditions: P_{Total} = 1.013 bar (0.005 bar P_{anisole}, balance H₂). The circles in red, green and purple refer to the TOS at which the spent catalysts were recovered for EXAFS and XPS analysis.

Figure 4.9 shows conversion of anisole at 1 bar, 320°C over Mo₂C/SiO₂ during a 25 h time period. Similar to HDO of 4-methylanisole, the catalyst featured constant high selectivity (~90%) to benzene, dominant HDO product. Notably, the catalyst appears to have three zones of deactivation as seen by the three different slopes. The deactivation profiles can be split into three time zones: 1) 0-2 h 2) 2- 13 h and 3) 13-25 h TOS with the first zone showing the fastest deactivation, followed by second and last. Towards the end of the experiment, the catalyst tends to approach a steady state exhibiting relatively constant conversions. The experiment was then repeated twice but the

reaction was now stopped at 1h and 9 h respectively to produce 2 other spent catalysts, ensuring that catalysts at all three deactivation zones are prepared for EXAFS analysis. However, X-ray absorption near edge structure (XANES) spectra reveal no appreciable changes in the bulk structure of the catalyst and that Mo₂C structure is retained throughout the reaction (see **Figure 4.10**).

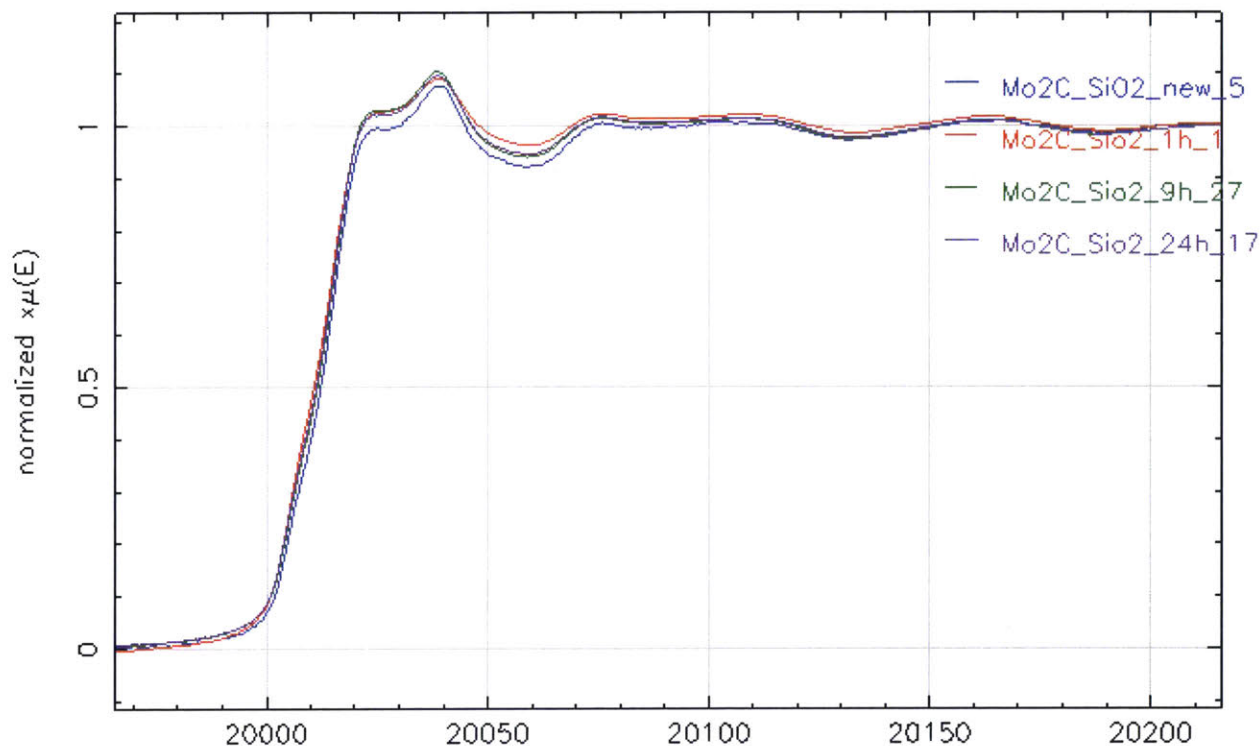


Figure 4.10 X-ray Absorption near edge structure (XANES) spectra of Mo K-edge for fresh and spent Mo₂C/SiO₂ catalysts after 1 h, 9 h and 24 h HDO reaction with anisole.

This invariance in XANES spectra across the spent catalysts indicates that bulk Mo₂C phase is maintained throughout the reaction and that no bulk oxidation to MoO_xC_yH_z and/or MoO₂ is observed. This negligible change in bulk structure of Mo₂C during HDO is in stark contrast with the bulk reduction of MoO₃ to a mixture of MoO₂ and MoO_xC_yH_z during HDO of m-cresol.^{52,53} Similar EXAFS measurements were also recorded on spent MoO₃ catalysts to compare the changes in bulk structure of the catalyst during HDO of anisole.

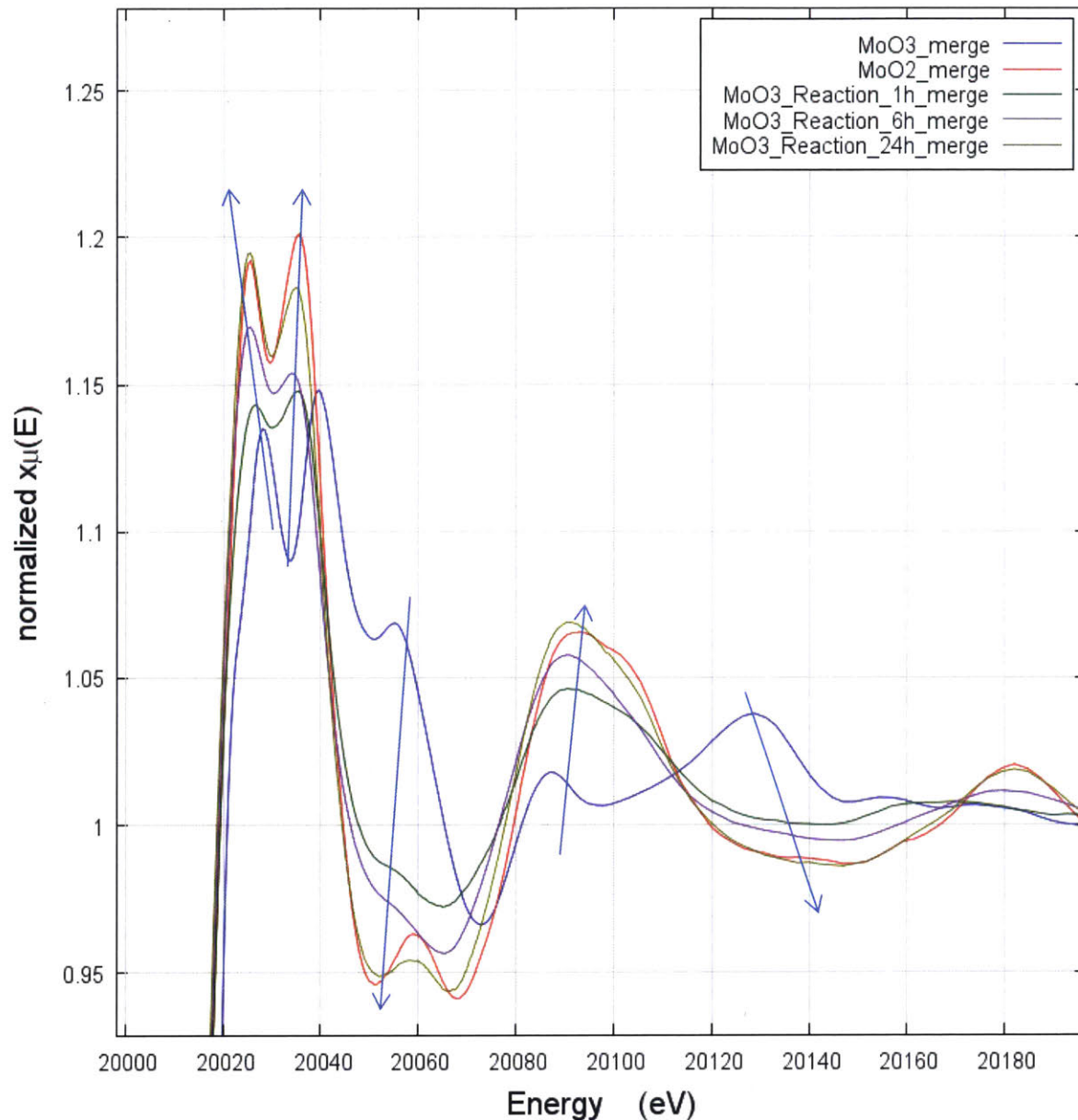


Figure 4.11 X-ray Absorption near edge structure (XANES) spectra of Mo K-edge for fresh and spent MoO₃ catalysts after 1 h, 6 h and 24 h of HDO reaction with anisole.

Mo K-edge XANES spectra (**Figure 4.11**) show a bulk transition from MoO₃ to MoO₂ after 24 h of HDO reaction with anisole. This bulk reduction observed during HDO of anisole is consistent with that observed during HDO of m-cresol, indicating that this bulk transformation is feed-independent.

3.6 XPS of spent $\text{Mo}_2\text{C}/\text{SiO}_2$

However, the surface oxidation of carbide cannot be ruled out solely based on EXAFS data since EXAFS is a bulk technique which cannot capture the changes on the surface of the catalyst. To complement this bulk characterization technique, the spent catalysts were subjected to surface-sensitive XPS analysis.

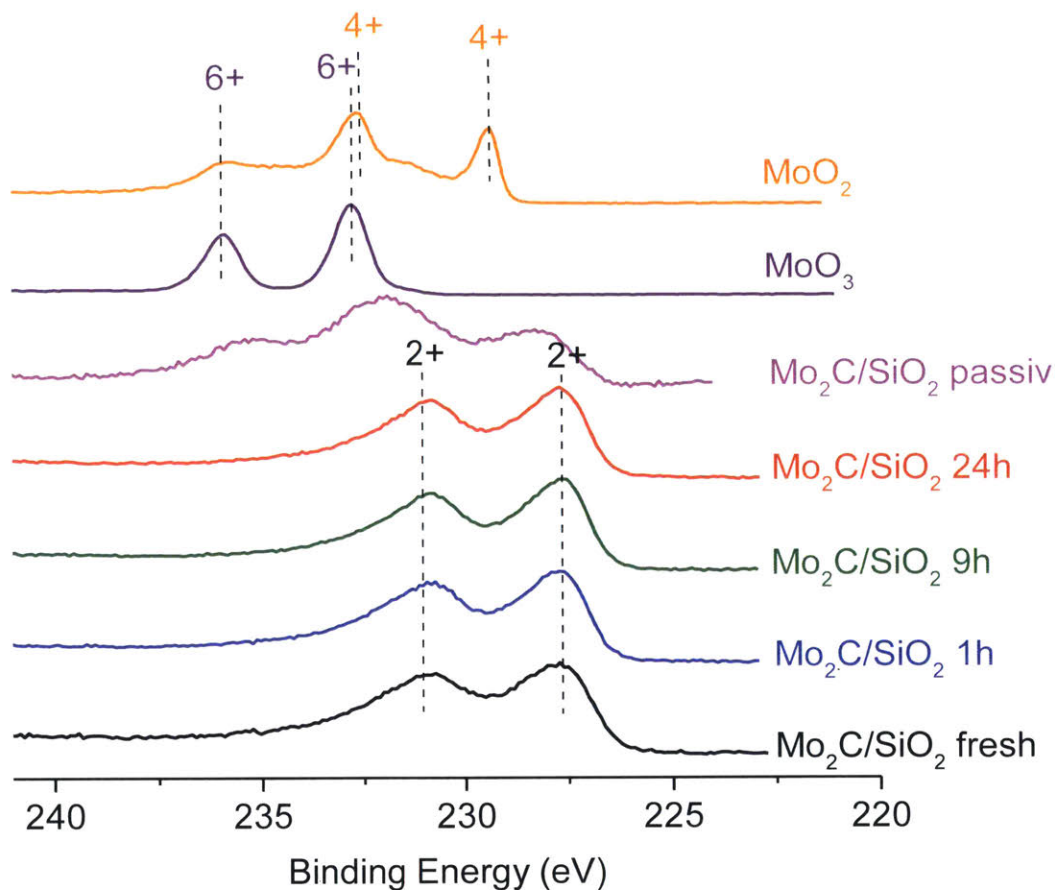


Figure 4.12 XPS spectra showing Mo 3d binding energy region of fresh and spent $\text{Mo}_2\text{C}/\text{SiO}_2$ after 1h, 9 h and 24 h of HDO reaction with anisole in comparison with MoO_2 , MoO_3 and passivated $\text{Mo}_2\text{C}/\text{SiO}_2$. Passivated Mo_2C refers to Mo_2C prepared under similar carburization conditions in a tube furnace, before being passivated with 1% $\text{O}_2\text{-N}_2$ mixture for 2 h and then being exposed to ambient atmosphere.

Interestingly, even the surface of the catalyst remained predominantly as a carbide after reaction. Post-reaction XPS spectra (**Figure 4.12**) revealed that dominant Mo^{2+} associated with Mo_2C is maintained throughout the reaction, identical to that

observed in the fresh catalyst. The absence of signals at higher binding energies corresponding to Mo^{4+} , Mo^{5+} or Mo^{6+} indicates that the catalysts did not undergo appreciable surface oxidation during the course of HDO reaction. Furthermore, C 1s region (**Figure 4.13**) shows that carbidic signal at 282.8 eV remains intact on all spent catalysts, confirming that the dominant phase on the surface is carbidic in nature throughout the reaction.

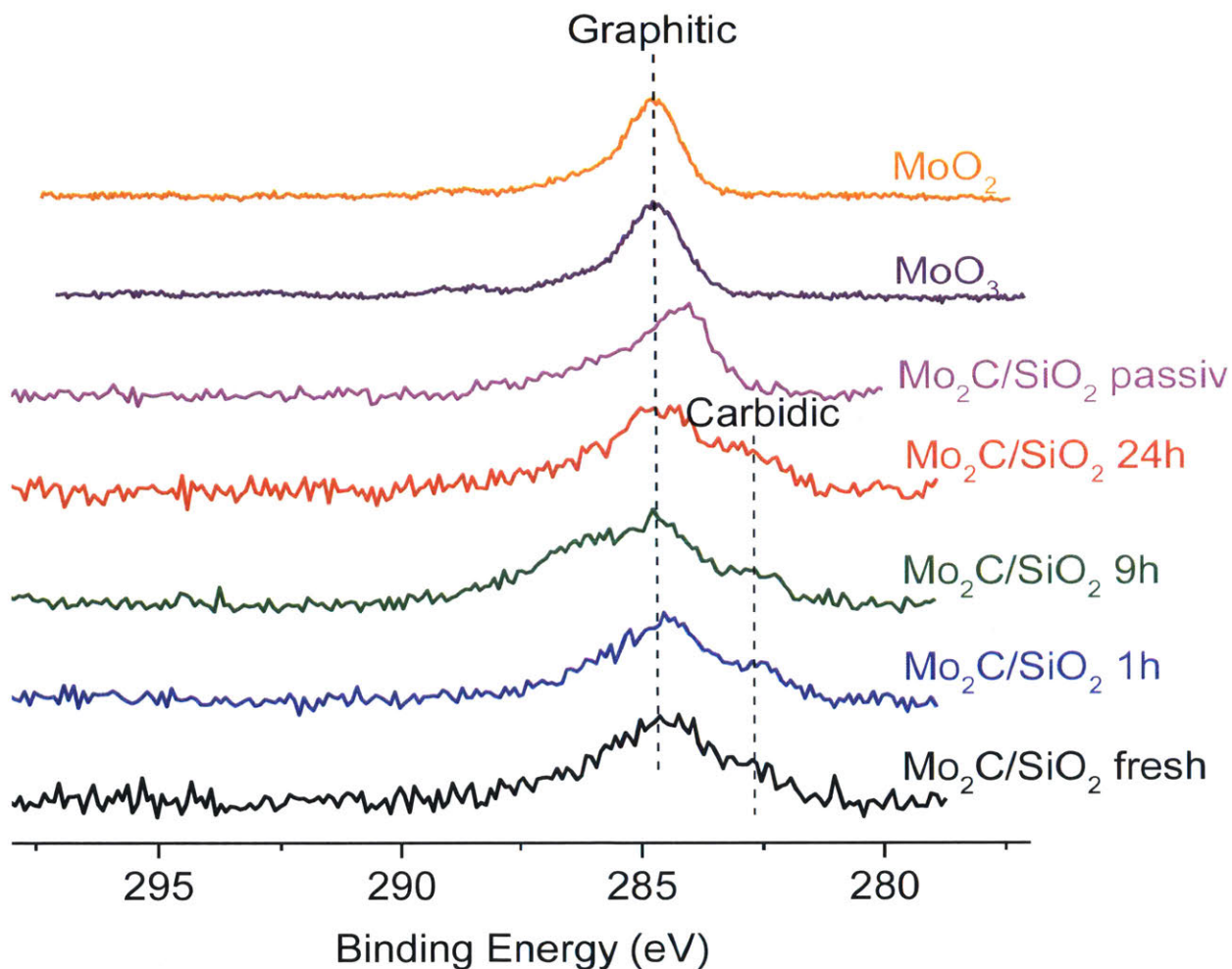


Figure 4.13 XPS spectra showing C 1s binding energy region of fresh and spent $\text{Mo}_2\text{C}/\text{SiO}_2$ after 1h, 9 h and 24 h of HDO reaction with anisole in comparison with MoO_2 , MoO_3 and passivated $\text{Mo}_2\text{C}/\text{SiO}_2$. Passivated Mo_2C refers to Mo_2C prepared under similar carburization conditions in a tube furnace, before being passivated with 1% $\text{O}_2\text{-N}_2$ mixture for 2 h and then being exposed to ambient atmosphere.

Taken together, EXAFS and XPS data indicate that both bulk and surface structure of Mo_2C do not change appreciably during the course of HDO reaction and that oxidation

cannot account for the observed drastic deactivation. Hence, deactivation is most likely due to the accumulation of carbon species on the catalyst surface.

4. Conclusions

In summary, phase pure $\text{Mo}_2\text{C}/\text{SiO}_2$ nanoparticles were synthesized and investigated for HDO of 4-methylanisole. $\text{Mo}_2\text{C}/\text{SiO}_2$ is an effective HDO catalyst that produces toluene from 4-methylanisole at high selectivities (97% on C_6^+ basis) at 320 and 350°C at atmospheric H_2 pressures. However, $\text{Mo}_2\text{C}/\text{SiO}_2$ catalyzed undesirable C-C bond breakage at a higher temperature of 400°C, thus leading to the formation of additional products such as toluene and anisole. Notably, at 1 bar, the catalyst displays rapid deactivation at all three temperatures. EXAFS and XPS were performed on spent $\text{Mo}_2\text{C}/\text{SiO}_2$ catalysts to gain insights into the causes of deactivation. However, both EXAFS and XPS data revealed that the bulk and surface structure of Mo_2C respectively remains relatively unchanged throughout the reaction, indicating that bulk or surface oxidation cannot account for the drastic deactivation. Deactivation is likely attributed to the build-up of carbonaceous species on the catalyst surface. To mitigate the effects of coking, the effect of H_2 pressures was investigated in this study. Clearly, higher H_2 pressures promote catalyst stability, with $\text{Mo}_2\text{C}/\text{SiO}_2$ at 5 bar, 350 °C featuring the lowest first-order deactivation rate constant of 0.017 h^{-1} . Specifically, $\text{Mo}_2\text{C}/\text{SiO}_2$ exhibited 40 % conversion even after 140 h time-on-stream with 4-methylanisole, indicating a highly stable catalyst. Again, the catalyst preferentially cleaved the stronger phenolic C-O bond to yield toluene as the major product. In contrast, $\text{MoO}_3/\text{SiO}_2$ operated at identical reaction conditions showed much lower conversions (~ 15%) and lower toluene selectivities (60% at steady state). The presence of oxygenates such as p-cresol throughout the reaction indicates that $\text{MoO}_3/\text{SiO}_2$ also cleaves the weaker aliphatic C-O bond, likely due to the presence of Brønsted acid sites.

Acknowledgements

Dr. Sean. T. Hunt is acknowledged for teaching me the RME synthesis protocols, acquiring TEM images, and for insightful discussions leading to this chapter.

Eric. M. Anderson, Tathiana Midori, Diego Carvalho and Prof. Daniela Zanchet are acknowledged for their assistance with EXAFS measurements at LNLS beamline, Brazil.

Chapter 5

Probing the nature of surface active sites on MoO₃ and Mo₂C during HDO of anisole using operando near-ambient XPS

1. Introduction

Hydrodeoxygenation (HDO) is an important upgrading strategy for converting lignocellulosic biomass to fuels and chemicals.^{10,29,58,96} Specifically, HDO uses hydrogen to selectively remove oxygen from biomass-derived molecules in the form of water.^{30,96-99} Recently, molybdenum trioxide (MoO₃) and molybdenum carbide (Mo₂C) have emerged as promising earth-abundant HDO catalysts that can selectively cleave C-O and C=O bonds in biomass-based oxygenates at atmospheric H₂ pressures producing valuable hydrocarbons, while concurrently minimizing undesirable hydrogenation and C-C bond breakage.

We have shown that MoO₃ converts a wide-range of linear and aromatic oxygenates into olefinic and aromatic hydrocarbons, respectively, with high selectivities (> 97%) using low H₂ pressures (≤ 1 bar) and temperatures ≤ 673 K.⁴¹ Post-reaction characterization studies revealed that MoO₃ underwent partial carburization to form an oxycarbonylhydride (MoO_xC_yH_z) featuring large proportion of surface Mo⁵⁺ species.⁵² It was hypothesized that the under-coordinated Mo⁵⁺ species (i.e. oxygen vacancies) were responsible for activating the C-O bond and that the lattice carbon in MoO_xC_yH_z played a crucial role in preventing the over-reduction of Mo⁵⁺ species into less active Mo⁴⁺ sites.

Similarly, Bhan and co-workers showed that Mo₂C is highly selective for cleaving strong phenolic C-O bonds at atmospheric hydrogen pressures and temperatures ranging from 420 to 553 K.^{44,45,49,50,93} For instance, Mo₂C converted anisole to benzene with selectivity values >90% at 423 K. Detailed kinetic studies revealed that HDO on Mo₂C requires two distinct sites: one for H₂ dissociative adsorption and one for oxygenate activation.^{44,49,50} The site required for oxygenate adsorption was hypothesized to be metal-like in nature based on the invariant product generation rates

normalized by *ex situ* CO chemisorption.^{44,49} In a subsequent study, an oxygen mass balance performed during transient HDO experiments revealed the incorporation of oxygen equivalent to ~0.29 monolayer in the carbide catalyst. Given the lack of bulk structure changes, this *in situ* oxidation was hypothesized to be a surface and/or a subsurface effect.^{49-51,93}

To date, however, the nature of the active sites in both materials remains contested. On the one hand, the presence of oxycarbide sites may suggest a common HDO pathway for both materials. Indeed, although CO chemisorption is typically used to titrate metallic sites that may be present in Mo₂C and not in MoO₃, CO can also bind to the under-coordinated sites in MoO_xC_yH_z.⁵¹ Hence, the potential active site for oxygenate adsorption in Mo₂C could be either metallic in nature or surface oxygen vacancies similar to that observed over MoO₃. On the other hand, reactivity data has shown drastically different HDO product distributions for both materials when compared at identical conditions, thus suggesting potentially different reaction pathways.

Unfortunately, *ex situ* characterization techniques do not allow us to establish clear structure-performance relationships for these materials. Although post-reaction XPS of spent MoO₃ have provided insights into the nature of the catalysts after reaction, this *ex situ* approach does not capture the dynamics of the catalyst surface under the reaction conditions.¹⁰⁰ More importantly, Mo₂C is highly oxophilic, requiring a surface passivation step with dilute O₂ before performing any post-reaction characterization.¹⁰¹⁻¹⁰³ This passivation step oxidizes the surface of the carbide, thereby changing the surface structure from that present during reaction.¹⁰² Since both the catalysts undergo significant structural variations and surface modifications during the course of HDO, an *in situ* surface characterization technique is required to close this knowledge gap on the understanding of the active sites responsible for HDO. To our knowledge, no *in situ* or *operando* studies have been performed to investigate HDO reactions on these materials.

Here, we use *operando* near ambient pressure XPS (NAP-XPS) to probe the nature of active sites over MoO₃ and Mo₂C catalysts during HDO of anisole at 593 K and H₂ pressures (≤ 1 mbar). Using synchrotron radiation, we were able to increase its surface sensitivity by modulating the photon energies to measure ejected

photoelectrons at lower kinetic energies than those that typically measured with traditional ultra high vacuum XPS.¹⁰⁰ Our study revealed that pre-reduced MoO₃ catalyst predominantly oxidizes upon introduction of the anisole feed as the surface oxidation states changed from ~40% Mo⁵⁺ and ~60% Mo⁶⁺ to ~ 10% Mo⁵⁺ and ~75% Mo⁶⁺ with remaining Mo present as Mo⁴⁺ species, despite the high H₂-anisole molar ratios (~215) used. This transient behavior was followed by a subsequent reduction of Mo⁶⁺ to regenerate a larger proportion of Mo⁵⁺ species at steady state. The subtle balance between Mo⁶⁺ and Mo⁵⁺ species at the surface is consistent with an oxygen vacancy driven mechanism wherein the oxygenate is activated at the under-coordinated Mo sites (i.e. Mo⁵⁺). In contrast, Mo₂C showed negligible oxidation state changes upon introduction of anisole, maintaining the carbidic phase (80-90% Mo²⁺) throughout the reaction. These data also showed that coking was the cause of deactivation for Mo₂C rather than surface oxidation.

2. Experimental Section

2.1 Preparation of materials

Anisole (99 %) was used as the reactant, and purchased from Sigma Aldrich. Bulk MoO₃ (≥99.5%) and molybdenum oxide (MoO₂, (≥99 wt%)) were purchased from Sigma-Aldrich. Bulk MoO₃ was pre-reduced for 3 h at 320°C, 1.013 bar under a H₂ flow (70 ml/min) to generate under-coordinated sites and remove the induction period reported in our previous study.⁵² Pre-reduced MoO₃ was transferred to the glovebox and sealed in a vial to prevent any oxidation. Fresh Mo₂C was synthesized from ammonium paramolybdate tetra (para)hydrate ((NH₄)₆Mo₇O₂₄·4H₂O, 99%, Alfa Aesar) using a temperature programmed reaction method. Ammonium paramolybdate was loaded into a ¼ inch U-tube reactor, dispersed on top of a quartz wool plug, in contact with a K-type thermocouple (Omega, model TJ36-CAXL-116u). The reactor was then placed in a furnace (Carbolite, model GTF 11/50/750B), connected to a temperature controller (Digi-Sense, model 68900-10). Ammonium paramolybdate tetra (para)hydrate was heated in a 21% CH₄-H₂ mixture (70 ml/min total flow) from room temperature to 650°C at 3°C/min and held at 650°C for 1 hour. The resulting sample (Mo₂C) was then held under pure H₂ flow (55 ml/min) at 650°C for another hour to scavenge residual

surface carbon. The sample was cooled down under H₂ flow to room temperature. This U-tube reactor was equipped with valves for isolation of the catalyst, to prevent any exposure to air. Once room temperature was reached, the U-tube was then transferred to a nitrogen-filled glove box and the resulting Mo₂C catalyst was transferred to a 5 ml borosilicate glass ampule (Wheaton) and capped with a septum. These ampules were then evacuated on a Schlenk line outside of the glovebox, before being flame sealed. Passivated Mo₂C was prepared under similar carburization conditions in a tube furnace, before being passivated with 1% O₂-N₂ mixture for 2 h and then being exposed to ambient atmosphere.

2.2 Powder X-ray Diffraction (PXRD)

PXRD was performed on a Bruker D8 diffractometer using Nickel-filtered Cu-K α radiation ($\lambda = 1.5418 \text{ \AA}$). PXRD patterns were acquired on a 2D image plate, rotated at 15 rpm for 2θ values ranging from 20° to 90° with a step size of 0.04° and a scan speed of 0.2 s per step.

2.3 Near Ambient Pressure-Xray Photoelectron Spectroscopy (NAP-XPS) Experiments

NAP-XPS experiments were performed at the ISIS end-station of the Bessy II synchrotron facility in Berlin, Germany.¹⁰⁰ The set up consists of a differentially pumped electrostatic lens system and a SPECS hemispherical electron analyzer. Detailed explanation of the set up can be found elsewhere.¹⁰⁰ To ensure equal surface sensitivity, Mo 3d, O 1s and C1s core-level regions were recorded using selected photon energies such that ejected photoelectrons had similar kinetic energy (~245 eV) across the different elements. This kinetic energy corresponds to 0.64 nm inelastic mean free path (IMFP) for Molybdenum based on the NIST Electron IMFP Database.¹⁰⁴ Information depth is roughly three times the IMFP, thus, 95% of ejected photoelectrons arise from this depth of ~1.9 nm.¹⁰⁵ The spot size was 300 μm x 100 μm and the beam was moved to a new spot on the catalyst pellet (described below) for every set of XPS spectra measurement to minimize beam-induced reduction of molybdenum species.¹⁰⁶ XPS spectra were acquired in normal emission geometry with a pass energy of 20 eV

and a step size of 0.05 eV for Mo 3d and 0.1 eV for C1s and O1s. Binding energies for each element were calibrated using their respective second-order peak. A 7-point Shirley background was applied to the spectra after correction. Mo 3d spectra were deconvoluted using the following set of constraints- 1) Spin-orbit splitting of 3.15 eV for Mo 3d_{5/2} and 3d_{3/2}, 2) Area ratio of 3:2 for Mo 3d_{5/2}-Mo 3d_{3/2}, and 3) equal full width at half maximum (FWHM) of Mo 3d_{5/2}-Mo 3d_{3/2}.

Pre-reduced MoO₃ and fresh Mo₂C catalyst powders were pressed into pellets (7 mm diameter) using a hand-held pellet press (Pike Technologies) in the nitrogen-filled glovebox. Fresh MoO₃, MoO₂ and passivated Mo₂C were pelletized in ambient atmosphere. The catalyst pellet was then placed between two stainless steel plates, which were then mounted onto a sapphire plate, and secured with screws. Temperature was measured using a K-type thermocouple, which was wound around the screws, pressed firmly against the back plate, very close to the catalyst pellet. The air-sensitive pellets were moved from the glovebox to the NAP-XPS set up using a transfer vessel, which was then mounted directly onto the XPS set up, thereby minimizing air exposure. The sample was locally heated using laser irradiation of the unpolished back plate. All NAP-XPS experiments were typically run at 1 mbar. The gas flows and pressure of the reaction chamber were regulated using multiple mass-flow controllers (Bronkhorst) and motorized control valves. Anisole feed was introduced to the reaction chamber using a stainless steel saturator in the form of a H₂-anisole saturated stream. H₂ gas was initially saturated with anisole in the saturator at room temperature and at 1.013 bar using a MFC set at 30 ml/min. This corresponds to a H₂/anisole molar ratio of ~ 215. A part of this flow was delivered to the reaction chamber held at 1 mbar via a low ΔP MFC (17-20 ml/min). Rest of the saturated gas stream was directed to the vent. All catalyst samples were heated at 5°C/min from room temperature to 320°C, and maintained at 320°C throughout the experiments. MoO₃ and MoO₂ were heated in a N₂ flow (10 ml/min) while Mo₂C catalysts were heated under a H₂ flow (10 ml/min), before switching to H₂-anisole mixture (17-20 ml/min) for all reactions at 320°C. During reaction, the gas phase composition was monitored using a 4-channel micro gas chromatograph (CP-4900, Varian Inc), equipped with a thermal conductivity detector. The micro-GC consists of 4 columns – 2 Molsieve 5 columns (10 m and 20 m), a PoraPLOT Q column (10 m) and

an Al₂O₃/KCl column (10 m). The poraPLOT Q (PPQ) column was predominantly used to track benzene and anisole. All the columns were held isothermal at the following temperatures: 2 Molsieve columns at 55°C and 42°C, PPQ column at 180°C and Al₂O₃/KCl column at 150°C. Each micro-GC run lasted for about 7.3 min, before the next injection was made. Typically, when no reactions were run, the anisole saturated H₂ stream was injected into the micro-GC via a bypass line (10 ml/min). When the reaction was started, the H₂-anisole mixture was delivered to the reaction chamber, while the bypass was switched off. The bypass served as a baseline reference for the amount of benzene observed in the absence of reaction.

3. Results

3.1 MoO₃

Mo 3d spectra of fresh MoO₃ acquired at 320°C in 1 mbar N₂ flow (**Figure S5.7**) predominantly features a combination of Mo⁶⁺ and Mo⁵⁺ states with the respective 3d_{5/2} peaks located at 232.8 eV¹⁰⁷ and 231.5 eV^{107,108}. The presence of Mo⁵⁺ species in a MoO₃ sample indicates thermal reduction of Mo⁶⁺ even in a N₂ environment. Similarly, fresh MoO₂ (**Figure S5.8**) also shows Mo⁵⁺ and Mo⁶⁺ states, but also a significant contribution of Mo⁴⁺ species, as expected. Mo⁴⁺ state is assigned to 2 sets of doublets with the Mo 3d_{5/2} peaks located at 229.3 and 230.6 eV. The narrow asymmetric doublets at lower binding energies are associated with screened metallic environment while the broader, more symmetric doublets are attributed to an unscreened environment, consistent with recent surface science studies.^{106,109}

PXRD pattern of pre-reduced MoO₃ shows that the bulk MoO₃ structure was preserved during 3 h H₂ reduction (**Figure S5.9**). Next, we investigated the effect of just H₂ flow on a pre-reduced MoO₃ pellet at 320°C. The proportion of Mo⁶⁺ species decreased from *ca.* 67% to 61% with a concomitant increase in Mo⁵⁺ from *ca.* 32% to 39% in the first 2.5 h, before approaching steady state distribution of *ca.* 31% Mo⁵⁺ and 66% Mo⁶⁺ thereafter (**Figure S5.10** and **S5.11**). Mo⁴⁺ contribution remained roughly constant at around 1-2% throughout the experiment.

Next, HDO of anisole was performed on pre-reduced MoO_3 . Benzene areas increased sharply to reach a maximum in about 1.3 h upon introduction of H_2 -anisole saturated stream to reaction chamber, before very slowly decreasing over the next 6.7 h (**Figure S5.12**), and subsequently dropping to initial baseline areas upon completion of the experiment. Anisole areas also decreased sharply initially, before steadily increasing to its baseline values throughout the experiment (**Figure S5.13**). This concomitant increase in benzene areas and decrease in anisole areas indicate that pre-reduced MoO_3 is indeed active for HDO of anisole to benzene. Benzene was the major product as no other peaks were observed in the micro-GC chromatogram. Minor products such as phenol, cresols, toluene and methane, typically observed during anisole HDO at 320°C , 1.013 bar were not observed here.⁵² Since the H_2 pressure employed in this study is 3 orders of magnitude lower, the catalyst is likely exhibiting such low reactivity that only benzene, being the major product, was detected in the micro-GC. Moreover, products such as phenol¹¹⁰ and cresols¹¹¹ have lower vapor pressures than anisole,¹¹² possibly condensing before reaching the micro-GC to be detected.

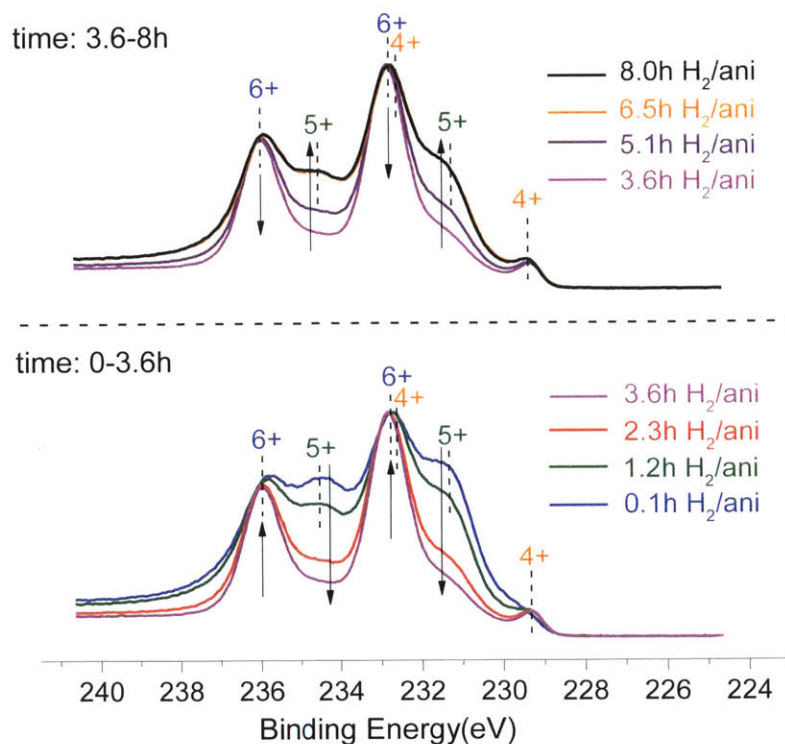


Figure 5.1 Normalized Mo 3d spectra of pre-reduced MoO_3 during HDO of anisole at $T = 320^\circ\text{C}$, $P_{\text{total}} = 1 \text{ mbar}$ ($P_{\text{anisole}} = 0.005$, balance H_2).

Figure 5.1 shows the Mo 3d XPS spectra acquired during the HDO reaction of anisole at 320°C and 1 mbar total pressure ($P_{\text{anisole}} = 0.005$, balance H_2). To better visualize the qualitative trends in Mo oxidation states, the XPS spectra data is split into 2 halves: time 0-3.6 h (lower panel) and time 3.6-8 h (upper panel). In the first 3.6 h of reaction, there is a clear continuous oxidation of Mo^{5+} to Mo^{6+} as seen by the lower intensities of Mo^{5+} peaks and the sharper Mo^{6+} peaks. This result suggests that the anisole feed oxidizes the Mo^{5+} surface species to Mo^{6+} species, even at the high H_2 -anisole molar ratios (~215) used. Interestingly, after ca. 4 h on stream, the proportion of Mo^{6+} starts to decline with a concomitant increase of Mo^{5+} states, ultimately reaching a steady state. No peaks corresponding to Mo^{2+} (Mo_2C) or Mo^0 (Mo metal) were detected in this experiment.

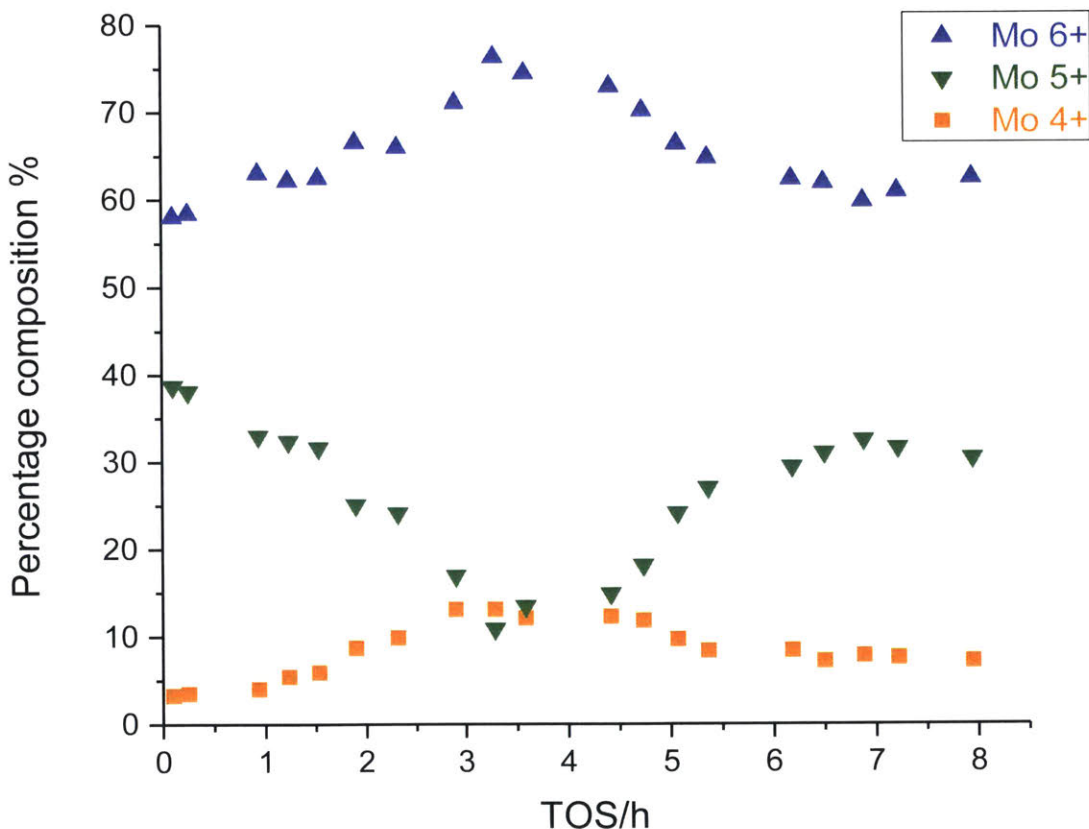


Figure 5.2 Proportion of Mo oxidation states with time for pre-reduced MoO_3 during HDO of anisole. Reaction conditions: $T = 320^\circ\text{C}$, $P_{\text{total}} = 1$ mbar ($P_{\text{anisole}} = 0.005$, balance H_2).

The distribution of Mo oxidation states was tracked with time as shown in **Figure 5.2**. Specifically, the proportion of Mo oxidation states changed from 39% Mo^{5+} and 58%

Mo⁶⁺ to 11% Mo⁵⁺ and 76% Mo⁶⁺ in the first 3.3 h, before reaching a steady state distribution of 31% Mo⁵⁺ and 61% Mo⁶⁺. Similarly, Mo⁴⁺ mirrored the trends observed with Mo⁶⁺ increasing from ~3% to 13% in the first 3.3 h, thus implying that some Mo sites were over-reduced to Mo⁴⁺, before decreasing to a steady state composition of ~8% Mo⁴⁺ species.

To further confirm the observed trends in Mo 3d spectra during HDO of anisole, the experiment was repeated with a new pre-reduced MoO₃ pellet under identical reaction conditions. Again, benzene was the major product and the trends in Mo 3d XPS spectra closely matched that observed in the prior experiment (**Figure S5.14, S5.15 and S5.16**).

3.2 Fresh Mo₂C

PXRD pattern of fresh Mo₂C showed only peaks associated with β-Mo₂C, with no peaks from MoO₂ indicating that complete carburization was achieved (**see Figure S5.17**). Mo 3d spectrum (**Figure 5.3a**) predominantly features a set of doublets corresponding to Mo²⁺ in Mo₂C with the Mo 3d^{5/2} peak located at 228.2 eV.^{113,114} Despite our attempts to minimize air exposure, a thin oxide layer exists on the Mo₂C surface as seen by the presence of broad shoulders at higher binding energies. Peak deconvolution reveals that ca. 60% of Mo species exist as Mo²⁺, attributed to carbidic Mo₂C while Mo⁴⁺, Mo⁵⁺ and Mo⁶⁺ constitute the remaining 17%, 18 % and 5% respectively, associated with oxidic species. The presence of residual oxygen on freshly synthesized Mo₂C was also observed by Bhan and co-workers.⁵⁰ An intense carbidic C 1s signal at ca. 283.1 eV¹¹⁵⁻¹¹⁷ is strong evidence that the surface is predominantly carbide in nature (**Figure 5.3b**). A signal at 284.5 eV associated with graphitic carbon¹¹³, and peaks at 285.9 and 288.1 eV corresponding to oxidized carbon entities (C-O¹¹⁸ and C=O respectively) are also visible in the spectrum.

As seen from **Figure S5.18**, H₂ flow at 320°C clearly reduces the oxide layer on the surface, thereby leaving a more pristine carbide surface. Specifically, the amount of Mo²⁺ increased from ca. 60% to 70% during 3 h H₂ flow, thereafter remaining relatively constant at this value. Since the proportion of Mo²⁺ did not increase any further, a

3 hour pre-reduction was deemed necessary to reduce the weakly bound surface oxide layer before performing HDO reaction. This observation also suggests that the

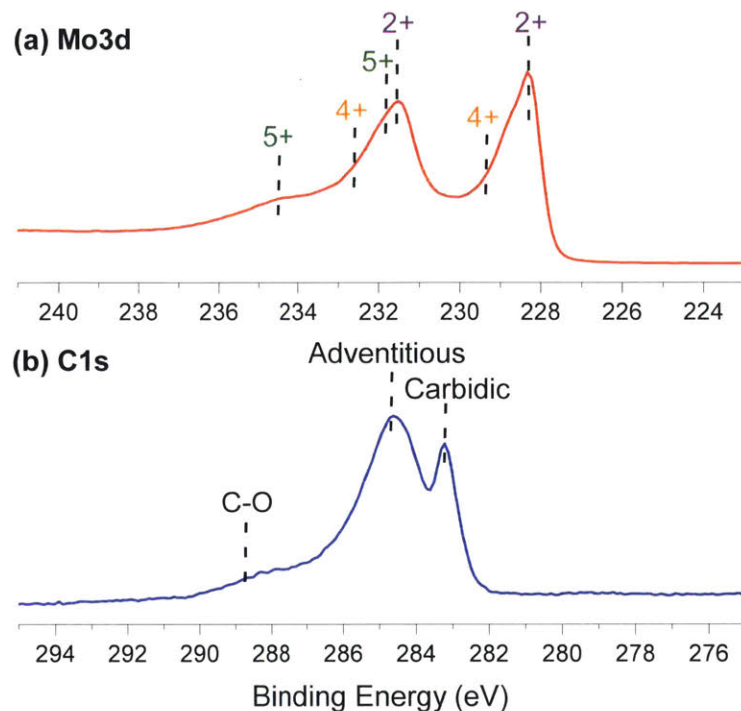


Figure 5.3 Normalized (a) Mo 3d and (b) C 1s spectra of Mo₂C at UHV and T = 25°C.

remaining oxide layer (corresponding to ~ 30% total Mo⁴⁺, Mo⁵⁺ and Mo⁶⁺) on the carbide is likely more tightly bound which might be difficult to remove under these mild reduction conditions, consistent with prior reports where temperature > 550°C was required to remove residual oxygen from fresh Mo₂C catalyst.

HDO of anisole was performed over Mo₂C after a 3 h reduction treatment with H₂. When H₂-anisole stream was switched from bypass to the reaction chamber, benzene areas increased very sharply to reach a maximum in the first 0.4 h, before dropping rapidly in the next 2.5 h (**Figure S5.20**). Benzene area continued to decrease thereafter, albeit at a slower rate (~ 4 times). Upon completion of the experiment, benzene areas reverted to the initial baseline values. These two different rates of deactivation are also consistent with observations from anisole HDO experiments performed at 320°C and atmospheric H₂ pressures over bulk and supported Mo₂C (**Figure S5.21 and S5.22**). The observed initial spike in benzene areas with Mo₂C was approximately 8 times higher than that observed with pre-reduced MoO₃. Though Mo₂C

(~25 m²/g) has a higher BET surface area than MoO₃ (~5 m²/g), this difference alone cannot account for the higher relative benzene yield obtained with Mo₂C, thereby indicating that Mo₂C is more active for HDO than MoO₃ under similar reaction conditions. Again, benzene was the dominant product, with no other products observed in the chromatogram, consistent with the high benzene selectivity (≥94% selectivity on C₆⁺ basis) observed during anisole HDO at 320°C, 1 bar H₂ pressure. This benzene selectivity is slightly higher than that observed by Bhan and co-workers during anisole HDO at 150°C^{49,51} and this difference can be attributed to the absence of cyclohexane formed from the sequential hydrogenation of benzene at 320°C. Thermodynamic calculations show that benzene hydrogenation to cyclohexane is unfavorable ($\Delta G_{\text{reaction}} = +16.69$ kJ/Mol) at 320°C¹¹⁹ (see SI Table S1), thereby also explaining the absence of cyclohexane in this study. Direct deoxygenation of anisole over Mo₂C typically yields benzene and methanol, with the latter undergoing further HDO to form methane and water. However, no peaks corresponding to methane or methanol were observed in this study, possibly due to the low amounts produced, which might be near the detection limit of the micro-GC.

Figure 5.4 shows normalized Mo 3d spectra acquired during HDO of anisole over Mo₂C. In stark contrast to the Mo 3d spectra of pre-reduced MoO₃, no significant changes were observed in the Mo oxidation states during the course of HDO. The multiple Mo 3d spectra acquired during reaction mostly overlapped completely with each other.

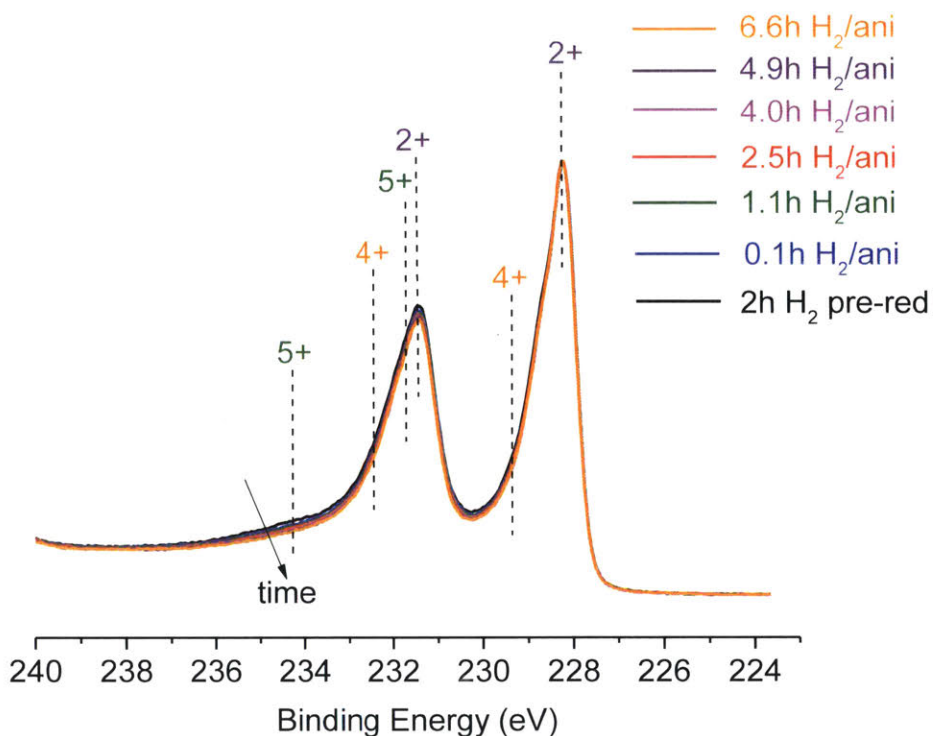


Figure 5.4 Normalized Mo 3d spectra of Mo_2C during HDO of anisole at $T = 320^\circ\text{C}$, $P_{\text{total}} = 1 \text{ mbar}$ ($P_{\text{anisole}} = 0.005$, balance H_2) and H_2 pre-reduction = 3 h.

The composition of Mo species remained relatively constant at ca. 84% Mo^{2+} , 14% Mo^{4+} , 1% Mo^{5+} and 1% Mo^{6+} throughout the reaction ($\sim 7 \text{ h}$), and resembled that obtained after 2 h reduction with H_2 (**Figure 5.5**). This suggests that the introduction of oxygenate anisole did not oxidize the Mo^{2+} species over the Mo_2C surface, contrary to that observed with MoO_3 . The dominant carbide phase is maintained throughout the reaction. Clearly, *in situ* oxidation of carbide cannot account for the catalyst deactivation in this study.

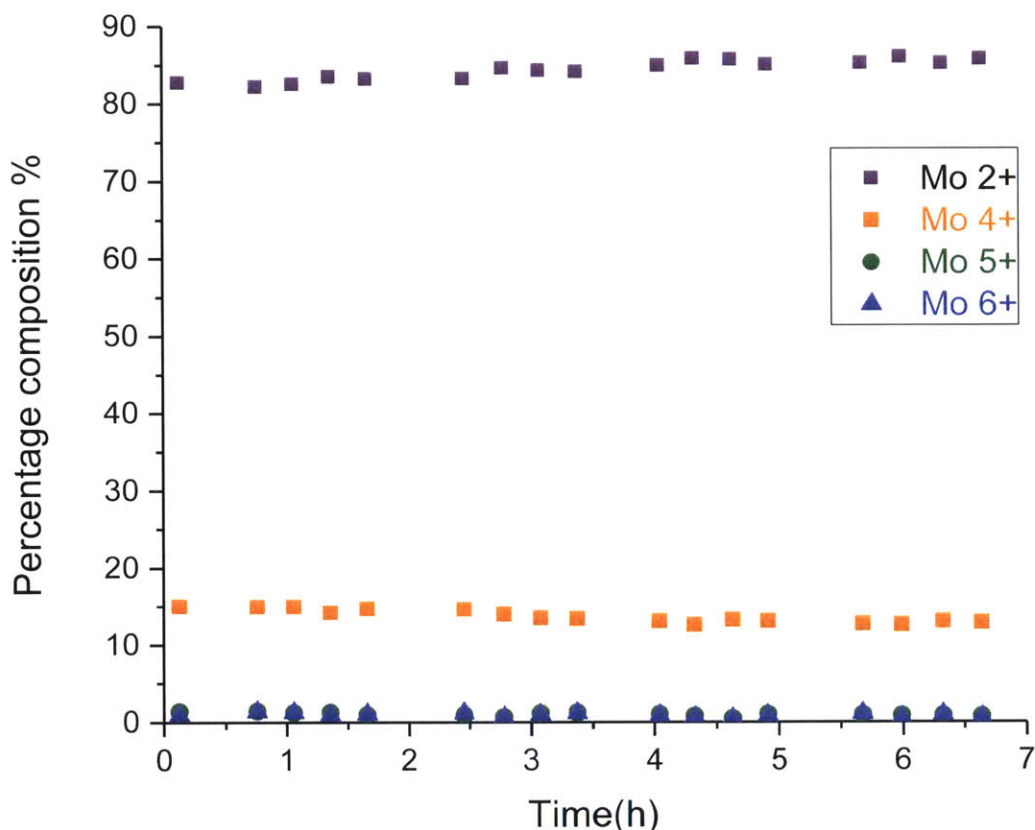


Figure 5.5 Proportion of Mo oxidation states over Mo_2C during HDO of anisole. Reaction conditions: $T = 320^\circ\text{C}$, $P_{\text{total}} = 1 \text{ mbar}$ ($P_{\text{anisole}} = 0.005$, balance H_2) and H_2 pre-reduction = 3 h.

O 1s spectra (**Figure S5.23**) features a signal at *ca.* 532.7 eV, which can be attributed to C-O bond¹²⁰, likely from adsorbed anisole or similar reaction intermediate on the catalyst surface. This signal increases in intensity during the reaction, implying increasing adsorption of such oxygen species on the surface, thereby possibly leading to deactivation by blocking some of the sites. No significant changes were observed in C 1s spectra (**Figure S5.24**), suggesting that the nature of the surface carbon species was largely invariant throughout the reaction. However, surface elemental quantification (**Figure S5.25**) reveals an increase (~6%) in proportion of C during the reaction. This trend is corroborated with an increase in atomic C/Mo ratio (**Figure S5.26**) from 2.9 to a maximum of 3.4, indicating an increasing amount of carbonaceous deposits on the surface during the course of reaction. Contrarily, O/Mo ratios (**Figure S5.27**) did not change significantly, though one might have expected this to increase based on the oxygenate adsorption seen in O 1s spectra. However, the oxidic layer on Mo_2C was

also getting reduced to a tiny extent with time, and this oxygen removal is balanced with the oxygenate adsorption on carbide surface, thereby leading to minimal changes on the quantity of O on the surface.

In order to confirm the trends observed with Mo₂C, HDO of anisole was repeated over a new Mo₂C pellet under identical reaction conditions. Again, benzene was the main product, and all the XPS spectra and surface elemental quantification showed consistent trends across both replicates (**Figure S5.28-S5.36**).

3.3 Passivated Mo₂C

To supplement the comparison of MoO₃ and fresh Mo₂C, identical reaction was performed over an intentionally passivated carbide. Passivated Mo₂C sample was prepared from ammonium paramolybdate precursor under similar carburization conditions to the fresh Mo₂C but the synthesized Mo₂C catalyst was treated with a 1% O₂-N₂ stream for 2 h at room temperature. As expected, Mo 3d spectrum features a huge passivation layer (**Figure S5.37**). In contrast to fresh Mo₂C (**Figure 5.3**), the presence of higher Mo oxidation states dominate the Mo 3d spectra, with a small contribution from the carbide Mo²⁺ species. Specifically, Mo²⁺ only accounts for ca. 20% of Mo surface species, significantly lower than the 60% observed for fresh Mo₂C. Higher Mo oxidation states including Mo⁴⁺, Mo⁵⁺ and Mo⁶⁺ attribute to the remaining 6%, 54% and 19% of Mo species respectively. C 1s spectra shows a carbidic signal at 283.2 eV, albeit less intense than that observed with fresh Mo₂C (**Figure S5.38**). As expected, the signals at 285.9 and 288.1 eV, associated with oxidized carbon moieties are stronger than those of fresh Mo₂C. **Figure S5.39** shows that the huge passivated layer gets continuously reduced during the H₂ treatment, as seen by an increase in the fraction of Mo²⁺ from 20% to 55%, indicating that higher Mo oxidation states were reduced to lower oxidation states. However, we note that this 3 h H₂ reduction might not be sufficient to reduce the oxide layer on this passivated Mo₂C since the catalyst was significantly more oxidized to begin with than fresh Mo₂C, as seen by the lower quantity of Mo²⁺ after H₂ reduction (~55%) than that of fresh Mo₂C (~70%).

After the H₂ reduction phase, when H₂-anisole was introduced to the system, benzene areas spiked sharply to reach a maximum value similar to that observed with

fresh Mo₂C within 1 h, and then gradually decreased during rest of the reaction (**Figure S5.40**). Similar increase in relative benzene yields indicates that the passivated Mo₂C has comparable reactivity to fresh Mo₂C after the H₂ activation. Again, benzene was the main product. However, another peak, right next to benzene was observed on the micro-GC chromatogram in small quantities throughout the reaction. This peak is likely toluene, an alkylation product typically observed on MoO₃^{41,52} and also a minor alkylation product observed on H₂-activated passivated Mo₂C during HDO of anisole.⁴⁹ We attribute the formation of alkylation product, toluene to the larger oxide character present on the surface of the passivated Mo₂C, compared to fresh Mo₂C. This toluene peak might not have been observed on the pre-reduced MoO₃ due to the lower HDO reactivity of MoO₃ observed compared to Mo₂C catalysts.

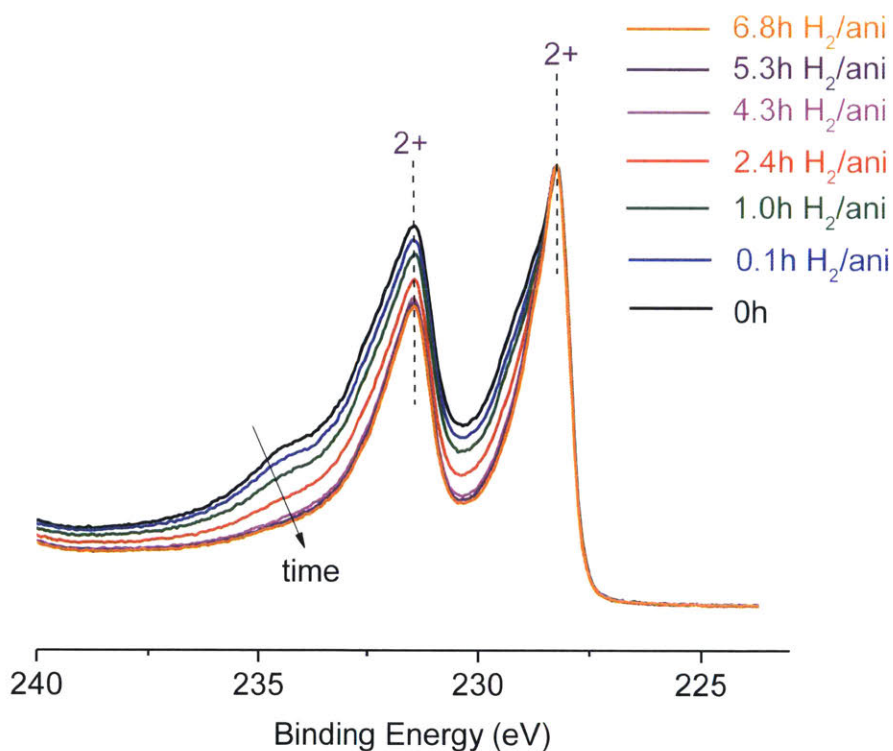


Figure 5.6 Normalized Mo 3d spectra of passivated Mo₂C during HDO of anisole at T=320°C, P_{total} = 1 mbar (P_{anisole} = 0.005, balance H₂) and H₂ pre-reduction = 3 h.

Similar to fresh Mo₂C, introduction of anisole did not oxidize the Mo species (see **Figure 5.6**). In fact, in contrast, the oxide layer continued to decrease in intensity during the reaction. **Figure S5.41** shows that the combined proportion of Mo⁴⁺, Mo⁵⁺ and Mo⁶⁺ decreased from ca. 43% to 25% during reaction, while the amount of Mo²⁺ concurrently

increased from 57% to 75%. This trend suggests that the oxide layer on the passivated Mo₂C was reduced during reaction, despite the introduction of an oxygenate anisole. Though Mo²⁺ signal was dominant throughout the reaction, the role of the oxide contributions on the Mo surface during HDO probably cannot be excluded, especially due to the observation of an additional alkylation product, toluene.

O 1s and C 1s spectra show very similar trends to that observed with fresh Mo₂C (**Figure S5.42 and S5.43**). O 1s signal at 532.7 eV associated with C-O bond increased in intensity during reaction, while C 1s spectra did not show any appreciable changes. Surface elemental quantification (**Figure S5.44**) reveals a 12% increase in the proportion of C, and a corresponding decrease in the O proportion. Atomic C-Mo ratios (**Figure S5.45**) continue to increase during reaction from 2.2 to a maximum of 3.5 while O-Mo ratio (**Figure S5.46**) decreases from 1.4 to 1.0. This increase in C-Mo ratio can be attributed to the deposition of carbonaceous species on the surface, thereby explaining the deactivation. The decrease in Mo-O ratio is consistent with the reduction of higher Mo oxidation states observed in Mo 3d spectra, suggesting that the passivated layer on the catalyst surface is undergoing reduction during the reaction even in the presence of anisole feed.

4. Discussion

4.1 MoO₃

The presence of Mo⁵⁺ on a MoO₃ sample could be attributed to an under-coordinated Mo site such as an oxygen vacancy.^{52,121} Though pre-reduced MoO₃ might have oxygen vacancies to begin with, H₂ treatment increases the number of these vacancies, till a steady state composition is achieved. This trend in the reduction of Mo⁶⁺ to Mo⁵⁺, followed by a constant composition of Mo⁵⁺/Mo⁶⁺ observed during H₂ flow (**Figure S5.11**) over pre-reduced MoO₃ is also consistent with an earlier surface science report.¹²¹ No significant increase in Mo⁴⁺ was seen even after 4 h of H₂ flow. This invariance in Mo⁴⁺ fraction can be attributed to the low H₂ pressure employed in this study which might not be reducing enough to generate significant quantities of Mo⁴⁺ moieties from the higher oxidation species.

Mo 3d spectra acquired during HDO of anisole over pre-reduced MoO₃ across both replicate experiments featured an initial oxidation phase (~4 h) followed by a reduction phase, before approaching a steady state composition. We note that all control experiments with MoO₃ in the absence of feed (anisole) only featured reduction of Mo⁶⁺ species. No oxidation was observed, thereby ruling out any significant oxygen contamination in the chamber. Since the oxidation was only observed upon introduction of feed into the chamber, this observed oxidation is a direct effect of the introduction of oxygenated anisole. The catalyst undergoes an initial transient oxidation-reduction cycle to move closer to the working state of the catalyst, as seen by the relatively constant distribution of Mo species towards the end of the experiment. Once the feed is introduced, oxygen from the anisole, can bind favorably to these under-coordinated Mo sites (Mo⁵⁺), thereby causing an oxidation of the Mo species. This is in line with observations by Delporte *et al.* wherein carbon atoms from the reactant rapidly fill oxygen vacancies to form an oxycarbohydride phase, thereby preventing the formation of MoO₂.¹²² Similarly, our previous work also revealed that introduction of feed (m-cresol) for 0.5 h on similar pre-reduced MoO₃ catalysts caused a bulk transformation of MoO₃ phase to a mixture of MoO_xC_yH_z and MoO₂.⁵² With introduction of more feed in this study, oxidation continues to happen up to ~ 4 h. At this point, we hypothesize that the anisole coverage might be reaching a maximum. Any extra flow of anisole beyond this point does not cause any more oxidation, and the adsorbed oxygenate (anisole) gets deoxygenated to form benzene and desorbed, thereby regenerating Mo⁵⁺. Given the low reactivity of MoO₃ compared to Mo₂C, this oxidation-reduction cycle could possibly depict the actual turnovers observed on the MoO₃ catalytic surface. Taken together, this interplay of Mo⁵⁺ and Mo⁶⁺ states strongly indicates that Mo⁵⁺ is the likely active site responsible for HDO of anisole under these reaction conditions. This is consistent with our hypothesis that an oxygenate binds to an under-coordinated Mo site (i.e. Mo⁵⁺) to form a Mo-O bond,^{41,52} thereby leading to an oxidation of Mo⁵⁺ to Mo⁶⁺. Adsorption of oxygenates onto such under-coordinated Mo sites is also consistent with mechanisms proposed during HDO of acrolein⁴⁰ and acetaldehyde³⁹ over MoO₃.

PXRD patterns of spent MoO₃ catalysts did not show any appreciable changes in the bulk MoO₃ structure. No new peaks corresponding to Molybdenum oxycarbide

($\text{MoO}_x\text{C}_y\text{H}_z$) or MoO_2 were observed, contrasting to the PXRD patterns observed after HDO of m-cresol at 320°C .⁵² This is likely due to the significantly lower H_2 pressure employed here which might not be harsh enough to cause a bulk transformation of the catalyst to $\text{MoO}_x\text{C}_y\text{H}_z$ or MoO_2 . Though bulk oxycarbide was not observed after reaction, we cannot rule out the formation of a surface oxycarbide as this is difficult to determine just based on XPS data, though some reports have done so.¹²³

4.2 Mo_2C

Mo 3d spectra obtained during HDO across both replicate experiments revealed that the dominant Mo^{2+} phase was maintained throughout the reaction, showing negligible oxidation even in the presence of oxygenate (anisole). *In situ* oxidation therefore definitely cannot account for the deactivation. If *in situ* oxidation was a major cause of deactivation, the proportion of higher Mo oxidation states (i.e. Mo^{4+} , Mo^{5+} and Mo^{6+}) would have increased with a concurrent decrease in the presence of Mo^{2+} species. Furthermore, XPS of spent supported Mo_2C catalysts (performed using a transfer vessel with UHV XPS) after HDO of anisole at 320°C , 1 bar H_2 also revealed that the dominant Mo^{2+} state was maintained during the reaction even after 24 h with no appreciable surface oxidation (**Figure S5.47**), thereby again excluding *in situ* oxidation as a cause for the observed deactivation even for atmospheric H_2 experiments. However, as mentioned earlier, an increase in adsorption of oxygen species was observed in O 1s spectra (**Fig S5.23**) in this study, consistent with the oxygen incorporation reported by Bhan.⁵¹ So, *in situ* oxygen incorporation over Mo_2C might still occur during anisole HDO even at 1 mbar H_2 pressure but this may not be significant enough to cause oxidation. This oxygen incorporation is also confirmed to be a minor effect as seen by the negligible changes in the O-Mo ratios.

However, the surface concentration of atomic carbon and C-Mo ratios increased across both replicate experiments, clearly indicating the accumulation of carbonaceous species on the catalyst surface during reaction. This is strong evidence that coking is a major cause of deactivation. PXRD patterns of spent Mo_2C catalysts reveal that the bulk structure of the Mo_2C was preserved during HDO reaction, in agreement with prior observations by Bhan.⁴⁹ Taken together, Mo_2C is highly active for HDO of anisole to

benzene and oxidation cannot account for deactivation. In fact, coking is a major cause of deactivation. A minor oxygen incorporation might still occur on the catalyst surface, however, this was not significant enough to cause oxidation of the Mo surface species.

4.3 Passivated Mo₂C

Passivated Mo₂C showed similar amounts of reactivity towards benzene production compared to fresh Mo₂C, albeit with an additional product of toluene. This alkylation product was attributed to the presence of larger oxide contributions on the catalyst surface, wherein alkylation is typically observed with the oxide analogue. Again, no significant oxidation was observed during reaction, thereby indicating that oxidation cannot explain the deactivation observed. In contrast, passivated Mo₂C with greater proportions of oxidic species, showed a decrease in the proportion of these higher oxidation states. This observation clearly suggests that the oxide layer on the catalyst surface was continuing to be reduced during the reaction, even in the presence of anisole. Similar to the fresh Mo₂C samples, coking was believed to be the main reason for deactivation as seen by a spike in the surface carbon concentration as well as C-Mo ratios during reaction. A minor oxygen incorporation was again visible in this sample. Overall, though Mo²⁺ signal was dominant throughout the reaction, the role of the oxide contributions on the Mo surface of passivated Mo₂C during HDO probably cannot be excluded, especially due to the observation of an additional alkylation product, toluene.

5. Conclusions

MoO₃ and Mo₂C are both promising HDO catalysts, capable of converting biomass-based oxygenate molecules to more valuable fuels and chemicals. Both these catalysts were investigated for HDO of anisole at 1 mbar, 320°C while measuring XPS spectra of Mo 3d, O 1s and C1s. Mo 3d spectra for pre-reduced MoO₃ shows that Mo⁵⁺ initially gets oxidized to Mo⁶⁺, followed by a reduction to regenerate Mo⁵⁺ during the course of HDO reaction. This seems to be consistent with an oxygen vacancy mechanism, wherein the oxygen from anisole binds to an under-coordinated site^{41,52}, possibly Mo⁵⁺, and then subsequently oxidizing the Mo⁵⁺ to Mo⁶⁺. Similar experiments on fresh Mo₂C

revealed that the dominant carbide phase is retained throughout the HDO reaction, with no significant changes in the distribution of surface Mo species. There was negligible *in situ* oxidation of Mo₂C during the course of HDO reaction and that coking was likely the major cause of deactivation over Mo₂C catalyst. NAP-XPS experiment with passivated Mo₂C revealed that the initially higher amounts of oxide on the surface continues to reduce during the reaction. This suggested that the dominant carbide phase was retained over both Mo₂C catalysts, and negligible oxidation occurred during the course of reaction, despite the oxophilic nature of Mo₂C.

6. Supporting Information

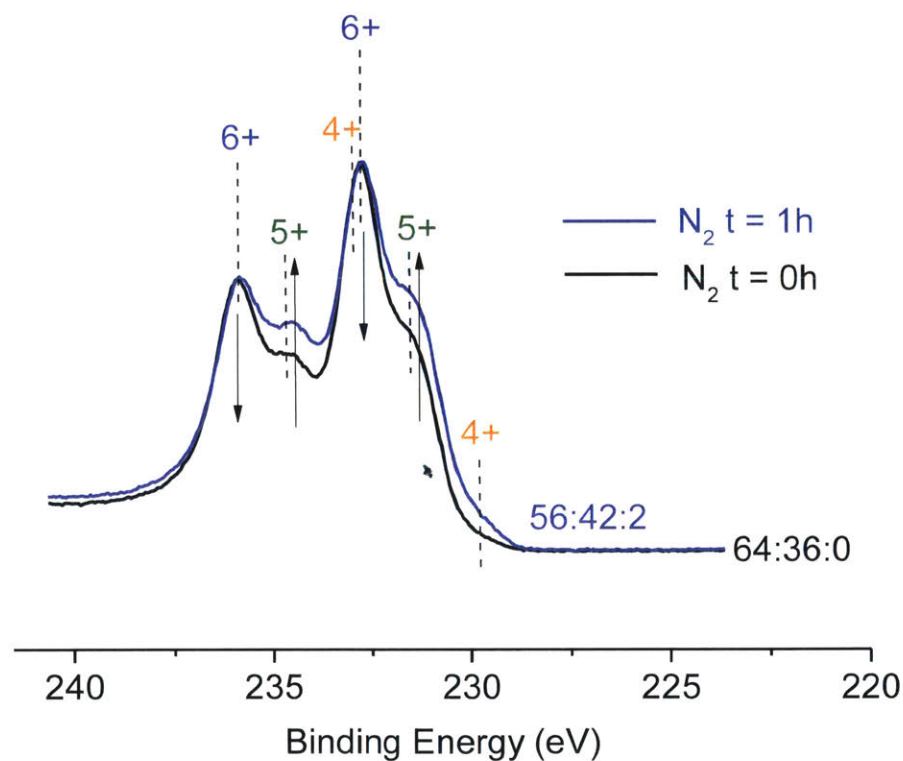


Figure S5.7 Normalized Mo 3d spectra of fresh MoO₃ at 320°C, 1 mbar N₂ at different times. The numbers correspond to the distribution of Mo oxidation states – Mo⁶⁺, Mo⁵⁺ and Mo⁴⁺ respectively.

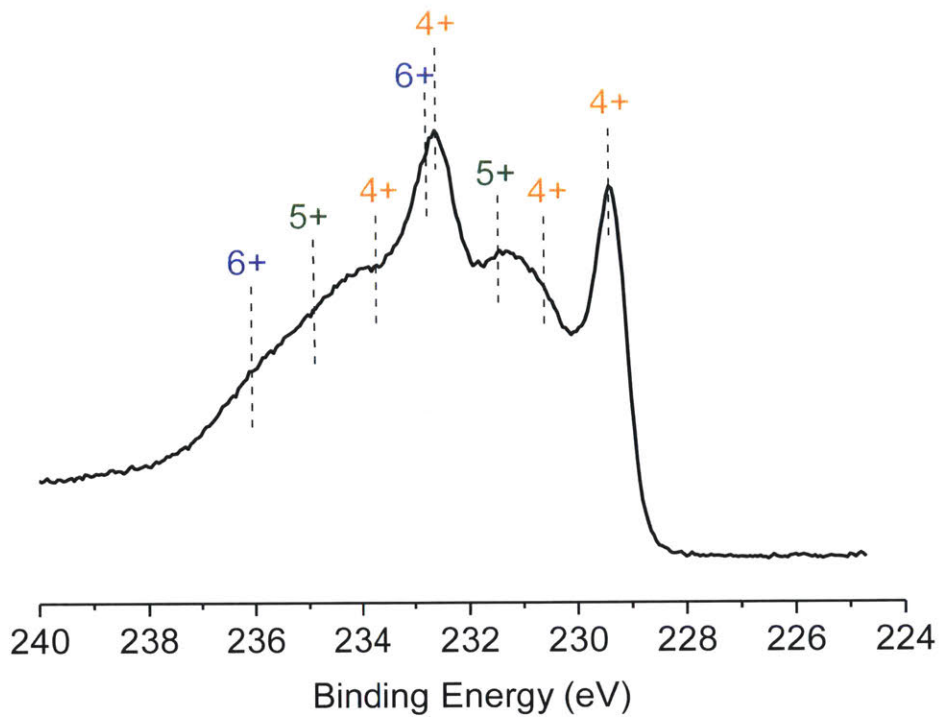


Figure S5.8 Normalized Mo 3d spectra of MoO₂ at 320°C, 1 mbar N₂.

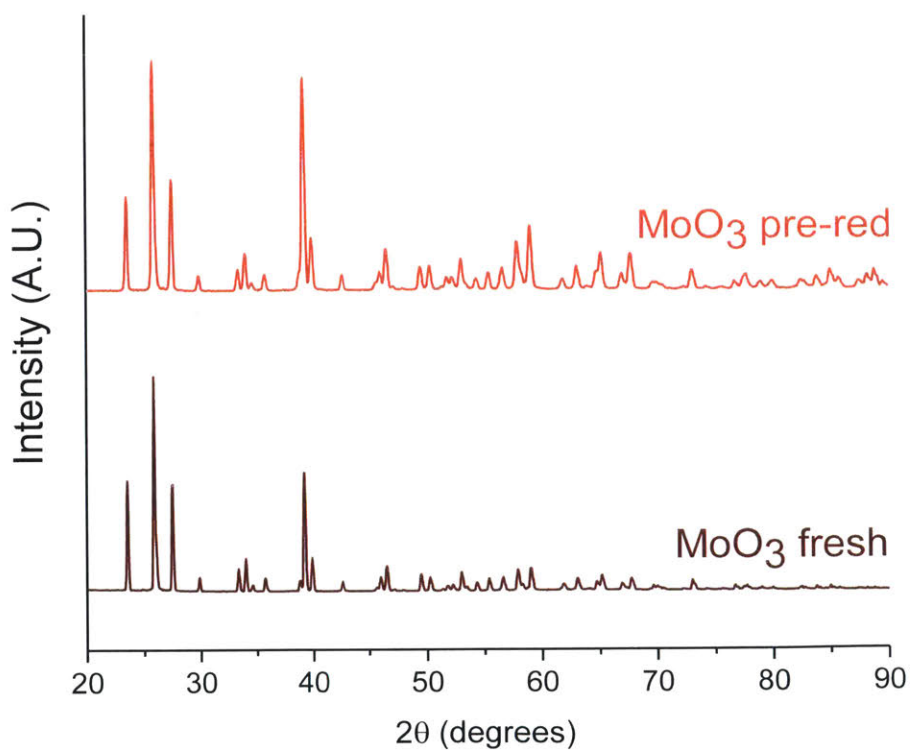


Figure S5.9 Normalized PXRD patterns of fresh and pre-reduced MoO₃. Pre-reduction conditions: T = 320°C, P_{total} = 1.013 bar H₂.

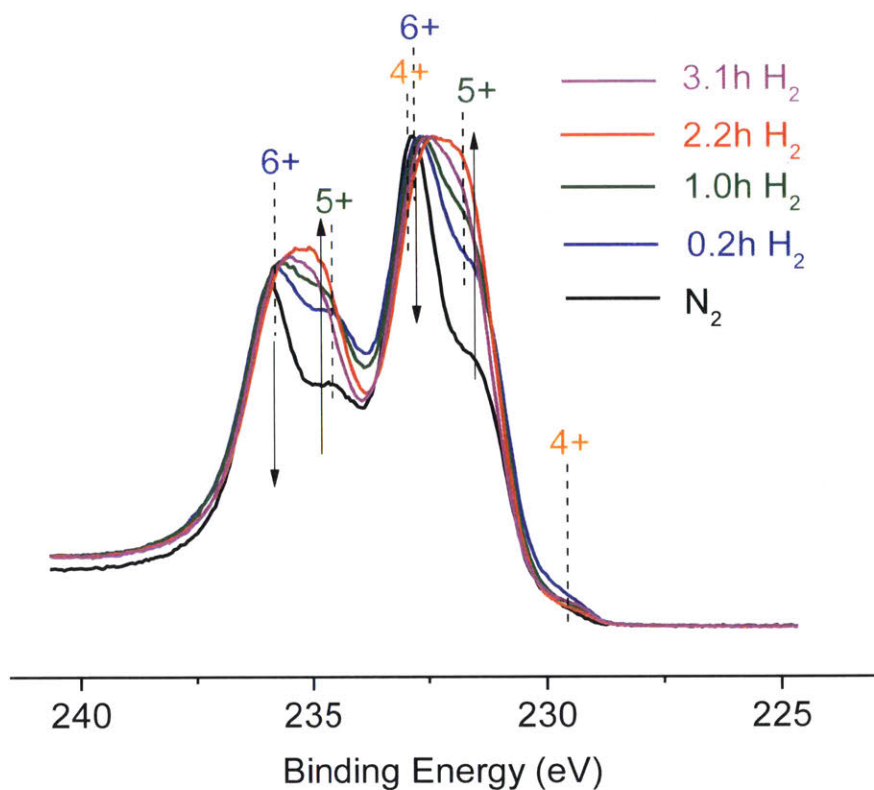


Figure S5.10 Normalized Mo 3d spectra of pre-reduced MoO₃ at 320°C, 1 mbar H₂.

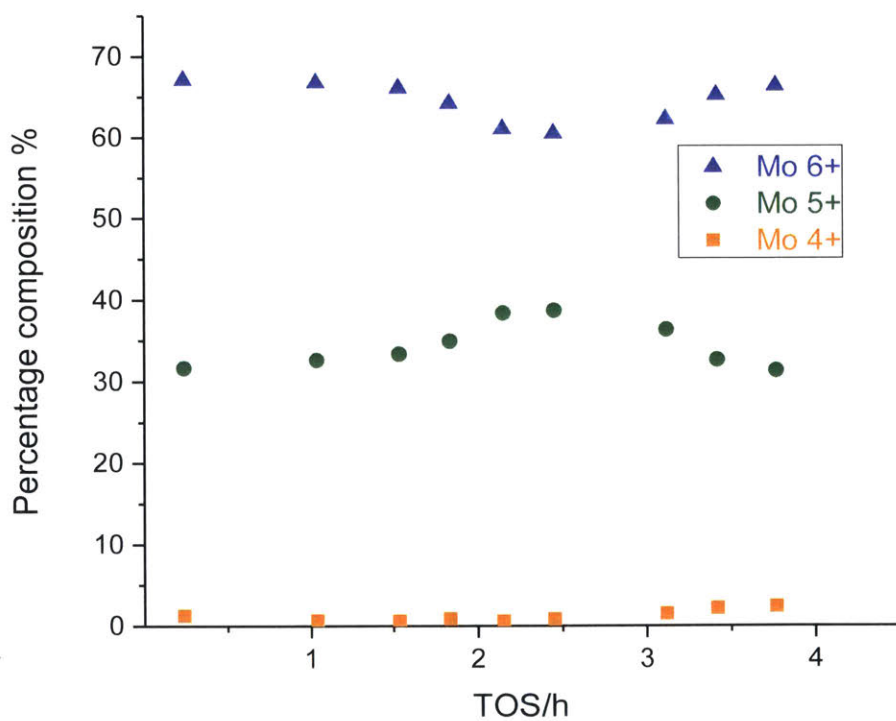


Figure S5.11 Proportion of Mo oxidation states with time for pre-reduced MoO₃. Reaction conditions: T = 320°C, P_{total} = 1 mbar H₂.

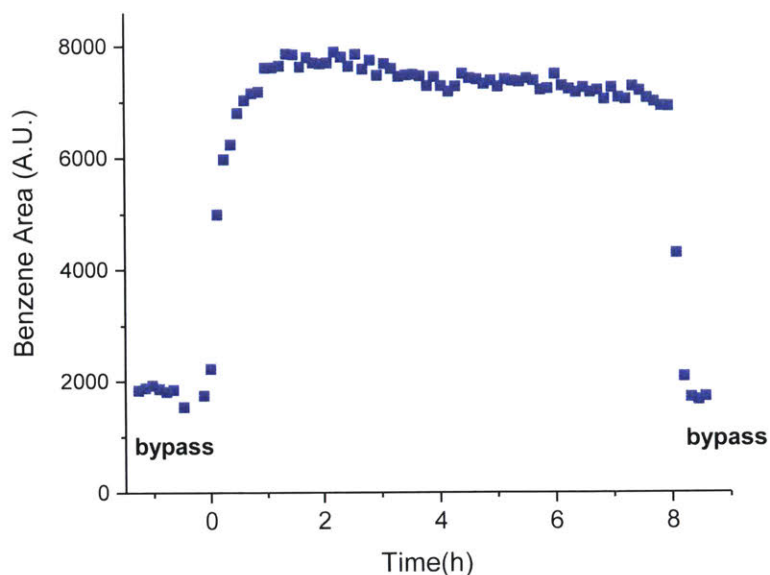


Figure S5.12 Relative benzene areas during HDO of anisole over pre-reduced MoO_3 . Reaction conditions: $T = 320^\circ\text{C}$, $P_{\text{total}} = 1 \text{ mbar}$ ($P_{\text{anisole}} = 0.005$, balance H_2) Non-zero benzene areas in bypass could possibly be due to trace amount of contaminant benzene originally present in anisole.

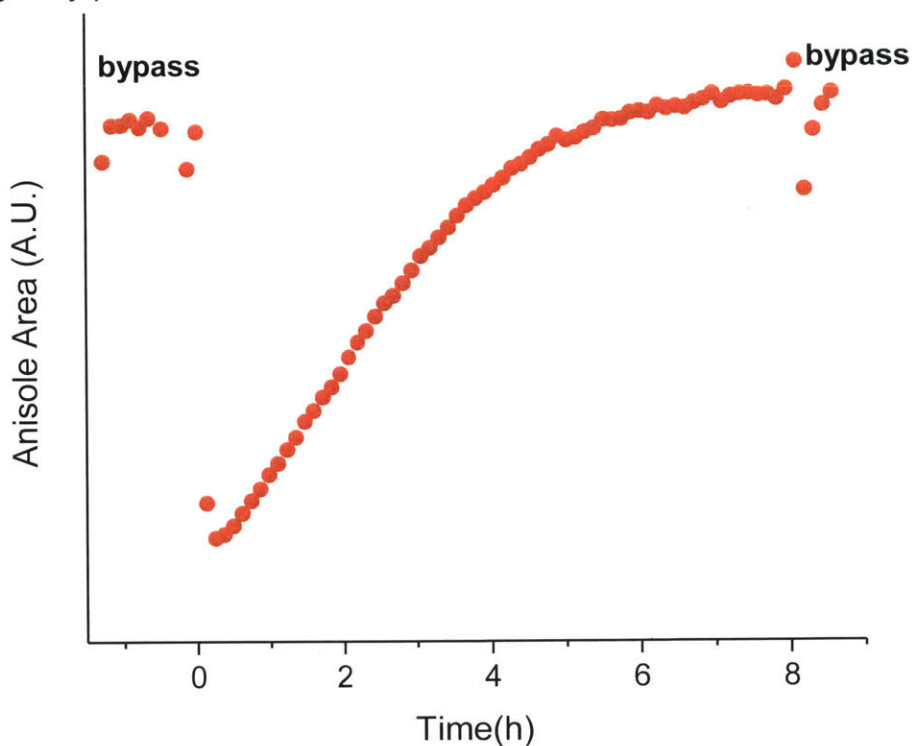


Figure S5.13 Relative anisole areas with time over pre-reduced MoO_3 . Reaction conditions: $T = 320^\circ\text{C}$, $P_{\text{total}} = 1 \text{ mbar}$ ($P_{\text{anisole}} = 0.005$, balance H_2).

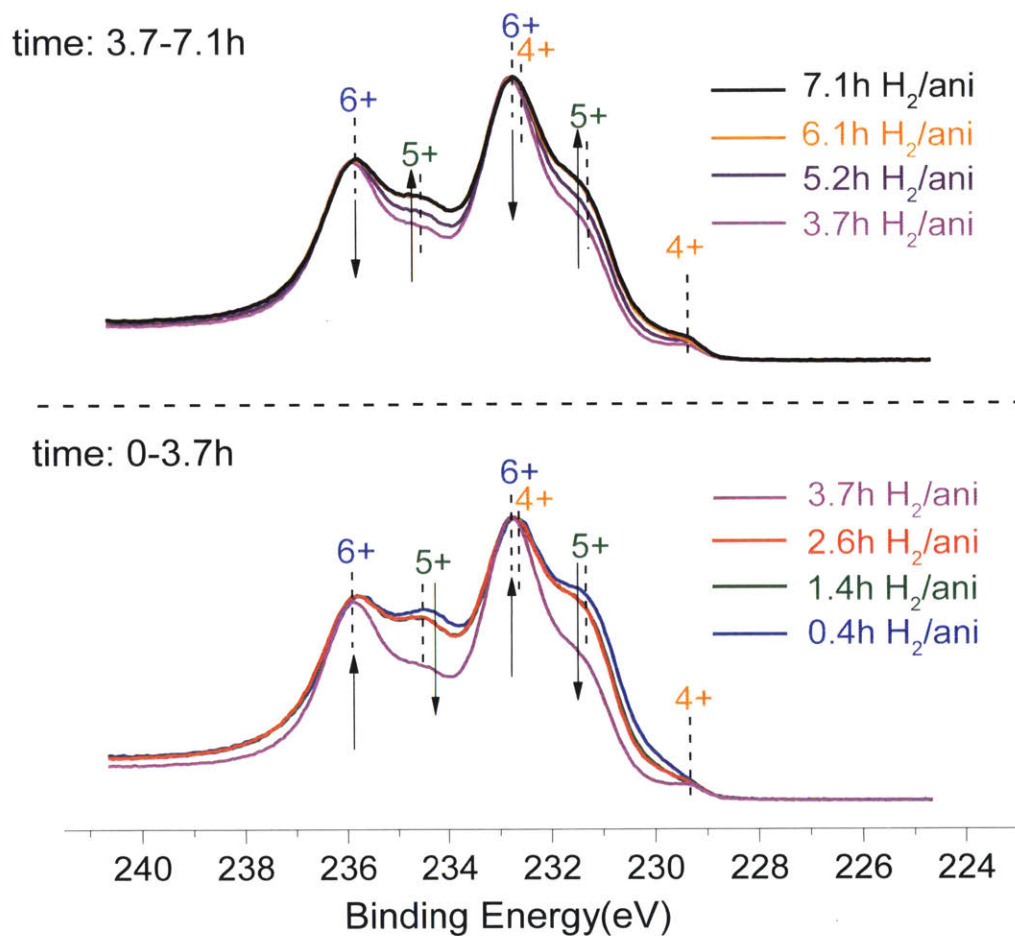


Figure S5.14 Normalized Mo 3d spectra of pre-reduced MoO₃ during HDO of anisole (replicate experiment) at T = 320°C, P_{total} = 1 mbar (P_{anisole} = 0.005, balance H₂).

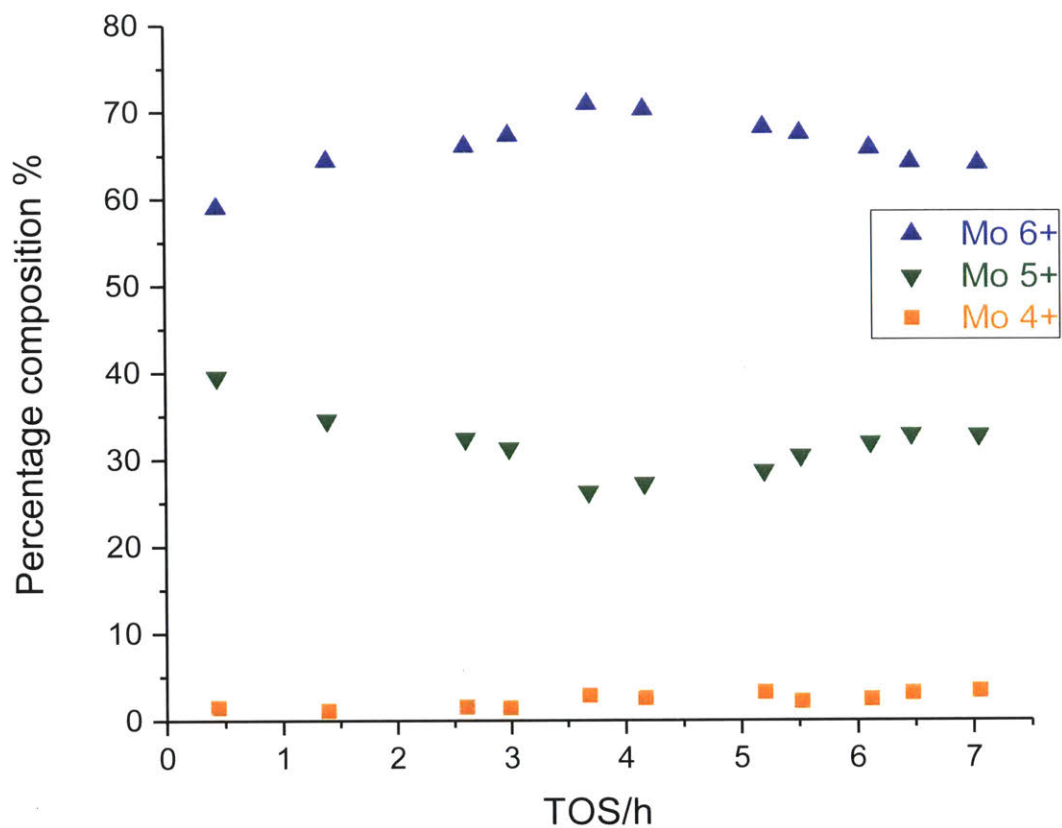


Figure S5.15 Proportion of Mo oxidation states with time for pre-reduced MoO₃ during HDO of anisole (replicate experiment). Reaction conditions: T = 320°C, P_{total} = 1 mbar (P_{anisole} = 0.005, balance H₂).

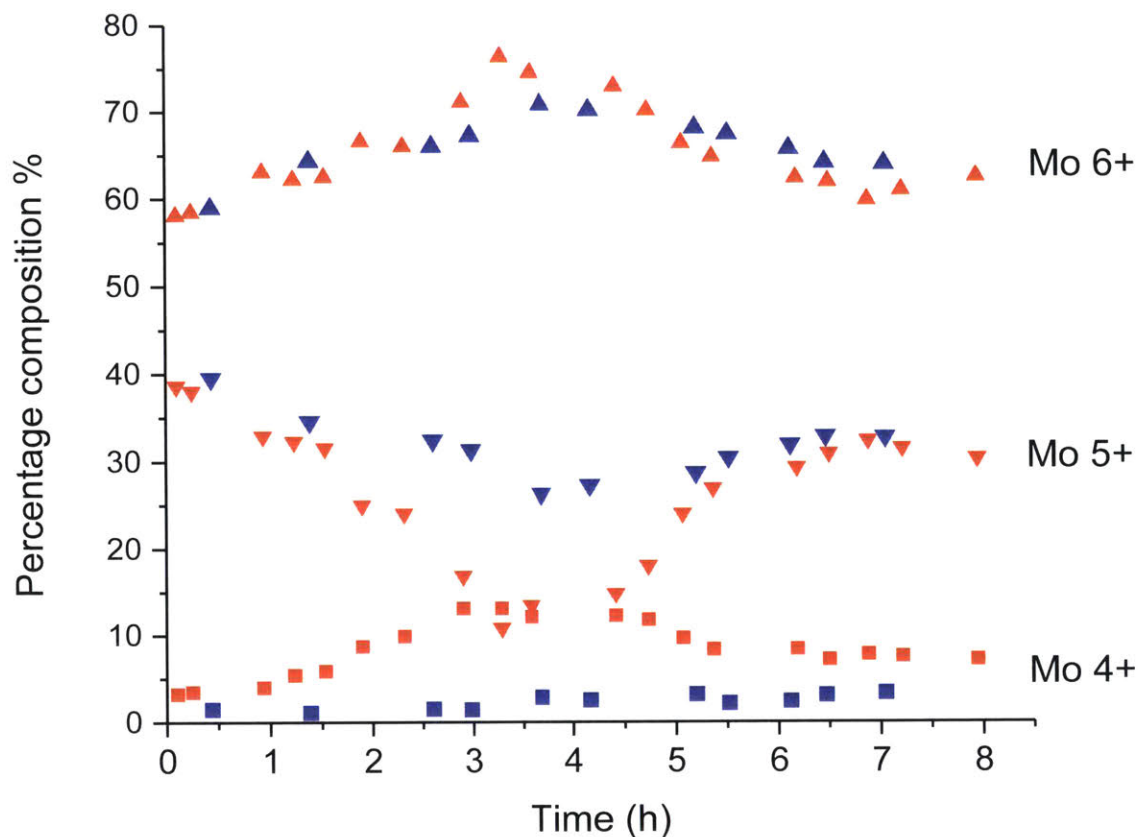


Figure S5.16 Overlay of proportion of Mo oxidation states with time over pre-reduced MoO_3 during HDO of anisole across the two replicate experiments. Reaction conditions: $T = 320^\circ\text{C}$, $P_{\text{total}} = 1 \text{ mbar}$ ($P_{\text{anisole}} = 0.005$, balance H_2). The labels in red correspond to the first HDO experiment with pre-reduced MoO_3 while the blue labels correspond to the replicate experiment.

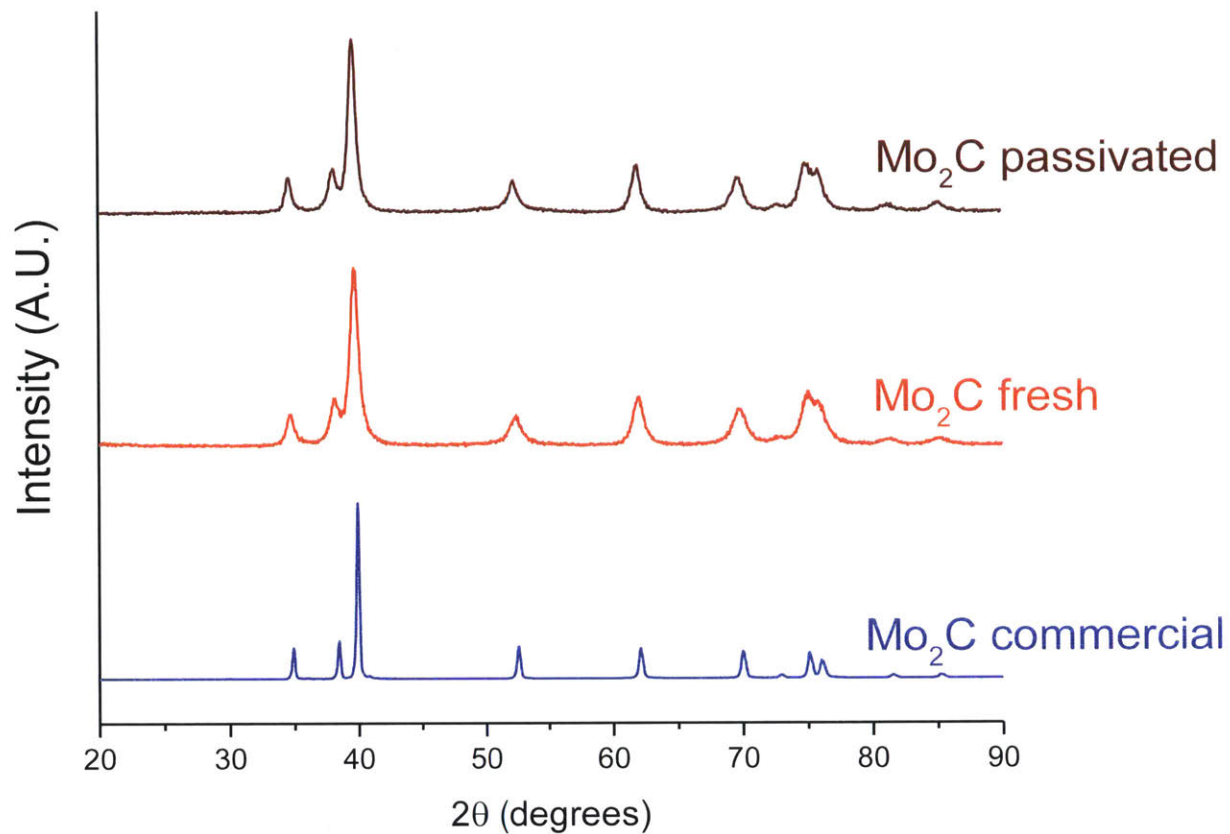


Figure S5.17 Normalized PXRD patterns of commercial, fresh and passivated Mo₂C. A small aliquot of freshly prepared Mo₂C was retrieved from the glovebox for PXRD characterization.

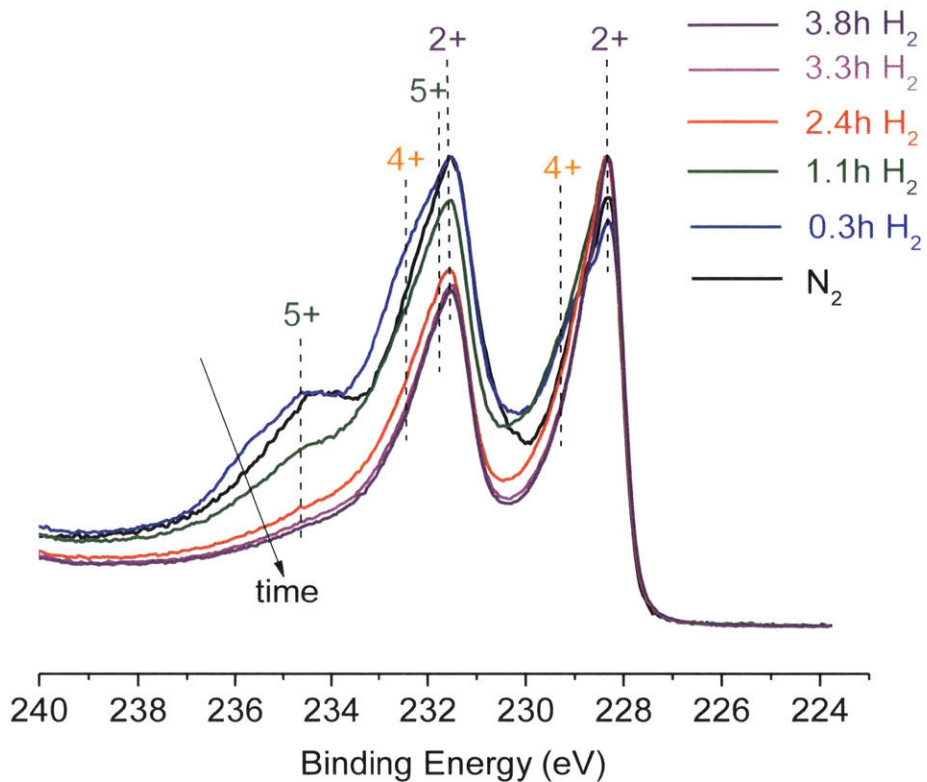


Figure S5.18 Normalized Mo 3d spectra of Mo₂C at T = 320°C, P_{total} = 1 mbar H₂.

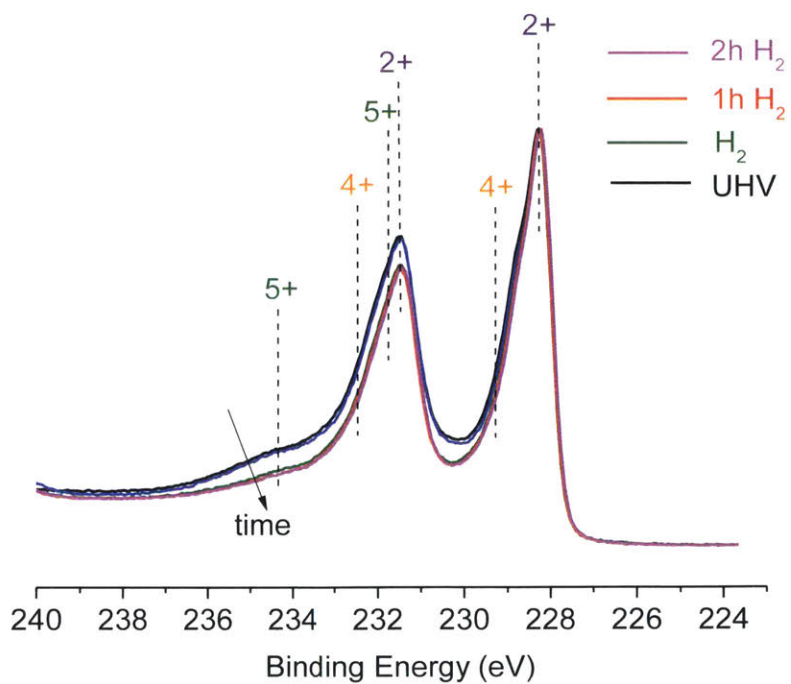


Figure S5.19 Normalized Mo 3d spectra of Mo₂C during pre-reduction with H₂ before HDO of anisole at T = 320°C, P_{total} = 1 mbar H₂.

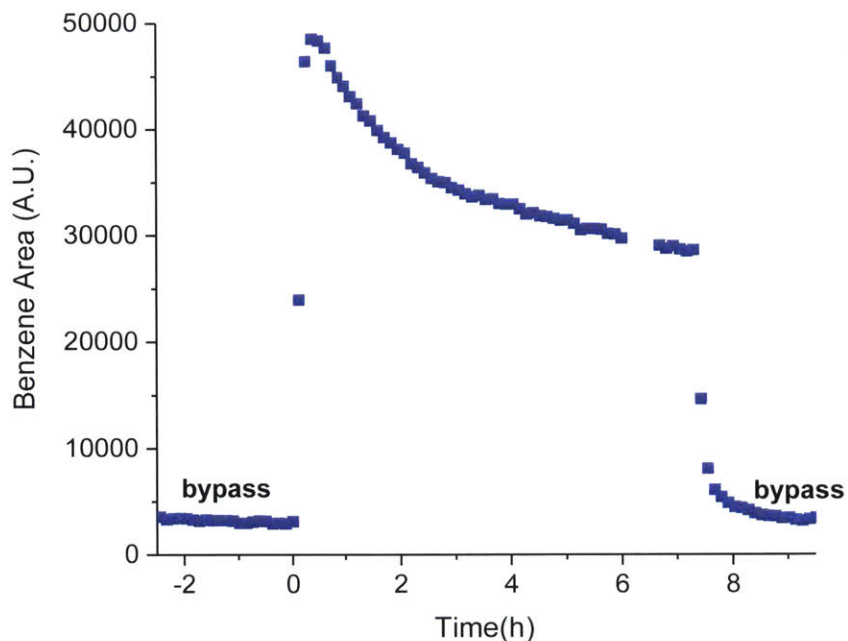


Figure S5.20 Relative benzene areas during HDO of anisole over Mo_2C . Reaction conditions: $T = 320^\circ\text{C}$, $P_{\text{total}} = 1 \text{ mbar}$ ($P_{\text{anisole}} = 0.005$, balance H_2), and H_2 pre-reduction = 3 h.

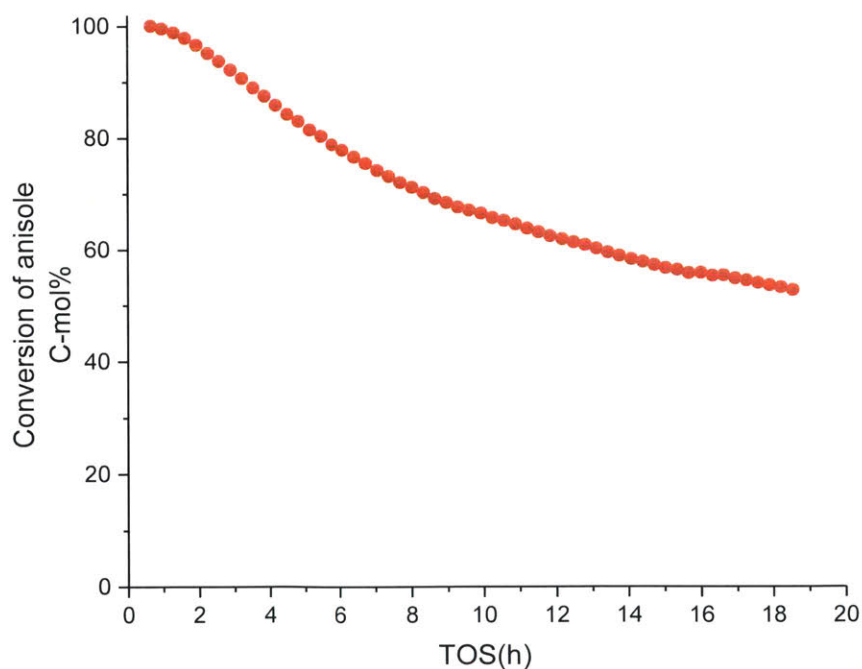


Figure S5.21 Conversion of anisole over fresh Mo_2C . 50 mg of Ammonium paramolybdate was carburized in-situ before HDO of anisole. Carburization conditions: 21% $\text{CH}_4\text{-H}_2$ at 650°C for 1h. Reaction conditions: 29 mg fresh Mo_2C , 320°C , $P_{\text{total}} = 1.013 \text{ bar}$ ($P_{\text{anisole}} = 0.005$, balance H_2).

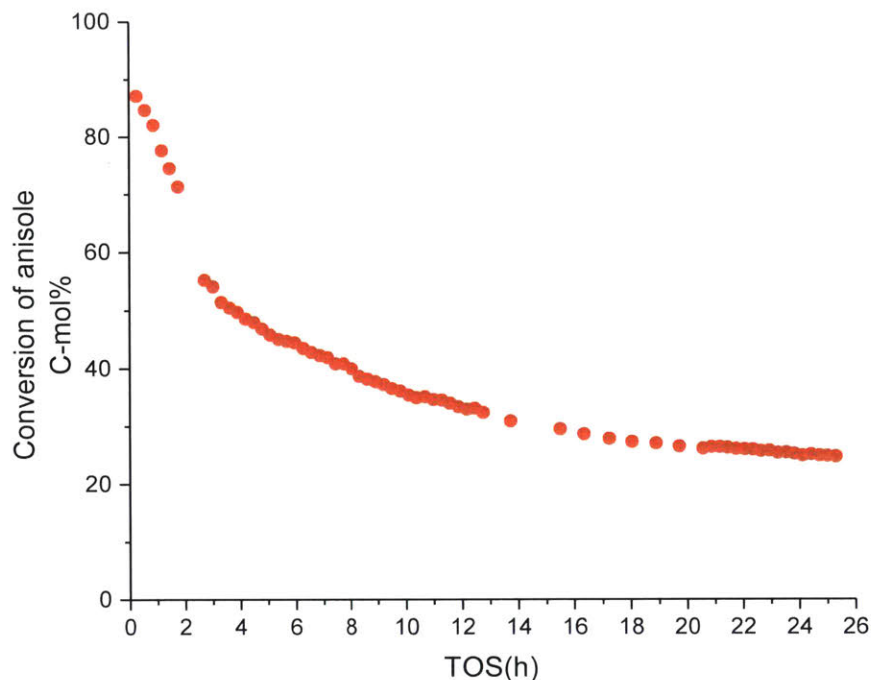


Figure S5.22 Conversion of anisole over $\text{Mo}_2\text{C}/\text{SiO}_2$ nanoparticles. 100 mg of $\text{MoO}_3/\text{SiO}_2$ (25 wt% Mo) was carburized in-situ before HDO of anisole. Carburization conditions: 21% $\text{CH}_4\text{-H}_2$ at 650°C for 1h. Reaction conditions: 320°C , $P_{\text{total}} = 1.013$ bar ($P_{\text{anisole}} = 0.005$, balance H_2).

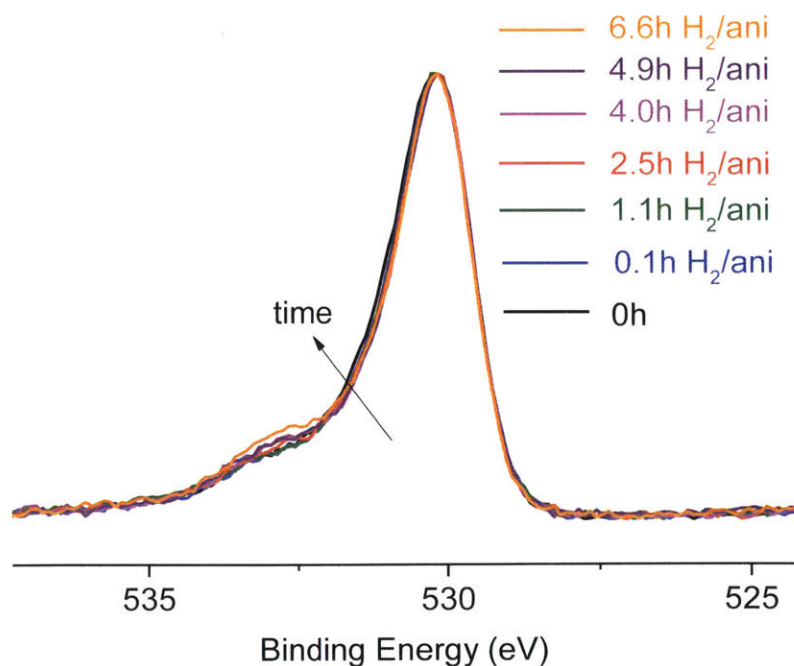


Figure S5.23 Normalized O 1s spectra of fresh Mo_2C during HDO of anisole at $T = 320^\circ\text{C}$, $P_{\text{total}} = 1$ mbar ($P_{\text{anisole}} = 0.005$, balance H_2) and H_2 pre-reduction = 3 h.

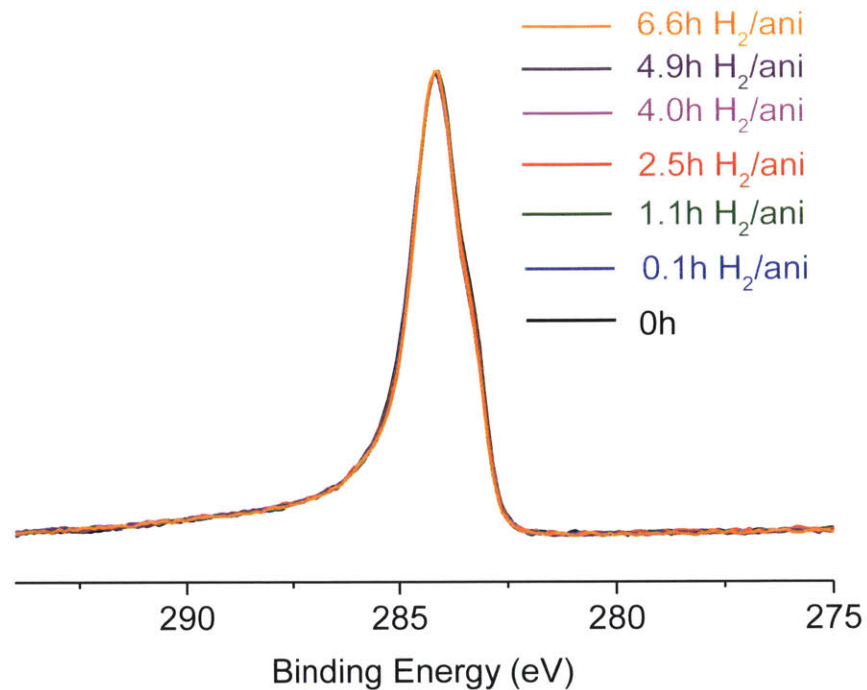


Figure S5.24 Normalized C 1s spectra of fresh Mo₂C during HDO of anisole at T = 320°C, P_{total} = 1 mbar (P_{anisole} = 0.005, balance H₂) and H₂ pre-reduction = 3 h.

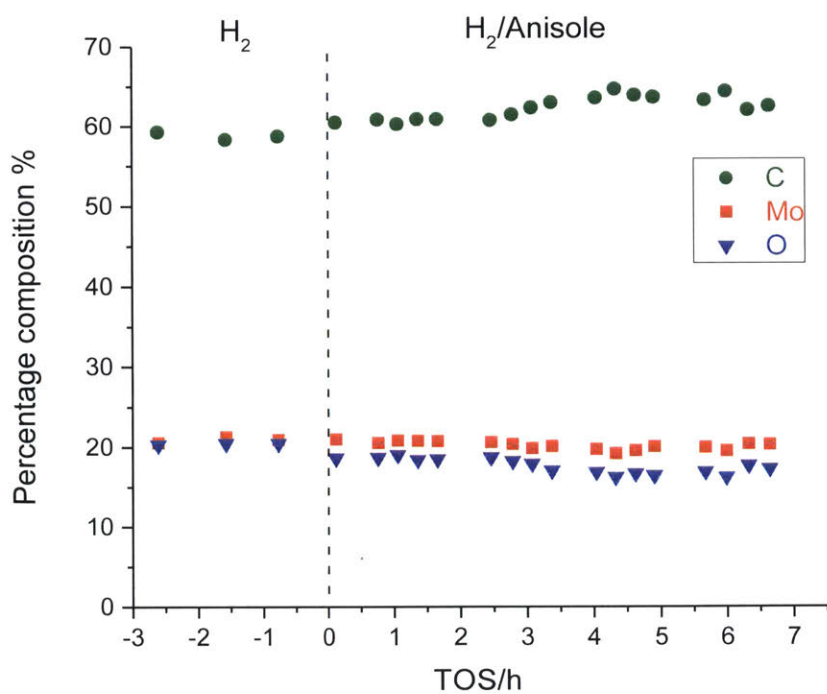


Figure S5.25 Surface elemental composition of fresh Mo₂C during HDO of anisole at T = 320°C, P_{total} = 1 mbar (P_{anisole} = 0.005, balance H₂) and H₂ pre-reduction = 3 h.

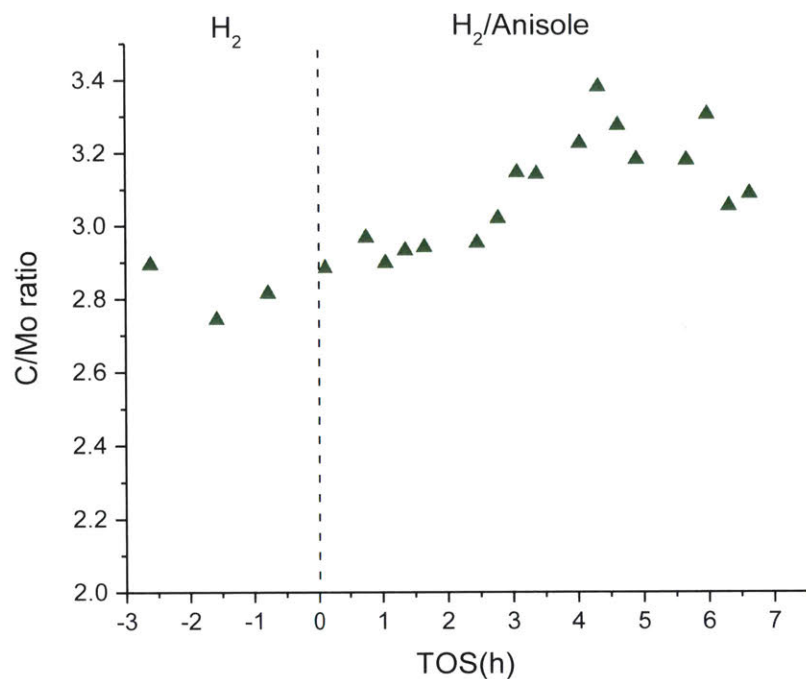


Figure S5.26 Overall C-Mo ratio on fresh Mo₂C during HDO of anisole at T = 320°C, P_{total} = 1 mbar (P_{anisole} = 0.005, balance H₂) and H₂ pre-reduction = 3 h.

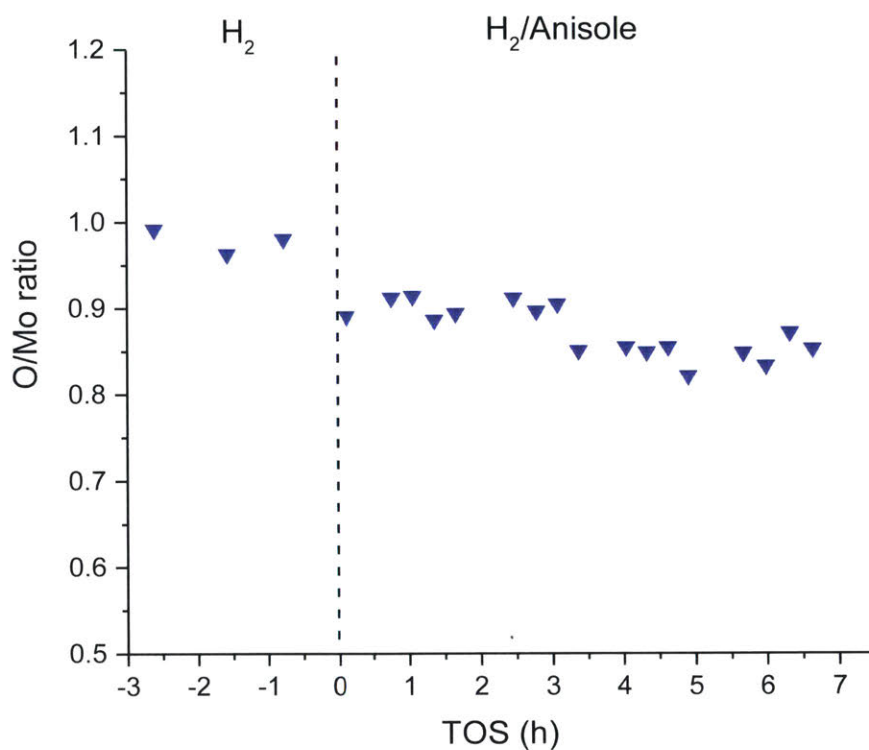


Figure S5.27 Overall O-Mo of fresh Mo₂C during HDO of anisole at T = 320°C, P_{total} = 1 mbar (P_{anisole} = 0.005, balance H₂) and H₂ pre-reduction = 3 h.

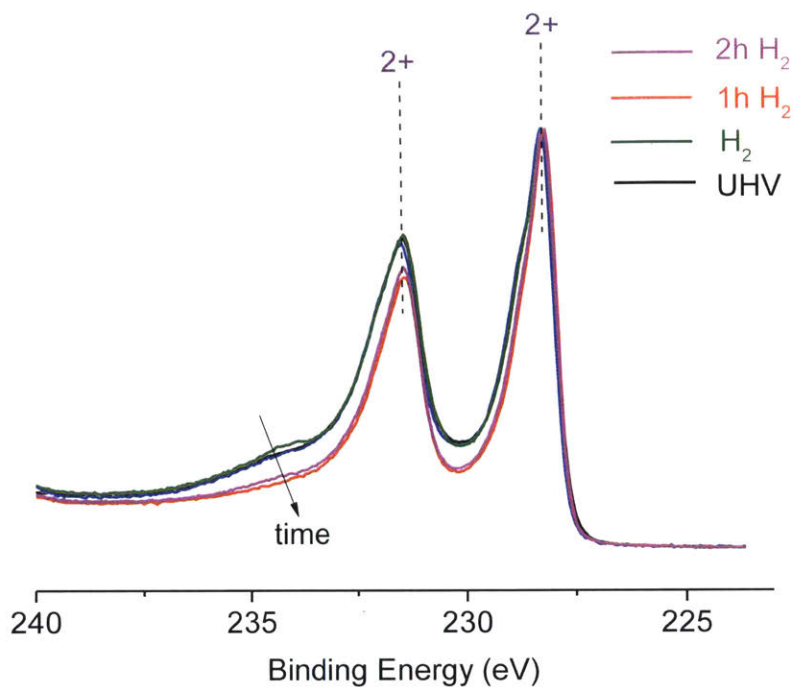


Figure S5.28 Normalized Mo 3d spectra of fresh Mo_2C during pre-reduction with H_2 (replicate experiment) at $T = 320^\circ\text{C}$, $P_{\text{total}} = 1 \text{ mbar H}_2$.

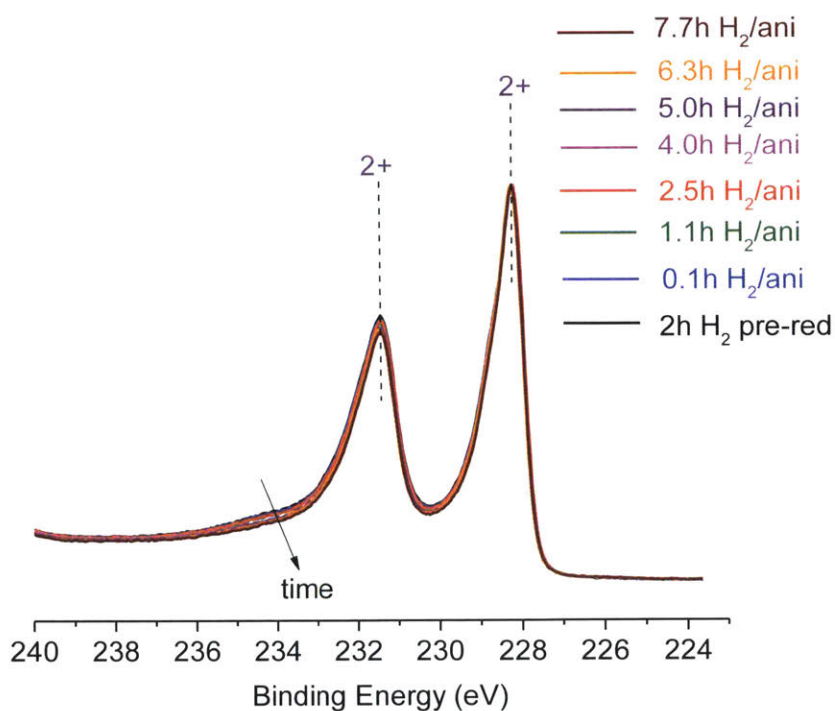


Figure S5.29 Normalized Mo 3d spectra of fresh Mo_2C during HDO of anisole (replicate experiment) at $T = 320^\circ\text{C}$, $P_{\text{total}} = 1 \text{ mbar}$ ($P_{\text{anisole}} = 0.005$, balance H_2) and H_2 pre-reduction = 3 h.

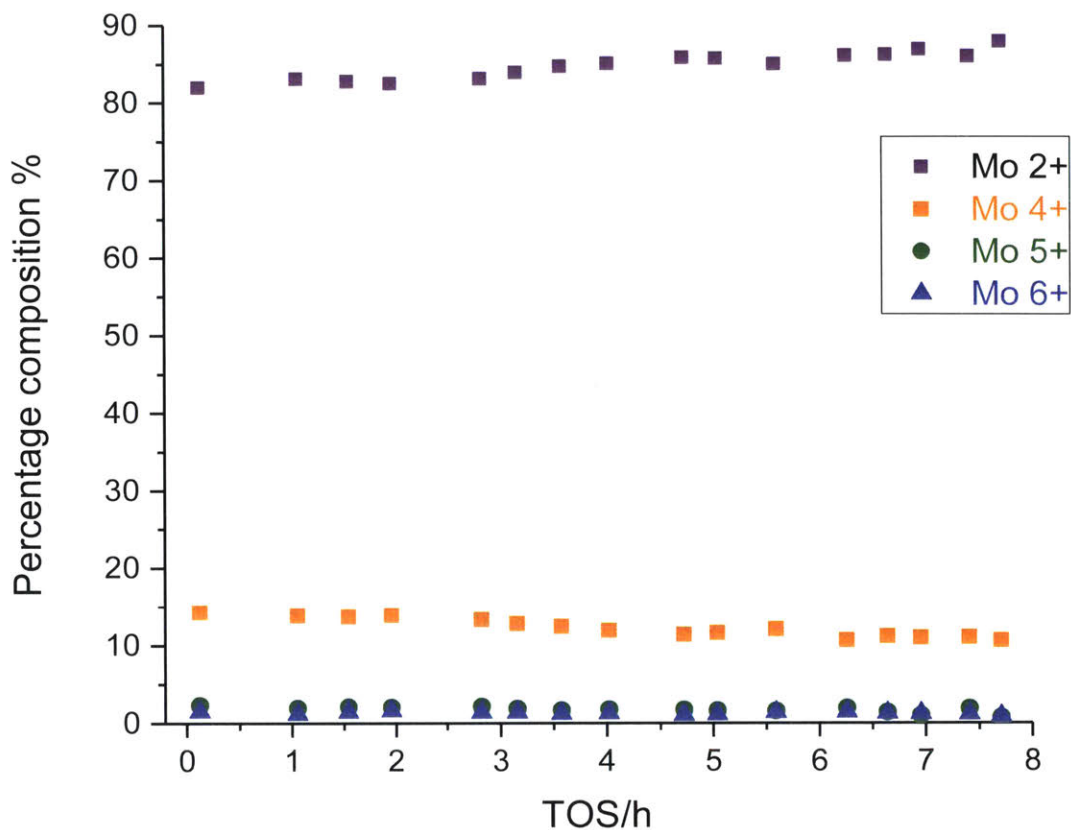


Figure S5.30 Proportion of Mo oxidation states with time for fresh Mo₂C during HDO of anisole (replicate experiment). Reaction conditions: T = 320°C, P_{total} = 1 mbar (P_{anisole} = 0.005, balance H₂) and H₂ pre-reduction = 3 h.

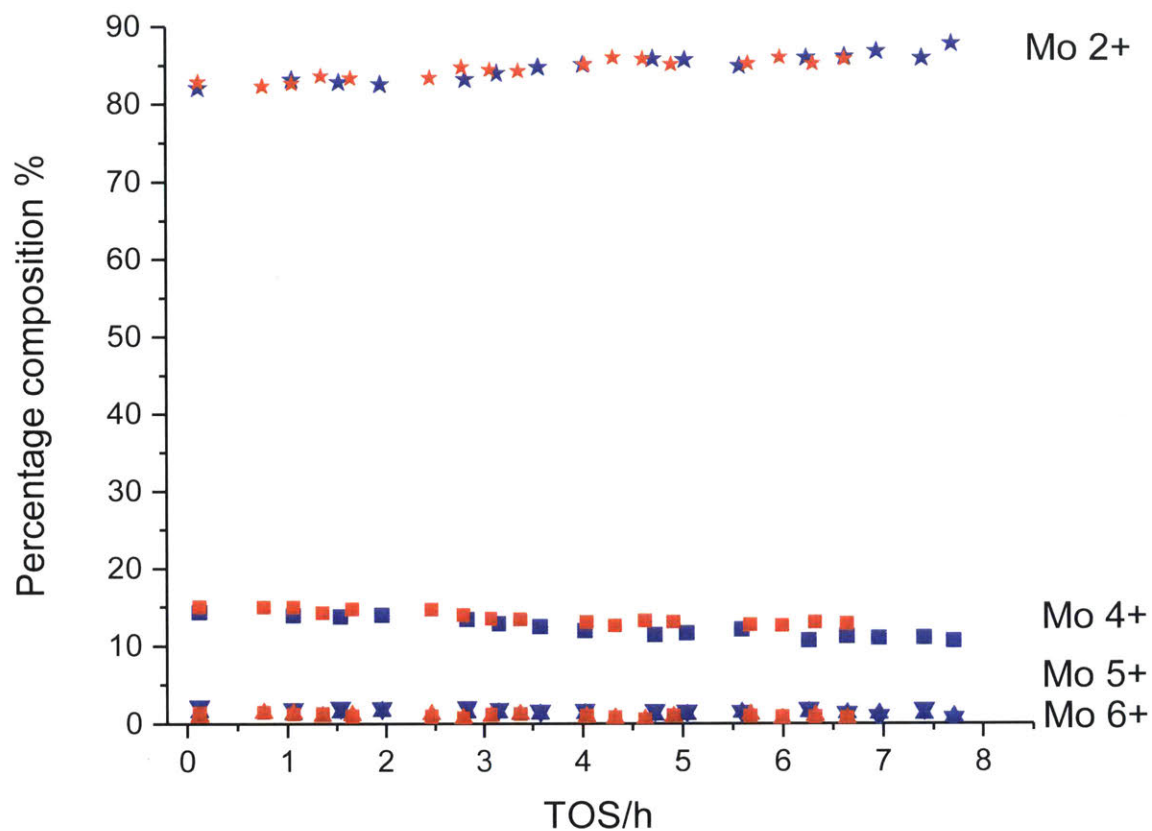


Figure S5.31 Overlay of proportion of Mo oxidation states with time over fresh Mo₂C during HDO of anisole across the two replicate experiments. Reaction conditions: T = 320°C, P_{total} = 1 mbar (P_{anisole} = 0.005, balance H₂) and H₂ pre-reduction = 3 h. The labels in red correspond to the first HDO experiment with Mo₂C while the blue labels correspond to the replicate experiment.

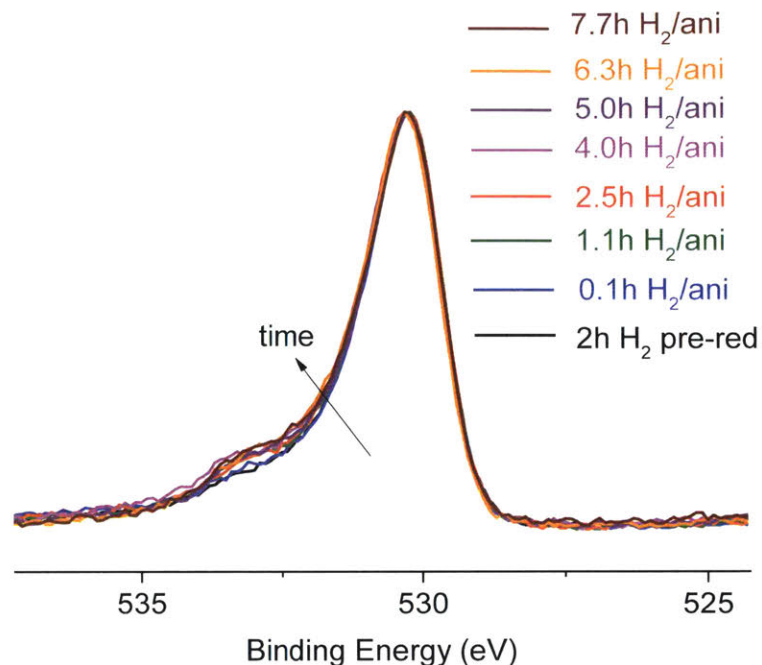


Figure S5.32 Normalized O 1s spectra of fresh Mo₂C during HDO of anisole (replicate experiment) at T = 320°C, P_{total} = 1 mbar (P_{anisole} = 0.005, balance H₂) and H₂ pre-reduction = 3 h.

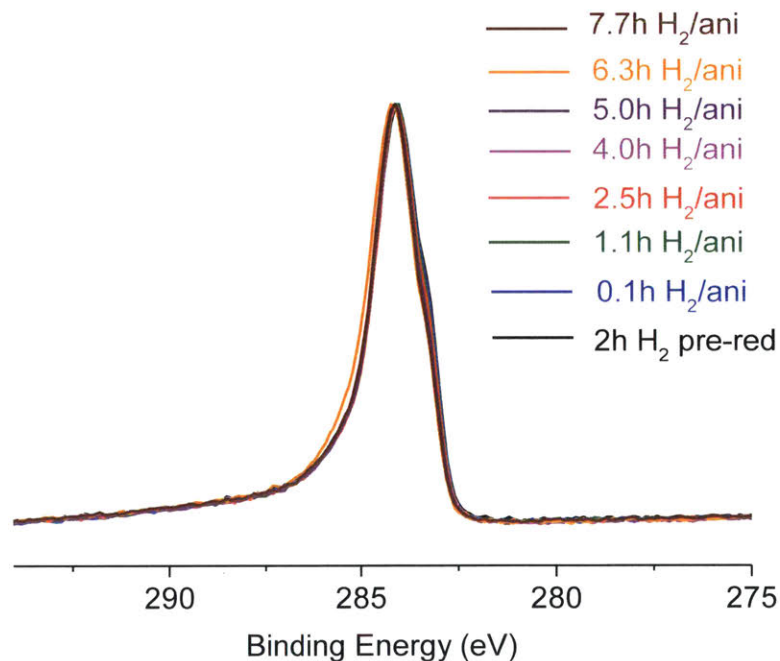


Figure S5.33 Normalized C 1s spectra of fresh Mo₂C during HDO of anisole (replicate experiment) at T = 320°C, P_{total} = 1 mbar (P_{anisole} = 0.005, balance H₂) and H₂ pre-reduction = 3 h.

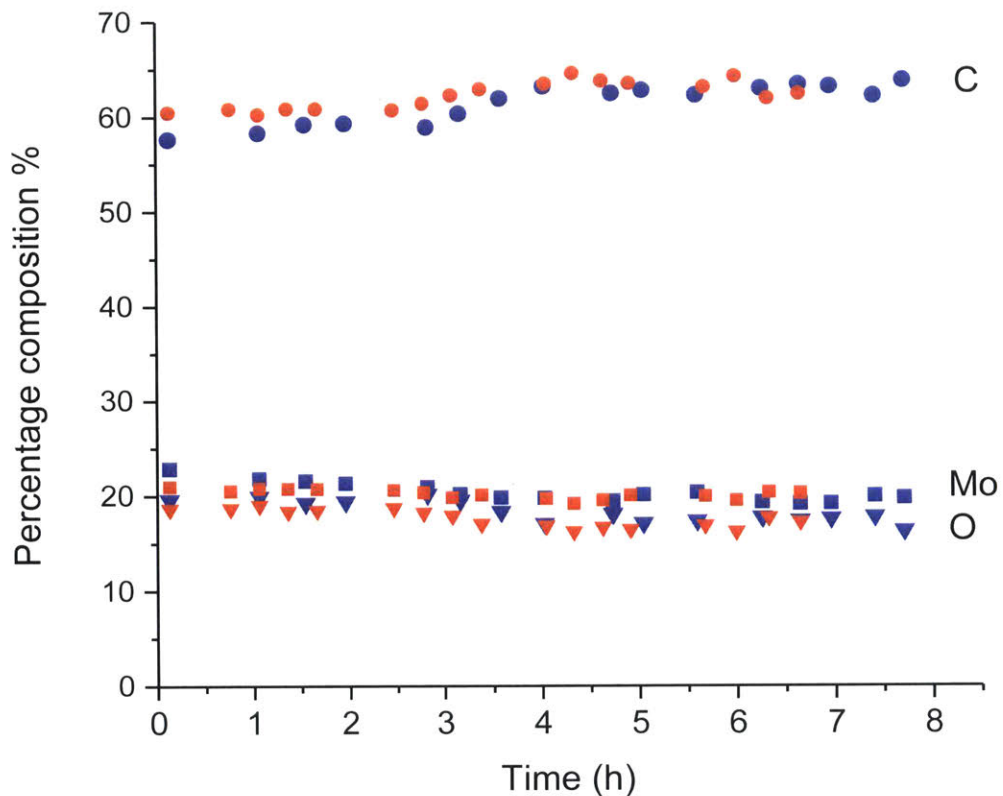


Figure S5.34 Surface elemental composition of fresh Mo_2C with time during HDO of anisole across the two replicate experiments. Reaction conditions: $T = 320^\circ\text{C}$, $P_{\text{total}} = 1$ mbar ($P_{\text{anisole}} = 0.005$, balance H_2) Circles represent C, squares represent Mo and triangles represent O. Red labels correspond to the first HDO experiment while blue labels correspond to the replicate experiment.

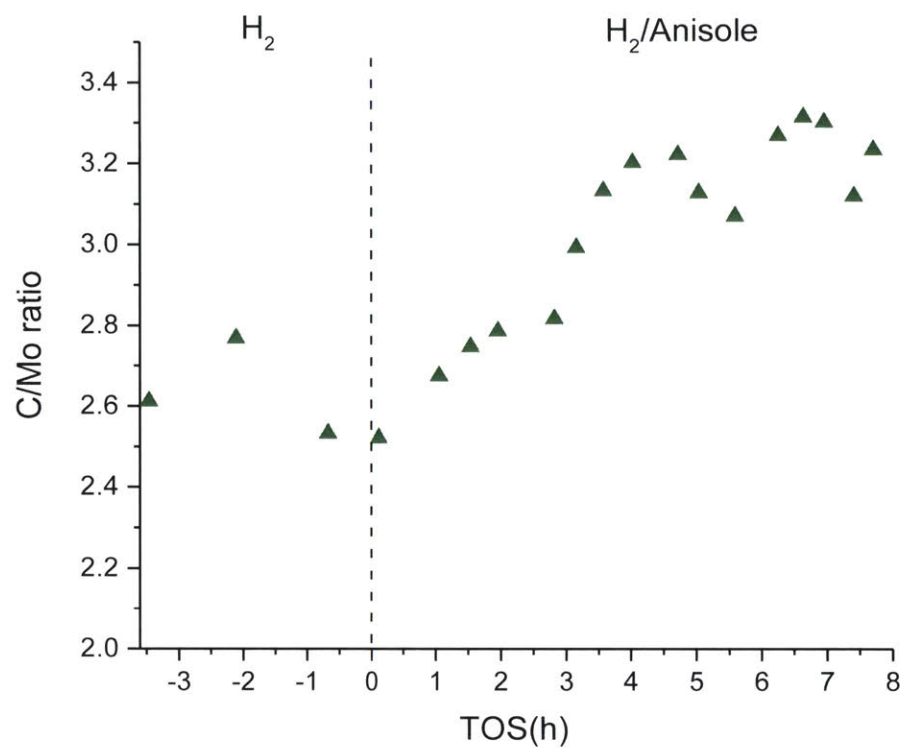


Figure S5.35 Overall C-Mo ratio on fresh Mo₂C during HDO of anisole (replicate experiment) at T = 320°C, P_{total} = 1 mbar (P_{anisole} = 0.005, balance H₂) and H₂ pre-reduction = 3 h.

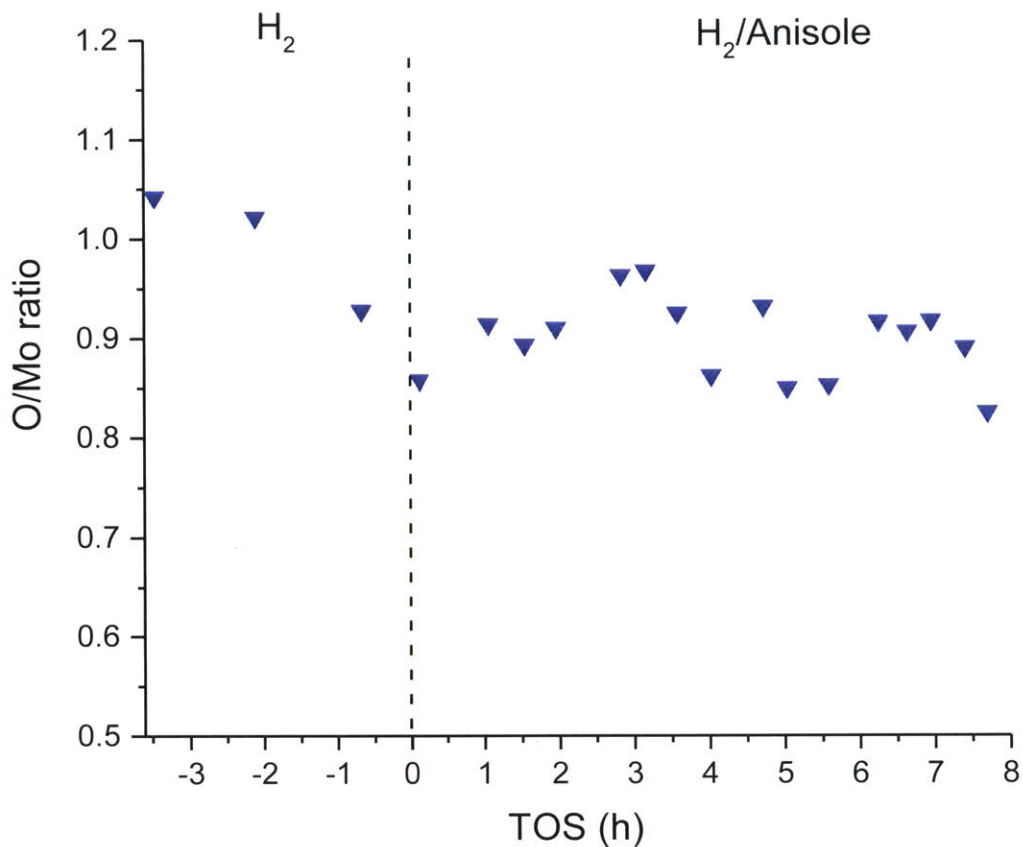


Figure S5.36 Overall O-Mo ratio on fresh Mo₂C during HDO of anisole (replicate experiment) at T = 320°C, P_{total} = 1 mbar (P_{anisole} = 0.005, balance H₂) and H₂ pre-reduction = 3 h.

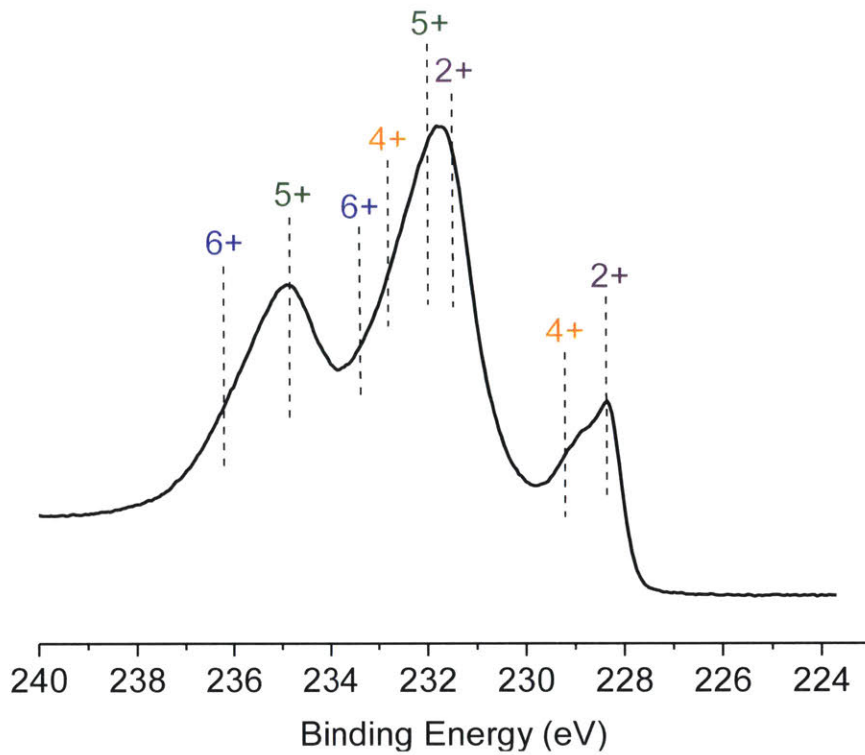


Figure S5.37 Normalized Mo 3d spectra of passivated Mo₂C at UHV and T = 25°C.

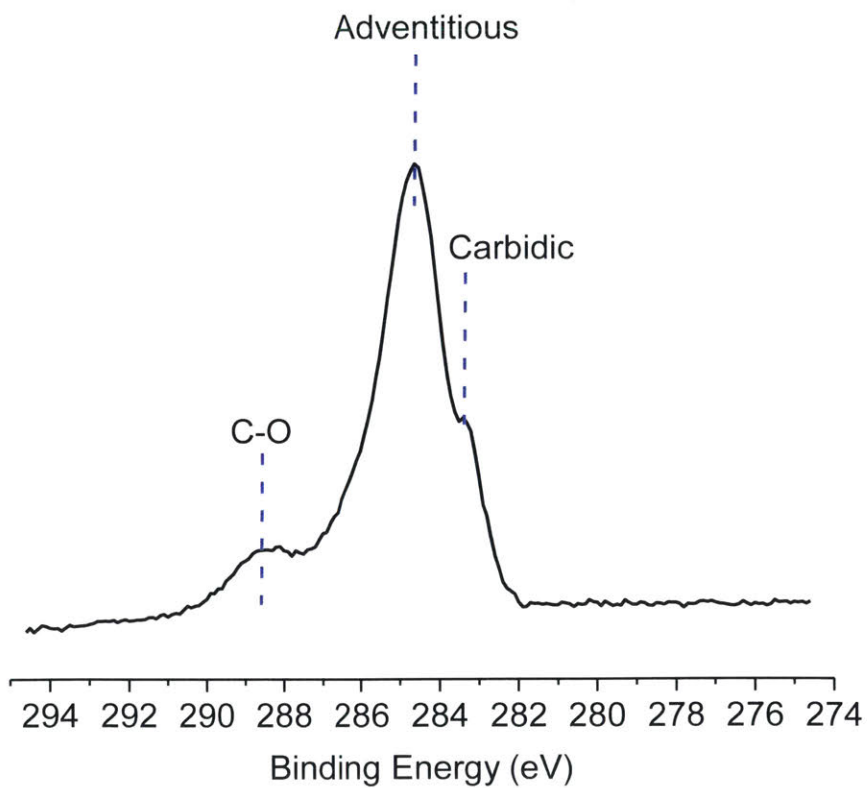


Figure S5.38 Normalized C 1s spectra of passivated Mo₂C at UHV and T = 25°C.

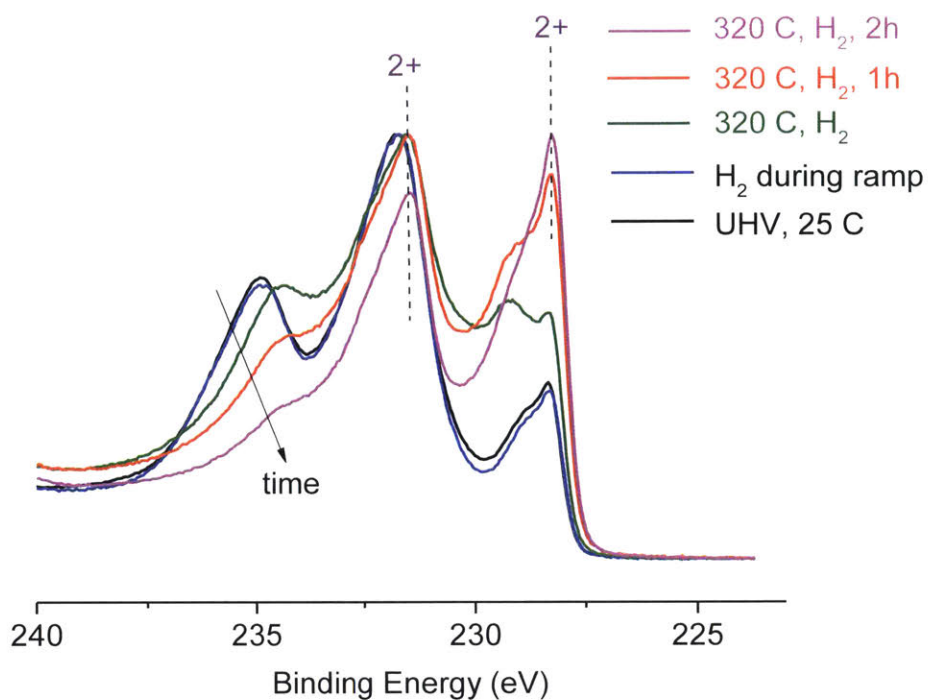


Figure S5.39 Normalized Mo 3d spectra of passivated Mo₂C during pre-reduction with H₂ at T = 320°C, P_{total} = 1 mbar H₂.

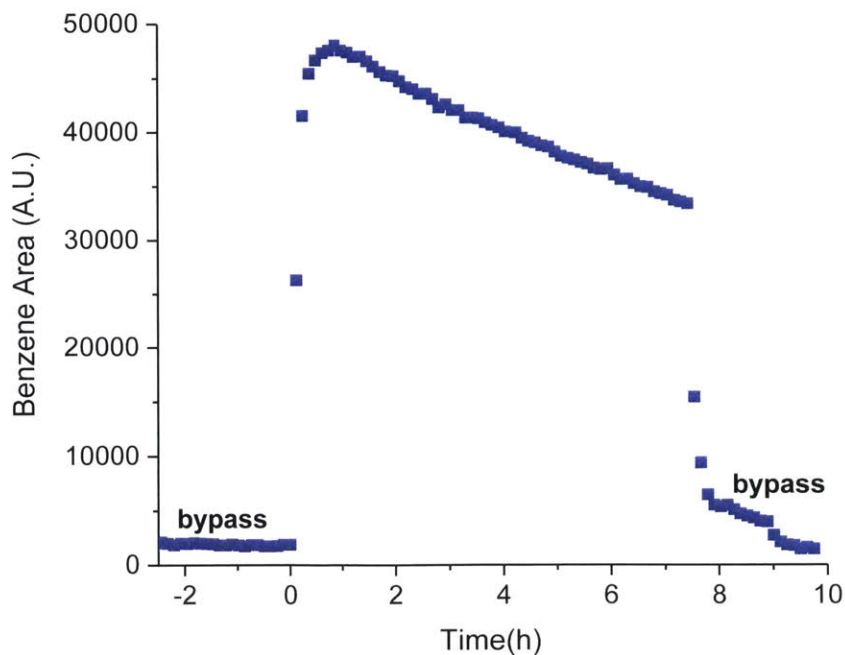


Figure S5.40 Relative benzene areas during HDO of anisole over passivated Mo₂C. Reaction conditions: T = 320°C, P_{total} = 1 mbar (P_{anisole} = 0.005, balance H₂), and H₂ pre-reduction = 3 h.

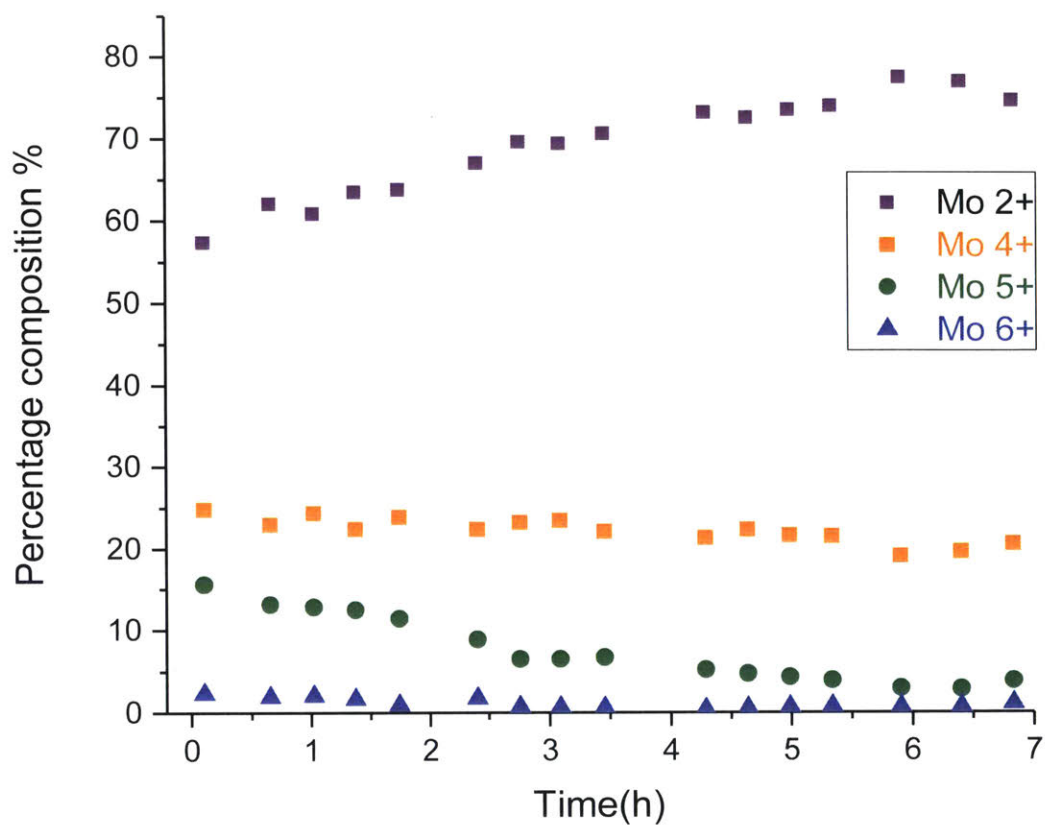


Figure S5.41 Proportion of Mo oxidation states with time for passivated Mo₂C during HDO of anisole. Reaction conditions: T = 320°C, P_{total} = 1 mbar (P_{anisole} = 0.005, balance H₂) and H₂ pre-reduction = 3 h.

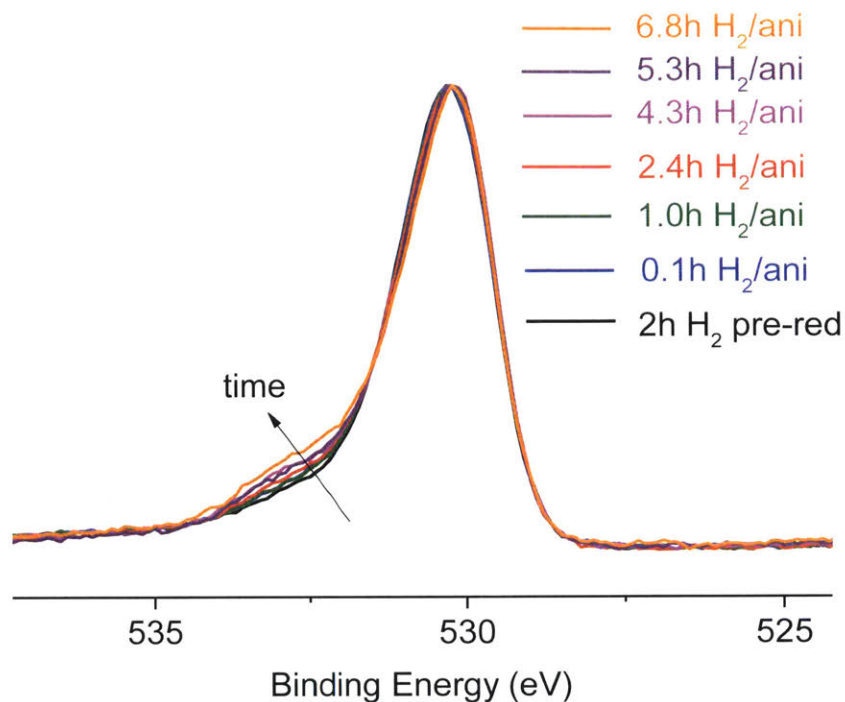


Figure S5.42 Normalized O 1s spectra of passivated Mo₂C during HDO of anisole at T = 320°C, P_{total} = 1 mbar (P_{anisole} = 0.005, balance H₂) and H₂ pre-reduction = 3 h.

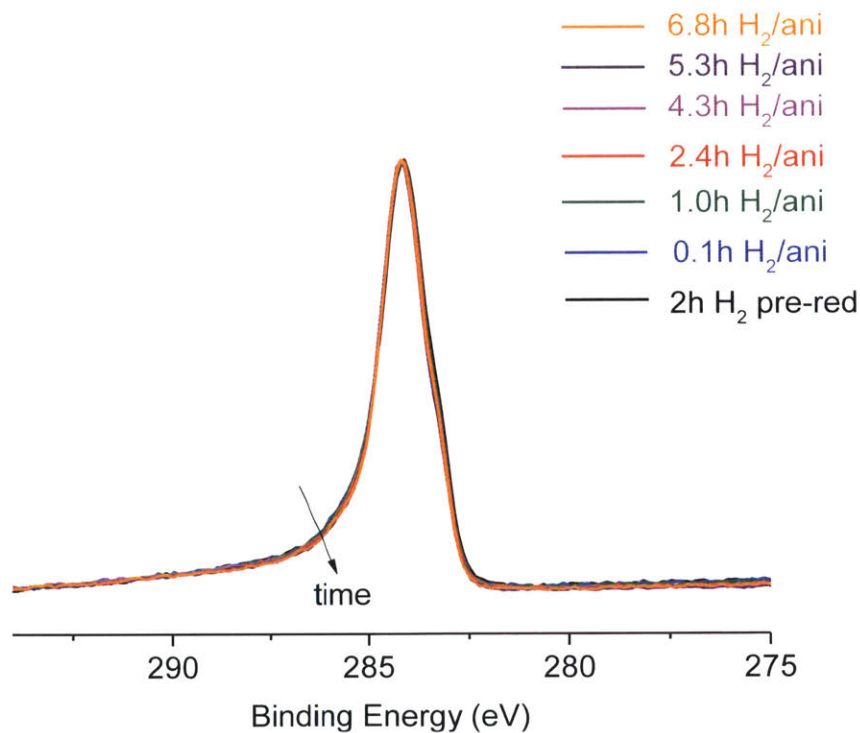


Figure S5.43 Normalized C 1s spectra of passivated Mo₂C during HDO of anisole at T = 320°C, P_{total} = 1 mbar (P_{anisole} = 0.005, balance H₂) and H₂ pre-reduction = 3 h.

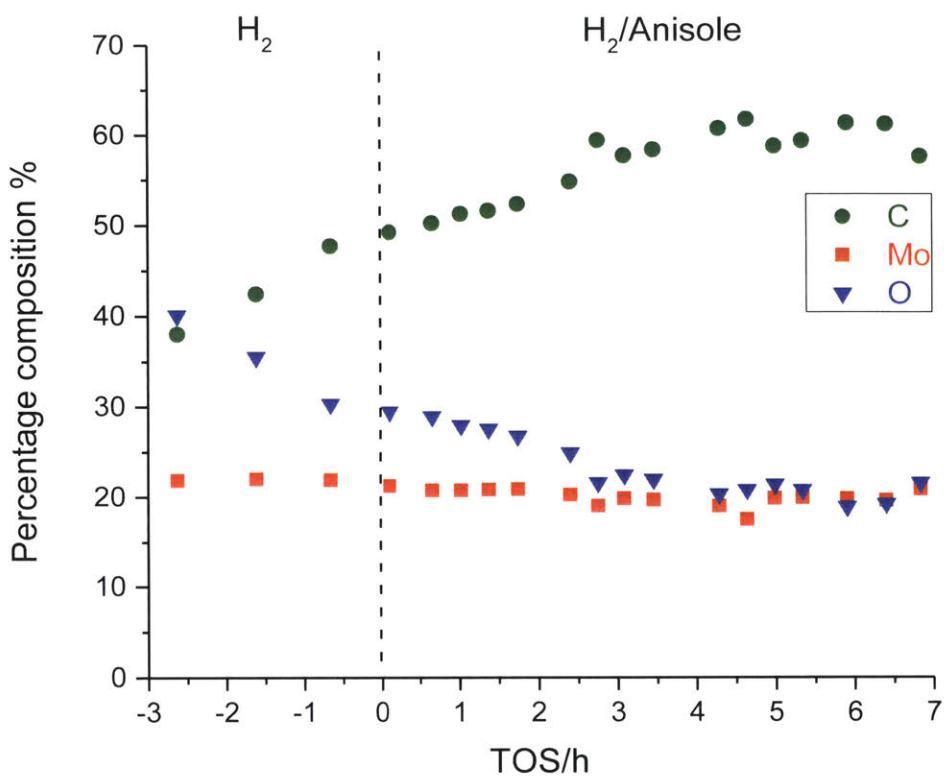


Figure S5.44 Surface elemental composition of passivated Mo₂C during HDO of anisole at T = 320°C, P_{total} = 1 mbar (P_{anisole} = 0.005, balance H₂) and H₂ pre-reduction = 3 h.

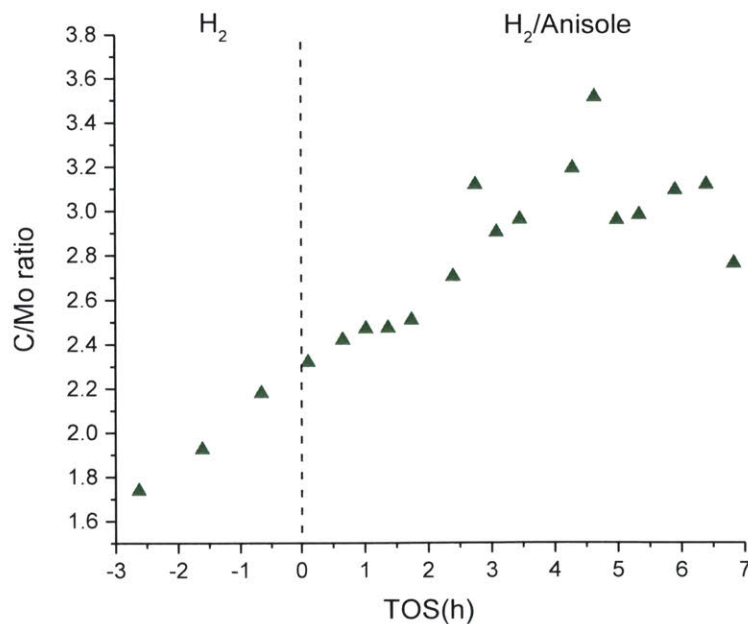


Figure S5.45 Overall C-Mo ratio on passivated Mo₂C during HDO of anisole at T = 320°C, P_{total} = 1 mbar (P_{anisole} = 0.005, balance H₂) and H₂ pre-reduction = 3 h.

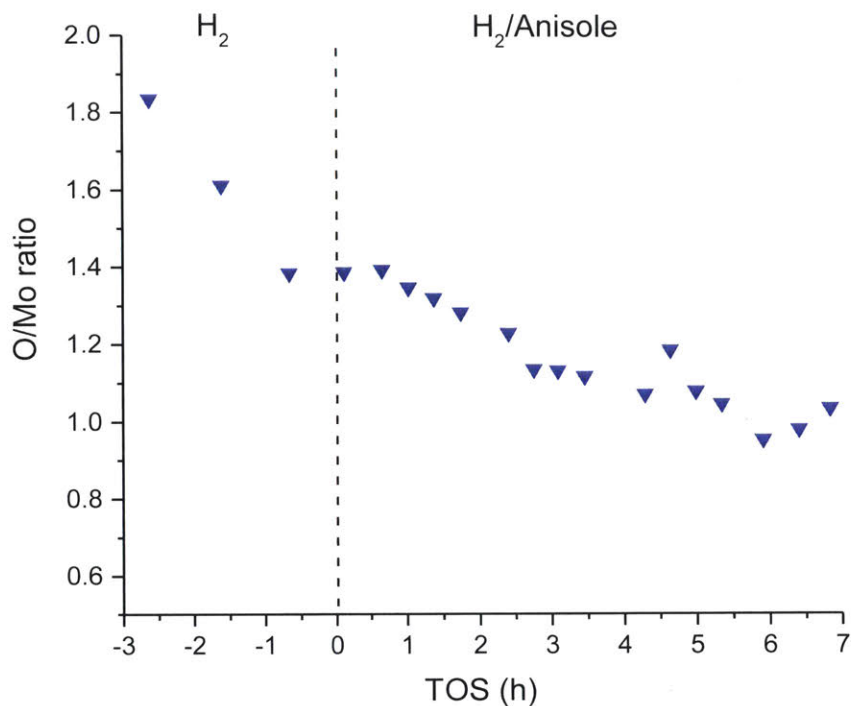


Figure S5.46 Overall O-Mo ratio on passivated Mo₂C during HDO of anisole at T = 320°C, P_{total} = 1 mbar (P_{anisole} = 0.005, balance H₂) and H₂ pre-reduction = 3 h.

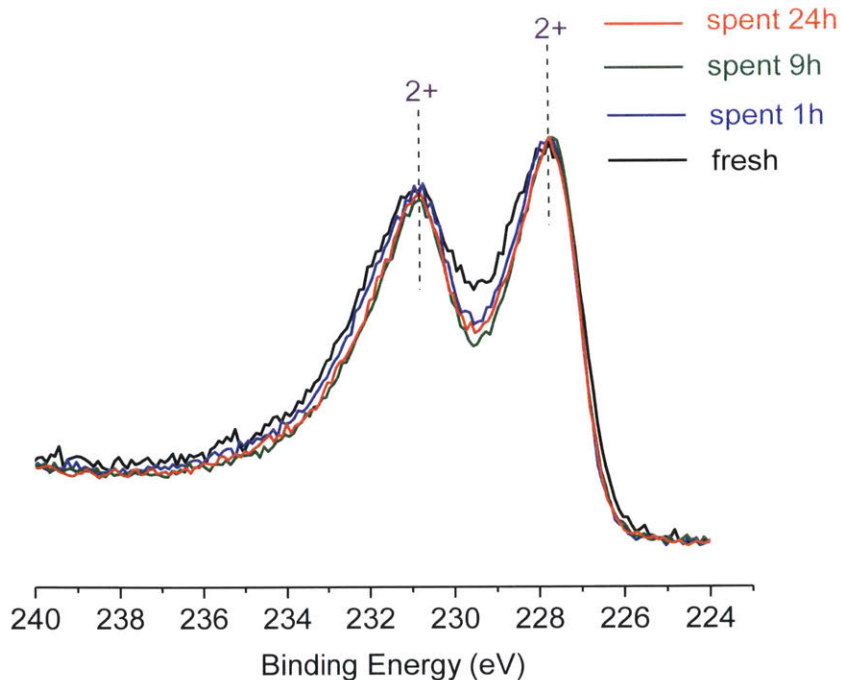
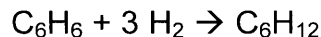


Figure S5.47 Normalized Mo 3d spectra of fresh and spent Mo₂C catalysts from 3 different after 1h, 9h, and 24h of HDO of anisole at T = 320°C, P_{total} = 1 mbar (P_{anisole} = 0.005, balance H₂). XPS spectra were acquired on a lab UHV XPS using Al K α source.

Table S1. Thermodynamics calculations for benzene hydrogenation at 590 K (317°C)

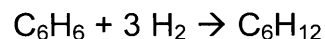
	ΔG_f (kcal/mol)	ΔG_f (kJ/mol)
C_6H_6	-20.97 ¹	-87.74
H_2	-19.2 ¹	-80.33
C_6H_{12}	-74.58 ¹	-312.04

$$\Delta G_{\text{rxn}} = \Delta G_f(\text{C}_6\text{H}_{12}) - 3 \cdot \Delta G_f(\text{H}_2) - \Delta G_f(\text{C}_6\text{H}_6) = +16.69 \text{ kJ/mol}$$

$$K_p = \exp(-\Delta G_{\text{rxn}}/RT) = 0.03326$$

Assuming 100% conversion of anisole to benzene, the initial molar fraction of benzene will be similar to that of anisole in the H_2 /anisole mixture = 0.00466

Assuming no cyclohexane to begin with, and based on the K_p calculated from above, an equilibrium conversion can be calculated.



	C_6H_6	H_2	C_6H_{12}
Initial mole fraction	0.00466	0.995	0
Change	-x	- 3x	+x
Equilibrium mole fraction	0.00466-x	0.995-3x	x

$$K_p = \frac{P_{\text{C}_6\text{H}_{12}}}{P_{\text{C}_6\text{H}_6} * P_{\text{H}_2}^3}$$

$$0.03326 = \frac{x}{(0.00466 - x) * (0.995 - 3x)^3}$$

Using goalseek in excel, the equation can be solved, thereby determining $x = 0.000148$

This translates to an equilibrium conversion of $0.000148/0.00466 = 3.18 \%$

Chapter 6

Mo₂C as a highly selective HDO catalyst for lignin upgrading

1. Introduction

Currently, various technologies already exist to utilize cellulose and hemicellulose fractions of biomass, but lignin valorization poses significant technical challenges. At present, lignin is mostly burnt for process heat and power.²² Several cellulosic ethanol plants have been commissioned in USA,²³ which will generate huge quantities of lignin by-product. Due to the technical barriers associated with lignin utilization, lignin produced in these plants is also designated for combustion to produce process heat and power. However, reports have indicated that ca. 60% more lignin will be produced than that will be required for energy needs.^{24,25} Furthermore, lignin valorization has shown to be critical for economics and sustainability of these cellulosic biorefineries,^{24,26} with a projected 30-40 % improvement in process economics.²⁷ Notably, lignin is also the largest renewable source of aromatics^{24,28} and with more second generation biofuel plants coming online, recently, increasing research efforts have focused on lignin extraction and transformation to valuable fuels and chemicals.¹⁷⁻²¹

Several strategies have been investigated to utilize lignin. Particularly, reductive catalytic fractionation (RCF) has gained significant traction as a viable process to effectively depolymerize lignin into its monomers at high yields while retaining cellulose and hemicellulose fractions intact for further processing.^{27,124-130} Overall, RCF allows the full utilization of all fractions of biomass via a lignin first approach, wherein lignin is first depolymerized for further upgrading before the carbohydrate fractions can be converted to valuable products. Though these RCF product streams i.e. lignin oil contain phenolic lignin monomers, deoxygenation is essential before these molecules can be utilized as fuels and chemicals. However, HDO of lignin oil and lignin-derived phenolic monomers typically yield in partially deoxygenation products, or mostly saturated products (i.e. cycloalkanes and cyclohexanols), thereby destroying the aromaticity of the molecules initially present in the monomers. Wang *et al.* investigated HDO of poplar wood based

lignin oil over supported PtCo nanoparticles at 100 bar H₂, 300°C. Though this study shows that almost all oxygen could be removed, PtCo nanoparticles featured a mixture of products in the form of ring-saturated cyclohexanes.¹³¹ Rinaldi and co-workers studied HDO of organosolv lignin over Raney Ni and H-BEA-35 to produce 40% yields of upgraded oil.¹³² However, this upgraded oil featured as many as 25 products, with a combination of arenes, alkanes, and some phenols.¹³² Similarly, HDO studies of propylguaiacol, a main RCF product, over Pd/C, Ru/C and Ni/SiO₂-Al₂O₃ led to products which were either ring-saturated or only partially deoxygenated.¹³³ Furthermore, Omar and co-workers demonstrated HDO of propylguaiacol, propylsyringol and a 50:50 mixture of propylguaiacol-propylsyringol over supported PtMo catalysts to produce >97% yields of propylcyclohexane and <1 % yield to propylbenzene. Recently, bifunctional molybdenum-based TiO₂ were also tested for HDO of propylguaiacol to produce propylbenzene in 41% yields, in addition to other alkylated aromatics, propylphenols and alkylated propylphenols.¹³⁴ To our knowledge, no studies have shown the production of just one single aromatic product from HDO of lignin oil and lignin-derived monomers in high yields and selectivities.

Herein, RCF was performed over Ni/C catalysts to depolymerize lignin from poplar wood and corn stover, producing high monomer yields (propylguaiacol and propylsyringol from poplar wood and corn stover; methylcoumarate and methylferulate only from corn stover). These RCF product streams were then extracted in a toluene phase, before being investigated for gas-phase HDO over Mo₂C catalyst. For the first time in this study, we demonstrate complete deoxygenation of all lignin monomers from both biomass substrates to produce propylbenzene and ethylbenzene as the main products. No products associated with ring saturation were observed.

2. Experimental

2.1 Catalyst synthesis

15 wt% Ni/C catalysts were synthesized by wet impregnation as reported previously. Stoichiometric quantity of nickel nitrate hexahydrate (Sigma-Aldrich) was dissolved in deionized water (8 ml) and added to appropriate amount of Darco carbon (Sigma-Aldrich). The slurry was stirred for 24 h so as to allow the nickel precursor to completely

wet the carbon. The catalyst was subsequently dried overnight at 120°C in an oven. The catalyst was reduced in a N₂ flow (100 ml/min) at 450°C for 2 h with a ramp rate of 7°C/min.

Molybdenum carbide (Mo₂C) was synthesized from ammonium paramolybdate tetra (para)hydrate ((NH₄)₆Mo₇O₂₄·4H₂O, 99%, Alfa Aesar) *in situ* prior to vapor phase HDO reactivity studies. Ammonium paramolybdate tetra (para)hydrate was heated in a 21% CH₄-H₂ mixture (70 ml/min total flow) from room temperature to 650°C at 3°C/min and held at 650°C for 1 hour. The carburized sample (Mo₂C) was then held under pure H₂ flow (55 ml/min) at 650°C for another hour to scavenge residual surface carbon. The catalyst was cooled under H₂ flow to reaction temperature (320°C).

2.2 RCF

Reactions were performed in batch mode using a Parr reactor. Typically, 1 g of biomass (poplar or corn stover, <250 μm) was loaded with 200 mg of 15 wt% Ni/C catalyst and 50 ml methanol (Sigma-Aldrich). Reactor was stirred at 1000 rpm using a magnetic stir bar. Reactor was initially sealed and purged with 30 bar N₂ 3 times, before being resealed and purged with 30 bar H₂. RCF was typically run at 30 bar H₂ pressures. The temperature was controlled by a K-type thermocouple (Omega, model TJ36-CAXL-116u), which was connected to a temperature controller (Digi-Sense, model 68900-10). The reactor was heated from room temperature to 200°C in about 30 min. Reactions were typically run for 6 h, before being quenched with an ice bath. The contents of the reactor were filtered with a 0.2 μm filter. The residual solids were rinsed with approximately 15 ml of methanol while the liquid stream was subjected to a threefold liquid-liquid extraction with water (10 ml) and dichloromethane (DCM, 3 x 10 ml) after removal of solvent methanol by vacuum evaporation. The DCM-extracted phase was then dried by vacuum evaporation to obtain DCM soluble lignin oil. Lignin oil yield was calculated as follows:

$$Yield_{oil} = \frac{oil\ mass}{dry\ biomass \times lignin\ content}$$

The lignin monomer products were analyzed by Gas chromatograph-mass spectrometer (GC-MS, GC-Agilent 7890A and MS-Agilent 5975C). MS was used for identification of species while GC was equipped with a flame ionization detector (FID) for quantification. Lignin oil was dissolved in methanol (15 ml) to a concentration of 5 mg/ml prior to GC-MS analysis on a DB-5 column (Agilent, 30 m length x 0.25 mm ID x 0.25 μm film). The following parameters were used: injector temperature 250°C, detector temperature 300°C, split ratio 1:10. The temperature program started initially by holding at 50°C for 1 min, before ramping at 10°C/min to 280°C. FID was calibrated with propylguaicol, allylsyringol, ethylphenol, methylcoumarate and methyl ferulate, using an external standard of dimethoxybenzene. The monomer yield was calculated using the following equation:

$$\text{Monomer Yield} = \frac{\sum \text{mass of each monomer}}{\text{Initial mass of biomass} \times \text{Total lignin content}}$$

2.3 HDO of RCF lignin oil

Typically, 2-3 batches of lignin oil from RCF of poplar wood and corn stover were independently quantified before being combined for toluene extraction prior to HDO reactivity studies. Assuming complete extraction, 2.5 wt% lignin monomers in toluene is the initial target concentration. Known quantities of toluene were added to dried lignin oil and sonicated to ensure good extraction of lignin monomers into toluene phase. An aliquot of the monomer-toluene phase was injected into the GC-MS to quantify the extraction efficiency.

$$\text{Extraction Efficiency} = \frac{\text{mass of monomer after extraction}}{\text{mass of monomer in dried lignin oil}}$$

Vapor phase HDO experiments were performed in a down-flow stainless steel tubular reactor (0.95 cm OD) with wall thickness (0.089 cm), which is mounted in a single-zone furnace (Applied Test Systems, Series 3210). Temperature is controlled by a temperature controller (Digi-Sense, model 68900-10), connected to a K-type thermocouple (Omega, model TJ36-CAXL-116u). The thermocouple is mounted downstream in the reactor, directly contacting the catalyst bed. 300 mg of ammonium

paramolybdate tetra (para)hydrate was mixed with inert SiC (total 1.0 g), before being placed between two layers of inert SiC (2.0 g SiC in the bottom layer and 1.0 g SiC in top layer). Ammonium paramolybdate tetra (para)hydrate was carburized *in situ* as outlined in section 2.1 prior to the HDO reaction. Typically *ca.* 1 wt% cyclohexane was added to the lignin monomer-toluene phase to serve as an internal standard. Lignin monomers in toluene was delivered to the reactor at 0.6 ml/h via a syringe pump (Harvard Apparatus, model 703005) and mixed with H₂ gas (70 ml/min) at the reactor inlet. This translates to about 170 mg of Mo₂C after carburization.

$$WHSV (h^{-1}) = \frac{\text{mass flow rate of monomers}}{\text{mass of equivalent Mo}_2\text{C}}$$

The reactor outlet lines were heated to 280°C to prevent any condensation. Gas phase composition was analyzed using the same GC-MS as outlined in section 2. The parameters for GC-MS analysis were: Injector temperature of 275°C, detector temperature of 300°C, and split ratio of 1:20. GC oven was initially held at 35°C for 5 min, followed by a 10°C/min ramp to 120°C, and then a 20°C/min ramp to 275°C. A 5-point calibration curve was made for propylbenzene and ethylbenzene using an internal standard of cyclohexane.

3. Results and Discussion

3.1 Product distribution of RCF

Products	Poplar wood Yield (wt%)	Corn stover Yield (wt%)
Ethylphenol	0.0	3.8
Propylguaiacol	8.5	2.7
Propylsyringol	14.1	4.7
Methyl coumarate	0.0	9.8
Methyl ferulate	0.0	9.1
Other	1.6	2.5
Total	24.2	32.7

Table 6.1 Product distribution obtained from RCF of poplar wood and corn stover. Reaction conditions: 1 g of biomass, 200 mg of 15 wt% Ni/C catalyst, 50 ml methanol, 30 bar H₂ at room temperature, 200°C, 6 h.

Table 6.1 shows the average monomer yields obtained after RCF of poplar wood and corn stover. Monomer yield represents the fraction of lignin that can be subsequently upgraded to more valuable fuels and chemicals. The total organic soluble oil yield indicates the extent of delignification. Notably, RCF from poplar wood yielded 24.2 wt% monomers, in close agreement with prior reports.^{18,27,126} Similarly, RCF of corn stover generated 32.7 wt% monomers, ca. 4% higher than that observed by Anderson *et al.* under similar reaction conditions.¹²⁸ This slightly higher yield could be attributed to the higher Nickel loading, larger catalyst mass and the smaller particle size of corn stover used in this study. As expected, monomers from RCF of poplar wood predominantly consist of propylguaiacol and propylsyringol²⁷ (**Figure 6.1**) with a total yield at 22.6 wt% while corn stover lignin oil featured high yields of 18.9 % to methyl coumarate and methyl ferulate¹²⁸ (**Figure 6.2**), typically only obtained from herbaceous feedstocks.

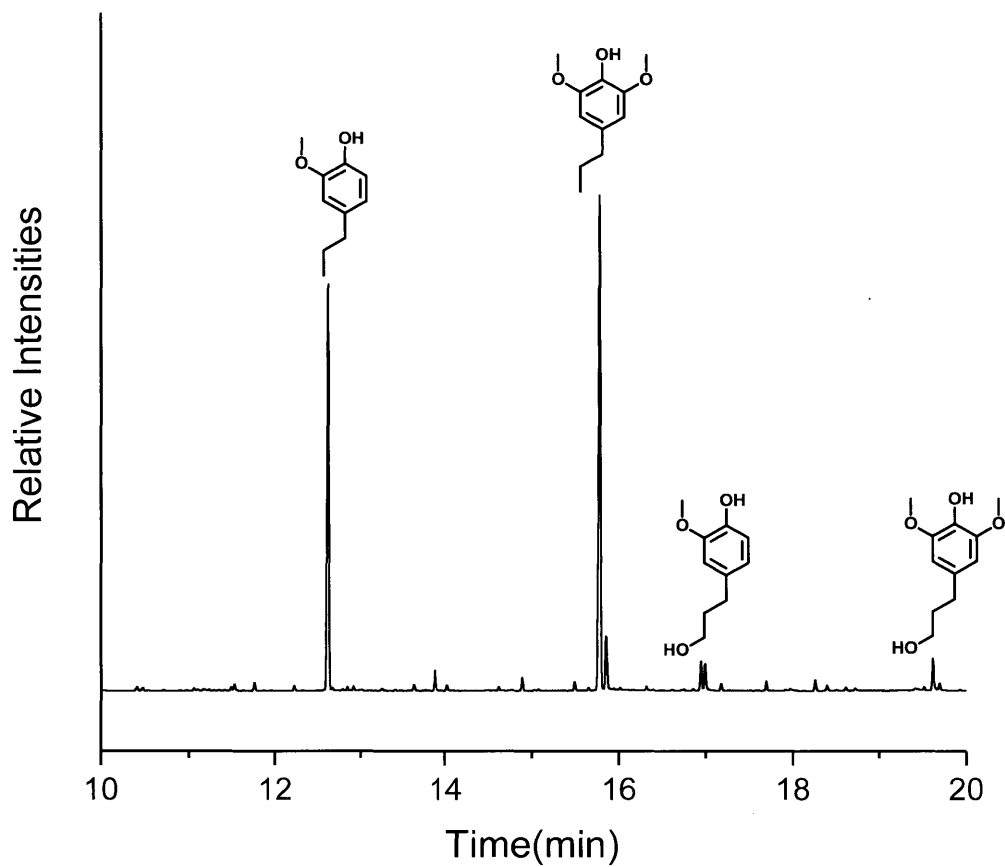


Figure 6.1 Chromatogram obtained after RCF of poplar wood. Reaction conditions: 1 g of biomass, 200 mg of 15 wt% Ni/C catalyst, 50 ml methanol, 30 bar H₂ at room temperature, 200°C, 6 h.

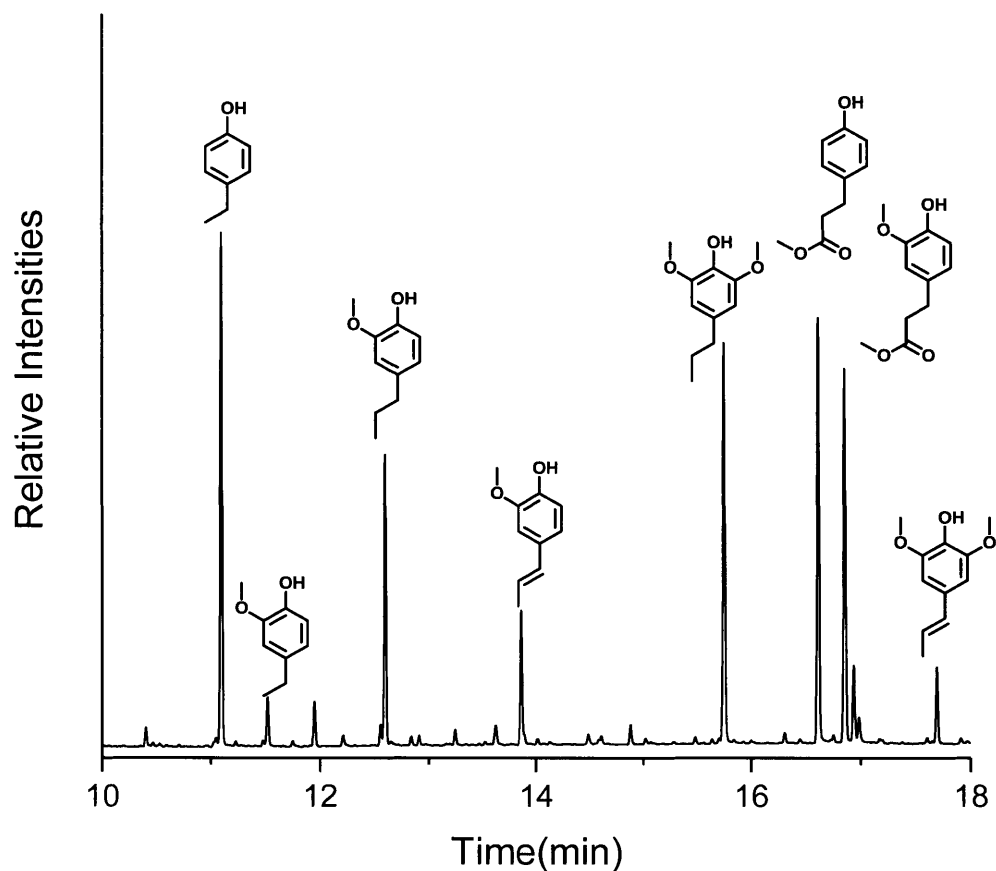


Figure 6.2 Chromatogram obtained after RCF of corn stover. Reaction conditions: 1 g of biomass, 200 mg of 15 wt% Ni/C catalyst, 50 ml methanol, 30 bar H₂ at room temperature, 200°C, 6 h.

3.2 Vapor phase HDO of RCF product - lignin oil

Lignin oils obtained from RCF were extracted in toluene, before being subjected to HDO over Mo₂C catalyst. Typically, the extraction efficiencies for propylguaiacol and propylsyringol units are around 80% while methyl coumarate and methyl ferulate in corn stover lignin oil show complete extraction into toluene phase. A sample chromatogram (**Figure 6.3**) acquired during HDO of lignin oil from poplar wood reveals that Mo₂C is an outstanding HDO catalyst, which fully deoxygenates all the four lignin monomers (Figure 6.1) to produce a single aromatic product – propylbenzene. The absence of ring-saturated products in the chromatogram indicates that Mo₂C catalyzes direct deoxygenation by cleavage of phenolic C-O bond instead of hydrogenation/dehydration

pathway, typically observed over noble metals.⁵⁷ All the oxygen is removed as water (not detected by FID) and methanol, wherein the latter can subsequently undergo HDO to produce methane, observed in the chromatogram. No other peaks were seen in the chromatogram. To our knowledge, this is the first study which converts lignin monomers to a single aromatic hydrocarbon product.

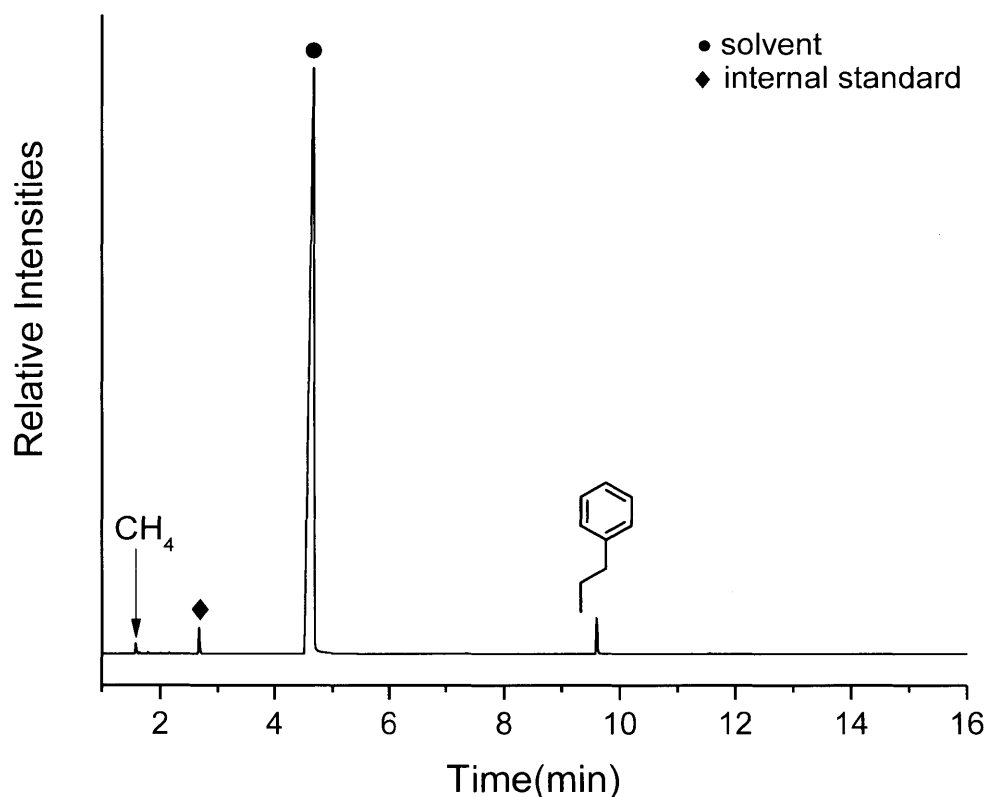


Figure 6.3 Sample chromatogram obtained during HDO of poplar wood lignin oil. Reaction conditions: 1:2.5:96.5 wt% cyclohexane:monomers:toluene at 0.6 ml/h, 300 mg of Ammonium paramolybdate (*in situ* carburized, translates to ~ 170 mg Mo₂C), 70 ml/min H₂, 320°C, P_{total}: 1.013 bar. • represents solvent toluene and ◆ corresponds to internal standard cyclohexane.

The reaction was ran for *ca.* 6 h. Mo₂C was operated at full conversions under these reaction conditions to allow maximum deoxygenation. We note that the product selectivities do not change during the course of reaction, indicating that the catalyst was fully active and producing propylbenzene as the single aromatic product, in addition to methane. Since the composition of monomers in lignin oil is known, their total molar

feed rate can be easily calculated. Assuming complete deoxygenation of each monomer, 1 mole of lignin monomer will yield 1 mole of propylbenzene (**Figure 6.4**).

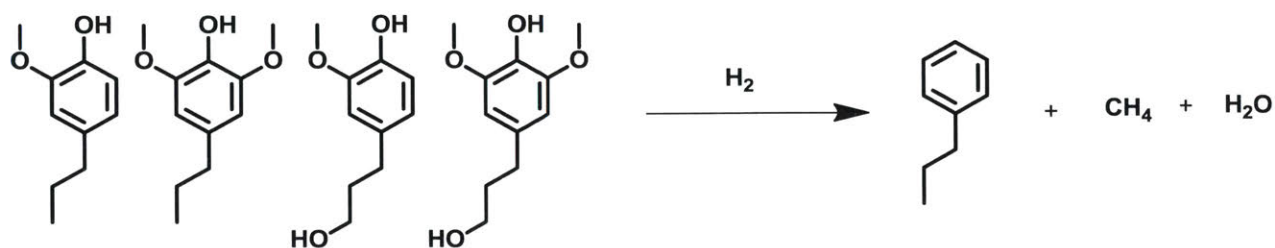


Figure 6.4 Scheme for HDO of lignin monomers in poplar wood lignin oil to produce propylbenzene

By integrating the total moles of propylbenzene produced and normalizing by the total moles of monomers fed, a near quantitative propylbenzene yield (ca. ~101 %) was determined (**Figure 6.5**). The rate of propylbenzene production was relatively constant throughout the reaction. These high yields signify that Mo_2C is an excellent HDO catalyst, capable of upgrading a variety of oxygen-rich monomers to one main aromatic product.

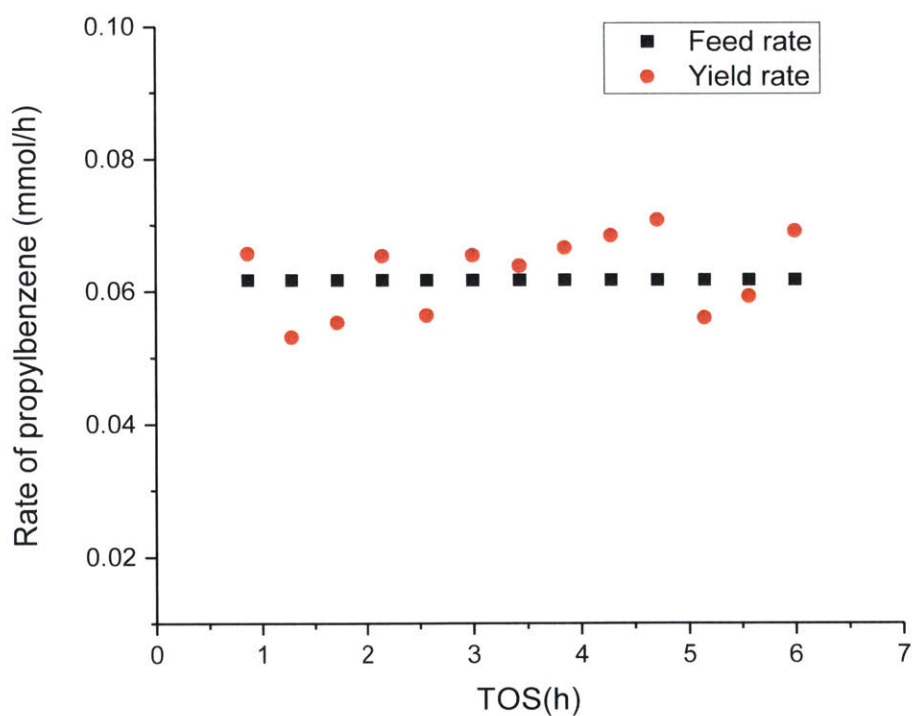


Figure 6.5 Molar feed rate of lignin monomers and propylbenzene during HDO of poplar wood lignin oil. Reaction conditions: 1:2.5:96.5 wt% cyclohexane:monomers:toluene at

0.6 ml/h, 300 mg of Ammonium paramolybdate (*in situ* carburized, translates to ~ 170 mg Mo₂C), 70 ml/min H₂, 320°C, P_{total}: 1.013 bar.

Similarly, corn stover lignin oil was also subjected to HDO after toluene extraction. Again, a sample chromatogram (**Figure 6.6**) obtained during HDO shows that Mo₂C is a highly effective HDO catalyst which deoxygenates all the monomers present in corn stover lignin oil to produce just two products – propylbenzene and ethylbenzene. The presence of ethylbenzene in addition to propylbenzene is expected since HDO of ethyl phenol and ethyl guaiacol initially present in lignin oil will result in ethylbenzene. However, the observed amount of ethylbenzene is greater than that would have been produced from just HDO of ethylphenol and ethylguaiacol. This implies that methylcoumarate and methylferulate undergo decarboxylation to form ethylbenzene, thereby explaining the higher amount of ethylbenzene observed (**Figure 6.7**). However, not all the methylcoumarate and methylferulate undergo decarboxylation to form ethylbenzene, as this would have given rise to a propylbenzene to ethylbenzene ratio of 0.3. The observed average ratio of propylbenzene to ethylbenzene was around 2.3, implying that both methylcoumarate and methylferulate undergo a combination of decarboxylation and reduction to produce ethylbenzene and propylbenzene as HDO products.

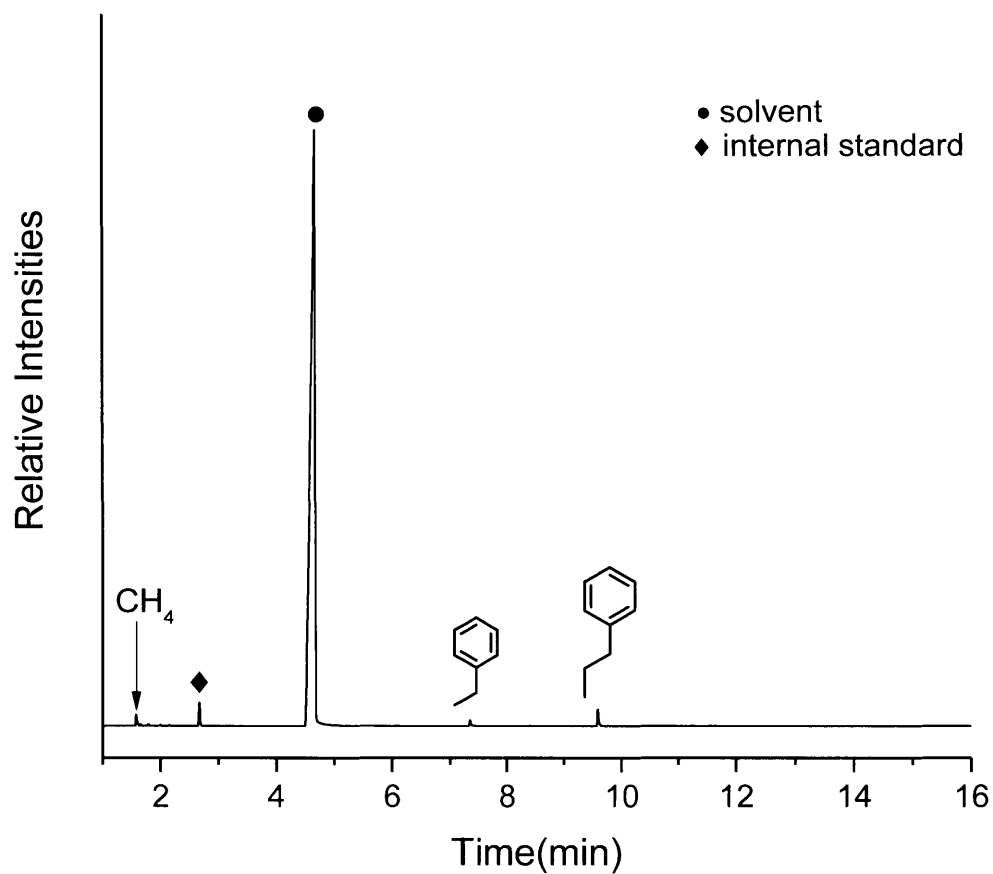


Figure 6.6 Sample chromatogram obtained during HDO of corn stover lignin oil. Reaction conditions: 1:2.5:96.5 wt% cyclohexane:monomers:toluene at 0.6 ml/h, 300 mg of Ammonium paramolybdate (*in situ* carburized, translates to ~ 170 mg Mo₂C), 70 ml/min H₂, 320°C, P_{total}: 1.013 bar. • represents solvent toluene and ◆ corresponds to internal standard cyclohexane.

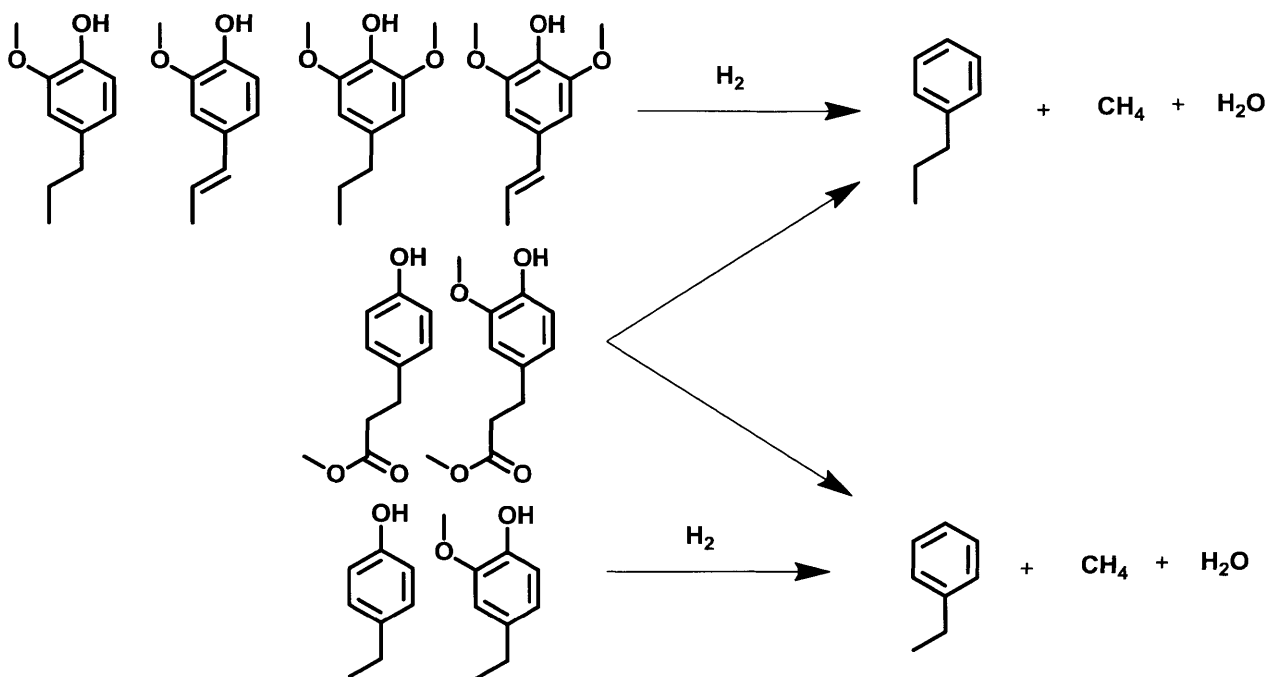


Figure 6.7 Scheme for HDO of lignin monomers in corn stover lignin oil to produce propylbenzene and ethylbenzene

The entire HDO reaction was ran for about 9 h. The total feed rate of monomers and the combined propylbenzene and ethylbenzene production rates are plotted in **Figure 6.8**. Integrating total product generation rates over time leads to a total yield of 66% of propyl and ethyl benzene on per mole basis of lignin monomers. This lower yield from corn stover lignin oil, in comparison to that from poplar wood, is likely due to the larger amount of oxygen present on methyl coumarate/ferulate per molecule than that on propylguaiacol and propylsyringol, thereby causing faster catalyst deactivation. This deactivation is also consistent with the presence of propylphenol peaks in chromatograms towards the end of the reaction, indicating only partial deoxygenation at this point.

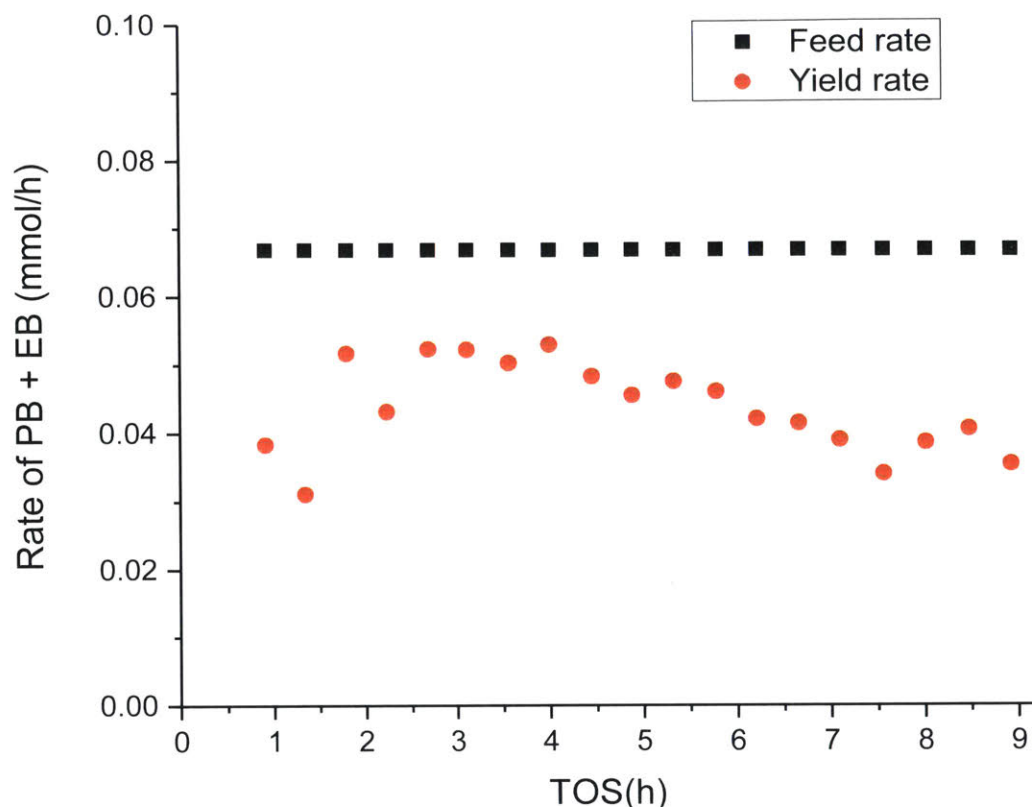


Figure 6.8 Molar feed rate of lignin monomers and combined yield of propylbenzene and ethylbenzene during HDO of corn stover lignin oil. Reaction conditions: 1:2.5:96.5 wt% cyclohexane:monomers:toluene at 0.6 ml/h, 300 mg of ammonium paramolybdate (*in situ* carburized, translates to ~ 170 mg Mo₂C), 70 ml/min H₂, 320°C, P_{total}: 1.013 bar.

3.3 Dehydrogenation of alkylbenzenes to alkenylbenzenes

In section 3.2, we have shown that regardless of the substrate used, a high purity propylbenzene and propylbenzene-ethylbenzene streams are produced after HDO of lignin oil from poplar wood and corn stover respectively. Both propylbenzene and ethylbenzene can undergo dehydrogenation to form methylstyrene and styrene respectively. In fact, dehydrogenation of ethylbenzene to styrene is done on an industrial scale¹³⁵ typically over Shell 105 catalyst (predominantly Fe₂O₃, mixed with Cr₂O₃ and K₂CO₃). Hence, using similar dehydrogenation processes to produce methylstyrene from propylbenzene should be fairly straightforward. Preliminary ASPEN simulations show that separation of propylbenzene from methylstyrene needs less theoretical stages during distillation than that used to separate styrene from

ethylbenzene. Overall, the dehydrogenation to propylbenzene to methylstyrene seems very promising. Methylstyrene, similar to styrene, can act as a viable monomer and polymerize to form polymethylstyrene. Preliminary results suggest that polymethylstyrene has very similar properties to that of polystyrene in terms of glass transition temperature (T_g) and melting point (T_m). Detailed characterization of polymethylstyrene is currently under way to gain more insights into its properties, and for comparison with the polymer polystyrene.

4. Conclusions

RCF of poplar wood and corn stover were performed over Ni/C catalysts in batch mode using Parr reactors to produce lignin oils with monomer yields of 24% and 33% respectively, in close agreement with prior reports. Lignin oils were extracted to a toluene phase, before being contacted with Mo_2C catalytic bed for vapor phase HDO. Remarkably, Mo_2C successfully deoxygenates all oxygen-rich monomers in both lignin fractions to yield only propylbenzene and ethylbenzene as the major products. Ethylbenzene was only observed with corn stover since ethylphenol, methylferulate and methylcoumarate present in corn stover lignin fraction can undergo HDO and decarboxylation to produce ethylbenzene. Both these alkylbenzenes can be dehydrogenated to produce styrene and methylstyrene in high purity. Preliminary ASPEN simulations also suggest that separation of methylstyrene from propylbenzene should be easier than that between styrene and ethylbenzene. Overall, using lignocellulosic biomass to produce potential styrene replacements has been demonstrated.

Acknowledgements

Eric. M. Anderson is greatly acknowledged for major contributions to this chapter.

Chapter 7

Conclusions and Outlook

7.1 Summary of key conclusions

This thesis investigated the reactivity differences between MoO_3 and Mo_2C for HDO of biomass-derived model compounds and used characterization techniques to gain fundamental insights into the catalytically active sites responsible for the reaction over both these materials. This knowledge obtained from model compounds were translated to applications for real biomass upgrading, wherein both these materials were shown to be indeed promising HDO catalysts for real biomass conversions.

First, MoO_3 was shown to be highly effective for HDO of m-cresol by producing predominantly just toluene at temperatures 573-673 K. Bulk and surface characterization reveal that the catalyst deactivates rapidly at high temperature (673 K) due to over-reduction to less active MoO_2 species. In contrast, a new phase, molybdenum oxycarbide, $\text{MoO}_x\text{C}_y\text{H}_z$ was observed at temperatures <623 K, indicating that the carbon incorporation in the MoO_3 lattice likely stabilizes the Mo^{5+} species observed in XPS, thus resulting in higher stability. The effect of reducibility of these dispersed molybdena species on various oxide supports were investigated in a detailed fashion to investigate the role of supports in HDO over m-cresol. Clearly, TiO_2 and ZrO_2 are shown to be ideal supports in promoting HDO reactivity and stability. Post reaction XPS reveal that these two supports stabilize intermediate Mo oxidation states while preventing the over-reduction to lower oxidation states which feature poor HDO reactivity. The reactivity data coupled with characterization studies performed over both bulk and support MoO_3 point to the role of coordinatively unsaturated (CU) sites in HDO, consistent with an oxygen vacancy driven mechanism.

Next, the best performing supported MoO_3 catalysts for HDO of m-cresol i.e. $\text{MoO}_3/\text{TiO}_2$ and $\text{MoO}_3/\text{ZrO}_2$ were selected for HDO of real lignocellulosic biomass (pine) pyrolysis vapors. For the first time, these supported MoO_3 catalysts were used for catalytic fast pyrolysis of real biomass and both these catalysts are shown to be promising HDO catalysts as they produce ca.30 C% hydrocarbon products from pine, comparable to conventional zeolites.

Mo₂C nanoparticles supported on SiO₂ were synthesized and investigated for HDO of 4-methylanisole. Though the catalyst featured high selectivity to aromatic hydrocarbon toluene (97% on C₆⁺ basis), but it suffered from rapid deactivation at atmospheric H₂ pressures. *Ex situ* Extended X-ray and Fine Structure (EXAFS) and XPS reveal that the bulk and surface structure of Mo₂C respectively remain relatively unchanged throughout the reaction, indicating that neither bulk nor surface oxidation can account for the drastic deactivation. Deactivation is likely attributed to the build-up of carbonaceous species on the catalyst surface. To mitigate the effects of coking, the effect of elevated H₂ pressures was investigated in this study. Clearly, higher H₂ pressures promote catalyst stability, with Mo₂C/SiO₂ at 5 bar still exhibiting 40 % conversion even after 140 h time-on-stream. In contrast, MoO₃/SiO₂ operated at identical reaction conditions showed significantly lower conversions (~ 15%) and toluene selectivities (60% at steady state). The presence of oxygenates such as p-cresol throughout the reaction indicates that MoO₃/SiO₂ also cleaves the weaker aliphatic C-O bond, likely catalyzed by the presence of Brønsted sites in MoO₃.

Though bulk and surface characterization of spent catalysts, as detailed in chapters 2-4, were employed to provide insights on the catalytically active phases responsible for HDO across these two materials, all these characterizations were performed on an *ex situ* basis, which do not capture the dynamics of the catalyst surface during the reaction. Hence, for the first time, an operando near-ambient XPS was performed during the course of HDO of biomass-based oxygenate (anisole) over both MoO₃ and Mo₂C to gain fundamental insights into the active sites responsible for HDO as well as attempt to understand the causes of deactivation. Briefly, near-ambient XPS studies reveal that MoO₃ goes through an initial oxidation followed by a subsequent reduction during HDO, consistent with an oxygen vacancy driven mechanism. In contrast, Mo₂C maintains its dominant Mo²⁺ speciation throughout the reaction. This invariance in Mo²⁺ contribution clearly indicates that *in situ* oxidation cannot account for the observed deactivation over Mo₂C, and that coking is indeed the likely cause of deactivation, in agreement with prior *ex situ* characterization. Overall, this ambient XPS study suggests that the HDO seems to operate via distinct active sites on both these Mo-based catalysts.

Since Mo_2C is more effective in selective HDO given its capability in breaking the strong phenolic C-O bonds, Mo_2C was investigated for HDO of lignin monomer stream obtained from poplar wood and corn stover. Mo_2C is shown to be a remarkable HDO catalyst capable of deoxygenating all lignin monomers obtained from both poplar wood and corn stover to produce propylbenzene and ethylbenzene as the main products. Both these alkylbenzenes can be dehydrogenated to produce styrene and methylstyrene in high purity. Preliminary ASPEN simulations also suggest that separation of methylstyrene from propylbenzene should be easier than that between styrene and ethylbenzene. Overall, using lignocellulosic biomass to produce potential styrene replacements has been demonstrated.

7.2 Limitations of this work

Though this thesis compared the reactivity across MoO_3 and Mo_2C in a detailed fashion as well as used ample characterization techniques to reconcile the differences across these two materials, there are still some limitations to this work. Though Mo^{5+} species observed over both bulk and supported MoO_3 is considered to be the likely active site responsible for HDO, the exact identify of this species could not be determined using the characterization techniques employed in this work. Mo^{5+} , a reduced Mo species, could be formed either by carbon incorporation of MoO_3 to form $\text{MoO}_x\text{C}_y\text{H}_z$ or just reduction of MoO_3 to MoO_{3-x} under H_2 flow.⁵² As such, the actual mechanism of HDO over MoO_3 is still yet to be developed.

Though the current work showed that supported MoO_3 catalysts serve as alternative upgrading catalysts to zeolites (e.g., HZSM-5) and that they can be indeed used for catalytic fast pyrolysis (CFP) of lignocellulosic biomass, we note that these experiments are proof-of-concept in nature and were performed in a micropyrolyzer GCMS system. In this system, the char accounts for a significant portion (~39 %) of the carbon from biomass, which does not even see the CFP catalyst. Hence, detailed scale-up studies in different reactor configurations such as FCC-like fluidized bed system will be crucial in better demonstrating the capabilities of these supported MoO_3 catalysts before they can be used commercially for CFP applications. Furthermore, though direct comparison results show that more favourable catalyst-to-biomass ratios can be

achieved with these Mo-based catalysts when compared to zeolites, this ratio needs to be optimized further.

We have shown that Mo₂C can be used for upgrading of lignin streams obtained from reductive catalytic fraction (RCF) process of real biomass to propylbenzene and ethylbenzene. However, this is a cumbersome multi-step process – RCF done in a batch Parr reactor, followed by an extraction to toluene phase, and then subsequent continuous vapor phase HDO of lignin monomers. Again, we note that these experiments were done in a lab-scale proof-of-concept fashion to demonstrate feasibility of Mo₂C as a potential HDO catalyst in upgrading lignin streams. Detailed process optimization needs to be done to potentially combine these multi-step unit operations in order to improve the process economics. Furthermore, current extractions with toluene seem to be pretty efficient with typical extraction efficiencies around 80% based on lignin monomers. However, this toluene extraction might also extract some lignin dimers and oligomers, which were not quantified. As such, more efficient extraction techniques need to be developed to ensure full extraction of monomers while minimizing transfer of dimers and oligomers as these might potentially coke up the catalyst bed since they probably cannot volatilize under the typical HDO conditions of 320°C.

7.3 Future outlook

Based on the limitations aforementioned, I list some ideas in terms of path forward.

Verifying oxygen vacancy driven mechanism over MoO₃

In addition to the reactivity and characterization studies performed in this work, preliminary kinetic experiments (not included in this thesis) were also performed to postulate a mechanism which is consistent with an oxygen vacancy driven mechanism. However, this mechanism needs to be verified, as other mechanisms that are consistent with observed rate orders respect to feed and H₂ cannot be excluded. One simple experiment which can be designed to verify this mechanism will be as follows: Use O¹⁸ labelled m-cresol for HDO over MoO₃. Hypothetically, for an oxygen vacancy based mechanism, this O¹⁸ will now become part of the MoO₃ lattice. The O¹⁸ labelled m-cresol feed can now be stopped and switched with regular m-cresol. The effluent from the reactor can be tracked with a stand-alone MS. If signal corresponding to H₂O¹⁸ i.e. m/z

of 20 increases in intensity upon switching of the cresols, this is a clear indication that the mechanism is indeed an oxygen vacancy driven mechanism as now the evolved water will have O^{18} from the MoO_3 lattice. A titration experiment with water can also confirm the importance of vacancy during HDO. If HDO is suppressed in the presence of water, this observation will indicate that the catalytically active site is likely a vacancy on the MoO_3 surface.

Industrial application of supported MoO_3 catalysts for CFP

As mentioned in chapter 3, coking is considered to be the likely cause of deactivation observed over supported MoO_3 during CFP. Furthermore, as outlined in the previous section, the micropyrolyzer-GCMS set up used in this work is not an ideal set up to mitigate char formation or coking. Hence, going forward, CFP of biomass over these supported MoO_3 catalysts needs to be tested in a FCC-like fluidized bed system. The catalyst lifetime can be prolonged in such systems as the vapor residence time is minimized to prevent secondary reactions, which can typically lead to excessive coking on the catalyst surface. Moreover, supported MoO_3 catalysts can be regenerated by simple calcination in air.⁵³ The FCC-like reactor system typically has a regenerator, which burns off the coke and regenerates the catalyst, which can then be recycled back into the ex situ CFP reactor.^{89,90} This mode of operation lowers the cost associated with purchasing fresh catalyst. Moreover, supported MoO_3 is also an economical catalyst that can be manufactured at scale. The current price for bulk MoO_3 is ca. \$0.02/gram.⁴² We note that sulfided Cobalt Molybdenum (CoMo) and Nickel Molybdenum (NiMo) catalysts supported on Al_2O_3 are already being synthesized and used industrially in hydrodesulfurization of petroleum fractions.⁸⁹ These catalysts are initially synthesized in the oxide forms, and presulfided to obtain sulfides prior to reaction.⁸⁹ In contrast to zeolite catalysts, however, these catalysts have not been formulated into attrition-resistant pellets compatible with FCC-like fluidized bed reactors.⁹⁰ Further studies in this direction will be critical in optimizing the catalyst performance before being used industrially. Process parameters⁹¹ such as temperature, biomass-catalyst ratio, biomass residence time, pyrolysis vapor residence time and catalyst regeneration conditions also need to be optimized prior to scale-up.⁹⁰

Coupling RCF with HDO in one unit operation

We envision a process wherein a single catalyst such as Mo₂C can be used for both RCF and HDO as this will allow both these unit operations to be combined into one. Currently, in our work, Ni/C is used for RCF in a batch reactor while Mo₂C is used for continuous vapor phase HDO. Combining RCF with HDO will eliminate many unit operations, and improve the process economics. However, detailed reaction studies need to be performed on this front. Typically, methanol and ethylene glycol have shown to be best solvents for the RCF process based on their 'lignin-first delignification efficiency' (LFDE) value.¹²⁹ However, both these molecules contain oxygens which will be deoxygenated by Mo₂C during HDO. Hence, oxygen-free solvents need to be systemically tested for RCF which can also be compatible with HDO such as toluene and xylene. However, based on their Reichardt parameter for solvent polarity both toluene and xylene have significantly lower relative polarity values (<0.1) than methanol and ethylene glycol (~0.8). This lower polarity will reduce the extent of delignification. Reaction conditions such as higher temperatures and lower space velocities need to be further optimized to allow the use of such solvents, thus striking a good balance between good delignification and effective HDO. Overall, the merits of combining these two unit operations into one should be compared with the current two-step process and weighed against the lignin and HDO yields to justify this strategy.

Valorization of lignin dimers and oligomers

While this work focused on conversion of lignin monomers to polymer precursors, these lignin monomers typically only comprise about 50 wt% of lignin present in RCF lignin oil.¹²⁸ The remaining constituents are about roughly equal mixtures of lignin dimers and oligomers. Processes aimed at valorizing lignin dimers and oligomers need to be developed to ensure utilization of all fractions of lignin. Specifically, similar to the lignin monomers, dimers also feature C-O ether linkages which can be selectively cleaved over Mo₂C to form hydrocarbons, which can potentially replace existing components in jet fuels as shown in **Figure 7.1**. Furthermore, unlike monomers which feature many C-O ether linkages, dimers and oligomers predominantly consist of monomeric units linked with C-C linkages. Mo₂C can also be used for C-C bond breaking wherein these

deoxygenated dimers could then be broken down into simpler valuable aromatic molecules such as benzene, ethylbenzene and propylbenzene. Mo_2C has shown to be effective in cracking linear alkanes under atmospheric H_2 pressures.¹³⁶ However, the C-C bonds between monomeric units could be much stronger, and thus require harsher conditions such as substantially higher reaction temperatures, which could increase the operating cost. Furthermore, lignin dimers and oligomers typically have much higher boiling points than their monomeric counterparts, thereby requiring derivatization steps to even allow for quantification using GC analysis.²⁷ Since even characterizing these heavier molecules is not that straightforward, careful optimization of reaction conditions for upgrading of dimers and oligomers needs to be performed before they can be completely valorized to useful aromatic molecules.

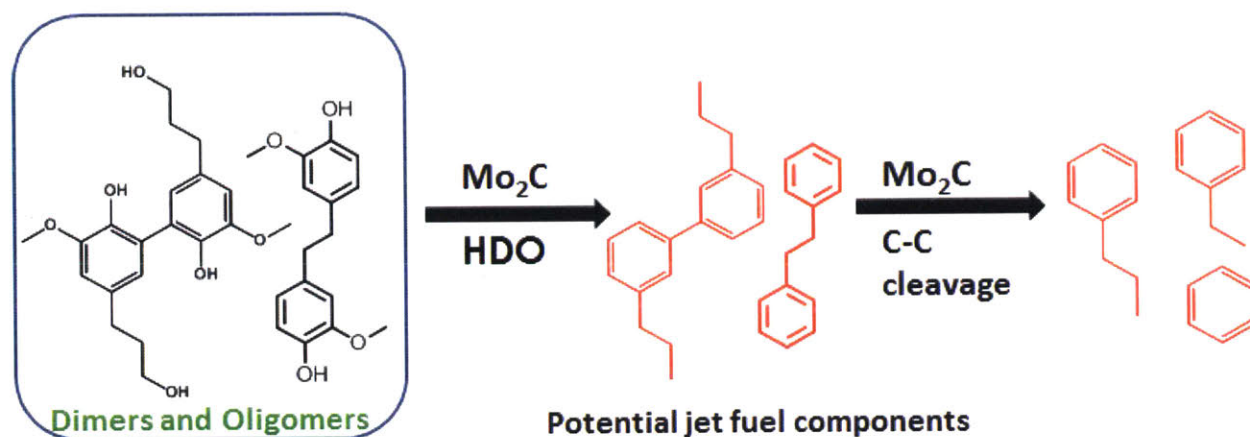


Figure 7.1 Schematic showing potential valorization of representative lignin dimers and oligomers to potential jet fuel components via HDO over Mo_2C , followed by C-C bond cleavage to produce benzene and alkylated benzenes.

References

- (1) *BP Energy Outlook*, 2017.
- (2) Regalbuto, J. R. *Science* **2009**, 325, 822.
- (3) Zhou, C.-H.; Xia, X.; Lin, C.-X.; Tong, D.-S.; Beltramini, J. *Chemical Society Reviews* **2011**, 40, 5588.
- (4) Jarvis, M. W.; Haas, T. J.; Donohoe, B. S.; Daily, J. W.; Gaston, K. R.; Frederick, W. J.; Nimlos, M. R. *Energy & Fuels* **2010**, 25, 324.
- (5) Nigam, P. S.; Singh, A. *Progress in energy and combustion science* **2011**, 37, 52.
- (6) Ralph Sims, M. T. *From 1st-to-2nd Generation Biofuel Technologies*, International Energy Agency, 2008.
- (7) Cherubini, F.; Strømman, A. H. *Biofuels, Bioproducts and Biorefining* **2011**, 5, 548.
- (8) Isikgor, F. H.; Becer, C. R. *Polymer Chemistry* **2015**, 6, 4497.
- (9) Faraco, V. *Lignocellulose conversion*; Springer, 2013.
- (10) Huber, G. W.; Iborra, S.; Corma, A. *Chemical reviews* **2006**, 106, 4044.
- (11) Wang, H.; Male, J.; Wang, Y. *Acs Catalysis* **2013**, 3, 1047.
- (12) Bridgwater, A.; Peacocke, G. *Renewable and sustainable energy reviews* **2000**, 4, 1.
- (13) Heo, H. S.; Park, H. J.; Park, Y.-K.; Ryu, C.; Suh, D. J.; Suh, Y.-W.; Yim, J.-H.; Kim, S.-S. *Bioresource technology* **2010**, 101, S91.
- (14) Asadullah, M.; Rahman, M. A.; Ali, M. M.; Motin, M. A.; Sultan, M. B.; Alam, M. R.; Rahman, M. S. *Bioresource Technology* **2008**, 99, 44.
- (15) Boateng, A. A.; Daugaard, D. E.; Goldberg, N. M.; Hicks, K. B. *Industrial & Engineering Chemistry Research* **2007**, 46, 1891.
- (16) Czernik, S.; Bridgwater, A. *Energy & Fuels* **2004**, 18, 590.
- (17) Galkin, M. V.; Samec, J. S. *ChemSusChem* **2016**, 9, 1544.
- (18) Renders, T.; Van den Bosch, S.; Vangeel, T.; Ennaert, T.; Koelewijn, S.-F.; Van den Bossche, G.; Courtin, C. M.; Schutyser, W.; Sels, B. F. *ACS Sustainable Chemistry & Engineering* **2016**, 4, 6894.
- (19) Kärkäs, M. D.; Matsuura, B. S.; Monos, T. M.; Magallanes, G.; Stephenson, C. R. *Organic & biomolecular chemistry* **2016**, 14, 1853.
- (20) Key, R. E.; Bozell, J. J. *ACS Sustainable Chemistry & Engineering* **2016**, 4, 5123.
- (21) Rinaldi, R.; Jastrzebski, R.; Clough, M. T.; Ralph, J.; Kennema, M.; Bruijninx, P. C.; Weckhuysen, B. M. *Angewandte Chemie International Edition* **2016**, 55, 8164.
- (22) Calvo-Flores, F. G.; Dobado, J. A. *ChemSusChem* **2010**, 3, 1227.
- (23) 2014.
- (24) Ragauskas, A. J.; Beckham, G. T.; Bidy, M. J.; Chandra, R.; Chen, F.; Davis, M. F.; Davison, B. H.; Dixon, R. A.; Gilna, P.; Keller, M. *Science* **2014**, 344, 1246843.
- (25) Sannigrahi, P.; Ragauskas, A. J. *Journal of Biobased Materials and Bioenergy* **2011**, 5, 514.

- (26) Holladay, J.; Bozell, J.; White, J.; Johnson, D. *DOE Report PNNL* **2007**, 16983.
- (27) Van den Bosch, S.; Schutyser, W.; Vanholme, R.; Driessen, T.; Koelewijn, S.-F.; Renders, T.; De Meester, B.; Huijgen, W.; Dehaen, W.; Courtin, C. *Energy & Environmental Science* **2015**, *8*, 1748.
- (28) Tuck, C. O.; Pérez, E.; Horváth, I. T.; Sheldon, R. A.; Poliakoff, M. *Science* **2012**, *337*, 695.
- (29) He, Z.; Wang, X. *Catalysis for sustainable energy* **2012**, *1*, 28.
- (30) Saidi, M.; Samimi, F.; Karimipourfard, D.; Nimmanwudipong, T.; Gates, B. C.; Rahimpour, M. R. *Energy & Environmental Science* **2014**, *7*, 103.
- (31) Elliott, D. C. *Energy & Fuels* **2007**, *21*, 1792.
- (32) Bridgwater, A. V. *Biomass and bioenergy* **2012**, *38*, 68.
- (33) Kubička, D.; Horáček, J. *Applied Catalysis A: General* **2011**, 394, 9.
- (34) Lee, C. R.; Yoon, J. S.; Suh, Y.-W.; Choi, J.-W.; Ha, J.-M.; Suh, D. J.; Park, Y.-K. *Catalysis Communications* **2012**, *17*, 54.
- (35) Lin, Y.-C.; Li, C.-L.; Wan, H.-P.; Lee, H.-T.; Liu, C.-F. *Energy & Fuels* **2011**, *25*, 890.
- (36) Ressler, T.; Walter, A.; Scholz, J.; Tessonier, J.-P.; Su, D. S. *Journal of Catalysis* **2010**, *271*, 305.
- (37) Al-Kandari, H.; Al-Kandari, S.; Al-Kharafi, F.; Katrib, A. *Energy & Fuels* **2009**, *23*, 5737.
- (38) Al-Kandari, H.; Al-Kharafi, F.; Katrib, A. *Journal of Molecular Catalysis A: Chemical* **2008**, *287*, 128.
- (39) Mei, D.; Karim, A. M.; Wang, Y. *The Journal of Physical Chemistry C* **2011**, *115*, 8155.
- (40) Moberg, D. R.; Thibodeau, T. J.; Amar, F. G.; Frederick, B. G. *The Journal of Physical Chemistry C* **2010**, *114*, 13782.
- (41) Prasomsri, T.; Nimmanwudipong, T.; Román-Leshkov, Y. *Energy & Environmental Science* **2013**, *6*, 1732.
- (42) InfoMINE: 2016.
- (43) Ren, H.; Yu, W.; Saliccioli, M.; Chen, Y.; Huang, Y.; Xiong, K.; Vlachos, D. G.; Chen, J. G. *ChemSusChem* **2013**, *6*, 798.
- (44) Lee, W.-S.; Wang, Z.; Zheng, W.; Vlachos, D. G.; Bhan, A. *Catalysis Science & Technology* **2014**, *4*, 2340.
- (45) Xiong, K.; Lee, W. S.; Bhan, A.; Chen, J. G. *ChemSusChem* **2014**, *7*, 2146.
- (46) Lee, W. S.; Wang, Z. S.; Wu, R. J.; Bhan, A. *J Catal* **2014**, *319*, 44.
- (47) Levy, R.; Boudart, M. *science* **1973**, *181*, 547.
- (48) Stottlemeyer, A. L.; Kelly, T. G.; Meng, Q.; Chen, J. G. *Surface Science Reports* **2012**, *67*, 201.
- (49) Lee, W.-S.; Wang, Z.; Wu, R. J.; Bhan, A. *Journal of Catalysis* **2014**, *319*, 44.
- (50) Chen, C.-J.; Bhan, A. *ACS Catalysis* **2017**, *7*, 1113.
- (51) Lee, W.-S.; Kumar, A.; Wang, Z.; Bhan, A. *ACS Catalysis* **2015**, *5*, 4104.
- (52) Prasomsri, T.; Shetty, M.; Murugappan, K.; Román-Leshkov, Y. *Energy & Environmental Science* **2014**, *7*, 2660.

- (53) Shetty, M.; Murugappan, K.; Prasomsri, T.; Green, W. H.; Román-Leshkov, Y. *Journal of Catalysis* **2015**, *331*, 86.
- (54) Murugappan, K.; Mukarakate, C.; Budhi, S.; Shetty, M.; Nimlos, M. R.; Román-Leshkov, Y. *Green Chemistry* **2016**, *18*, 5548.
- (55) Bouchy, C.; Pham-Huu, C.; Heinrich, B.; Chaumont, C.; Ledoux, M. J. *Journal of catalysis* **2000**, *190*, 92.
- (56) Bouchy, C.; Pham-Huu, C.; Heinrich, B.; Derouane, E. G.; Hamid, S. B. D.-A.; Ledoux, M. J. *Applied Catalysis A: General* **2001**, *215*, 175.
- (57) Nie, L.; Resasco, D. E. *Journal of Catalysis* **2014**, *317*, 22.
- (58) Ruddy, D. A.; Schaidle, J. A.; Ferrell III, J. R.; Wang, J.; Moens, L.; Hensley, J. E. *Green Chemistry* **2014**, *16*, 454.
- (59) Choi, J.-G.; Thompson, L. *Applied Surface Science* **1996**, *93*, 143.
- (60) Nag, N. K. *Journal of Catalysis* **1985**, *92*, 432.
- (61) Heracleous, E.; Machli, M.; Lemonidou, A. A.; Vasalos, I. A. *Journal of Molecular Catalysis A: Chemical* **2005**, *232*, 29.
- (62) Yildiz, G.; Pronk, M.; Djokic, M.; van Geem, K. M.; Ronsse, F.; Van Duren, R.; Prins, W. *Journal of Analytical and Applied Pyrolysis* **2013**, *103*, 343.
- (63) Liu, C.; Wang, H.; Karim, A. M.; Sun, J.; Wang, Y. *Chemical Society Reviews* **2014**, *43*, 7594.
- (64) Wan, S.; Wang, Y. *Frontiers of Chemical Science and Engineering* **2014**, *8*, 280.
- (65) Zhang, H.; Xiao, R.; Huang, H.; Xiao, G. *Bioresource Technology* **2009**, *100*, 1428.
- (66) Dutta, A.; Sahir, A.; Tan, E.; Humbird, D.; Snowden-Swan, L. J.; Meyer, P.; Ross, J.; Sexton, D.; Yap, R.; Lukas, J. *Process design and economics for the conversion of lignocellulosic biomass to hydrocarbon fuels. Thermochemical research pathways with in situ and ex situ upgrading of fast pyrolysis vapors*, 2015.
- (67) Li, B.; Ou, L.; Dang, Q.; Meyer, P.; Jones, S.; Brown, R.; Wright, M. *Bioresource technology* **2015**, *196*, 49.
- (68) Mukarakate, C.; Zhang, X.; Stanton, A. R.; Robichaud, D. J.; Ciesielski, P. N.; Malhotra, K.; Donohoe, B. S.; Gjersing, E.; Evans, R. J.; Heroux, D. S.; Richards, R.; Lisa, K.; Nimlos, M. R. *Green Chemistry* **2014**, *16*, 1444.
- (69) Adjaye, J. D.; Bakhshi, N. *Fuel Processing Technology* **1995**, *45*, 161.
- (70) Jae, J.; Tompsett, G. A.; Foster, A. J.; Hammond, K. D.; Auerbach, S. M.; Lobo, R. F.; Huber, G. W. *Journal of Catalysis* **2011**, *279*, 257.
- (71) Mihalcik, D. J.; Mullen, C. A.; Boateng, A. A. *Journal of Analytical and Applied Pyrolysis* **2011**, *92*, 224.
- (72) Jackson, M. A.; Compton, D. L.; Boateng, A. A. *Journal of Analytical and Applied Pyrolysis* **2009**, *85*, 226.
- (73) Mukarakate, C.; Watson, M. J.; ten Dam, J.; Baucherel, X.; Budhi, S.; Yung, M. M.; Ben, H.; Lisa, K.; Baldwin, R. M.; Nimlos, M. R. *Green Chemistry* **2014**, *16*, 4891.
- (74) Zhang, H.; Cheng, Y.-T.; Vispute, T. P.; Xiao, R.; Huber, G. W. *Energy & Environmental Science* **2011**, *4*, 2297.
- (75) Scahill, J.; Diebold, J.; Porwer, A. In *Research in Thermochemical Biomass Conversion*; Springer: 1988, p 927.

- (76) Carlson, T. R.; Tompsett, G. A.; Conner, W. C.; Huber, G. W. *Topics in Catalysis* **2009**, *52*, 241.
- (77) Cheng, Y. T.; Jae, J.; Shi, J.; Fan, W.; Huber, G. W. *Angewandte Chemie* **2012**, *124*, 1416.
- (78) Horne, P. A.; Williams, P. T. *Journal of analytical and applied pyrolysis* **1995**, *34*, 65.
- (79) Sullivan, M. M.; Bhan, A. *ACS Catalysis* **2016**, *6*, 1145.
- (80) Lee, W.-S.; Kumar, A.; Wang, Z.; Bhan, A. *ACS Catal.* **2015**, *5*, 4104.
- (81) Sullivan, M. M.; Held, J. T.; Bhan, A. *J Catal* **2015**, *326*, 82.
- (82) Budhi, S.; Mukarakate, C.; Iisa, K.; Pylypenko, S.; Ciesielski, P. N.; Yung, M. M.; Donohoe, B. S.; Katahira, R.; Nimlos, M. R.; Trewyn, B. G. *Green Chemistry* **2015**, *17*, 3035.
- (83) Nolte, M. W.; Zhang, J.; Shanks, B. H. *Green Chemistry* **2015**.
- (84) Howe, D.; Westover, T.; Carpenter, D.; Santosa, D.; Emerson, R.; Deutch, S.; Starace, A.; Kutnyakov, I.; Lukins, C. *Energy & Fuels* **2015**, *29*, 3188.
- (85) Wang, Y.; Van de Vyver, S.; Sharma, K. K.; Román-Leshkov, Y. *Green Chemistry* **2014**, *16*, 719.
- (86) Evans, R. J.; Milne, T. A. *Energy & Fuels* **1987**, *1*, 123.
- (87) Thangalazhy-Gopakumar, S.; Adhikari, S.; Gupta, R. B.; Tu, M.; Taylor, S. *Bioresource technology* **2011**, *102*, 6742.
- (88) Nam, I. S.; Kittrell, J. *Industrial & Engineering Chemistry Process Design and Development* **1984**, *23*, 237.
- (89) Gary, J. H.; Handwerk, G. E.; Kaiser, M. J. *Petroleum refining: technology and economics*; CRC press, 2007.
- (90) Yildiz, G.; Ronsse, F.; van Duren, R.; Prins, W. *Renewable and Sustainable Energy Reviews* **2016**, *57*, 1596.
- (91) Venderbosch, R. *ChemSusChem* **2015**, *8*, 1306.
- (92) Wang, K.; Johnston, P. A.; Brown, R. C. *Bioresource Technology* **2014**, *173*, 124.
- (93) Chen, C.-J.; Lee, W.-S.; Bhan, A. *Applied Catalysis A: General* **2016**, *510*, 42.
- (94) Hunt, S. T.; Nimmanwudipong, T.; Román-Leshkov, Y. *Angewandte Chemie International Edition* **2014**, *53*, 5131.
- (95) Rostrup-Nielsen, J. R. *Catalysis Today* **1997**, *37*, 225.
- (96) Bu, Q.; Lei, H.; Zacher, A. H.; Wang, L.; Ren, S.; Liang, J.; Wei, Y.; Liu, Y.; Tang, J.; Zhang, Q. *Bioresource technology* **2012**, *124*, 470.
- (97) Furimsky, E. *Applied Catalysis A: General* **2000**, *199*, 147.
- (98) Tran, N.; Uemura, Y.; Chowdhury, S.; Ramli, A. In *Applied Mechanics and Materials*; Trans Tech Publ: 2014; Vol. 625, p 255.
- (99) Choudhary, T.; Phillips, C. *Applied Catalysis A: General* **2011**, *397*, 1.
- (100) Knop-Gericke, A.; Kleimenov, E.; Hävecker, M.; Blume, R.; Teschner, D.; Zafeiratos, S.; Schlögl, R.; Bukhtiyarov, V. I.; Kaichev, V. V.; Prosvirin, I. P. *Advances in Catalysis* **2009**, *52*, 213.
- (101) Patt, J.; Moon, D. J.; Phillips, C.; Thompson, L. *Catalysis Letters* **2000**, *65*, 193.

- (102) Sullivan, M. M.; Chen, C.-J.; Bhan, A. *Catalysis Science & Technology* **2016**, *6*, 602.
- (103) Choi, J.-S.; Bugli, G.; Djéga-Mariadassou, G. *Journal of catalysis* **2000**, *193*, 238.
- (104) Powel, C.; Jablonski, A. *National Institute of Standards and Technology, Gaithersburg, MD, USA* **2010**.
- (105) Lee, J.; Gilmore, I.; Vickerman, J.; Gilmore, I.; Chichester, Wiley, 2009) p: 2009.
- (106) Baltrusaitis, J.; Mendoza-Sanchez, B.; Fernandez, V.; Veenstra, R.; Dukstiene, N.; Roberts, A.; Fairley, N. *Applied Surface Science* **2015**, *326*, 151.
- (107) Song, Z.; Cai, T.; Chang, Z.; Liu, G.; Rodriguez, J. A.; Hrbek, J. *Journal of the American Chemical Society* **2003**, *125*, 8059.
- (108) Clayton, C.; Lu, Y. *Surface and Interface Analysis* **1989**, *14*, 66.
- (109) Scanlon, D. O.; Watson, G. W.; Payne, D.; Atkinson, G.; Egdell, R.; Law, D. *The Journal of Physical Chemistry C* **2010**, *114*, 4636.
- (110) Jones, A. *Journal of Chemical and Engineering Data* **1960**, *5*, 196.
- (111) O-CRESOL, O. S.
- (112) Ambrose, D.; Ellender, J.; Sprake, C.; Townsend, R. *The Journal of Chemical Thermodynamics* **1976**, *8*, 165.
- (113) Oshikawa, K.; Nagai, M.; Omi, S. *The Journal of Physical Chemistry B* **2001**, *105*, 9124.
- (114) Ledoux, M. J.; Huu, C. P.; Guille, J.; Dunlop, H. *Journal of Catalysis* **1992**, *134*, 383.
- (115) Óvári, L.; Kiss, J.; Farkas, A. P.; Solymosi, F. *Surface science* **2004**, *566*, 1082.
- (116) Clair, T. P. S.; Oyama, S. T.; Cox, D. F.; Otani, S.; Ishizawa, Y.; Lo, R.-L.; Fukui, K.-i.; Iwasawa, Y. *Surface science* **1999**, *426*, 187.
- (117) Sugihara, M.; Ozawa, K.-i.; Edamoto, K.; Otani, S. *Solid state communications* **2001**, *121*, 1.
- (118) Gao, Q.; Zhao, X.; Xiao, Y.; Zhao, D.; Cao, M. *Nanoscale* **2014**, *6*, 6151.
- (119) Janz, G. J. *The Journal of Chemical Physics* **1954**, *22*, 751.
- (120) Liang, J.; Ding, R.; Wu, Y.; Chen, Y.; Wu, K.; Meng, Y.; Yang, M.; Wang, Y. *Journal of Molecular Catalysis A: Chemical* **2016**, *411*, 95.
- (121) Deng, X.; Quek, S. Y.; Biener, M. M.; Biener, J.; Kang, D. H.; Schalek, R.; Kaxiras, E.; Friend, C. M. *Surface Science* **2008**, *602*, 1166.
- (122) Delporte, P.; Pham-Huu, C.; Vennegues, P.; Ledoux, M. J.; Guille, J. *Catalysis today* **1995**, *23*, 251.
- (123) Porosoff, M. D.; Yang, X.; Boscoboinik, J. A.; Chen, J. G. *Angewandte Chemie International Edition* **2014**, *53*, 6705.
- (124) Song, Q.; Wang, F.; Cai, J.; Wang, Y.; Zhang, J.; Yu, W.; Xu, J. *Energy & Environmental Science* **2013**, *6*, 994.
- (125) Parsell, T. H.; Owen, B. C.; Klein, I.; Jarrell, T. M.; Marcum, C. L.; Hauptert, L. J.; Amundson, L. M.; Kenttämaa, H. I.; Ribeiro, F.; Miller, J. T. *Chemical Science* **2013**, *4*, 806.
- (126) Ferrini, P.; Rinaldi, R. *Angewandte Chemie International Edition* **2014**, *53*, 8634.

- (127) Pepper, J.; Lee, Y. *Canadian Journal of Chemistry* **1969**, *47*, 723.
- (128) Anderson, E. M.; Katahira, R.; Reed, M.; Resch, M. G.; Karp, E. M.; Beckham, G. T.; Román-Leshkov, Y. *ACS Sustainable Chemistry & Engineering* **2016**, *4*, 6940.
- (129) Schutyser, W.; Van den Bosch, S.; Renders, T.; De Boe, T.; Koelewijn, S.-F.; Dewaele, A.; Ennaert, T.; Verkinderen, O.; Goderis, B.; Courtin, C. *Green Chemistry* **2015**, *17*, 5035.
- (130) Galkin, M. V.; Sawadjoon, S.; Rohde, V.; Dawange, M.; Samec, J. S. *ChemCatChem* **2014**, *6*, 179.
- (131) Wang, G. H.; Cao, Z.; Gu, D.; Pfänder, N.; Swertz, A. C.; Spliethoff, B.; Bongard, H. J.; Weidenthaler, C.; Schmidt, W.; Rinaldi, R. *Angewandte Chemie International Edition* **2016**, *55*, 8850.
- (132) Wang, X.; Rinaldi, R. *Angewandte Chemie International Edition* **2013**, *52*, 11499.
- (133) Schutyser, W.; Van den Bossche, G.; Raaffels, A.; Van den Bosch, S.; Koelewijn, S.-F.; Renders, T.; Sels, B. F. *ACS Sustainable Chemistry & Engineering* **2016**, *4*, 5336.
- (134) Anderson, E. M.; Crisci, A.; Murugappan, K.; Roman-Leshkov, Y. *ChemSusChem* **2017**.
- (135) Sanfilippo, D.; Rylander, P. N. *Ullmann's Encyclopedia of Industrial Chemistry* **2009**.
- (136) Toosi, M.; Peyrovi, M.; Mondgarian, R. *Reaction Kinetics and Catalysis Letters* **2009**, *98*, 133.